VOLUME 80 JULY 1, 1976 NUMBER 14

JPCHAx

THE JOURNAL OF PHYSICAL CHEMISTRY

PUBLISHED BIWEEKLY BY THE AMERICAN CHEMICAL SOCIETY

THE JOURNAL OF

PHYSICAL CHEMISTRY

Published by the
AMERICAN CHEMICAL SOCIETY
BOOKS AND JOURNALS DIVISION
D. H. Michael Bowen, Director

Editorial Department: Charles R. Bertsch, Head; Marianne C. Brogan, Associate Head; Celia B. McFarland, Joseph E. Yurvati, Assistant Editors
Graphics and Production Department: Bacil Guiley, Head
Research and Development Department: Seldon W. Terrant, Head

Advertising Office: Centcom, Ltd., 50 W. State St., Westport, Conn. 06880.

Published biweekly by the American Chemical Society at 20th and Northampton Sts., Easton, Pennsylvania 18042 Second class postage paid at Washington, D.C. and at additional mailing offices.

Editorial Information

Instructions for authors are printed in the first issue of each volume. Please conform to these instructions when submitting manuscripts.

Manuscripts for publication should be submitted to *The Journal of Physical Chemistry*, Department of Chemistry, University of Minnesota, Minneapolis, Minn. 55455. Correspondence regarding **accepted papers and proofs** should be directed to the Editorial Department at the ACS Easton address.

Page charges of $60.00 per page are assessed for papers published in this journal. Ability to pay does not affect acceptance or scheduling of papers.

Bulk reprints or photocopies of individual articles are available. For information write to Business Operations, Books and Journals Division at the ACS Washington address.

Requests for **permission to reprint** should be directed to Permissions, Books and Journals Division at the ACS Washington address. The American Chemical Society and its Editors assume no responsibility for the statements and opinions advanced by contributors.

Subscription and Business Information

1976 Subscription rates—including surface postage

	U.S.	PUAS	Canada, Foreign
Member	$24.00	$29.75	$30.25
Nonmember	96.00	101.75	102.25
Supplementary material	15.00	19.00	20.00

Air mail and air freight rates are available from Membership & Subscription Services, at the ACS Columbus address.

New and renewal subscriptions should be sent with payment to the Office of the Controller at the ACS Washington address. **Changes of address** must include both old and new addresses with ZIP code and a recent mailing label. Send all address changes to the ACS Columbus address. Please allow six weeks for change to become effective. **Claims** for missing numbers will not be allowed if loss was due to failure of notice of change of address to be received in the time specified; if claim is dated (a) North America—more than 90 days beyond issue date, (b) all other foreign—more than 1 year beyond issue date; or if the reason given is "missing from files". Hard copy claims are handled at the ACS Columbus address.

Microfiche subscriptions are available at the same rates but are mailed first class to U.S. subscribers, air mail to the rest of the world. Direct all inquiries to Business Operations, Books and Journals Division, at the ACS Washington address or call (202) 872-4444. **Single issues** in hard copy and/or microfiche are available from Special Issues Sales at the ACS Washington address. Current year $4.75. Back issue rates available from Special Issues Sales. **Back volumes** are available in hard copy and/or microform. Write to Special Issues Sales at the ACS Washington address for further information. **Microfilm** editions of ACS periodical publications are available from volume 1 to the present. For further information, contact Special Issues Sales at the ACS Washington address. **Supplementary material** must be ordered directly from Business Operations, Books and Journals Division, at the ACS Washington address.

Microfiche	U.S.	PUAS, Canada	Other Foreign
Photocopy	$2.50	$3.00	$3.50
1–7 pages	4.00	5.50	7.00
8–20 pages	5.00	6.50	8.00

Orders over 20 pages are available only on microfiche, 4 × 6 in., 24X, negative, silver halide. Orders must state photocopy or microfiche if both are available. Full bibliographic citation including names of all authors and prepayment are required. Prices are subject to change.

American Chemical Society
1155 16th Street, N.W.
Washington, D.C. 20036
(202) 872-4600

Member & Subscription Services
American Chemical Society
P.O. Box 3337
Columbus, Ohio 43210
(614) 421-7230

Editorial Department
American Chemical Society
20th and Northampton Sts.
Easton, Pennsylvania 18042
(215) 258-9111

Notice to Authors last printed in the issue of January 1, 1976

THE JOURNAL OF

PHYSICAL CHEMISTRY

Volume 80, Number 14 July 1, 1976

JPCHAx 80(14) 1519–1644 (1976)

ISSN 0022-3654

COMMUNICATIONS TO THE EDITOR

■ Supplementary material for this paper is available separately (consult the masthead page for ordering information); it will also appear following the paper in the microfilm edition of this journal.

* In papers with more than one author, the asterisk indicates the name of the author to whom inquiries about the paper should be addressed.

AUTHOR INDEX

THE JOURNAL OF
PHYSICAL CHEMISTRY

VOLUME 80, NUMBER 14 JULY 1, 1976

Reactions of Atomic Hydrogen and Deuterium with HBr and DBr

H. Endo and G. P. Glass*

Department of Chemistry, William Marsh Rice University, Houston, Texas 77001 (Received August 29, 1975; Revised Manuscript Received February 5, 1976)

Publication costs assisted by the Petroleum Research Fund

The reactions H + HBr, D + HBr, H + DBr, and D + DBr have been studied directly over the temperature range 230–318 K using a discharge flow apparatus equipped for EPR detection of atoms. Absolute rate constants of $(2.77 \pm 0.32) \times 10^{-10} \exp\{-(2570 \pm 110)/RT\}$, $(6.40 \pm 0.57) \times 10^{-11} \exp\{-(2130 \pm 80)/RT\}$, $(1.09 \pm 0.08) \times 10^{-10} \exp\{-(2190 \pm 110)RT\}$, and $(2.27 \pm 0.21) \times 10^{-11} \exp\{-(1690 \pm 130)/RT\}$ cm^3 molecule^{-1} s^{-1} were obtained for the reactions H + HBr, D + HBr, H + DBr, and D + DBr, respectively. At 295 K, rate constants for the exchange reactions H + DBr → D + HBr and D + HBr → H + DBr were measured as $\leq 3.9 \times 10^{-14}$ and $1.3 \pm 0.4 \times 10^{-14}$ cm^3 molecule^{-1} s^{-1}, respectively.

Introduction

Hydrogen bromide is an effective flame inhibitor. It reduces the rate of flame propagation, decreases flammability, and raises explosion limits.[1-7] It is widely accepted that inhibition results from reactions of HBr with reactive chain centers such as H and OH.

The reaction of atomic hydrogen with HBr has also been a useful testing ground for theories of chemical reaction rates. In 1931, Eyring and Polanyi[8] calculated the H_2Br potential energy surface in their historic paper on the LEP (London–Eyring–Polanyi) method. Since that time many semiempirical surfaces have been constructed, and many transition state calculations have been performed using them.[9-12] Recently, extensive classical trajectory calculations have been made by White,[13] and by White and Thompson[14] using a surface developed following a formalism employed by Raff et al.[15] From these calculations, reactive cross sections and thermal rate constants for the abstraction reaction

$$H + HBr \rightarrow H_2 + Br \quad (1a)$$

and for the atom exchange reaction

$$H' + BrH \rightarrow H'Br + H \quad (1b)$$

have been computed, and the dependence of these parameters on the initial reactant vibrational and rotational states has been determined. The product state distributions and the branching ratios (k_{1a}/k_{1b}) estimated by White[13] have been used by Levine and Bernstein[16] in a test of their information theoretic approach to chemical rate theory.

In this study we have used a discharge flow apparatus equipped for EPR detection to measure directly the absolute rate constants for the reactions of H + HBr, H + DBr, D + HBr, and D + DBr at temperatures between 230 and 318 K. Also, branching ratios have been measured at 295 K for the reactions H + DBr and D + HBr.

Prior to this investigation, the reaction between atomic hydrogen and HBr had been studied directly only at room temperature.[17] At 300 K two measurements[18,19] of the branching ratio for H + DBr have been made. These gave values for k_{1a}/k_{1b} of 13.3 and 170, respectively. These numbers are much higher than that computed by White[13] (0.2–1.0). However, White's computations are supported by measurements made using translationally hot hydrogen atoms,[20] and by the results of a recent molecular beam investigation.[21] Therefore, a reinvestigation of the room temperature measurements seemed particularly appropriate.

Experimental Section

The discharge flow/EPR apparatus was similar to that described in detail previously.[17] For this study two modifications were made. The flow tube was redesigned as shown in Figure 1, and a new improved EPR spectrometer was used. The changes in the flow tube design allowed a constant temperature bath to be installed immediately upstream of the EPR cavity. Slush baths were used to attain temperatures below 295 K. An ice–water mixture was used at 273 K, a dry ice–carbon tetrachloride slush at 252 K, and a dry ice–diethyl ketone slush at 230 K. Temperatures above 295 K were obtained by electrical heating of a well-stirred water bath. A

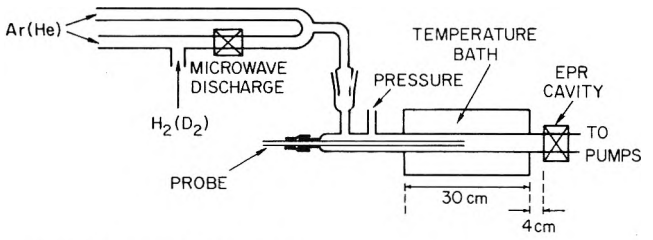

Figure 1. Diagram of apparatus.

strong current of air, directed at the section of the flow tube between the temperature bath and the EPR cavity, ensured that the latter remained at room temperature.

The flow tube was split into two sections in the discharge region in order to reduce free-radical impurities. Only 5% of the carrier gas (Ar or He) passed through the discharge itself. Clyne and Cruse[22] have shown that small atom concentrations are better controlled, and impurity levels much reduced when this arrangement is used. In this study, the bypass was particularly effective in reducing the hydrogen atom concentrations to less than 2% of the D atom concentration.

Deuterium bromide (99%) was obtained from Stohler Isotope Chemicals. It was transferred to a storage bulb using a moderately high vacuum system (10^{-6} Torr), and its isotopic purity periodically checked by running infrared spectra on samples withdrawn from the bulb. Its isotopic purity remained greater than 95% throughout the experiments.

EPR signals were recorded with a Varian E12 spectrometer equipped with an E-235 large access cavity. Relative concentrations of H and D were determined from EPR peak heights. Absolute concentrations were determined by double integration of the spectrometer output, using known pressures of O_2 as calibration standards. Transition probabilities for all of these species are known.[23] The improved sensitivity of the new spectrometer allowed H to be detected at concentrations of 5×10^{11} molecule/cm^3.

In order to prevent atom recombination, the flow tube walls were coated with fluorinated halocarbon wax.[17] Flow tubes were used for experiments only when a direct test, described in detail previously,[17] showed them to be inert to bromine atom recombination.

Results

The overall chemistry of the reaction between atomic hydrogen and HBr has been studied previously.[17] In the absence of wall recombination of H and Br, the stoichiometry is particularly simple, and rate constants can be estimated from measurements of the H(D) concentration. In the present study, the detector sensitivity toward H(D) was high, and rate constants were measured by monitoring H(D) atom decay in mixtures containing an excess of HBr(DBr). In a typical experiment the 20 mm i.d. flow tube was operated at pressures of 1.25 Torr and at linear flow speeds of 1600–2100 cm/s. The initial concentration of HBr(DBr) was 5 to 12 times greater than that of the atoms, and the concentration of the latter was followed for 5–10 ms (10–20 cm). Under these conditions the atom decay was pseudo-first order, and rate constants were estimated from the slopes of plots of log (H) vs. reaction time. Westenberg[24] has shown that the pseudo-first-order rate constant characteristic of the region *within* the temperature bath can be determined from such plots even when the atom concentrations are measured at a fixed point *outside* of this region.

In a few experiments bromine atom production was monitored, and the rate constant for abstraction estimated from plots of ln $[(HBr)_0 - (Br)]$ vs. reaction time.

The results of all of our rate measurements are tabulated in Table I. The experimental conditions pertaining during the study are also listed. At each temperature studied, five to ten rate measurements were usually made. Rate constants obtained from these measurements were corrected for the effects of axial diffusion of atomic hydrogen (deuterium) using the procedure employed by Dickens et al.[25] Binary diffusion coefficients for atomic hydrogen dilute in argon and helium were taken from the work of Khouw, Morgan, and Schiff,[26] while those for atomic deuterium were calculated assuming an inverse square root dependence on reduced mass.[26] Viscous pressure drop along the flow tube amounted to less than 2%/10 cm, and its effects were neglected.

Arrhenius plots for the various reactions are shown in Figure 2. From these, rate constants for the reactions, H + HBr, H + DBr, D + HBr, and D + DBr were estimated as $(2.77 \pm 0.32) \times 10^{-10} \exp\{-(2570 \pm 110)/RT\}$, $(1.09 \pm 0.08) \times 10^{-10} \exp\{-(2190 \pm 110)/RT\}$, $(6.40 \pm 0.57) \times 10^{-11} \exp\{-(2130 \pm 80)/RT\}$, and $(2.27 \pm 0.21) \times 10^{-11} \exp\{-(1690 \times 130)/RT\}$ cm^3 molecule^{-1} s^{-1}, respectively.

At 295 K, branching ratios were measured for the following pairs of reactions

$$H + DBr \rightarrow HD + Br \quad \text{(abstraction)} \qquad (2a)$$

$$H + DBr \rightarrow D + HBr \quad \text{(exchange)} \qquad (2b)$$

and

$$D + HBr \rightarrow HD + Br \quad \text{(abstraction)} \qquad (3a)$$

$$D + HBr \rightarrow H + DBr \quad \text{(exchange)} \qquad (3b)$$

The branching ratio for H + DBr was estimated from measurements of the concentrations of atomic hydrogen and deuterium using the mechanism:

$$H + DBr \rightarrow HD + Br \qquad (2a)$$

$$H + DBr \rightarrow D + HBr \qquad (2b)$$

$$D + DBr \rightarrow D_2 + Br \qquad (4)$$

$$H + HBr \rightarrow H_2 + Br \qquad (1)$$

$$D + HBr \rightarrow DH + Br \qquad (3a)$$

$$D + HBr \rightarrow DBr + H \qquad (3b)$$

When the branching ratio (k_{2b}/k_{2a}) is very small (an assumption justified a posteriori), reactions 1, 3a, and 3b can be neglected and the mechanism simplified to include only reactions 2a, 2b, and 4. Then

$$d(D)/d(H) = [k_4(D)/(H) - k_{2b}]/(k_{2a} + k_{2b}) \qquad (5)$$

This equation can be integrated to give

$$\frac{(D)}{(H)} - \frac{(D)_0}{(H)_0}\left[\frac{(H)_0}{(H)}\right]^a = b\left\{\left[\frac{(H)_0}{(H)}\right]^a - 1\right\} \qquad (6)$$

where

$$a = (k_{2a} + k_{2b} - k_4)/(k_{2a} + k_{2b})$$

$$b = k_{2b}/(k_{2a} + k_{2b} - k_4)$$

and $(H)_0$ and $(D)_0$ are the initial concentrations of H and D, respectively. Since $(k_{2a} + k_{2b})$ and k_4 are known, k_{2b} can be evaluated from eq 6 and the measured concentrations of H and D.

TABLE I: Summary of Measurements of the Rate Constants k^a

H + HBr

T, K	Carrier	P, Torr	V, cm/s	$(HBr)_0$ $\times 10^{-13}$	$(H)_0$ $\times 10^{-13}$	$k \times 10^{12}$
318	Ar	1.28	2110	9.03	1.19	4.33
	Ar	1.28	2110	9.59	1.80	5.11
	Ar	1.28	2110	9.74	1.96	4.79
	Ar	1.28	2110	9.34	1.48	4.83
	Ar	1.36	2010	7.97	1.26	5.00
						4.81 ± 0.30
295	Ar	1.42	1770	9.65	1.49	3.62
	Ar	1.42	1770	10.7	1.23	3.85
	Ar	1.42	1770	9.56	1.83	3.77
	Ar	1.37	1830	10.6	1.23	3.89
	Ar	1.36	1840	11.2	2.63	3.81
	Ar	1.36	1840	13.2	2.21	3.80
	Ar	1.36	1840	13.2	1.52	3.61
	Ar	1.36	1840	11.8	1.64	3.50
	Ar	1.36	1840	12.4	1.83	3.57
						3.71 ± 0.14
273	Ar	1.42	1630	8.56	0.68	1.93
	Ar	1.42	1630	8.56	0.84	1.99
	Ar	1.45	1600	7.36	1.22	2.40
	Ar	1.45	1600	9.02	1.26	2.09
	Ar	1.44	1610	10.7	2.18	2.03
	Ar	1.44	1610	10.7	1.20	2.53
	Ar	1.44	1610	9.81	1.25	2.50
	Ar	1.44	1610	8.57	2.36	2.32
	Ar	1.44	1610	8.94	2.41	2.41
	Ar	1.44	1610	8.63	2.38	2.66
	Ar	1.44	1610	8.21	2.06	2.11
						2.27 ± 0.25
252	Ar	1.44	1490	7.69	1.18	1.71
	Ar	1.44	1490	7.69	1.60	1.29
	Ar	1.44	1490	7.69	0.72	1.59
	Ar	1.43	1490	14.9	2.60	1.45
	Ar	1.44	1490	9.96	2.24	1.65
	Ar	1.44	1490	9.96	2.20	1.31
	Ar	1.44	1490	9.85	2.86	1.35
						1.48 ± 0.17
230	Ar	1.22	1560	13.1	0.709	1.14
	Ar	1.22	1560	13.1	1.22	1.15
	Ar	1.25	1530	10.3	1.26	1.22
	Ar	1.25	1530	11.8	1.28	1.14
	Ar	1.25	1530	11.3	1.28	1.05
						1.14 ± 0.06

D + HBr

T, K	Carrier	P, Torr	V, cm/s	$(HBr)_0$ $\times 10^{-13}$	$(D)_0$ $\times 10^{-13}$	$k \times 10^{12}$
318	He	1.25	2040	11.6	0.596	2.07
	He	1.25	2040	11.6	1.21	2.19
	He	1.25	2040	10.5	1.24	2.03
	He	1.20	2110	9.80	1.22	2.14
	He	1.20	2110	9.80	1.08	2.11
	He	1.20	2110	10.9	0.840	1.92
						2.08 ± 0.09
295	He	1.25	2050	13.7	1.76	1.61
	He	1.25	2050	13.7	1.31	1.81
	He	1.15	1840	13.5	1.68	1.84
	He	1.15	1840	13.5	2.05	1.90
	He	1.15	1840	12.8	2.04	1.74
	He	1.15	1840	12.6	2.09	1.79
						1.78 ± 0.10

Table I (*Continued*):

D + Hbr

T, K	Carrier	P, Torr	V, cm/s	$(HBr)_0$ $\times 10^{-13}$	$(D)_0$ $\times 10^{-13}$	$k \times 10^{12}$
295	Ar	0.96	2037	19.0	2.92	2.06
	Ar	0.95	2058	12.8	2.12	1.81
	Ar	0.98	1995	17.2	2.40	1.64
	Ar	0.98	2058	21.8	2.63	1.82
	Ar	0.96	2037	16.2	2.53	1.73
						1.82 ± 0.16
295[b]	Ar	0.96	2030	2.23	14.3	1.69
	Ar	0.93	2095	1.98	14.3	1.86
	Ar	0.96	2030	2.04	16.2	1.65
	Ar	0.96	2142	2.19	12.4	1.76
	Ar	0.96	2142	2.04	20.2	1.51
						1.69 ± 0.13
273	He	1.18	1760	12.6	1.12	1.21
	He	1.18	1760	12.8	1.22	1.32
	He	1.18	1760	12.8	2.53	1.23
	He	1.18	1760	11.6	1.86	1.25
	He	1.15	1820	18.7	1.19	1.39
	He	1.15	1820	18.7	2.06	1.42
						1.30 ± 0.09
252	He	1.08	1740	13.7	1.12	0.950
	He	1.08	1740	13.9	2.58	0.738
	He	1.08	1740	13.4	2.46	1.05
	He	1.12	1780	12.8	0.988	0.920
	He	1.12	1780	12.8	1.09	0.912
	He	1.12	1780	12.1	1.24	0.727
						0.883 ± 0.126
230	He	1.05	1820	14.9	0.821	0.642
	He	1.05	1820	14.9	0.764	0.664
	He	1.31	1390	18.4	1.24	0.559
	He	1.31	1390	18.4	1.09	0.552
	He	1.31	1390	18.0	1.13	0.603
						0.604 ± 0.049

H + DBr

T, K	Carrier	P, Torr	V, cm/s	$(DBr)_0$ $\times 10^{-13}$	$(H)_0$ $\times 10^{-13}$	$k \times 10^{12}$
318	He	1.32	2020	10.1	0.763	3.12
	He	1.28	2080	9.82	1.24	3.53
	He	1.28	2080	9.82	1.13	3.36
	He	1.15	1680	9.07	1.88	3.37
	He	1.15	1680	9.25	0.974	3.40
						3.36 ± 0.15
295	He	1.28	2040	10.7	1.05	2.65
	He	1.28	2040	10.4	1.13	2.73
	He	1.28	2040	10.4	1.05	2.85
	He	1.28	2040	10.8	1.43	2.74
	He	1.28	2040	10.8	1.27	2.49
						2.69 ± 0.13
273	He	1.32	2020	13.7	1.52	1.74
	He	1.32	2020	13.5	1.68	1.88
	He	1.28	2020	13.9	1.59	1.95
	He	1.28	2020	13.5	1.46	1.88
	He	1.28	2020	12.8	1.63	1.99
						1.89 ± 0.10
252	He	1.25	1680	13.0	1.79	1.69
	He	1.25	1680	13.0	1.82	1.34
	He	1.25	1680	12.6	1.65	1.22
	He	1.25	1680	12.6	1.69	1.31
	He	1.25	1680	10.7	1.20	1.37
						1.39 ± 0.18

Table I (*Continued*):

D + DBr

T, K	Carrier	P, Torr	V, cm/s	$(DBr)_0$ $(D)_0$ $\times 10^{-13}$		$k \times 10^{12}$
318	He	1.25	2100	10.2	1.45	1.63
	He	1.25	2100	10.2	1.63	1.58
	He	1.25	2100	11.4	1.58	1.52
	He	1.25	2100	8.87	1.34	1.54
	He	1.25	2100	8.87	1.24	1.63
						1.58 ± 0.05
295	He	1.30	1920	10.1	1.42	1.51
	He	1.30	1900	12.0	1.01	1.18
	He	1.31	1900	10.1	1.11	1.19
	He	1.31	1900	10.1	1.21	1.16
	He	1.31	1900	9.62	1.01	1.18
						1.24 ± 0.15
273	He	1.23	1820	11.6	1.77	0.876
	He	1.23	1820	11.6	1.94	0.956
	He	1.23	1820	10.1	1.63	1.04
	He	1.23	1820	12.0	1.29	1.04
	He	1.23	1820	11.9	1.53	1.12
						1.01 ± 0.09
252	He	1.15	1680	12.1	1.88	0.841
	He	1.15	1680	12.1	1.64	0.624
	He	1.15	1680	12.9	1.53	0.821
	He	1.15	1680	13.4	1.62	0.723
	He	1.15	1680	15.4	1.86	0.805
	He	1.15	1680	15.4	1.37	0.873
						0.781 ± 0.092

[a] All concentrations in units of molecules cm^{-3}. Rate constants in units of cm^3 $molecule^{-1}$ s^{-1}. [b] Rate constants measured from bromine atom growth measurements.

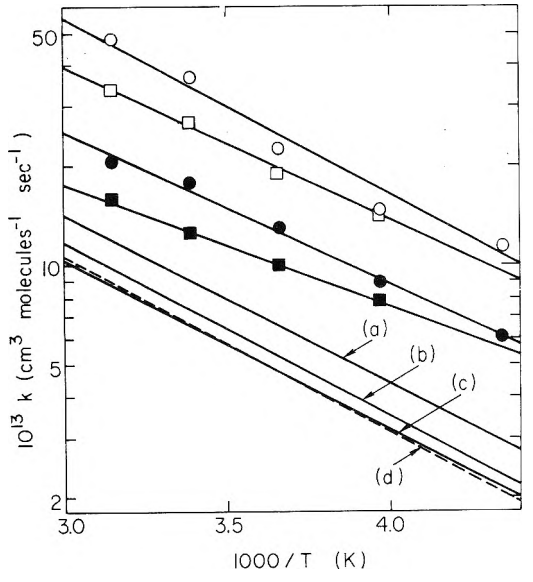

Figure 2. Arrhenius plots (ln k vs. T^{-1}) for H + HBr (○), H + DBr (□), D + HBr (●), and D + DBr (■). The lines marked (a), (b), (c), (d) are BEBO[10] estimates for H + HBr, H + DBr, D + HBr, and D + DBr, respectively.

Measurements of (H) and of (D) made while studying the reactions D + HBr and H + DBr are listed in Table II. From these measurements k_{2b} was estimated, at 295 K, as

$$k_{2b} \leq 3.9 \times 10^{-14} \text{ cm}^3 \text{ molecule}^{-1} \text{ s}^{-1} \quad (7)$$

and k_{3b} estimated as

$$k_{3b} = (1.3 \pm 0.4) \times 10^{-14} \text{ cm}^3 \text{ molecule}^{-1} \text{ s}^{-1} \quad (8)$$

The uncertainty in these rate constants arises mainly as a result of uncertainty in the measured concentration of the exchange product. The noise level on the EPR signal for atomic hydrogen was equivalent to a concentration of 5×10^{11} cm^{-3}, while that for atomic deuterium was equivalent to a concentration of 1.2×10^{12} cm^{-3}. Thus, in the reaction D + HBr, (H) was measured with an uncertainty of between 25 and 50%, while in the reaction H + DBr, the concentration of deuterium was such that only an upper limit for it could be given. In comparison with these uncertainties, those introduced due to our lack of knowledge of the true rate constants and due to uncertainties in reactant atom concentrations are of minor importance. For example, the standard deviations for $(k_{2a} + k_{2b})$ and for k_4, listed in Table I, introduce an uncertainty into k_{2b} of only 5%. The error in $(H)_0/(H)$ amounts to ±2%, and this introduces an uncertainty of only ±3% into k_{2b}.

From the measured rate constants, the branching ratios can be estimated as

$$k_{2a}/k_{2b} > 69 \quad (9)$$

and

$$k_{3a}/k_{3b} = 137(-32 + 60) \quad (10)$$

It is clear that abstraction is overwhelmingly dominant at room temperature.

Discussion

A comparison of the rate constants for the reaction, H + HBr → H_2 + Br, obtained in this study with those obtained in several of the more recent indirect investigations, is shown

TABLE II: Measurements of the Exchange Rate Constants

D + HBr

$(HBr)_0$	$(D)_0$	$(D)_t$	$(H)_0$	$(H)_t$		
10^{14} molecule/cm^3			10^{12} molecule/cm^3		t, ms	k_{3b} 10^{-14} cm^3 molecule^{-1} s^{-1}
2.19	2.13	1.13	2.40	1.66	3.2	0.76
2.19	2.13	1.01	5.40	1.50	3.8	1.24
1.05	2.18	1.44	2.90	1.45	3.2	0.81
1.05	2.18	1.31	2.90	1.54	3.9	1.87
1.05	2.18	1.26	2.90	1.27	4.6	1.15
1.93	1.34	0.62	3.06	0.83	2.3	1.18
1.66	2.89	1.38	6.05	1.94	2.0	1.64
1.66	2.89	1.17	6.05	1.55	2.6	1.67
1.66	2.89	0.94	6.05	1.08	3.6	1.45

$k_{3b} = (1.31 \pm 0.38) \times 10^{-14}$ cm^3 molecule^{-1} s^{-1}

H + DBr

$(DBr)_0$	$(H)_0$	$(H)_t$	$(D)_0$	$(D)_t$		
10^{14} molecule/cm^3			10^{12} molecule/cm^3		t, ms	k_{3b} 10^{-14} cm^3 molecule^{-1} s^{-1}
2.02	1.94	0.80	0	<1.3	2.5	<3.9

$k_{2b} \leq 3.9 \times 10^{-14}$ cm^3 molecule^{-1} s^{-1}

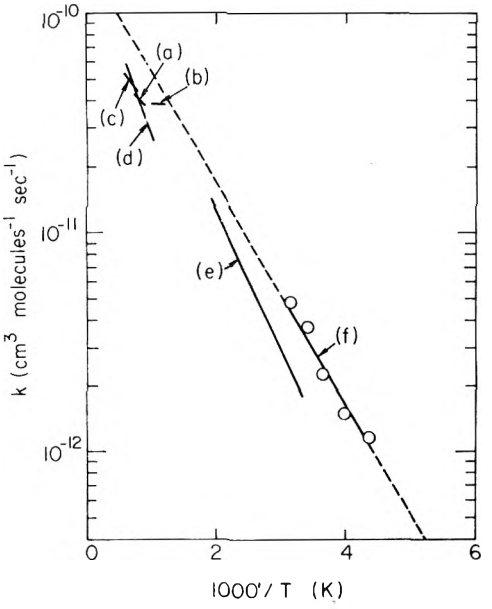

Figure 3. Arrhenius plot showing a comparison of the present results for H + HBr ((O) and (f)) with previous estimates. (a) G. B. Steiner and G. H. Ringrose, *J. Chem. Phys.*, **43**, 4129 (1965). (b) H. Steiner, *Proc. R. Soc., Ser. A*, **173**, 531 (1939). (c) D. Britton and R. M. Cole, *J. Phys. Chem.*, **65**, 1302 (1961). (d) S. D. Cooley and R. C. Anderson, *Ind. Eng. Chem.*, **44**, 1402 (1952). (e) R. A. Fass, *J. Phys. Chem.*, **74**, 984 (1970).

in Figure 3. All of the previous estimates were made either from measurements on the back reaction, or from measurements of the ratio of k_1 to the rate constant for the reaction, H + Br_2 → HBr + Br. The expression $k = 2.77 \times 10^{-10}$ exp(−2570/RT) cm^3 molecule^{-1} s^{-1}, determined from this study, fits all of the data within a factor of 2 over the entire temperature range 230–1673 K.

The only previous measurement of kinetic isotope effects in the H_2Br system was made by Timmons and Weston[11] who studied the reactions Br + H_2, Br + HD, Br + D_2, and Br + HT. Over the temperature range 438–623 K, the ratios of the second-order rate constants were estimated by them as k(Br + H_2)/k(Br + D_2) = (1.32 ± 0.04) exp(1253 ± 37/RT) and k(Br + H_2)/k(Br + HD) = (1.14 ± 0.01) exp(591 ± 4/RT). Since our results refer almost exclusively to the abstraction reaction, they can be cast into this form by multiplication by the appropriate equilibrium constants. Between 230 and 318 K we estimate k(Br + H_2)/k(Br + D_2) as 12.3 ± 2.5 exp(−220 ± 240/RT) and k(Br + H_2)/k(Br + HD) as 4.5 ± 0.9 exp(−580 ± 220/RT). The contribution to k(Br + HD) from reaction −2a is approximately ten times greater than that from reaction −3a.

Although the temperature dependence predicted by our experiments differs from that measured by Weston and Timmons (TW),[11] the absolute values of the ratios between 300 and 500 K are not greatly different. For example, an extrapolation of the data of TW to 300 K gives a value for k(Br + H_2)/k(Br + D_2) 26% greater and a value for k(Br + H_2)/k(Br + HD) 81% greater than that derived in this study. On the average, the kinetic isotope effects measured in this study are a little less than those measured by TW, but they are still greater than those predicted using BEBO calculations,[10] or calculations based on the LEP and LEPS potential energy surfaces discussed by TW.[11] This fact is well illustrated in Figure 2 which, in addition to the various experimental rate constants, contains predictions made from BEBO calculations.

The above comparison between our work and that of Timmons and Weston[11] must be treated with some caution. At least three factors could invalidate such a comparison:

(1) Departures from equilibrium brought about by reaction of the excited atom Br($^2P_{1/2}$). This species has been observed in the reaction H + HBr by Davies et al.[27] in 8% yield. Its initial yield from the reaction might be much higher than this, since it is quenched efficiently by both H and HBr.[28] The heat of formation of Br($^2P_{1/2}$) is 10.5 kcal/mol greater than that of the ground state atom Br($^2P_{3/2}$). Therefore, it may not have been maintained at equilibrium concentration throughout the experiments of Timmons and Weston.

(2) Non-Arrhenius behavior of the rate constants. All of the data presented here has been analyzed assuming an Arrhenius form for the various rate constants. However, marked curva-

ture occurs in the Arrhenius plots for $k_{H_2}/\Sigma k_{HD}$ computed using the BEBO method by Timmons and Weston.[11]

(3) Systematic errors in the rate constants caused by the use of isotopically impure halides. Infrared analysis of the source gases indicated that little initial contamination occurred. However, isotopic impurities could have been introduced by isotope exchange of DBr(HBr) with water molecules absorbed on the flow tube walls. This possibility was explored by measuring, at 295 K, the rate of the reaction D + HBr (a) in the presence of excess HBr by monitoring D atom decay, and (b) in the presence of a large excess of atomic deuterium by monitoring Br atom growth. In the latter case, if wall exchange were important, deuterium atoms would exchange constantly with absorbed water molecules, maintaining D_2O on the flow tube walls. This in turn would transform HBr to DBr, and since $k_4 < k_3$, this would decrease the rate of overall reaction. In our experiments the rate constant measured in the presence of excess D was 7% smaller than that measured in the presence of a large excess of HBr. This difference of one standard deviation is consistent with a 17% conversion of HBr to DBr in the presence of excess D. The percentage transformation should be smaller than this in the more HBr-rich mixtures that were usually studied when measuring rate constants and branching ratios.

The negative temperature dependence estimated in this study for the ratios $k(Br + H_2)/k(Br + D_2)$ and $k(Br + H_2)/k(Br + HD)$ is puzzling. It is contrary to all previous theoretical calculations on the system. However, $Br(^2P_{1/2})$ has always been ignored in such calculations. It is possible that the negative temperature dependence arises as a result of a difference in activation energy between the reactions yielding $Br(^2P_{3/2})$ and those yielding $Br(^2P_{1/2})$. However, it is also possible that it arises as a result of small systematic errors of the type outlined above. These could have a disproportionate effect on the estimated activation energies. For example, a systematic error of only 10% in our lower temperature results would produce an error of 300 cal/mol in our estimated activation energy.

The branching ratios measured in these experiments are in reasonable agreement with those measured previously[18,19] at room temperature. For example, the branching ratio for H + DBr was measured as >69, whereas, previous estimates gave values of 13.3(−5 + 21) and 99(−75 + ∞), respectively. All of these values are much higher than those reported for the hot atom reactions. The branching ratio for H* + DBr, using translationally hot hydrogen atoms, produced with an average energy of 1 eV by photolysis of $DBr-H_2-Br_2$ mixtures, has been measured by Su et al.[20] as 0.2 to 0.8. Also, a branching ratio less than unity can be inferred from the results of a recent hot atom beam experiment. This experiment was conducted by McDonald and Herschbach.[21] They crossed a thermal D beam at 2800 K with an HBr beam at 250 K and determined the cross section for exchange, at a collision energy of 9 kcal/mol, as 1–10 Å^2. No products from the abstraction reaction could be detected.

At first sight, these different experimental measurements of the branching ratio seem inconsistent. However, if the exchange reaction has an activation energy of 5–6 kcal/mol, all of the various measurements are reconciled. A rate constant of $10^{-10}\exp(-5200/RT)$ cm^3 molecule^{-1} s^{-1} for the reaction D + HBr → H + DBr is consistent with a cross section at 9 kcal/mol collision energy of ~10 Å^2, a hot atom branching ratio less than unity, and a room temperature rate constant of 1.3×10^{-14} cm^3 molecule^{-1} s^{-1}. Some support for an activation energy of this magnitude comes from a recent ab initio calculation on the related system HFH. Schaefer et al.[29] found a barrier to exchange in this system of approximately 40 kcal/mol.

TABLE III: Properties of Various H_2Br Potential Energy Surfaces[a]

Model	Properties of the H–H–Br transition state				
	R_{H-H}, Å	R_{H-Br}, Å	ω, cm^{-1}	E_A	E_A'
BEBO[10]	1.43	1.44	2340	2.57	NA
Weston–Timmons[11]	1.62	1.42	2472	0.1	0.001
White[13]	1.24	1.46		1.15	0.9
Parr–Kuppermann[12]	1.15	1.49	1420	1.6	4.0
H_2	0.74		4395		
HBr		1.41	2650		

[a] ω is the symmetric stretch frequency. E_A and E_A' are the potential energies of activation for H–H–Br and H–Br–H, respectively, in kcal/mol.

Many potential energy surfaces have been constructed for the H_2Br system, but few of these are capable of reproducing the absolute rate constants, kinetic isotope effects, and branching ratios determined in this study. It seems that several features must be present in the surface if it is to correctly predict the experimental data. A potential barrier of approximately 2 kcal/mol must be present in the linear H–H–Br surface if the correct rate of the abstraction reaction is to be obtained, and a barrier of approximately 5 kcal/mol present in the H–Br–H surface if the low temperature branching ratio is to be reproduced. In addition, the H–H–Br transition state must not lie too far into the reactant entrance valley. If it does, the symmetric stretching frequency of the transition state is close to that of the isolated HBr molecule, and the computed kinetic isotope effect is much too small.

Several critical parameters of a few representative surfaces are listed in Table III. The BEBO method[10] predicts a transition state that lies far in the entrance valley of the H- - - - HBr system, and yields kinetic isotope effects much smaller than those measured. The LEPS surface of Timmons and Weston[11] similarly underestimates the kinetic isotope effect, and, in addition, severely overestimates the rate of the room temperature exchange reaction. Kinetic isotope effects were not estimated by White,[13] but at room temperature, he overestimated the rate of abstraction by a factor of 6, and the rate of exchange by more than two orders of magnitude. The most accurate predictions are obtained from the multiparameter LEPS surface constructed by Parr and Kuppermann.[12] This surface was constructed to reproduce the low temperature branching ratio.[19] However, it is surprisingly successful in reproducing the measured kinetic isotope effects.

Acknowledgments. Acknowledgment is made to the Donors of the Petroleum Research Fund, administered by the American Chemical Society, for the partial support of this work. The EPR spectrometer was purchased with a grant from the National Science Foundation (GP-32824).

References and Notes

(1) D. R. Clark, R. F. Simmons, and D. A. Smith, *Trans. Faraday Soc.*, **66**, 1423 (1970).
(2) C. Powell and R. F. Simmons, *Symp. (Int.) Combust., [Proc.], 13th*, 585 (1971).
(3) M. J. Day, D. V. Stamp, K. Thompson, and G. Dixon-Lewis, *Symp. (Int.)*

Combust., [*Proc.*], *13th*, 705 (1971).
(4) R. N. Butlin and R. F. Simmons, *Combust. Flame*, **12**, 447 (1968).
(5) W. E. Wilson, Jr., J. T. O'Donovan, and R. M. Fristrom, *Symp. (Int.) Combust.*, [*Proc.*] *12th*, 929 (1969).
(6) D. R. Blackmore, G. O'Donnel and R. F. Simmons, *Symp. (Int.) Combust.*, [*Proc.*], *10th*, 303 (1965).
(7) W. A. Rosser, H. Wise, and J. Miller, *Symp. (Int.) Combust.*, [*Proc.*], *7th*, 175 (1959).
(8) H. Eyring and M. Polanyi, *Z. Phys. Chem.*, **B12**, 279 (1931).
(9) A. Wheeler, B. Topley, and H. Eyring, *J. Chem. Phys.*, **4**, 178 (1936).
(10) S. W. Mayer and L. Schieler, *J. Phys. Chem.*, **72**, 236 (1968).
(11) R. B. Timmons and R. E. Weston, Jr., *J. Chem. Phys.*, **41**, 1654 (1964).
(12) C. A. Parr and D. G. Truhlar, *J. Phys. Chem.*, **75**, 1844 (1971). This review reports new experimental measurements by C. A. Parr and A. Kuppermann.
(13) J. M. White, *J. Chem. Phys.*, **58**, 4482 (1973).
(14) J. M. White and D. L. Thompson, *J. Chem. Phys.*, **61**, 719 (1974).
(15) L. M. Raff, L. Stivers, R. N. Porter, D. L. Thompson, and L. Sims, *J. Chem. Phys.*, **52**, 3449 (1970).
(16) R. D. Levine and R. B. Bernstein, *Chem. Phys. Lett.*, **29**, 1 (1974).
(17) (a) G. A. Takacs and G. P. Glass, *J. Phys. Chem.*, **77**, 1060 (1973); (b) J. E. Breen and G. P. Glass, *J. Chem. Phys.*, **52**, 1082 (1970).
(18) A. Persky and A. Kuppermann, *J. Chem. Phys.*, **61**, 5035 (1974).
(19) Reported in ref 20 of this paper as ref 26.
(20) H. Y. Su, J. M. White, L. M. Raff, and D. L. Thompson, *J. Chem. Phys.*, **62**, 1435 (1975).
(21) J. D. McDonald and D. R. Herschbach, *J. Chem. Phys.*, **62**, 4740 (1975).
(22) M. A. A. Clyne and H. W. Cruse, *J. Chem. Soc., Faraday Trans. 2*, **68**, 1281 (1972).
(23) A. A. Westenberg, *Prog. React. Kinet.*, **7**, 24 (1973).
(24) A. A. Westenberg and N. deHaas, *J. Chem. Phys.*, **46**, 490 (1967).
(25) P. G. Dickens, R. D. Gould, L. W. Linnett, and A. Richmond, *Nature (London)*, **187**, 686 (1960).
(26) B. Khouw, J. E. Morgan, and H. I. Schiff, *J. Chem. Phys.*, **50**, 66 (1969).
(27) P. B. Davies, B. A. Thrush, A. J. Stone, and F. D. Wayne, *Chem. Phys. Lett.*, **17**, 19 (1972).
(28) R. J. Donovan and D. Husain, *Chem. Rev.*, **70**, 509 (1970).
(29) C. F. Bender, B. J. Garrison, and H. F. Schaefer, III, *J. Chem. Phys.*, **62**, 1188 (1975).

Oxidation of HCO Radicals

T. L. Osif and Julian Heicklen*

Department of Chemistry and Ionosphere Research Laboratory, Pennsylvania State University, University Park, Pennsylvania 16802 *(Received August 11, 1975; Revised Manuscript Received February 4, 1976)*

Mixtures of Cl_2, O_2, CH_2O, and sometimes N_2 or He at room temperature (~23 °C) or −7 °C were irradiated at 3660 Å to photodecompose the Cl_2. The chlorine atoms abstract a hydrogen atom from CH_2O to produce HCO radicals which can react with O_2: HCO + O_2 → HCO_3 (1a); HCO + O_2 → CO + HO_2 (1b); HCO + O_2 → CO_2 + HO (1c). The HCO_3 radical ultimately becomes HCOOH, so that HCOOH, CO, and CO_2 become measures of the relative importance of the three reaction paths. It was found that $k_{1a}/k_{1b} = 5 \pm 1$ and $k_{1c}/k_{1b} \leq 0.19$ at ~23 °C (total pressure = 62–704 Torr) and −7 °C (total pressure = 344–688 Torr). As the $[Cl_2]/[O_2]$ ratio increases, the HCO radical can also react with Cl_2: HCO + Cl_2 → Cl + HClO → HCl + CO + Cl (3a); HCO + Cl_2 → $HCOCl_2$ → termination (3b). At both temperatures $k_{3a}/k_{3b} \sim 7.5$ and $k_{3b}/k_{1b} = 6$ (+7, −2).

Introduction

The reactions of HCO with O_2 are important in flames and combustion, in the chemistry of the upper atmosphere, and in the production of oxidants in photochemical smog. Therefore a complete characterization of HCO + O_2 chemistry is important for understanding these processes.

The three possible reactions of HCO with O_2 are:

$$HCO + O_2 \rightarrow HCO_3 \quad (1a)$$

$$\rightarrow CO + HO_2 \quad (1b)$$

$$\rightarrow CO_2 + HO \quad (1c)$$

The HCO_3 ultimately becomes HCOOH, either by proceeding through HCO_3H or HCO_2 as an intermediate. Thus the amounts of HCOOH, CO, and CO_2 produced are measures of the relative efficiencies of reactions 1a, 1b, and 1c, respectively.

The photooxidation of CH_2O, which almost certainly involves the oxidation of HCO radicals, was studied by Carruthers and Norrish[1] who found CO, H_2, HCOOH, and smaller amounts of CO_2 as products, but no peroxides or peracid. They reported quantum yields of CH_2O removal of 8.5–12.6 at 100 °C. Horner et al.[2] studied the photochemical oxidation of CH_2O from 100 to 275 °C and the thermal oxidation to 375 °C and found the same products.

Rate coefficients have been reported by three groups, but they are not in good agreement. Peeters et al.[3] studied low-pressure methane–oxygen flames and reported $k_{1b} \sim 5 \times 10^{-11}$ cm^3/s for 1400 K < T < 1800 K. Demerjian et al.[4] selected the following rate constant values such that simulated data were optimized to fit experimental data.

$$k_{1b} \sim 1.7 \times 10^{-13} \text{ cm}^3/\text{s}; \; k_{1a} \sim 6.8 \times 10^{-14} \text{ cm}^3/\text{s};$$
$$k_{1a}/k_{1b} \sim 0.4$$

Washida et al.[5] measured HCO radical concentrations with a photoionization mass spectrometer and reported $k_{1b} = (5.7 \pm 1.2) \times 10^{-12}$ cm^3/s at 297 K and for total pressures of 1.5–5 Torr.

In this study mixtures of Cl_2, O_2, CH_2O, and sometimes N_2 or He were irradiated with the 3660-Å line of a medium-pressure mercury arc at ~23 and −7 °C. The chlorine photodissociates and the chlorine atoms abstract an H atom from CH_2O to produce HCO radicals. The products measured were HCOOH, CO, and CO_2 so that the above branching ratios for reaction 1 could be obtained.

Experimental Section

Mixtures of Cl_2, CH_2O, O_2, and in some cases an inert gas were irradiated at 3660 Å and at ~23 and −7 °C. The products

TABLE I: Extinction Coefficients at 3660 Å to Base 10, $Torr^{-1}$ cm^{-1}

Temp, °C	$CH_3N_2CH_3$	Cl_2
25	1.87×10^{-4}	1.39×10^{-3}
−7	1.85×10^{-4}	1.53×10^{-3}

CO, CO_2, and HCOOH were measured. The reactions were carried out in a cylindrical quartz cell 5 cm in diameter and 10 cm long. Irradiation was from a Hanovia utility ultraviolet quartz lamp which passed through a Corning 7-37 filter. Since this filter passes light from ~3800 to ~3300 Å, the effective radiation was at 3660 Å.

A conventional high-vacuum line utilizing Teflon stopcocks with Viton "O" rings and glass stopcocks greased with Apiezon N was used to handle the gases. Pressures were measured with a silicone oil manometer in conjunction with a cathetometer, a 0–800 Torr Wallace and Tiernan absolute pressure indicator, and a Veeco thermocouple gauge.

For the studies done at −7 °C, the reaction cell was housed in a box constructed of Dyfoam (made by Zonolite). Two evacuated cylindrical Pyrex cells with quartz windows were placed through the box wall, one through each of two opposite sides. In this way light entered the box from one side via one Pyrex cell, passed through the photolysis cell, and passed out of the other side of the box through the second Pyrex cell to impinge on a RCA 935 phototube.

The temperature inside the box was lowered by passing nitrogen gas through a copper coil immersed in liquid nitrogen and flushing this cold nitrogen through the box. The temperature was measured with an iron vs. constantan thermocouple and was controlled by changing the flow rate.

Actinometry was done by photolyzing $CH_3N_2CH_3$ for which $\Phi\{N_2\} = 1.0$.[6] The light intensity after passing through the cell, I, was always monitored with the RCA 935 phototube. From the N_2 produced, measured by gas chromatography, the measured extinction coefficient of azomethane (see Table I), the light intensity, I_0 (mTorr/min), was calculated using Beer's law. Since I_0 is proportional to the phototube signal when the cell is empty, the now calibrated phototube signal gave a measure of I_0 before each run with chlorine. Thus the absorbed light intensity, I_a, for the runs with chlorine was calculated from Beer's law, knowing I_0, the measured extinction coefficient of Cl_2, and the average Cl_2 pressure (computed as the initial chlorine pressure minus 1/4 the CO produced, since each Cl atom consumed produces one CO molecule). This was done instead of matching absorbances because I_a/I_0 was always less than 16% and was usually 4–5%.

The formaldehyde was prepared from Fisher Scientific paraformaldehyde by a procedure patterned after that of Spence and Wild,[7] and was stored at −196 °C. The chlorine was obtained from the Matheson Co. It was degassed at −160 °C and distilled from −130 °C (n-C_5H_{12} slush) to −160 °C (i-C_5H_{12} slush). After purification it was stored at room temperature in a darkened storage bulb. The azomethane was prepared as described elsewhere.[8]

The oxygen and nitrogen were also obtained from the Matheson Co. The nitrogen was always passed through a trap containing glass wool immersed in liquid nitrogen. The oxygen was treated the same, except the liquid nitrogen was replaced with liquid argon when the total pressure was greater than about 130 Torr. The oxygen and nitrogen were then analyzed by gas chromatography and found to be free of CO_2. The oxygen was also free of CO, but the nitrogen contained 0.035% CO. The CO yields were appropriately corrected in the runs with nitrogen. Runs were also done with helium instead of nitrogen to avoid this problem. This helium was taken from the carrier gas stream of the gas chromatograph and was used without purification.

After photolysis, the noncondensables at −196 °C (or −186 °C, depending on the oxygen pressure) were analyzed for CO by gas chromatography using a 12 ft. × 0.25 in. o.d. copper column packed with 13X molecular sieves, operated at 0 °C. The condensables were distilled from −130 to −196 °C. The gases condensed by liquid nitrogen were analyzed for CO_2 by gas chromatography using a 10 ft. × 0.25 in. o.d. copper column packed with 50–80 mesh Porapak Q. The condensables at −130 °C were then transferred to an ir cell and analyzed for HCOOH. Most, if not all, the CH_2O was removed at −130 °C. If small amounts of CH_2O remained, they would not interfere with the HCOOH analysis, because the HCOOH spectrum is much stronger than that of CH_2O.

Since formic acid exists as a mixture of dimer and monomer, the ir was calibrated for HCOOH by placing known "total" pressures of formic acid (measured on a manometer) in the ir cell and measuring the absorbance at 2940, 1740, and 1213 cm^{-1}. These were plotted in the usual manner. The equilibrium constant, $K = 2.85$ Torr at 300 °C,[9] was used to convert the "total" formic acid pressure in a run to the pressure it would be if it were all monomer. All formic acid numbers reported here have been thus corrected.

Results

When Cl_2 was photolyzed at 3660 Å in the presence of CH_2O and O_2 the products measured were CO, CO_2, and HCOOH. The HCOOH exists as a mixture of the dimer and monomer. However from the known equilibrium constant, $K = 2.85$ Torr at 300 °C,[9] the total HCOOH yield (assuming all monomer) could be obtained and these values are listed in Tables II and III, along with quantum yields of CO and CO_2.

The parameters were varied as follows:

Room temperature: $[O_2]$ from 696 to 1.88 Torr, $[Cl_2]$ from 5.41 to 1.04 Torr, $[CH_2O]$ from 11.2 to 2.32 Torr, $[Cl_2]/[O_2]$ from 0.807 to 0.0020, I_a from 75.4 to 8.4 mTorr/min, the irradiation time from 17.5 to 0.25 min, and total pressure from 704 to 62 Torr.

-7 ± 1 °C: $[O_2]$ from 645 to 1.53 Torr, $[Cl_2]$ from 4.59 to 1.13 Torr, $[CH_2O]$ from 10.1 to 2.84 Torr, $[Cl_2]/[O_2]$ from 0.91 to 0.0022, I_a from 30.0 to 7.18 mTorr/min, the irradiation time from 60 to 1.5 min, and total pressure from 688 to 344 Torr.

The product yields were independent of the variation in all parameters except the ratio $[Cl_2]/[O_2]$. As this ratio increased $\Phi\{CO\}$ increased from a lower limiting value of 2.0 to an upper limiting value of 15 at both temperatures. $\Phi\{HCOOH\}$ however was measured only at low $[Cl_2]/[O_2]$. At high $[Cl_2]/[O_2]$ ratios, it would have been difficult to obtain enough HCOOH to measure accurately, without decomposing an excessive amount of CH_2O. At low $[Cl_2]/[O_2]$ ratios, scatter is not surprising, considering the difficulties in measuring HCOOH. One problem is that some of the acid may be lost to the walls. In the room temperature runs, the HCOOH pressure could usually be measured at 2940, 1740, and 1213 cm^{-1}. The three values obtained usually differed by only a few percent. However, at −7 °C, a different ir instrument was used and the 2940-cm^{-1} peak was usually impossible to measure accurately, and the 1213-cm^{-1} peak was sometimes obscurred by an unknown peak. Nevertheless, when the 1213-cm^{-1} peak could be used the pressure calculated from it was usually less than 10% different from the pressure calculated from the 1740-cm^{-1} peak.

TABLE II: Product Quantum Yields in the Photolysis in Chlorine at 3660 Å in the Presence of O_2 and CH_2O at Room Temperature (~23 °C)

$[Cl_2]/[O_2]$	$[Cl_2]$, Torr[a]	$[O_2]$, Torr	$[CH_2O]$, Torr	$[N_2]$, Torr	[He], Torr	I_a, mTorr/min	Irradiation time, min	$\Phi\{CO\}$	$\Phi\{HCOOH\}$	$\Phi\{CO_2\}$
0.0020	1.29	659	3.71	0	0	20.8	2.0		10.8	
0.0021	1.37	655	3.50	0	0	22.2	4.0	1.63		
0.0021	1.39	655	3.47	0	0	22.0	6.5	1.87	9.0	
0.0021	1.38	649	10.0	0	0	21.0	3.0	1.58	10.3	
0.0024	1.47	609	3.83	0	0	24.4	9.45	1.86	8.50	
0.0024	1.38	570	6.44	0	0	21.8	5.0	1.91	11.1	
0.0031	2.15	696	6.27	0	0	18.7	17.5			0.16
0.0039	1.36	345	3.30	0	0	20.2	5.0	2.15		
0.0040	1.34	339	4.22	0	0	20.4	4.0	2.10	8.67	
0.0040	1.36	346	3.77	0	0	21.2	4.0	2.20		
0.0040	1.38	349	4.18	0	0	20.8	4.0	2.08	8.92	
0.0042	1.40	332	8.93	0	0	23.2	3.5	2.10	10.3	
0.0044	1.49	337	3.18	0	0	22.4	11.0	2.08		
0.0045	1.50	334	4.82	0	0	23.3	6.25	2.24	8.50	
0.0046	1.46	319	9.90	316	0	23.6	3.5	1.34	9.67	
0.014	1.30	90	9.06	0	0	19.7	4.0	2.98	11.8	
0.015	1.53	105	5.65	0	0	21.6	2.0	3.27	11.8	
0.016	1.54	95	6.90	0	0	23.2	4.0	2.87		
0.016	5.41	331	8.90	0	0	75.4	1.0	2.20	9.42	
0.017	1.57	95.0	3.28	0	0	24.4	2.0	2.51	11.2	
0.021	1.04	48.8	5.66	0	590	17.4	10.0	3.17		
0.023	1.20	52.8	5.94	0	590	20.1	10.0	3.04		
0.024	2.35	100	5.96	524	0	22.8	17.5	3.33		0.27
0.028	1.47	52.5	7.90	0	0	60.4	2.75	3.18	10.3	
0.035	1.08	30.6	5.11	0	608	18.0	4.0	4.50		
0.037	2.04	55.4	4.51	0	588	33.0	1.5	3.83		
0.050	2.44	48.8	10.8	584	0	26.0	8.0	5.40		0.17
0.070	1.13	16.1	5.35	0	631	19.2	2.0	5.53		
0.081	1.07	13.2	5.19	625	0	8.4	4.0	9.92		0.13
0.083	2.23	27.0	11.0	613	0	20.5	7.0	8.75		0.13
0.100	2.63	26.2	11.2	615	0	21.8	2.0	9.92		0.36
0.167	2.15	12.9	7.30	627	0	22.2	12.5	7.96		0.15
0.172	2.23	13.0	7.11	627	0	22.3	4.0	10.1		0.15
0.222	1.25	5.62	3.86	0	641	20.6	2.0	8.92		
0.226	2.62	11.6	7.41	638	0	25.8	2.0	11.8		0.14
0.234	2.78	11.9	7.41	618	0	27.5	0.75	11.8		0.33
0.382	3.90	10.2	7.42	0	597	51.4	0.25	12.9		
0.396	2.02	5.1	4.66	0	638	34.0	2.0	12.0		
0.697	1.31	1.88	6.20	0	610	17.9	1.75	12.9		
0.714	1.47	2.06	9.74	0	605	20.2	0.75	16.4		
0.725	1.50	2.07	2.32	0	606	20.5	0.75	14.6		
0.740	2.47	3.34	11.0	639	0	26.9	5.0	14.8		
0.807	4.63	5.74	2.49	0	605	62.9	0.25	11.4		

[a] $[Cl_2] = [Cl_2]_{initial} - [CO]/4$.

The values of $\Phi\{CO_2\}$ are widely scattered, probably because of the low CO_2 yields in general, and the fact that there may be several sources of CO_2. $\Phi\{CO_2\}$ varies from 0.36 to 0.13 at room temperature and from 0.37 to 0.02 at −7 °C.

It was observed that the CH_2O tended to polymerize on the walls of the reaction vessel. Thus irradiation done in the absence of added CH_2O also gave some products. In one run $\Phi\{CO_2\} = 0.49$ and $\Phi\{CO\} = 1.55$. However in the presence of gaseous CH_2O, all the chlorine atoms produced in the photolysis should react with gaseous CH_2O and the wall reaction is ignored (k for $Cl + CH_4 = (1.5 \pm 0.1) \times 10^{-13}$ cm^3/s[15] and the reaction of Cl with CH_2O should be faster).

Some products were also found in dark runs. The yields presented in Tables II and III are corrected accordingly. Usually the time necessary to add the gases to the cell and analyze the products was comparable or greater than the irradiation time. Therefore no attempt was made to measure the dark yield per unit time.

At room temperature the dark correction for CO was 40 mTorr when the O_2 pressure was ~600 Torr, 20 mTorr when the O_2 pressure was ~300 Torr, and no correction when the O_2 pressure was ≤ 100 Torr. The maximum correction was 30%, but the vast majority of the corrections were less than 10%.

The dark production of CO_2 at room temperature was ~2 mTorr. The CO_2 measured after irradiation was usually between 10 and 20 mTorr, but the values ranged from 6.7 to 103 mTorr.

No products from the dark could be seen by ir at room temperature.

At −7 °C, the dark production of CO when the Cl_2 pressure was ~1.5 Torr and the O_2 pressure was ~600 Torr was ~20 mTorr. At other O_2 pressures, the dark production was from 5 to 10 mTorr. The maximum correction was 11% and most were ~5%. However, when the Cl_2 was ~4.5 Torr, ~50 to 70% of the CO found in the light runs was found in the dark

TABLE III: Product Quantum Yields in the Photolysis of Chlorine at 3660 Å in the Presence of O_2 and CH_2O at −7 ± 1 °C

$[Cl_2]/[O_2]$	$[Cl_2]$, Torr	$[O_2]$, Torr	$[CH_2O]$, Torr	[He], Torr	I_a, mTorr/min	Irradiation time, min	$\Phi\{CO\}$	$\Phi\{HCOOH\}$	$\Phi\{CO_2\}$
0.0022	1.43	645	3.37	0	8.85	8.0	2.30		0.21
0.0022	1.33	609	9.80	0	8.33	8.0	3.27	11.5	
0.0023	1.42	558	3.46	0	8.24	12.0	2.22		
0.0023	1.45	628	2.94	0	9.28	8.0	2.84	9.33	0.11
0.0023	1.46	625	3.07	0	8.66	8.0	2.37	8.25	0.13
0.0023	1.41	603	9.80	0	9.37	8.0	3.46	8.66	0.03
0.0024	1.48	622	3.18	0	9.64	8.0	2.82	9.71	0.08
0.0034	1.16	338	7.65	0	7.19	16.0	3.48	11.8	0.04
0.013	4.24	330	10.1	0	26.5	3.0		11.2	0.03
0.017	1.13	65.2	6.94	275	7.18	60.0	3.17	6.77	0.15
0.020	1.32	65.4	6.17	276	8.35	17.1	3.75	10.8	0.08
0.020	1.37	67.6	9.50	350	9.37	5.0	4.12	13.7	0.06
0.021	1.47	68.9	6.34	269	13.3	10.0	3.4	9.46	0.09
0.023	1.51	66.2	9.72	262	9.69	16.0	3.94	11.2	0.07
0.050	1.46	29.3	4.90	309	8.86	8.0	4.18	9.9	
0.093	1.51	16.2	9.18	314	9.90	3.0	6.30		0.17
0.093	1.32	14.2	5.46	314	7.90	11.25	6.22	8.95	
0.094	4.59	49.1	9.30	288	30.0	3.0		13.4	
0.096	1.40	14.6	4.54	321	8.95	7.0	6.2	11.8	0.02
0.099	1.44	14.6	4.00	240	8.75	3.0	6.46		
0.202	1.50	7.44	9.96	326	9.50	3.0	9.37		0.14
0.208	1.45	6.99	7.72	324	9.50	3.0	9.46	9.12	0.27
0.70	1.49	2.13	2.84	329	9.40	2.0	8.83		0.16
0.73	1.34	1.84	8.87	324	9.04	1.5	13.4		0.37
0.91	1.39	1.53	8.70	323	9.06	2.0	15.1		0.11

[a] Pressures reported are at room temperature.

runs. These CO yields were disregarded and are not reported here.

The CO_2 dark production at −7 °C was ~2 mTorr. The CO_2 measured after irradiation was usually less than 10 mTorr, but ranged from 3 to 63 mTorr.

No HCOOH was ever produced in the dark. However, there was another product which was sometimes seen in both light and dark runs at −7 °C. Its largest absorption was at 1185 and 1175 cm^{-1}, and it also absorbs at 2865, 2855, 2800, 2790, 2780, 980, 970, 965, 960, and 950 cm^{-1}. (There may be more than one compound.) No correlation could be found between this "unknown" and the experimental parameters or product quantum yields.

Discussion

At 3660 Å only the Cl_2 absorbs and it photodecomposes to give chlorine atoms which can then react with CH_2O

$$Cl_2 + h\nu\ (3660\ Å) \rightarrow 2Cl \quad \text{rate} = I_a$$

$$Cl + CH_2O \rightarrow HCl + HCO \tag{2}$$

The HCO can react with O_2 or Cl_2

$$HCO + O_2 \rightarrow HCO_3 \tag{1a}$$

$$\rightarrow HO_2 + CO \tag{1b}$$

$$\rightarrow HO + CO_2 \tag{1c}$$

$$HCO + Cl_2 \rightarrow HClCO + Cl \rightarrow HCl + CO + Cl \tag{3a}$$

Reaction 1a should be pressure dependent at sufficiently low pressures, but at the pressures used in our studies, there is no indication of a total pressure effect so we can consider reaction 1a to be in the second-order region.

The fates of the species produced from the HCO reactions are as follows: HCO_3 ultimately gives HCOOH. The route we favor is

$$HCO_3 + H_2CO \rightarrow HCO_3H + HCO \tag{4}$$

$$HCO_3H \rightarrow HCOOH + (1/2)O_2 \text{ on the wall} \tag{5}$$

There is no direct evidence for reaction 4. Performic acid was never observed in this study. However it was always at least 45 min after the run that the ir spectrum was taken. It was assumed that all the HCO_3H decomposed in that time.

It has been shown that for the analogous oxidation of CH_3CHO, the sole initial acid is peracetic acid and it decomposes quantitatively to CH_3COOH.[10] We would expect the same behavior for HCO oxidation with the conversion of HCO_3H to HCOOH being even faster. Performic acid has been observed to be much less stable than peracetic acid, its decomposition being appreciable even at 0 °C.[11] Bone et al.,[12] however, in the thermal oxidation of CH_2O reported observing peroxides, "one which behaved as though it were the performic acid", and formic acid. Formic acid has also been seen by many other workers in the photooxidation of CH_2O.[1,2,13,14]

The HO_2 radical is removed by

$$2HO_2 \rightarrow H_2O_2 + O_2 \tag{6}$$

which proceeds with a rate coefficient of $k_6 = 3.3 \times 10^{-12}$ cm^3/s.[15] The possible competing reaction

$$HO_2 + CH_2O \rightarrow H_2O_2 + HCO$$

is so slow ($k = 1.7 \times 10^{-12} \exp\{-8000/RT\}$ cm^3/s[15]) that it never makes more than an 8% contribution to $\Phi\{CO\}$ and usually much less. Since this is within the experimental uncertainty of the CO measurements, this reaction can be ignored.

The OH radical reacts rapidly with H_2CO

$$OH + H_2CO \rightarrow H_2O + HCO \tag{7}$$

The rate coefficient for the reaction of Cl with CH_4 is k = (1.5

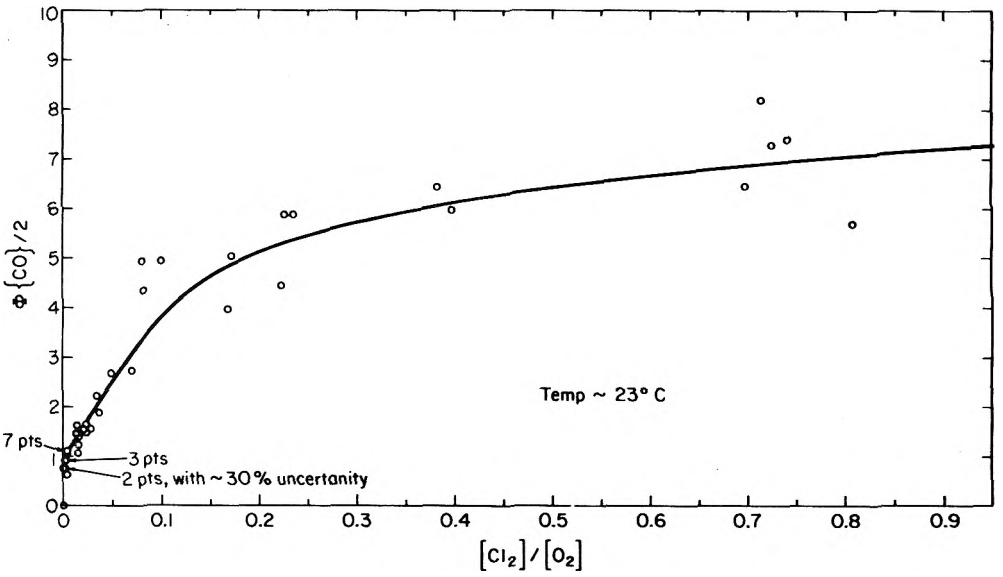

Figure 1. Plot of $\Phi\{CO\}/2$ vs. $[Cl_2]/[O_2]$ in the photolysis of Cl_2 in the presence of O_2 and CH_2O at room temperature (~23 °C).

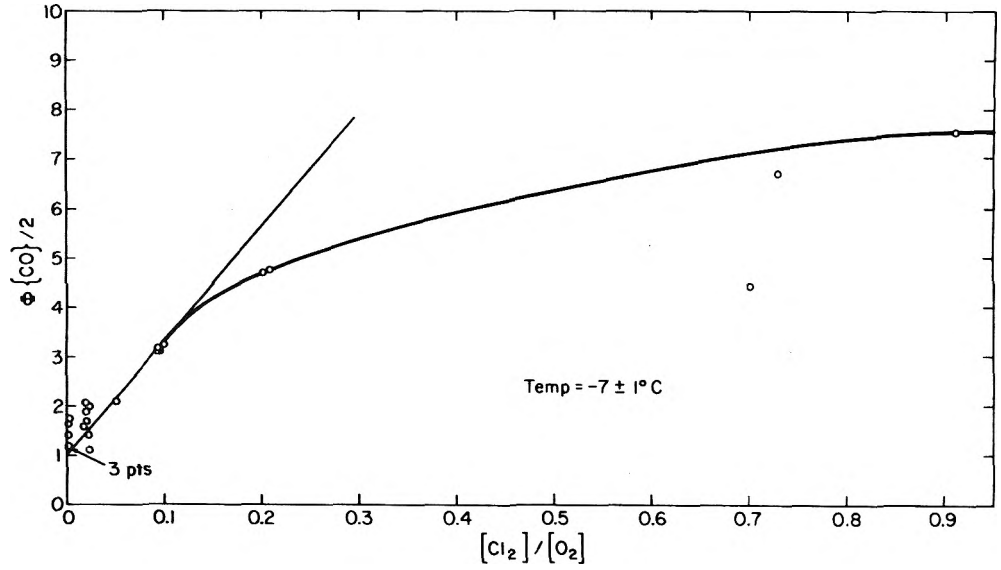

Figure 2. Plot of $\Phi\{CO\}/2$ vs. $[Cl_2]/[O_2]$ in the photolysis of Cl_2 in the presence of O_2 and CH_2O at −7 °C.

± 0.1) × 10^{-13} cm^3/s.[15] The rate coefficient k_2 is probably faster. The rate coefficient $k_7 = 1.4 \times 10^{-11}$ cm^3/s.[15] These rate coefficients are so large that competing reactions can be ignored. Even the reaction of Cl with O_2 plays no role since it is highly reversible

$$Cl + O_2 \rightleftarrows ClO_2$$

Finally the HClCO species is known to decompose readily to HCl and CO.[16] To check that all the HClCO was decomposed before analysis at room temperature, the gases of two runs were allowed to remain in the photolysis cell for 1 h after photolysis before the analysis was started. Normally, the time between the end of photolysis and the start of the analysis was less than 1 min. If all the HClCO were not decomposed, these two runs should contain an excess of CO relative to the others. They did not. At −7 °C, the gases were permitted to warm for ~25 min after photolysis before the analysis was started.

The above mechanism predicts that $\Phi\{CO\}$ should continually increase with increasing $[Cl_2]/[O_2]$. Figures 1 and 2 show plots of $\Phi\{CO\}/2$ vs. $[Cl_2]/[O_2]$ at room temperature and −7 °C, respectively, and it is clear that an upper limiting value is reached at each temperature. Consequently an additional terminating step is needed which is important at high $[Cl_2]/[O_2]$ ratios but which is independent of I_a or any of the individual reactant pressures. The indicated step is the analogous one to reaction 1a.

$$HCO + Cl_2 \rightarrow HCOCl_2 \rightarrow \text{termination} \qquad (3b)$$

The production of formyl chloride from the photolysis of Cl_2 in the presence of formaldehyde was shown by Krauskopf and Rollefson.[17] They reported quantum yields of ~10^4 at total pressures of 30–60 Torr at 80 °C. Presumably, the product of the HCO + Cl_2 termination reaction postulated here is unstable under their conditions and thus would not be an effective termination, allowing larger quantum yields to be obtained in their system.

The mechanism now predicts that at high values of $[Cl_2]/[O_2]$, the upper limiting value of $\Phi\{CO\}/2$ should be equal to

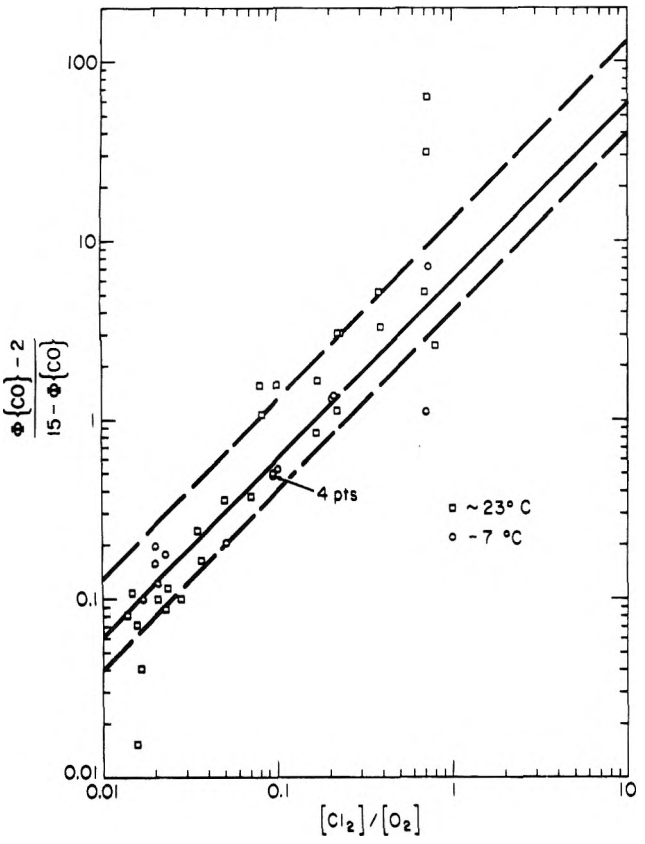

Figure 3. Log–log plot of $(\Phi\{CO\} - 2)/(15 - \Phi\{CO\})$ vs. $[Cl_2]/[O_2]$ in the photolysis of Cl_2 in the presence of O_2 and CH_2O at room temperature (~23 °C) and −7 °C.

k_{3a}/k_{3b}. The data in Figure 1 indicate an upper limiting value of ~7.5 for $\Phi\{CO\}/2$ at high values of $[Cl_2]/[O_2]$. In Figure 2, the data are much more limited, but the same upper limiting value for $\Phi\{CO\}/2$ is not unreasonable, and this is assumed to be the case. Application of the steady-state hypothesis to the mechanism gives

$$[HCO] = 2I_a/(k_{1b}[O_2] + k_{3b}[Cl_2])$$

and the quantum yields of each of the measured products should follow the rate laws:

$$\frac{\Phi\{CO\} - 2}{2k_{3a}/k_{3b} - \Phi\{CO\}} = \frac{k_{3b}[Cl_2]}{k_{1b}[O_2]} \quad (I)$$

$$\Phi\{HCOOH\}^{-1} = \frac{k_{1b}}{2k_{1a}} + \frac{k_{3b}[Cl_2]}{2k_{1a}[O_2]} \quad (II)$$

$$\Phi\{CO_2\}^{-1} = \frac{k_{1b}}{2k_{1c}} + \frac{k_{3b}[Cl_2]}{2k_{1c}[O_2]} \quad (III)$$

Figure 3 shows log–log plots of the left-hand side of eq I vs. $[Cl_2]/[O_2]$ at room temperatures and −7 °C, where the values of $k_{3a}/k_{3b} \sim 7.5$ is used to evaluate the ordinate. In Figure 3 the points at low and high values of $[Cl_2]/[O_2]$ are inaccurate because they are computed from small differences of similar numbers. Since the slope of the log–log plot is forced to unity, the dashed lines represent outside reasonable limits for the points at $[Cl_2]/[O_2]$ between 0.02 and 0.6. From these lines outside limits to k_{3b}/k_{1b} are found to be 4 and 13. The solid line represents the best fit to the data and gives $k_{3b}/k_{1b} = 6$. Thus $k_{3b}/k_{1b} = 6\ (+7, -2)$.

TABLE IV: Summary of Rate Coefficient Ratios at Room Temperature and −7 °C, and for Total Pressures of 704–62 and 688–344 Torr, respectively

k_{3b}/k_{1b}	$6(+7, -2)$
k_{1a}/k_{1b}	5 ± 1
k_{1c}/k_{1b}	≤ 0.19
k_{3a}/k_{3b}	~7.5

All of the data obtained for $\Phi\{HCOOH\}$ were at low values of $[Cl_2]/[O_2]$, where the last term in eq II is negligible. The values for $\Phi\{HCOOH\}$ generally lie between 8 and 12 at −7 °C and room temperature, so that $k_{1a}/k_{1b} = 5 \pm 1$. The pressure ranged from 704 to 62 Torr at room temperature and from 688 to 344 Torr at −7 °C.

The data for CO_2 were badly scattered but at both temperatures they never exceeded 0.38, so that the upper limiting value for k_{1c}/k_{1b} is 0.19 at both temperatures. The low yield of CO_2 is in agreement with work done by Carruthers and Norrish[1] and Horner et al.[2] who found low yields of CO_2 in the photochemical oxidation of formaldehyde.

The rate coefficient ratios obtained in this study are summarized in Table IV.

Finally we comment on the lack of pressure dependence on the ratio k_{1a}/k_{1b}. If the pressure is sufficiently reduced, k_{1a} must fall off and ultimately into the third-order regime. The fall off might be expected to start at ~50 Torr, so that, because of the scatter in our data, we would not see it. At 1.5–5 Torr, where Washida et al.[5] worked, reaction 1a would make a 15–47% contribution to reaction 1. Thus the value of $5.7 \pm 1.2 \times 10^{-12}$ cm^3/s they report for k_{1b} would include a 31 ± 16% contribution from reaction 1a. The regular trend of reaction 1a may not have been seen.

Acknowledgment. We wish to thank R. Simonaitis for useful discussions. This work was supported by the Atmospheric Sciences Section of the National Science Foundation through Grants No. GA-33446X and GA-42856 and by the Environmental Protection Agency through Grant No. R800874 for which we are grateful.

References and Notes

(1) J. E. Carruthers and R. G. W. Norrish, *J. Chem. Soc.*, 1036 (1936).
(2) E. C. A. Horner, D. W. G. Style, and D. Summers, *Trans. Faraday Soc.*, **50**, 1201 (1954).
(3) J. Peeters and G. Mahnen, *Symp. (Int.) Combust., [Proc.], 14th, 1972*, 133 (1973).
(4) K. L. Demerjian, J. A. Kerr, and J. G. Calvert, *Adv. Environ. Sci. Technol.*, **4**, 189 (1974).
(5) N. Washida, R. I. Martinez, and K. D. Bayes, *Z. Naturforsch. A*, **29**, 251 (1974).
(6) J. G. Calvert and J. N. Pitts, Jr., "Photochemistry", Wiley, New York, N.Y., 1966, p 463.
(7) R. Spence and W. Wild, *J. Chem. Soc.*, 338 (1935).
(8) R. Renaud and L. C. Leitch, *Can. J. Chem.*, **32**, 545 (1954).
(9) A. S. Coolidge, *J. Am. Chem. Soc.*, **50**, 2166 (1928).
(10) J. Weaver, J. F. Meagher, R. Shortridge, and J. Heicklen, *J. Photochem.*, **4**, 341 (1975).
(11) P. A. Giguère and A. W. Olmos, *Can. J. Chem.*, **30**, 821 (1952).
(12) W. A. Bone and J. B. Gardner, *Proc. R. Soc. London, Ser. A*, **154**, 297 (1936).
(13) E. C. A. Horner and D. W. G. Style, *Trans. Faraday Soc.*, **50**, 1197 (1954).
(14) D. W. G. Style and D. Summers, *Trans. Faraday Soc.*, **42**, 338 (1946).
(15) D. Garvin and R. F. Hampson, National Bureau of Standards Report NBSIR 74-430 (1974).
(16) E. Sanhueza, I. C. Hisatsune, and J. Heicklen, Presented at the 169th National Meeting of the American Chemical Society, Philadelphia, Pa., April, 1975.
(17) K. B. Krauskopf and G. K. Rollefson, *J. Am. Chem. Soc.*, **56**, 2542 (1934).

Gas Phase Radiation Chemistry of Ethyl Bromide

Arthur J. Frank and Robert J. Hanrahan*

Department of Chemistry, University of Florida, Gainesville, Florida 32611 *(Received December 19, 1975)*

Publication costs assisted by the University of Florida

The γ radiolysis of ethyl bromide has been investigated at 100 Torr pressure and 23 °C. In the pure system between an absorbed dose of 1.0×10^{20} and 1.5×10^{20} eV/g the major products and their respective G values are as follows: hydrogen bromide, 3.89; ethane, 2.70; ethylene, 2.17; acetylene, 0.31; hydrogen, 1.39; 1,1-dibromoethane, 0.88; 1,2-dibromoethane, 0.12; vinyl bromide, 0.32; methane, 0.083; methyl bromide, 0.080; and bromoform, 0.0078. When oxygen is added, the G values in this dose range become the following: hydrogen bromide, 4.89; ethane, 0.31; ethylene, 0.78; acetylene, 0.27; hydrogen, 1.38; 1,1-dibromoethane, 0.028; 1,2-dibromoethane, 0.56; vinyl bromide, 0.0; methane, 0.03; methyl bromide, 0.32; and bromoform, 0.0034. Bromine is also formed with a G value of 2.4 when oxygen is added. The presence of hydrogen and acetylene in the radiolysis indicates that these species must be formed from higher energy processes not accessible in the 253.7-nm photolysis, which was studied in a parallel investigation. The product distribution indicates that the probabilities of single bond rupture in the primary event are approximately C_2H_5–Br:C_2H_4Br–H:CH_3–CH_2Br = 1.00:0.40:0.06. Either a hot hydrogen atom abstraction reaction or direct molecular H_2 elimination accounts for about 16% of the hydrogen yield. Strong similarities in dose–yield plots suggest that many of the secondary processes involved in the photolysis are important in the radiolysis of ethyl bromide as well. The high pressure mass spectrometry of the system indicates the role of ionic species. Differences in radiolytic behavior of ethyl chloride, bromide, and iodide can largely be explained in terms of the energetics of the primary and secondary processes in each system.

Introduction

Although the gas phase radiolyses of ethyl chloride[1] and ethyl iodide[2] have been investigated, no work on ethyl bromide has been reported. Prior to the advent of gas chromatography, however, the fast electron and x-ray decomposition of liquid phase ethyl bromide was studied.[3]

The investigation of the γ radiolysis of ethyl bromide at room temperature in the gas phase was undertaken to study the primary and secondary processes leading to its decomposition. Parallel studies of the 253.7-nm photolysis[4] and high pressure mass spectrometry of the system provided supplementary information on the decomposition mechanism. Oxygen was added to identify free radical processes and to determine their contribution to the observed stable products.

An additional goal of this investigation was to compare the radiation chemistry of ethyl bromide with that of ethyl chloride[1] and ethyl iodide[2] since the chemical kinetics and product distributions of these systems differ dramatically. In contrast to ethyl iodide, carbon–hydrogen rather than carbon–halogen bond rupture is the major primary event in the chloride. Also, formation of C_4 products is important in the ethyl chloride system but not in the ethyl iodide system. These observations as well as others can be explained in terms of bond-energy arguments. Such comparisons are considered only briefly here; further discussion is given elsewhere.[5]

Experimental Section

Methods used for purification of the ethyl bromide, preparation of samples, and analysis of organic products, HBr, and Br_2 will be described in a companion paper on the photolysis of ethyl bromide;[4] further details are given elsewhere.[5] Hydrogen was measured using a thermal conductivity gas chromatograph, or alternatively using a combined Toepler pump–McLeod gauge, making corrections as necessary for the volatile organic component (mostly CH_4) based on analysis of the gas by flame ionization gas chromatography.

In all irradiations, ethyl bromide was at a pressure of 100 Torr except in those experiments intended for HBr analysis where the pressure was 300 Torr. In the majority of scavenger experiments, added oxygen was 5% of the total pressure; in the HBr determination runs, it was 12%. To accommodate the analytical methods employed in sample analysis, two types of radiolysis vessels were employed. Each was made of Pyrex and equipped with a single breakseal. For spectrophotometric analysis of bromine, an annular-shaped 355-cm^3 vessel with a 10-cm path quartz optical cell was used. Samples intended for gas chromatography and HBr analysis were irradiated in 30-cm^3 cylindrical vessels. Irradiations were performed at room temperature using a cobalt-60 γ source.[6] At maximum dosage the net amount of ethyl bromide consumed was less than 1%. The energy absorbed per unit mass of ethyl bromide was calculated relative to $G(H_2) = 1.2$ in ethylene[7] applying the correction factor 0.729 for the difference in the mass-stopping powers.[8]

For a brief reinvestigation of ion–molecule reactions we utilized a Bendix Model 14 time-of-flight mass spectrometer modified as described by Futrell.[9] All source potentials were as described[9] except that the innermost ion grid (no. 1) was pulsed at +23 V rather than +25 V.

Experimental Results

A total of 29 products were observed from the gas phase radiolysis of ethyl bromide; the yields of the 11 most important, which we designate as major or semimajor, are listed in Table I. These include HBr, C_2H_4, CH_4, CH_3Br, C_2H_3Br, 1,1-$C_2H_4Br_2$, 1,2-$C_2H_4Br_2$, and C_2H_6, all of which were also significant products in the photolysis. In addition, H_2 and C_2H_2 are important products in the radiolysis, although they are not formed in photolysis at 253.7 nm. As in the photolysis, Br_2 is observed in the presence of oxygen, but not in its ab-

TABLE I: *G* Values for Major and Semimajor Radiolysis Products from Ethyl Bromide Vapor at 100 Torr as a Function of Radiation Dose Range

	Pure system				O_2 scavenged system[b]			
	Absorbed dose/g × 10^{-20}				Absorbed dose/g × 10^{-20}			
Product[a]	0–0.5	1.0–1.5	3.5–4.0	4.5–5.0	0–0.5	1.0–1.5	3.5–4.0	4.5–5.0
Convex upward								
HBr[c]	≃6.02	3.89	0	0	4.89	4.89	4.89	4.89
Br_2	0	0	0	0	2.4	2.4	0.12	*d*
C_2H_4	0.78	2.17	2.07	0.86	0.78	0.78	0	*d*
C_2H_2	0.16	0.31	0.31	0.13	0.13	≃0.27	0.33	*d*
Concave upward								
CH_4	0.083	0.083	0.26	0.26	0.030	0.030	0.06	*d*
CH_3Br	0.080	0.080	0.24	0.24	0.32	≃0.32	1.30	1.30
C_2H_3Br	0.32	0.32	0.75	0.75	0	0	0	0
1,1-$C_2H_4Br_2$	0.88	0.88	1.66	(≤1.66)	0.028	0.028	0.31	0.31
1,2-$C_2H_4Br_2$	0.12	0.12	0.31	0.31	0.56	≃0.56	1.22	1.22
Linear								
H_2	1.39	1.39	1.39	1.39	1.38	1.38	1.38	1.38
C_2H_6	2.70	2.70	2.70	2.70	0.31	0.31	0.31	0.31

[a] The dose-yield plots for the listed products are found in Figures 1–7. The *G* values for the minor radiolysis products are given in Table VII, ref 5. [b] Oxygen comprised 5% of the total pressure except in the case of samples intended for HBr analysis, where it was 12%. [c] Irradiated ethyl bromide was at 300 Torr. [d] No data points were taken in this absorbed dose regime. [e] The compound was not detected.

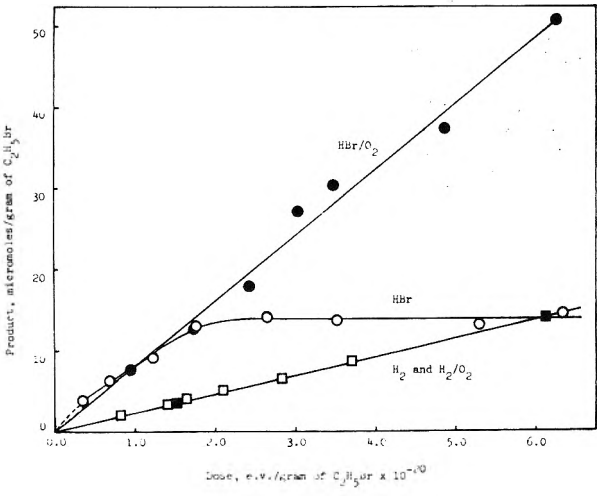

Figure 1. Production of hydrogen bromide (pure, O; 12% O_2, ●) and hydrogen (pure, □; 5% O_2, ■) as a function of dose.

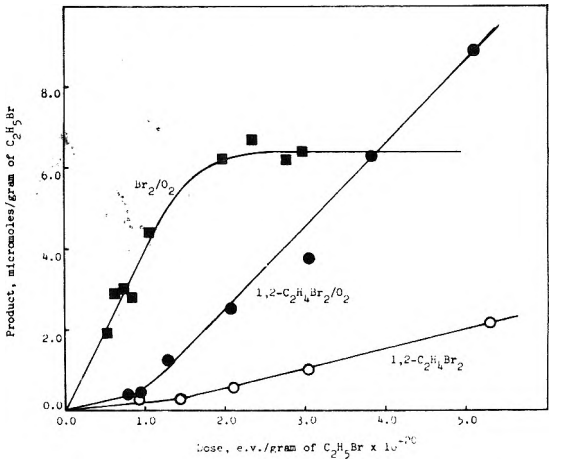

Figure 2. Production of bromine (5% O_2, ■) and 1,2-dibromoethane (pure, O; 5% O_2, ●) as a function of dose.

sence. Since many of the radiolytic yields vary throughout each experiment, Table I records differential yields for several dose ranges, from (0–0.5) × 10^{20} to (4.5–5.0) × 10^{20} eV/g, both with and without added oxygen. The yields are also displayed graphically in Figures 1–7.

Further details on 18 additional products which were observed in the radiolysis are given elsewhere.[5] Fourteen of these were definitely identified, three tentatively identified, and one high boiling species remains unidentified. None of these species represents a significant pathway for decomposition of ethyl bromide, however, since all are formed with *G* values of 0.03 or less. A few have some mechanistic interest, including $CHBr_3$ (G = 0.03), CH_2Br_2 (G = 0.0072), C_4H_{10} (G = 0.002), and 1,1,2-$C_2H_3Br_3$ (G = 0.007). The latter was somewhat more prominent among photolytic products, being classified as a semimajor product in that case.

As in the photolysis of ethyl bromide,[4] the various major

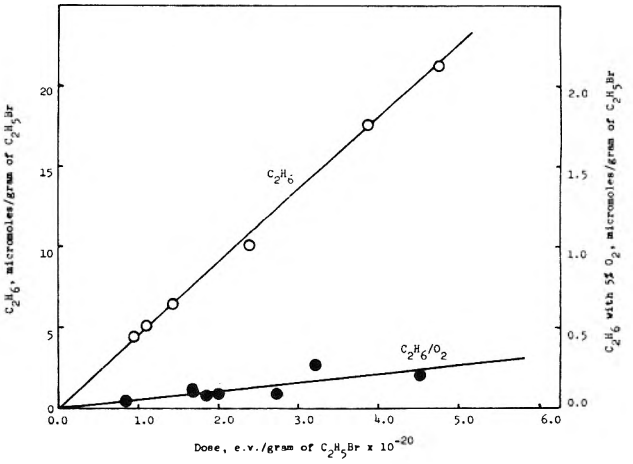

Figure 3. Production of ethane (pure, O, 5% O_2, ●) as a function of dose.

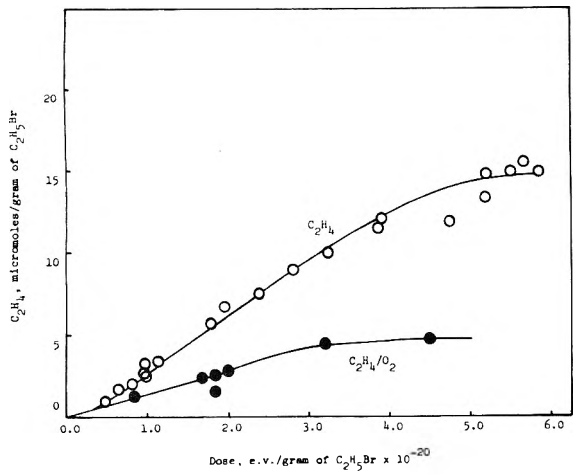

Figure 4. Production of ethylene (pure, O; 5% O_2, ●) as a function of dose.

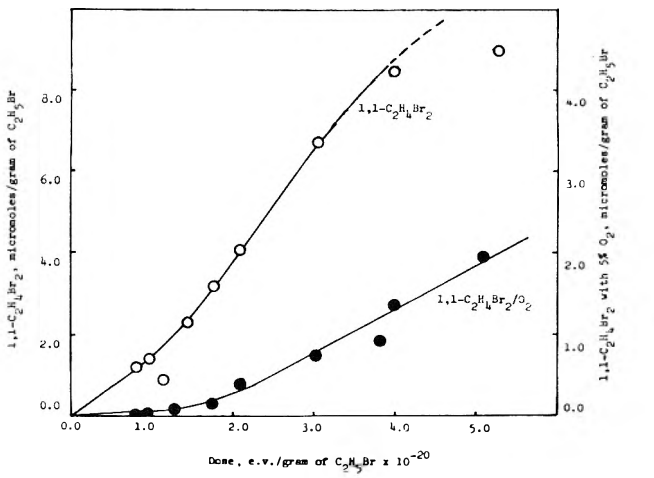

Figure 6. Production of 1,1-dibromoethane (pure, O; 5% O_2, ●) as a function of dose.

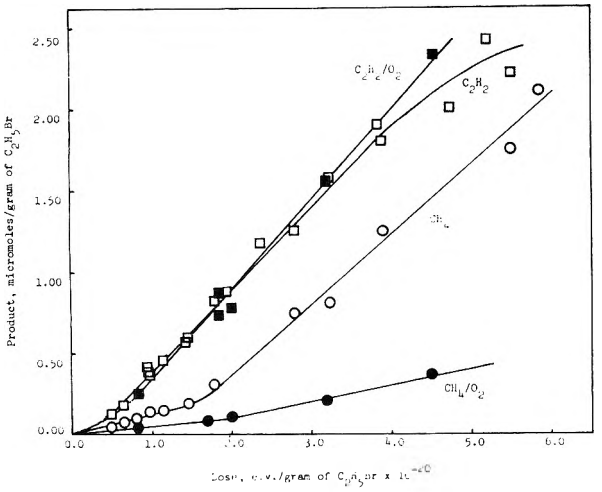

Figure 5. Production of methane (pure, O; 5% O_2, ●) and acetylene (pure, □; 5% O_2, ■) as a function of dose.

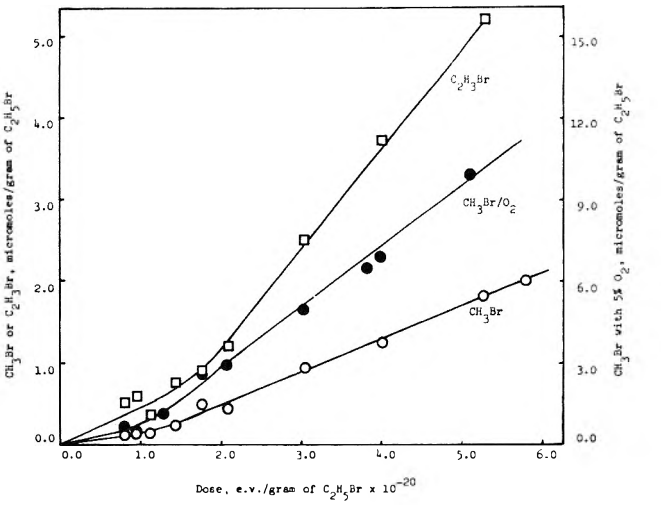

Figure 7. Production of methyl bromide (pure, O; 5% O_2, ●) and vinyl bromide (pure, □) as a function of dose.

and semimajor products can be categorized with respect to the shape of their yield–dose curves. In the absence of added oxygen, G values for HBr and C_2H_4 are maximum at low dose, and fall to zero at higher doses (Figures 1 and 4). The products 1,1-$C_2H_4Br_2$, 1,2-$C_2H_4Br_2$, CH_4, C_2H_3Br, and CH_3Br all show an induction period and/or a G value which increases with dose, although only slightly, in certain instances (Figures 2, 5, 6, and 7). Within the limits of our experimental precision, the yields of H_2 and C_2H_6 are strictly linear, both in the presence and absence of oxygen (Figures 1 and 3). The yield–dose graphs for C_2H_4 and C_2H_2 do not quite extrapolate through the origin (Figures 4 and 5) but this effect may well be an artifact of the analytical procedure. Our interpretation of the mechanism, as discussed below, indicates that C_2H_4 and C_2H_2 are direct radiolysis products which should show maximum G value at zero dose. A decrease of G value with dose is reasonable for these unsaturated species. This is clearly seen for C_2H_4 (Figure 3) and suggested by the data for C_2H_2 (Figure 4).

As in the photolysis of ethyl bromide, the most notable effect of added oxygen is net production of Br_2; the initial G value is 2.4, falling off to zero at high dose. Other major yields which are enhanced in the presence of oxygen include those of 1,2-$C_2H_4Br_2$, CH_3Br, and HBr (at high dose). All other yields are decreased except for H_2, which is unaffected; C_2H_2 is essentially unaffected as well.

The material balance in the radiolysis of C_2H_5Br is only moderately satisfactory; the ratio C/H/Br = 1.75/5.00/0.84 in the dose range (1.0–1.5) × 10^{20} eV/g and 2.02/5.00/0.62 in the dose range (3.0–3.5) × 10^{20} eV/g. It is clear that the major stoichiometric difficulty is a shortage of bromine, particularly at higher dose.

It is interesting to make direct comparisons between the photolytic and radiolytic decomposition of ethyl bromide. For instance, it will be noted that our longest photolysis experiments ran for 10 min, corresponding to absorption of 8 × 10^{13} quanta/cm^3 × 600 s × 91 cm^3, or 4.37 × 10^{18} quanta total. Taking into account the energy per photon at 253.7 nm, which is 4.89 eV, it is found that the actual energy input in a 10-min photolysis was 2.15 × 10^{19} eV. Similarly, the maximum dose in the radiolysis experiments was 6 × 10^{20} eV/g in a sample weighing 1.76 × 10^{-2} g, or 1 × 10^{19} eV total dose. Thus the termination of the curves in Figures 1–7 corresponds in energy input to about 5-min photolysis under the conditions stated. At that point, the actual product yields under photolysis were generally about twice the corresponding yields in the radiolysis. Thus, on the basis of total energy deposited, light of 253.7 nm is approximately twice as effective in decomposing ethyl

TABLE II: Relative Product Distribution of the Major and Semimajor Products from the Radiolysis and Photolysis of Ethyl Bromide Vapor at 100 Torr

	Pure radiolysis				Pure photolysis			
	Absorbed dose/g × 10^{-20}				Photolysis times, min			
Products[a]	0–0.5	1.0–1.5	3.5–4.0	6.0–7.0	0–0.5	1.0–1.5	3.5–4.0	6.0–7.0
Convex upward								
HBr[b]	1.64	1.64	≃0	≃0	0.90	0.65	0.54	≃0
C_2H_4	0.45	0.80	0.77	0.32	0.07	0.07	0.07	≃0
C_2H_2	0.06	0.11	0.11	0.05	*c*	*c*	*c*	*c*
1,1,2-$C_2H_3Br_3$	0.00	0.00	0.00	0.00	*c*	0.01	0.01	0.01
Concave upward								
CH_4	0.03	0.03	0.10	0.10	0.00	0.00	0.01	0.01
CH_3Br	0.03	0.03	0.09	0.09	*c*	0.00	0.01	0.01
C_2H_3Br[d]	0.12	0.12	0.28	0.28	0.04	0.02	≃0	−0.02
1,1-$C_2H_4Br_2$	0.33	0.33	0.61	(≦0.61)	0.26	0.26	0.70	0.70
1,2-$C_2H_4Br_2$	0.04	0.04	0.11	0.11	0.00	0.02	0.06	0.07
Linear								
H_2	0.51	0.51	0.51	0.51	*c*	*c*	*c*	*c*
C_2H_6[e]	1.00	1.00	1.00	1.00	1.00	1.00	1.00	1.00

[a] All values given in Table II were determined from the yields listed in Table I, this paper, and ref 4. Relative yields of all products not included in this table are less than 0.01. [b] The γ irradiated ethyl bromide was at 300 Torr. [c] The compound was not detected. [d] C_2H_3Br is concave upward in the radiolysis but convex upward in the photolysis. [e] C_2H_6 is linear in the radiolysis but convex upward in the photolysis.

bromide as 1.25 MeV γ radiation (or, more correctly, the secondary electrons from the vessel walls).

Discussion

Based upon the marked similarity of the product yields from the radiolysis of ethyl bromide, shown in Table I, with the yields from the photolysis of this compound, listed in Table I of the companion paper,[4,5] it is evident that there must be considerable commonality of decomposition pathways under these two modes of activation. To facilitate further comparisons, we show in Table II the yields of major products from radiolysis and photolysis, normalized in each case to the basis that the ethane yield equals unity. It will be seen that in most cases the major products of the radiolysis are important products in photolysis as well. Furthermore, as mentioned in the Results section, it is found that the shapes of the yield–dose curves are similar in most instances. Additional similarities include the fact that 1,1- and 1,2-dibromoethane have comparable yields in both cases; C_3 and C_4 yields are very small under both photolysis and radiolysis; C_1 yields are also small in both cases, although somewhat greater under radiolysis; and C_2H_6 yields (used as a standard of comparison) are major in both cases. Also, in both the radiolysis and photolysis, net Br_2 formation is seen in the presence of O_2 but not in its absence. As explained further below, however, we feel that the following differences are significant: hydrogen and acetylene are formed in the radiolysis, but not in the photolysis; ethylene is a much more significant product in the radiolysis, and vinyl bromide is somewhat more important in the radiolysis than the photolysis.

The elementary processes which we propose for the photolysis of ethyl bromide[4] are listed as neutral secondary processes in Table III of this paper; an examination of the table will indicate that the reactions in question would necessarily occur whenever ethyl radicals, bromine atoms, ethylene, and hydrogen bromide are present simultaneously in ethyl bromide vapor at appropriate conditions of temperature and concentration. Accordingly, we postulate that the same set of secondary neutral reactions must contribute in the radiolysis as well as in the photolysis. However, there must be significant differences regarding the relative importance of certain of the reactions, as will be discussed further below.

It has long been recognized that high energy radiation causes both excitation and ionization in a chemical system. In Table III we list neutral primary processes, ionic primary processes, ionic secondary processes, as well as neutral secondary processes, which we consider important in the radiolysis of ethyl bromide vapor. The neutral primary processes, reactions 1, 2, and 3, are the same as we will postulate in connection with the photolysis. Although higher energy excited states may be accessible under radiolytic conditions, it is reasonable to presume that the lowest $n\sigma^*$ repulsive state plays a major role in radiolysis as in photolysis. Dissociation of the repulsive state into both $C_2H_5\cdot$ plus $Br\cdot$ (reaction 1) and C_2H_4 plus HBr (reaction 2) is indicated by our photolysis results. We found some evidence supporting reaction 3 in the photolysis; since there is a somewaht larger yield of CH_4 and CH_3Br in the radiolysis, it could be suggested that reaction 3 is more important under radiolysis. For convenience and simplicity, we formulate the mechanism in terms of the neutral process only, although ionic fragmentation of C_2H_5Br into $CH_3\cdot + CH_2Br^+$ (1.8%) and into $CH_3^+ + CH_2Br\cdot$ (0.6%) also must contribute somewhat to the radiolytic yields of CH_4 and CH_3Br. (Percent abundances refer to mass spectral fragmentation.[10b])

We make the reasonable simplifying assumption that the ionic primary processes which occur in the radiolysis of ethyl bromide are the same as the fragmentation processes seen in the mass spectrometer under low pressure conditions. (For a molecule as small as ethyl bromide, unimolecular fragmentation processes should be so rapid that any "time scale difference" between radiolysis and mass spectrometry should be slight.) Reactions 4–9 in Table I suffice to describe formation of major ions in the mass spectrum of ethyl bromide, under bombardment with 70-V electrons.[10] Although only the ionic fragments are seen directly, a reasonable overall reaction can be formulated in each case. Essentially the only point of debate would arise in reaction 6, where the products could be listed either as $H_2 + Br\cdot$ or $HBr + H\cdot$. We have shown the former, since it is more favorable energetically.

TABLE III: Reactions in Ethyl Bromide Radiolysis

Neutral Primary Processes

$$C_2H_5Br \xrightarrow{\sim} C_2H_5\cdot + Br\cdot \quad (1)$$

$$\xrightarrow{\sim} C_2H_4 + HBr \quad (2)$$

$$\xrightarrow{\sim} CH_3\cdot + CH_2Br\cdot \quad (3)$$

Ionic Primary Processes

$$C_2H_5Br \xrightarrow{\sim} C_2H_5Br^+ + e^- \ (31.9\%) \quad (4)$$

$$\xrightarrow{\sim} C_2H_5^+ + Br\cdot + e^- \ (25.3\%) \quad (5)$$

$$\xrightarrow{\sim} C_2H_3^+ + H_2 + Br\cdot + e^- \ (22.0\%) \quad (6)$$

$$\xrightarrow{\sim} C_2H_4^+ + HBr + e^- \ (5.0\%) \quad (7)$$

$$\xrightarrow{\sim} C_2H_2^+ + H_2 + HBr + e^- \ (7.3\%) \quad (8)$$

$$\xrightarrow{\sim} Br^+ + C_2H_5\cdot + e^- \ (2.2\%) \quad (9)$$

$$e^- + C_2H_5Br \rightarrow C_2H_5\cdot + Br^- \quad (10)$$

Ionic Secondary Processes

$$C_2H_4^+ + C_2H_5Br \rightarrow C_2H_4 + C_2H_5Br^+ \quad (11)$$

$$C_2H_2^+ + C_2H_5Br \rightarrow C_2H_2 + C_2H_5Br^+ \quad (12)$$

$$C_2H_5Br^+ + C_2H_5Br \rightarrow (C_2H_5Br)_2^+ \quad (13)$$

$$\rightarrow C_2H_5Br^+C_2H_5 + Br\cdot \quad (14)$$

$$Br^+ + C_2H_5Br \rightarrow C_2H_5Br^+ + Br\cdot \quad (15)$$

$$C_2H_3^+ + C_2H_5Br \rightarrow C_2H_5Br^+H + C_2H_2 \quad (16)$$

$$C_2H_5^+ + C_2H_5Br \rightarrow C_2H_5Br^+H + C_2H_4 \quad (17)$$

$$C_2H_5Br^+H + C_2H_5Br \rightarrow C_2H_5Br^+C_2H_5 + HBr \quad (18)$$

Neutral Secondary Processes

$$Br\cdot + Br\cdot \xrightarrow{(M)} Br_2 \quad (19)$$

$$C_2H_5\cdot + C_2H_5Br \rightarrow C_2H_6 + CH_3\dot{C}HBr \quad (20)$$

$$C_2H_5\cdot + HBr \rightarrow C_2H_6 + Br\cdot \quad (21)$$

$$C_2H_5\cdot + Br_2 \rightarrow C_2H_5Br + Br\cdot \quad (22)$$

$$C_2H_5\cdot + Br\cdot \rightarrow C_2H_5Br \quad (23)$$

$$Br\cdot + C_2H_5\cdot \rightarrow C_2H_4 + HBr \quad (24)$$

$$Br\cdot + C_2H_4 \rightarrow \cdot CH_2CH_2Br \quad (25)$$

$$\cdot CH_2CH_2Br \rightarrow Br\cdot + C_2H_4 \quad (26)$$

$$\cdot CH_2CH_2Br \rightarrow CH_3\dot{C}HBr \quad (27)$$

$$\cdot CH_2CH_2Br + HBr \rightarrow Br\cdot + C_2H_5Br \quad (28)$$

$$\cdot CH_2CH_2Br + Br_2 \rightarrow BrCH_2CH_2Br + Br\cdot \quad (29)$$

$$\cdot CH_2CH_2Br + Br\cdot \rightarrow BrCH_2CH_2Br \quad (30)$$

$$Br\cdot + C_2H_5Br \rightarrow CH_3\dot{C}HBr + HBr \quad (31)$$

$$CH_3\dot{C}HBr + HBr \rightarrow Br\cdot + C_2H_5Br \quad (32)$$

$$CH_3\dot{C}HBr + Br_2 \rightarrow CH_3CHBr_2 + Br\cdot \quad (33)$$

$$CH_3\dot{C}HBr + Br\cdot \rightarrow CH_3CHBr_2 \quad (34)$$

$$Br\cdot + CH_3\dot{C}HBr \rightarrow C_2H_3Br + HBr \quad (35)$$

$$Br\cdot + C_2H_3Br \rightarrow Br\dot{C}HCH_2Br \quad (36)$$

$$Br\dot{C}HCH_2Br + HBr \rightarrow Br\cdot + BrCH_2CH_2Br \quad (37)$$

Percent figures indicated for reactions 4–9 are the abundances of the corresponding ionic species as reported in the API mass spectral tables.[10a] We suggest that formation of the ethyl ion mostly proceeds by reaction 5, giving bromine atom plus an electron. It is known that ion pair formation ($C_2H_5^+ + Br^-$) is important just above threshold energy;[11] however, radiolytic processes generally occur at moderately higher energies. Replacement of reaction 5 with the ion pair process would not alter our interpretation in a major way, in any event.

Secondary ionic processes in ethyl bromide have been investigated by several research groups. Hamill and co-workers[12,13] as well as Sieck and Gordon[14] have studied ion–molecule reactions in ethyl bromide using magnetic deflection techniques. Beauchamp et al.[15] studied the system using ICR mass spectrometry. We have also briefly reinvestigated the subject, using a high-pressure time-of-flight mass spectrometer. Hamill[12,13] and Sieck and Gordon[14] both observed the simple dimer $(C_2H_5Br)_2^+$ as well as the ether-type ion $(C_2H_5)_2Br^+$; they suggest formation reactions 13 and 14. Reactions 14–18 were postulated by Beauchamp[15] to interpret the results of his ICR experiments; a number of the ionic pathways were observed by the other workers as well.

We have also seen evidence for reactions consuming $C_2H_5Br^+$, $C_2H_5^+$, and $C_2H_3^+$, as well as processes producing $C_2H_5BrH^+$ and the two "dimeric" ions. Accordingly, our observations (which are described further elsewhere[5]) are in agreement with postulated reactions 13–18; it should be noted that each of the secondary ionic reactions 11–18 either produces the etherlike dimer or else produces another ion which, in turn, leads to it. Reaction 13 would appear to be an exception; no route for decomposition of $(C_2H_5Br)_2^+$ is shown. Our own work indicates, however, that the relative yield of $(C_2H_5Br)_2^+$ decreases above 0.2 Torr pressure, while $(C_2H_5)_2Br^+$ continues to increase. We suggest that reaction 13 is reversible, and that at sufficiently high pressures all positive ions in the system are ultimately converted to the "ether" structure.[16]

Reactions 11 and 12 are postulated to account for the fact that $C_2H_4^+$ and $C_2H_2^+$ are moderately important in the low pressure mass spectrum of ethyl bromide[10] (abundances 5.0 and 7.3%, respectively) but are not significant under the conditions of high pressure mass spectrometry. Both $C_2H_4^+$ and $C_2H_2^+$ have ionization potentials which are close to, but slightly greater than, ethyl bromide. Accordingly, the charge transfer reactions 11 and 12 should be quite efficient. We have not attempted to account for a number of even more minor species seen in the electron bombardment of ethyl bromide.

We conclude that the primary ionic fragments formed in ethyl bromide radiolysis all ultimately evolve into $(C_2H_5)_2Br^+$, as shown in Table IV. In each case except the first, two successive ion–molecule reactions are involved in order to reach the ultimate etherlike species. The percentage yields shown in Table III were converted to approximate G values as follows: We assume for convenience a W value of 25 eV/ion pair for ethyl bromide;[18] this corresponds to a total G value for all ionic products of 4.0. This value was then multiplied by the fractional abundance of each ion to give a resulting G' value: the prime (G') indicates inferred yield of the ionic process. (The G' value of the parent $C_2H_5Br^+$ ion is not shown separately in Table IV; it would be 4.0×0.32, or 1.28).

It is expected that all electrons formed in the system, also amounting to a G' value of 4.0, undergo dissociative electron capture, reaction 10.[19,20] Since the electron affinity of ethyl bromide is 3.36 eV,[21] the dissociative process is 9.5 kcal/mol exoergic. It is known to proceed through a compound negative ion state having a lifetime of less than 10^{-13} s.[19] Nondissociative electron capture leading to a negative ion with a lifetime much greater than bond vibration times is also known; however, this species can autoionize,[19] giving a free electron back again, which could subsequently undergo reaction 14.

TABLE IV: Evolution of Neutral Species from Primary Ions

First generation[a]	Second generation	Third generation	Neutralization	*G* values[b]
$C_2H_5Br^+$	$C_2H_5Br^+$	$(C_2H_5)_2Br^+ + Br\cdot$	$\rightarrow C_2H_5\cdot + Br\cdot$	8.0
$C_2H_5^+ + Br$	$C_2H_5BrH^+ + C_2H_4 + Br$	$(C_2H_5)_2Br^+ + HBr + C_2H_4 + Br\cdot$	$HBr + C_2H_4$	1.01
$C_2H_3^+ + H_2 + Br\cdot$	$C_2H_5BrH^+ + C_2H_2 + H_2 + Br\cdot$	$(C_2H_5)_2Br^+ + HBr + C_2H_2 + H_2 + Br\cdot$	$HBr + C_2H_2 + H_2$	0.88
$C_2H_2^+ + H_2 + HBr$	$C_2H_5Br^+ + C_2H_2 + H_2 + HBr$	$(C_2H_5)_2Br^+ + Br\cdot + C_2H_2 + H_2 + HBr$	$C_2H_2 + H_2 + HBr$	0.29
$C_2H_4^+ + HBr$	$C_2H_5Br^+ + C_2H_4 + HBr$	$(C_2H_5)_2Br^+ + Br\cdot + C_2H_4 + HBr$	$C_2H_4 + HBr$	0.20
$C_2H_5\cdot + Br^+$	$C_2H_5Br^+ + Br + C_2H_5\cdot$	$(C_2H_5)_2Br^+ + Br\cdot + Br\cdot + C_2H_5$	$C_2H_5\cdot + Br\cdot$	0.09

[a] Plus, $(G = 4)e^- + C_2H_5Br \rightarrow C_2H_5\cdot + Br^-$. [b] The first line would actually total $G = 7.5$ since the total intensity of the primary ions listed is only 93.7% rather than 100%. We set the total G value at $C_2H_5\cdot$ and Br· equal to 8.0 on the assumption that most of the other minor ions would also ultimately react to give $(C_2H_5)_2Br^+$. Note that these predicted G values refer to ionic processes only. Additional yields of some species also result from neutral processes.

Accordingly, we conclude that nondissociative electron capture, even if it occurs to an appreciable extent, has no net effect upon the system.

The dissociative electron capture process, reaction 10, produces ethyl radical and Br^- ion, with an assumed G' value of 4.0. It then follows that Br^- undergoes a neutralization reaction with $(C_2H_5)_2Br^+$ (expected to be the major long-lived ion in the system),[16] with subsequent fragmentation of the compound structure. At this point, we make the arbitrary assumption that one ethyl bromide molecule survives the neutralization process intact. We defend this assumption on the basis of the obviously stable valence structure of the etherlike complex (implying a rather small neutralization energy, perhaps 7 or 8 eV), the necessity of furnishing energy corresponding to the electron affinity of bromine (3.4 eV),[22] and the large number of modes over which the remaining energy can be dissipated. If our assumption is too conservative, it would simply imply that the total yield of the radical pair $C_2H_5\cdot$ + Br· would be somewhat greater than shown in Table IV. By our model, the total yield of these species is 8.09, including a small additional yield formed as shown in the last line of the table.

It will be noted in Table IV that a variety of other small molecules are formed as the ion–molecule reactions progress, and in the original ionization steps. Summing up the yields of each product as shown at the right of Table III, we find $G'(HBr) = 2.38$, $G'(C_2H_4) = 1.21$, $G'(C_2H_2) = 1.17$, and $G'(H_2) = 1.17$. The additional HBr and C_2H_4 yields are modified by participation in an extensive series of secondary reactions, as noted in our photolysis work.[4,5] The postulated acetylene yield of 1.17 would also be modified by secondary reactions; much of it is probably converted into vinyl bromide:

$$Br\cdot + C_2H_2 \rightarrow BrCHCH\cdot \quad (38)$$

$$BrCHCH\cdot + HBr \rightarrow C_2H_3Br + Br\cdot \quad (39)$$

At this point, we find that it has been possible to account for every case shown in Table II in which the relative yields under radiolysis are greater than those during photolysis. (The two C_1 species are an exception; as mentioned above, we assume that there is a somewhat larger yield of C–C bond rupture under radiolysis.)

We suggest that C_2H_6, 1,1-$C_2H_4Br_2$, and 1,2-$C_2H_4Br_2$ are formed predominantly in secondary radical processes, as shown in Table III and in the companion paper.[4] It is also apparent that the net yields of HBr and C_2H_4 are modified by the occurrence of free radical processes. It may be significant that the actual hydrogen yield, $G = 1.39$, is rather close to the value of 1.17 predicted from Table IV. Furthermore, the sum of the experimentally observed yields of acetylene plus vinyl bromide, approximately 1.06 during intermediate stages of the radiolysis experiments, is quite close to the prediction of 1.17 derived from Table IV. Since these are both labile species, it is to be expected that their yields would be diminished by further reactions.

Thus far we have postulated no role for hydrogen atoms in the radiolysis of ethyl bromide. It seems likely that at least a small yield of H· would be formed; those which react "hot" could produce an additional component of the H_2 yield, which is entirely unscavengeable, according to our results. Thermal hydrogen atoms probably form HBr in preference to H_2:

$$C_2H_5Br \rightsquigarrow C_2H_4Br\cdot + H\cdot \quad (40)$$

$$H\cdot (hot) + C_2H_5Br \rightarrow H_2 + C_2H_4Br\cdot (+ \text{some HBr}) \quad (41)$$

$$H\cdot (thermal) + C_2H_5Br \rightarrow HBr + C_2H_5\cdot \quad (42)$$

We can make a very rough estimate of the "hot atom" H_2 yield from $G(H_2) = 1.39$ (experimental) − 1.17 (predicted, ionic) = 0.22, or 16% of the total. This result depends on the rather rough analysis presented in Table IV; furthermore, the residual nonionic hydrogen yield could be due to direct molecular H_2 elimination as well as to hot hydrogen atoms. Nevertheless, a hot hydrogen atom yield of 16% would compare favorably with previous estimates that 15% of the H_2 yield from ethyl iodide[2] and 20% of the yield from ethyl chloride[1] is formed from translationally hot hydrogen atoms, based on mass spectrometric isotope studies.

As mentioned earlier, it is to be expected that the relative contributions of the various neutral secondary reactions (Table III) are different under radiolysis than photolysis. In particular, the energy deposited in a 10-min photolysis experiment corresponds approximately to a 24-h radiolysis, that is, there is a difference of about 10^2 in the rate of energy deposition, a corresponding difference in the rate of generation of free radical species, and consequently a difference of the order of 10^4 in the rate of radical–radical reactions. Accordingly, we conclude that most of the radical–radical reactions shown in Table III are relatively less important in radiolysis than in photolysis. Clearly, however, one or more radical–radical reactions must persist during radiolysis as a termination step. We suggest that the bromine atom combination reaction may be the most important radical termination step during radiolysis. HBr is a fairly good radical scavenger, and is present in substantial concentration throughout the experiment; most other radicals would abstract hydrogen from HBr, yielding bromine atoms which would ultimately feed into the Br_2 steady state.[4]

The effects of adding 5% O_2 during the radiolysis of ethyl bromide parallel closely those seen in the photolysis. In both

TABLE V: Comparison of G Values in Radiolysis of Pure Ethyl Chloride, Ethyl Bromide, and Ethyl Iodide

Product	Ethyl chloride Ref 1b	Ethyl chloride Ref 1a	Ethyl bromide[a]	Ethyl iodide[b]
HX	(0.37(?))[c]	4.5	3.89	*d*
X_2	*d*	*d*	*e*	*d*
H_2	4.41	2.44	1.39	0.73
CH_4	1.09	0.24	0.08	0.02
CH_3X	*d*	0.05	0.08	≃0.02
CH_2X_2	*d*	0.06	≃0.01	≃0.05
CHX_3	*d*	*d*	0.01	*d*
C_2H_6	2.40	2.11	2.70	1.34
C_2H_4	4.08	2.06	2.17	1.57
C_2H_2	1.72	0.75	0.31	0.48
C_2H_3X	*d*	0.66	0.32	≃0.04
1,1-$C_2H_4X_2$	*d*	*d*	0.88	0.2
1,2-$C_2H_4X_2$	*d*	*d*	0.12	"negligible"
1,1,2-$C_2H_3X_3$	*d*	*d*	≃*0.01*	*d*
1,2-$C_3H_6X_2$	*d*	0.05	0.01	*d*
1,3-$C_3H_6X_2$	*d*		<0.01	*d*
C_4H_{10}	*d*	0.10	<0.01	*e*
1-C_4H_9X	*d*	0.05	<0.01	*d*
2-C_4H_9X	1.44	0.49	<0.01	*d*
meso-2,3-$C_4H_8X_2$	3.00	0.76	<0.01	*d*
rac-2,3-$C_4H_8X_2$		0.80	<0.01	*d*
1,3-$C_4H_8X_2$	0.47	0.35	<0.01	*d*
1,4-$C_4H_8X_2$	*d*	0.03	<0.01	*d*

[a] This work. Yields refer to dose range from 1.0 to 1.5 × 10^{20} eV/g; several have different values at higher and lower doses. See Table I and Table VII, ref 5. [b] Reference 2. [c] This G value for HCl was not experimentally determined but was calculated using the material balance relationship given on p 433 in ref 1b. [d] The G value is not reported. [e] The product was not observed in the pure system.

TABLE VI: Relative Bond Rupture in Radiolysis of Ethyl Chloride, Ethyl Bromide, and Ethyl Iodide

	C_2H_5-X	C_2H_4X-H	CH_3-CH_2X
Cl	1.00	1.3	0.2
Br	1.00	0.4	0.03
I	1.00	0.06	0.01

TABLE VII: Bond and Activation Energies for the Ethyl Halides

Bond Energies, kcal/mol[a]

E(bond)	X = Cl	X = Br	X = I
$E(C_2H_5$-X)	83	68	52
E(H-X)	103.1	87.4	71.4
E(X-X)	57.87	46.08	46.05
$E(CH_3CHX$-H) ≃ 95[b]			
$E(CH_3$-$CH_3)$ ≃ 83[a]			

Activation Energies, kcal/mol

Reactions	X = Cl	X = Br	X = I
X· + C_2H_5X → C_2H_4X· + HX	<1[c]	13[d]	20[e]
HX + C_2H_5· → C_2H_6 + X·	3 ± 2[c]	2[f]	1 ± 1[e]
·CH_2CH_2-X → C_2H_4 + X·	22.2[g]	11.1[g]	6 ± 2[e]

[a] *Reference 23.* [b] Estimated value for the ethyl halides. [c] Reference 1a. [d] Reference 24. [e] Estimated value on the basis of the reactions involving the Br· and Cl· radicals. [f] Reference 25. [g] Reference 26.

cases, the high-dose yield of HBr is increased substantially. (Initial yields follow somewhat different patterns; see Figure 1 of this paper and Figure 1 of ref 4.) Under both modes of activation, Br_2 is formed only in the presence of added oxygen. A well-defined plateau is formed under radiolysis conditions, whereas there is only a moderate fall-off in the production rate during photolysis. Yields of C_2H_6, C_2H_4, CH_4, and 1,1-$C_2H_4Br_2$ are decreased under both photolysis and radiolysis, and to a similar extent in each case. As in the photolysis, adding O_2 prior to radiolysis causes an increase in the yields of CH_3Br and 1,2-$C_2H_4Br_2$. The yield of vinyl bromide is decreased to zero in both experiments. The yields of hydrogen and acetylene, which are seen only in the radiolysis, are essentially unaffected by added oxygen.

Most of the effects of added oxygen are straightforward in the photolysis,[4] and, for the most part, in the radiolysis as well. Although there are some difficulties in understanding the increased yields of CH_3Br and 1,2-$C_2H_4Br_2$, the explanation of this behavior almost certainly lies in the secondary neutral reactions, since the same behavior is seen in photolysis. The lack of effect of O_2 on the hydrogen yield is compatible with our assumption that this product is formed only in ionic processes, hot-hydrogen abstraction reactions, and/or H_2 elimination. As suggested regarding the effect on the ethylene yield during photolysis,[4] the effect of oxygen on the acetylene yield is probably a trade-off between protection from free radical attack (which would enhance the yield) and additional consumption reactions.

As mentioned in the Introduction, one of our purposes in undertaking this work was to make possible a comparison of the radiation chemistry of gaseous ethyl bromide with the previously studied ethyl chloride[1] and ethyl iodide[2] systems. To facilitate the comparisons, radiolytic yields are recorded in a common format for gaseous ethyl chloride, ethyl bromide, and ethyl iodide in Table V. Table VI presents comparative data on C–X, C–H, and C–C bond rupture in the three compounds as estimated from end-product analysis in the present work and in previous investigations.[1,2] Although approximate stoichiometric arguments are involved, the broad trends evident in the table would be unaffected by variations in assumed details of reaction mechanism. Table VII presents data on bond energies and activation energies which are relevant to understanding the trends seen in Tables V and VI.

On the basis of bond energy arguments, it is possible to correlate the extent of C–X (X = Cl, Br, or I), C–H, and C–C bond rupture in the three compounds. The probability of C–X bond fission is smallest for ethyl chloride and largest for ethyl iodide because of the differences in the carbon–halogen bond energies. To the extent that the C–X bond is much weaker than the C–H bond, the C–X bond breaks preferentially. Thus there is more C–I than C–H bond breakage. In ethyl chloride the C–X and C–H bond energies are much closer in value than in ethyl iodide and so the probabilities of C–Cl and C–H bond fission are expected to be more nearly equal. Thus less C–H bond rupture is anticipated in ethyl bromide than in ethyl chloride, and still less in ethyl iodide. The probability of C–C bond scission is greater in ethyl chloride and least in ethyl iodide. The C–Cl bond is energetically equivalent to a C–C bond, whereas in ethyl iodide the C–C bond is substantially

stronger, by about 30 kcal/mol, than the C–I bond. Again, the C–I bond breaks preferentially. Experimental trends shown in Table VI are clearly compatible with the arguments given.

It is also possible to understand the relative contribution of secondary processes in the radiolysis of ethyl chloride, bromide, and iodide on the basis of energy arguments. Probability of halogen abstraction from the substrate falls in the order Cl > Br > I; corresponding activation energies are ca. 1, 13, and 20 kcal, respectively (Table VII). In consequence the Cl_2 steady-state concentration is probably negligibly small, Br_2 is small but significant, while observable I_2 almost certainly accumulates, although its yield has not been reported. Accordingly, scavenging by I_2 must be a predominant effect, scavenging by Br_2 must be less important, but still significant, and scavenging by Cl_2 would clearly be negligible. Additionally, the scavenging ability of the hydrogen halides falls in the order HCl < HBr < HI (cf. Table VII). It is thus to be expected that C_4H_9Cl and $C_4H_8Cl_2$ are found with moderate yields, whereas the corresponding bromide and iodide products are found in small yields. By contrast, formation of C_2H_6 involves a balance of factors, specifically $C_2H_5\cdot$ yield, HX yield, and the scavenging ability of HX. The latter maximizes for the C_2H_5I case, but the HI yield is only moderate (C–I rupture predominates). HCl is formed in good yield but it is a somewhat poorer scavenger than HBr or HI; additionally, the $C_2H_5\cdot$ yield is lower in the chloride case due to competing reactions. The best balance is found in C_2H_5Br, which accordingly shows a maximum C_2H_6 yield. Several other trends involving primary and secondary processes can also be pointed out; details are given elsewhere.[4]

Acknowledgment. These results were presented in part at the 170th National Meeting of the American Chemical Society, Chicago, Ill., Aug 25–29, 1975. A.J.F. wishes to acknowledge receipt of a Fellowship from Proctor and Gamble Co., which he held during part of this work. This research was supported by the University of Florida Nuclear Science Program and by the U.S. Energy Research and Development Administration under Contract No. E-(40-1)-3106. This is Document No. ORO-3106-53.

References and Notes

(1) (a) R. N. Schindler, *Radiochim. Acta*, **2**, 62 (1963); (b) T. O. Tiernan and B. M. Hughes, *Adv. Chem. Ser.*, **No. 82** (1968).
(2) R. N. Schindler and M. H. J. Wijnen, *Z. Phys. Chem. (Frankfurt am Main)*, **38**, 285 (1963).
(3) R. H. Schuler and W. H. Hamill, *J. Am. Chem. Soc.*, **74**, 6171 (1952).
(4) A. J. Frank and R. J. Hanrahan, to be submitted for publication.
(5) A. J. Frank, Ph.D. Dissertation, University of Florida, 1975. Available from University Microfilms, Ann Arbor, Mich.
(6) R. J. Hanrahan, *Int. J. Appl. Radiat. Isotopes*, **13**, 254 (1962).
(7) G. G. Meisels, *J. Chem. Phys.*, **41**, 51 (1964), and earlier references cited therein.
(8) E. Heckel and R. J. Hanrahan, *Adv. Chem. Ser.*, **No. 82**, 120 (1968).
(9) J. H. Futrell, T. O. Tiernan, F. P. Abramson, and C. D. Miller, *Rev. Sci. Instrum.*, **39**, 340 (1968).
(10) (a) American Petroleum Institute Project 44, Catalog of Mass Spectral Data, Serial No. 607; (b) E. Stenhagen, S. Abrahamsson, and F. W. McLafferty, "Atlas of Mass Spectral Data", Wiley-Interscience, New York, N.Y., 1969.
(11) S. Tsuda and W. H. Hamill, *J. Chem. Phys.*, **41**, 2713 (1964).
(12) R. F. Pottie and W. H. Hamill, *J. Phys. Chem.*, **63**, 877 (1959).
(13) L. P. Theard and W. H. Hamill, *J. Am. Chem. Soc.*, **84**, 1134 (1962).
(14) L. W. Sieck and R. Gordon, Jr., *Int. J. Chem. Kinet.*, **5**, 445 (1973).
(15) J. L. Beauchamp, D. Holtz, S. D. Woodgate, and S. L. Patt, *J. Am. Chem. Soc.*, **94**, 2798 (1972).
(16) The relative importance of several possible "condensed" ionic species in ethyl bromide at pressures of several torr and above is not known. The model which we present is based on our own data,[5] which show a substantial shift in the ratio of $(C_2H_5)_2Br^+$ to $(C_2H_5Br)_2^+$ in favor of the "ether" species at pressures from 150 to 300 μ, from about 3:2 to 4:1. This trend was not observable at pressures below 100 μ, as investigated by Sieck and Gordon.[14] It is not clear whether the reaction channel leading to the "ether" is independent of that leading to the simple dimer; the latter may rearrange to the former in a unimolecular rote process, or upon collision. It is also possible that both species would be further solvated by ethyl bromide molecules at pressures of 100 Torr, as used in the radiolysis. In any event, such distinctions would effect our ionic model only to the extent of changing the predicted G for $(C_2H_5\cdot + Br\cdot)$, probably decreasing it somewhat below 8.0.
(17) R. W. Kiser, "Introduction to Mass Spectrometry and Its Applications", Prentice Hall, Englewood Cliffs, N.J., 1965, pp 312–313.
(18) W for ethyl bromide has been reported as 24.2 eV/ion pair by Adler and Bothe, *Z. Naturforsch. A*, **20**, 1700 (1965). (We thank the reviewer for this reference.)
(19) A. A. Christodoulides and L. G. Christophorou, *J. Chem. Phys.*, **54**, 4691 (1971).
(20) K. M. Bansal and R. W. Fessenden, *Chem. Phys. Lett.*, **15**, 21 (1972).
(21) L. G. Christophorou, J. G. Carter, P. M. Collins, and A. A. Cristodoulides, *J. Chem. Phys.*, **54**, 4706 (1971).
(22) L. G. Christophorou, "Atomic and Molecular Radiation Physics", Wiley-Interscience, London, 1971, p 550.
(23) T. L. Cottrell, "The Strengths of Chemical Bonds", Academic Press, New York, N.Y., 1958, p 277.
(24) S. W. Benson, "Thermochemical Kinetics", Wiley, New York, N.Y., 1968, pp 195–215.
(25) E. W. R. Steacie, "Atomic and Free Radical Reactions", Vol. 2, Reinhold, New York, N.Y., 1954.
(26) S. W. Benson and H. E. O'Neal, *Natl. Stand. Ref. Data Ser., Natl. Bur. Stand.*, **No. 21** (1970).

Positron Decay in Benzene Solutions of 3d Transition Metal Acetylacetonates and Dipivaloylmethanates

Kazutoyo Endo, Michiaki Furukawa, and Hideo Yamatera*

Department of Chemistry, Faculty of Science, Nagoya University, Chikusa, Nagoya, 464 Japan *(Received February 23, 1976)*

Publication costs assisted by Nagoya University

The lifetime spectra of positrons and positronium were measured in benzene solutions containing metal acetylacetonates and dipivaloylmethanates. The lifetime of orthopositronium (o-Ps) observed in pure benzene, 3.20 ns, was not significantly affected by the diamagnetic aluminum, nickel(II), and zinc complexes dissolved in benzene, whereas the lifetime was reduced by the paramagnetic manganese(III), iron(III), chromium(III), cobalt(II), and diamagnetic cobalt(III) complexes with the increase in their concentration, e.g., down to 1.60 ns in the case of 0.20 M $Mn(acac)_3$. The intensity (I_2) of o-Ps decreased rapidly with an increase in the solute concentration and became saturated at about 0.05 M. The rate constants of the o-Ps annihilation were correlated with polarographic apparent half-wave potentials of the complexes. The large reaction rate constants for $Mn(acac)_3$ and $Fe(acac)_3$ were attributed to the oxidation of o-Ps by the complexes, which show the potentials less negative than −0.5 V vs. mercury pool in benzene–methanol (1:1).

Introduction

Since the existence and formation of positronium (Ps), the short-lived quasi-stable positron–electron pair, was demonstrated by Deutsch,[1] a number of studies have been made on the interactions of positrons and Ps with matter. In condensed media, the lifetime spectrum of positrons and Ps, collectively, shows usually two components; the shorter lifetime (τ_1) is attributed to the annihilation of a free positron and p-Ps, while the longer one (τ_2) is related to the annihilation of o-Ps. The lifetime of o-Ps strongly depends on the electronic state and electron density of the surrounding substance. Thus, the experimental studies of positrons and Ps give valuable information on the electronic state of the substance. Ps can be regarded as the lightest hydrogen isotope, and can take part in such chemical reactions as oxidation, compound formation, substitution, and spin conversion before it annihilates.

Investigations have been made on the interaction of o-Ps with metal ions in aqueous solutions by many workers.[2-9] Among others, McGervey et al. have measured the lifetime of o-Ps in aqueous metal chloride solutions and evaluated the oxidation potential of o-Ps from the reaction rate constants derived from the lifetime.[2] Recently, Ache and his co-workers have studied the reaction of o-Ps with a series of diamagnetic species in aqueous solutions and estimated a "hypothetical standard redox potential", $E°$, at about −0.9 to −1.4 V.[10-16] However, nonaqueous systems have not systematically been studied on the interaction of o-Ps with metal ions or metal complexes, although few data are available on some particular systems such as pyridine solutions of chromium chloride and acetone solutions of tin(II) chloride.[13,16] Nonaqueous solvents, in which the τ_2 value is much greater than that in water, are more suitable for examining the interaction of o-Ps with metal complexes dissolved in that solvent (τ_2 = 1.78 ns in water and τ_2 = 3.20 ns in benzene, for example). In the present study, β-diketonato chelates are chosen as the metal complex to be dissolved in benzene. With a variety of metal ions, acetylacetone forms chelates of similar structures soluble in benzene. The derivatives such as dipivaloylmethane also form similar chelates. Such similarity in the structure favors a comparison between complexes of different metal ions. The o-Ps lifetime spectra were measured on benzene solutions of acetylacetonato (acac) and dipivaloylmethanato (dpm) complexes of 3d transition metal ions. The observed rate constants of o-Ps decay ranged from 0.313 ns^{-1} (in pure benzene) to 0.68 ns^{-1} depending on the kind of the solute and its concentration. The differences in the o-Ps decay rate constants observed for different complexes of the same concentration were attributed to the different rate constants of the reaction of o-Ps with the complexes. In order to correlate the reaction rate constants with the redox potentials of the complexes, polarographic measurements were carried out in benzene–methanol (1:1) solutions. A plot of the reaction rate constants against half-wave potentials (Figure 3) shows vividly plausible mechanisms of o-Ps decay.

Experimental Section

Construction of a Fast–Slow Coincidence System. A conventional fast–slow coincidence system was used for the lifetime measurements; Figure 1 shows the block diagram of the system. The electronic circuits were constructed with commercially available transistors and integrated circuits. The NE-111 scintillators (1 in. in diameter and 1 in. long) were surrounded by magnesium oxide as reflector. A pair of Philips 56AVP photomultipliers was set to operate at the photocathode potential of −1870 V with respect to the ground. A voltage divider of the B′ type was used for fast timing.[17] Slow signals for energy selection were derived from the tenth dynode of each photomultiplier. The output signals from a preamplifier were doubly differentiated with a resister–capacitor combination of a main amplifier. A timing single-channel analyzer (SCA) selects the 1.28-MeV γ rays, and the other SCA selects one of the annihilation radiations. Each SCA furnishes output signals, which occur when the bipolar signals of the main amplifier pass across zero. The timing was adjusted by making use of the hysterisis in the lower level discriminator which is essentially a Schmidt trigger circuit. A slow coincidence circuit was constructed with an ordinary AND gate. Fast timing signals from the anode of each counter were fed through a 50-Ω coaxial cable to a fast discriminator of the constant fraction type. A tunnel diode was used for the

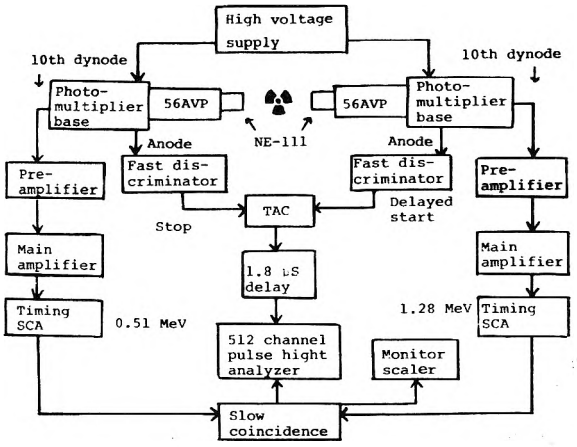

Figure 1. Block diagram of the fast–slow coincidence system.

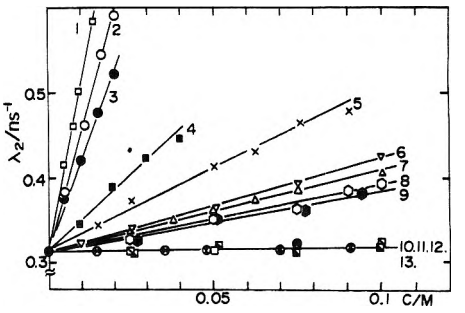

Figure 2. Decay rate constants λ_2 (= τ_2^{-1}) vs. the solute concentration: 1 (□) $Mn(acac)_3$, 2 (○) $Fe(acac)_3$, 3 (●) $Fe(dpm)_3$, 4 (■) $Mn(dpm)_3$, 5 (×) $Cu(dpm)_2$, 6 (▽) $Co(acac)_2$, 7 (△) $Co(acac)_3$, 8 (◇) $Cr(acac)_3$, 9 (◆) $Cr(dpm)_3$, 10 (⊖) $Ni(dpm)_2$, 11 (⊕) $Zn(dpm)_2$, 12 (⊠) $Al(acac)_3$, 13 (▣) $Al(dpm)_3$.

pulse shaper. A time-to-amplitude converter (TAC) is of the pulse-overlap type with Motorola ultra-fast ECL gates.[18] A square pulse of 50 ns duration was triggered by a pulse from each discriminator. When the start counter accepts the 1.28-MeV γ ray and the stop counter accepts the 0.51-MeV radiation within a fixed range of time (30 ns), the TAC gives a signal of the amplitude proportional to the interval of the signals from the two counters. The output is then integrated and shaped to give a bipolar signal, which is fed to a Hitachi 512 channel pulse height analyzer. This fast–slow coincidence system gave a resolution (fwhm) of 750 ps for prompt γ rays of ^{60}Co and a 25 ns range of linear conversion.

Synthesis of the Metal Complexes. The acetylacetonato (acac) and dipivaloylmethanato (dpm) complexes were synthesized according to the literature.[19,20] The complexes were purified by crystallization from a benzene–hexane mixture and then by repeated vacuum sublimations.

Lifetime Measurement. For lifetime measurement, each complex was dissolved in reagent-grade benzene except in the cases of moisture-sensitive $Mn(acac)_3$ and $Ni(dpm)_2$, where the benzene used was dried with anhydrous calcium chloride and then distilled. The sample to be measured was put in a pyrex tube of 11 mm diameter containing a positron source, and degassed by the vacuum freeze–thaw technique before the lifetime measurement. The positron source was about 6 μCi of ^{22}Na (as NaCl) obtained from the Radiochemical Centre in England through Japan Radioisotope Association. A drop of the ^{22}Na (NaCl) solution was evaporated on aluminum foil 6.75 mg/cm^2 thick and sandwitched with another foil. A lifetime spectrum was obtained after 40 h accumulation at 25 °C. The mean lifetime of the long-lived component (τ_2) was obtained from the slope of the exponential tail of the spectrum. The intensity (I_2) of the component was obtained as the ratio of an area under the long-lived component to the total area. A correction for finite resolution of the circuit was made according to the literature.[6]

Polarography. Polarograms of the complexes were taken with 2 mM solutions in a benzene–methanol (1:1) mixture containing 0.3 M LiCl as a supporting electrolyte. The half-wave potential was measured with respect to a mercury pool.

Results and Discussion

Lifetimes (τ_2) of o-Ps. The Ps lifetime spectra were measured on benzene solutions of the complexes in the concentrations range 0–0.1 M. Figure 2 gives plots of the observed decay rate constants λ_2 (= τ_2^{-1}) against the solute concentration. The good linear relationship observed is consistent with the following equation:

$$\lambda_2 = \lambda_i + \lambda_p + k[C]$$

where λ_i is the intrinsic decay rate constant of o-Ps, λ_p the decay rate constant for the pick-off process in benzene, [C] the molar concentration of the complex, and k the rate constant for the o-Ps reaction with the solute. Since $\lambda_i + \lambda_p$ is practically equal to the observed decay rate constant in pure benzene, the above equation can be rewritten as

$$\lambda_2 = 0.313 + k[C]$$

The rate constant k for the reaction of o-Ps with each complex was obtained from the slope of the plot; the k values are listed in Table I. The diamagnetic aluminum, nickel(II), and zinc complexes effected no significant change in the lifetime of o-Ps; these results are in agreement with the results observed in aqueous solutions of aluminum and zinc chlorides.[4,6] Cobalt(III) acetylacetonate which is also diamagnetic caused a decrease in the o-Ps lifetime, however.[21] Other complexes examined are paramagnetic and have unpaired electrons. In the presence of paramagnetic manganese(III) and iron(III) complexes, the o-Ps decay rate constant linearly increased with an increase in solute concentration. Although the process of spin conversion has often been regarded as the main process of o-Ps decay in a system containing species with

TABLE I: Reaction Rate Constants and Saturation Intensities of o-Ps

	Reaction rate constants $10^{-9}\,k/s^{-1}\,M^{-1}$		Saturation intensities[a] $10^2\,I_2$	
	acac	dpm	acac	dpm
Al^{3+}	0	0	25.6	29.5
Cr^{3+}	0.74	0.66	24.1	28.7
Mn^{3+}	18.70	3.52	23.4[b]	27.4[c]
Fe^{3+}	15.64	10.55	22.0[b]	27.0[c]
Co^{2+}	0.99		26.0	
Co^{3+}	1.13		12.9	
Ni^{2+}		0		28.8
Cu^{2+}		2.00		26.6
Zn^{2+}		0		30.7

[a] Listed values of I_2 are those for 0.1 M solution of each complex unless otherwise stated. [b] Values for 0.02 M solutions. [c] Values for 0.04 M solutions.

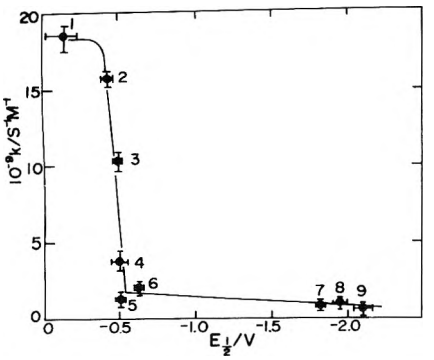

Figure 3. Reaction rate constants of o-Ps vs. the polarographic half-wave potentials measured in benzene–methanol (1:1) solutions: 1 $Mn(acac)_3$, 2 $Fe(acac)_3$, 3 $Fe(dpm)_3$, 4 $Mn(dpm)_3$, 5 $Co(acac)_3$, 6 $Cu(dpm)_2$, 7 $Cr(acac)_3$, 8 $Co(acac)_2$, 9 $Cr(dpm)_3$.

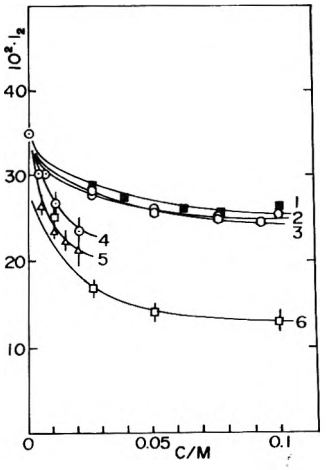

Figure 4. Intensities (I_2) of o-Ps vs. the concentrations of metal acetylacetonates in benzene: 1 (■) $Co(acac)_2$, 2 (○) $Al(acac)_3$, 3 (○) $Cr(acac)_3$, 4 (⊙) $Mn(acac)_3$, 5 (△) $Fe(acac)_3$, 6 (□) $Co(acac)_3$.

unpaired spins, chemical reaction is also a possible process of o-Ps decay; actually McGervey et al.[4] and Ache and Bartal[12] concluded that oxidation by metal ions such as copper(II) and iron(III) is the main process of o-Ps decay in the system containing their chlorides. The present results given in Table I strongly indicate that oxidation of o-Ps is the dominant decay process in some cases. Thus the o-Ps decay rate constant was much greater in solutions of the manganese(III) and iron(III) complexes than in solutions of the less oxidizing chromium(III) and cobalt(II). A qualitative conclusion can be drawn that a more oxidizing complex in general gives a higher decay rate of o-Ps. In order to make a more detailed discussion possible, polarographic measurements of these complexes were carried out in benzene–methanol (1:1) solutions. The polarographic waves observed were not always of reversible oxidation–reduction; the apparent half-wave potentials with reference to the mercury pool were taken as a first approximation. In Figure 3, the rate constant k for the o-Ps reaction with each complex was plotted against the apparent half-wave potential of the complex. A drastic change in the rate constant was observed at about −0.5 V.

The processes accelerating the o-Ps decay are spin conversion producing p-Ps and oxidation yielding a free positron; both p-Ps and the positron rapidly annihilate. For the spin conversion to occur in an appreciable probability, the orbital of the bound electron of o-Ps must appreciably overlap a molecular orbital containing an unpaired electron of the metal complex with which o-Ps interacts. This condition was experimentally confirmed by the fact that dipivaloylmethanato complexes of gadolinium, terbium, dysprosium, holmium, and erbium did not accelerate the o-Ps decay.[22] Although these rare-earth complexes are highly paramagnetic due to the presence of several unpaired 4f electrons, the 4f orbitals lie inside the outer shell of the rare-earth ions and thus hardly overlap the bound-electron orbital of o-Ps. In the case of the 3d transition metals, the unpaired electron lies near the surface of the ion; in their complexes, however, the access of o-Ps to the metal ion is more or less hindered by the ligands. Thus it is questionable that spin conversion occurs in a high probability. When the complex is oxidizing sufficiently, the o-Ps can decay through oxidation. The reduction of the complex by o-Ps may not necessarily result in the ground state of the reduced complex; if energetically allowed, excited states may also be formed. Thus the probability of oxidation process occurring is much greater than that of spin conversion process occurring. The manganese(III) and iron(III) complexes with high redox potentials can be classified in this category. For these complexes, the Ps decay constant was considerably greater for the acac complex than for the corresponding dpm complex; the latter has many methyl groups, which release electron and thus make the complex less oxidizing, or makes the LUMO higher. The diamagnetic tris(acetylacetonato)-cobalt(III) shows a slight but appreciable increase in the Ps decay constant and its redox potential seems to lie near the limit of oxidation process occurring. This complex has an apparent half-wave potential similar to that for tris(dipivaloylmethanato)iron(III), although a minute comparison of their redox potentials cannot be made because of the irreversible nature of their polarographic waves. The cobalt(III) complex is of low-spin type ($S = 0$), whereas the corresponding cobalt(II) complex is of high-spin type ($S = 3/2$). The addition of an electron to the cobalt(III) complex results in an excited electronic state ($S = 1/2$) of the cobalt(II) complex, which at the same time should be highly excited vibrationally if the Frank–Condon principle is considered. Therefore, the reduction of the cobalt(III) complex requires an extra activation energy; the reaction possibly proceeds at a lower rate than can be expected from the redox potential of the complex, although the exact value of the redox potential is not known. The other metal complexes seem to be incapable of oxidizing o-Ps; then the spin-conversion process plays a dominant role for paramagnetic complexes. In these cases, the rate of o-Ps decay depends on how easily the electron of o-Ps can reach the orbitals containing unpaired electrons, as illustrated by the observation that each of the less crowded acac complexes gives a higher rate of o-Ps decay than that for the corresponding one of the more crowded dpm complexes.

Intensities (I_2) of o-Ps. As is well known,[23] Ps formation occurs when the energy of positrons becomes within the range from I_A to (I_A − 6.8) eV, where I_A is the ionization energy of the substance with which positrons interact. If the excitation energy, E, of an excitation level of the substance exists within this range, excitation collisions compete with the Ps formation. Then Ps formation occurs mainly in the range from E to (I_A − 6.8) eV. A simple treatment can be made by assuming a flat energy distribution of positrons during the slowing down process. A simple system such as pure benzene can be roughly treated in this way. On the basis of the ionization energy obtained by photoelectron spectroscopy[24] and the excitation energy obtained by uv spectrophotometry,[25] the value of the I_2 in benzene was calculated to be 30.4%, assuming that three

quarters of the initially formed Ps is o-Ps. The I_2 value of (34.3 ± 1.0)% obtained in the present experiment agrees fairly well with the rough estimate. The situation becomes complicated for the positrons interacting with a solution containing a complex. The I_2 values for acac complexes are plotted against solute concentration in Figure 4; for $Mn(acac)_3$ and $Fe(acac)_3$, the reaction rate of o-Ps is very rapid and the measurement of I_2 was hardly possible at concentrations above 0.04 M. A general trend was found that the I_2 value decreased with increase in the concentration of the complex and reached saturation at about 0.05 M. In a benzene–acetylacetone mixture without complexes, the I_2 value decreased with increasing concentration of acetylacetone; the lifetime of o-Ps, however, remained unchanged. The experiment gave the I_2 value of 25.5% at 0.3 M. This value is in good agreement with the I_2 value of 25.6% observed for 0.1 M $Al(acac)_3$, i.e., 0.3 M in the acac ligand. Similarly, solutions of the bis-type $Co(acac)_2$ and the Hacac solutions showed the same I_2 values within the range of the experimental error when they contained acac (free or as ligated) at the same concentration; the I_2 value of 26.6% for 0.1 M $Co(acac)_2$ and 26.4% for 0.2 M in free Hacac. These facts seem to suggest that the electronic state of the acac ligands in these complexes is only slightly different from free Hacac, probably of the enol form. On the other hand, solutions containing $Co(acac)_3$ showed smaller I_2 values than those containing $Al(acac)_3$. This can be explained by the presence of low-lying excited states in the cobalt complex; excitation collisions compete with Ps formation, resulting in low I_2 values. $Co(acac)_2$ also has low-lying excited levels. However, this divalent cobalt complex is easily oxidizable or has a relatively low ionization potential; this favors Ps formation. The two opposite effects may counterbalance to give practically the same I_2 values as those for free Hacac and $Al(acac)_3$. The I_2 values of the dpm complexes, on the other hand, show no significant feature of each metal, and the values are 4–5% higher than those of the acac complex as shown in Table I. This can be attributed to the lower ionization energies of the dpm complexes due to the electron releasing property of the substituted methyl groups.

Acknowledgments. The authors are grateful to Mr. Atsushi Ogata formerly of the Institute of Plasma Physics of Nagoya University (presently of Japan Atomic Energy Research Institute) for advice in the construction of the fast–slow coincidence system, and to Mr. Ken-ichi Sasaki of Department of Chemistry of Nagoya University for the design of the photomultiplier base. The authors are also indebted to Dr. Yukio Nakamura of Osaka City University for helpful suggestions in the preparations of the metal complexes.

References and Notes

(1) M. Deutsch, *Phys. Rev.*, **76**, 462 (1949); **83**, 866 (1951); **85**, 371 (1951).
(2) R. E. Green and R. E. Bell, *Can. J. Phys.*, **35**, 398 (1957); **36**, 1683 (1958).
(3) G. Trumpy, *Phys. Rev.*, **118**, 688 (1960).
(4) J. D. McGervey, H. Horstman, and S. DeBenedetti, *Phys. Rev.*, **124**, 1113 (1961).
(5) J. E. Jackson and J. D. McGervey, *J. Chem. Phys.*, **38**, 300 (1963).
(6) H. Horstman, *J. Inorg. Nucl. Chem.*, **27**, 1191 (1965).
(7) S. J. Tao and J. H. Green, *J. Phys. Chem.*, **73**, 882 (1969).
(8) V. I. Goldanskii, T. A. Solonenko, and V. P. Shantarovich, *Dokl. Akad. Nauk SSSR*, **151**, 608 (1963).
(9) V. I. Goldanskii, V. G. Firsov, and V. P. Shantarovich, *Kinet. Katal.*, **6**, 564 (1956).
(10) T. L. Williams and H. J. Ache, *J. Chem. Phys.*, **50**, 4493 (1969).
(11) J. B. Nicholas, R. E. Wild, L. J. Bartal, and H. J. Ache, *J. Phys. Chem.*, **77**, 178 (1973).
(12) L. J. Bartal and H. J. Ache, *Radiochim. Acta*, **17**, 205 (1972).
(13) L. J. Bartal, J. B. Nicholas, and H. J. Ache, *J. Phys. Chem.*, **76**, 1124 (1972).
(14) L. J. Bartal and H. J. Ache, *J. Inorg. Nucl. Chem.*, **36**, 267 (1974).
(15) A. L. Nichols, R. E. Wild, L. J. Bartal, and H. J. Ache, *Appl. Phys.*, **4**, 37 (1974).
(16) G. J. Celitans and J. Lee in "Positron Annihilation", A. T. Stewart and L. O. Roellig, Ed., Academic Press, New York, N.Y., 1967, p 365.
(17) Philips Data Handbook, Electron Tubes, Part 6 (April 1969).
(18) J. B. Wang, S. Y. Chuang, S. J. Tao, and A. Ogata, *Nucl. Instrum. Methods*, **108**, 253 (1973).
(19) For acac complexes, see, for example, T. Moeller, *Inorg. Syn.*, **5**, 130, 188 (1957); W. C. Fernelius, *ibid.*, **2**, 25 (1946).
(20) G. S. Hammond, D. C. Nonhebel, and Chin-Hua S Wu, *Inorg. Chem.*, 2, 73 (1963).
(21) Although a preliminary experiment with a 10 μCi positron source showed little dependence of the o-Ps lifetime on the $Co(acac)_3$ concentration [*Radiochem. Radioanal. Lett.*, **21**, 307 (1975)], a closer examination of repeated experiments with a weaker (6 μCi) positron source revealed a concentration dependence of the lifetime.
(22) K. Endo, M. Furukawa, and H. Yamatera, unpublished results.
(23) A. Ore and J. L. Powell, *Phys. Rev.*, **83**, 866 (1951).
(24) P. G. Wilkinson, *Can. J. Phys.*, **34**, 596 (1956).
(25) K. Kimura and S. Nagakura, *Mol. Phys.*, **9**, 117 (1965).

Atom Recombination in Liquids on a Picosecond Timescale

Glenn T. Evans and Marshall Fixman*

Department of Chemistry, Yale University, New Haven, Connecticut 06520 *(Received February 19, 1976)*

Publication costs assisted by Yale University

Diffusion-controlled recombination in a liquid is considered using (1) the standard Fick's law model for diffusion and (2) an improvement of Fick's law which includes an effective spatial dependence in the relative diffusion constant. The results are viewed in light of the recent picosecond optical experiments of Eisenthal et al.

A. Introduction

The problem of diffusion-controlled recombination of spherical bodies in a liquid is a time-honored one originally considered by Smoluchowski[1a] and solved to desired accuracy by Noyes[1b] in the mid 1950's. Evidence from chemically induced dynamic nuclear polarization (CIDNP)[2] in the late 1960's and, more recently, picosecond optical studies[3] have refocused our attention to a more detailed solution to the problem.

An improved theory describing the time dependent recombination rate of spherical bodies in a normal liquid must account for: (1) the relative translational motion of the spheres subject to the constraint that the spheres do not overlap, owing to hard core repulsion; and (2) the chemical reaction of the spheres to form a recombination product, occurring at a separation slightly greater than the sum of the hard sphere radii. In terms of the equation of motion for the relative two body distribution function, $P(r, t)$, the independent translational motion of the spheres can be accomplished by including a function of the Laplacian of the relative separation, and the chemical reaction achieved by the inclusion of a spherically symmetric sink. Thus, the equation of motion for $P(r, t)$ will have the form[4,5]

$$\frac{\partial P(r, t)}{\partial t} = -\nabla \cdot \mathbf{J} - K(r)P(r, t) \tag{1a}$$

where the flux, $\mathbf{J}$, is

$$\mathbf{J} = -\nabla(f(P(r, t))) \tag{1b}$$

f is yet an unspecified function which includes diffusion constants and possible refinements of a diffusional theory. The hard core of the spheres is enforced by restricting the spherically averaged normal component of $\mathbf{J}$ to vanish at the hard core separation, $r = a$.

$$\int_{|r|=a} ds\, \mathbf{n} \cdot \mathbf{J} = 0 \tag{2}$$

The sink will operate only if the spheres are in contact. This process can be accommodated by the use of a delta function on a sphere of radius, a', in which a' is infinitesimally greater than a. Thus, $K(r)$ will have the form[4,5]

$$K(r) = K\delta(r - a')/4\pi a'^2 \tag{1c}$$

The strength of this pseudopotential, K, has been discussed elsewhere.[4a]

The solution of an equation similar to eq 1 is known[4c] for the simple case of Fick's law translational diffusion and has been applied to chemically induced dynamic nuclear polarization (CIDNP). From the rather sparse CIDNP evidence[4b] it seems adequate to neglect the explicit sink term in eq 1, and simply calculate $P(r = a', t)$, which is the probability density of attaining the separation, a', required for chemical reaction. Allowing $a' \to a$ amounts to solving eq 1 subject to the reflecting sphere boundary condition and evaluating the solution at this reflecting separation, $r = a$. Aside from the implementation of a boundary condition, this is basically the physical content of the Noyes theory[1b] of diffusion-controlled recombination. In the Appendix we give a stronger demonstration that neglecting $K(r)$ does not affect the form of the time dependence of the solutions.

The motivation for a more detailed study of recombination dynamics arises primarily from the recent work of Eisenthal et al.[4] wherein picosecond optical methods are utilized in the direct detection of the time dependence of the diffusion-controlled recombination of iodine atoms. The work presented in section B of this paper will invoke a Fick's law representation for the flux, $\mathbf{J}$, and will be applied to the interpretation of Eisenthal's data. In section C we shall improve Fick's law by including higher order spatial derivatives in the flux and comment on the timescale requirements necessary for the detection of the new effects.

B. Fick's Law Recombination

1. *Basic Theory.* The equation of motion for the two body distribution function, $P^0(r, t)$, describing the relative translational diffusion of two spheres is

$$\frac{\partial P^0(r, t)}{\partial t} = D_1 \nabla^2 P^0(r, t) + S^0(r, t) \tag{3}$$

$S^0(r, t)$ is a point source

$$S^0(r, t) = \delta(r - r_0)\delta(t)/4\pi r_0^2$$

and D_1 the pair diffusion constant. The source in eq 3 was chosen in order that the solution, $P^0(r, r_0, t)$, has the property of a Green's function. Equation 3 will be solved subject to the initial condition, $P^0(r, r_0, t = 0) = 0$; the reflecting sphere boundary condition using $\mathbf{J} = -D_1 \nabla P^0$ in eq 2; and the requirement that $P(r, r_0, t)$ vanishes at $r = \infty$.

Equation 3 can be solved by Laplace transformation with respect to time, thereby generating a linear second-order differential equation with constant coefficients which is easily handled. After inverse Laplace transformation, we find the time-dependent solution evaluated at the collisional separation, $r = a$, to be

$$P^0(r = a, r_0, t) = (4\pi r_0 D_1 \tau_a)^{-1}\{[\tau_a/\pi t]^{1/2} \times \exp(-(r_0 - a)^2/4D_1 t) - \exp((r_0 - a)/a + t/\tau_a)\ \mathrm{erfc}\ ([t/\tau_a]^{1/2} + (r_0 - a)[4D_1 t]^{-1/2})\} \quad (4)$$

with $\tau_a = a^2/D_1$. A term, $4\pi a D_1$, may be factored from the denominator of eq 4 ensuring that the time integral of $P^0(a, r_0, t)$ evaluated at infinite time equals a/r_0, as discussed in the Appendix.

2. *Application to the Iodine Recombination Experiment.* For the case considered by Eisenthal et al.,[3] the source function, $S(r, t)$ has contributions, S_1 and S_2, from: (1) direct photolysis of I_2 which produces an isotropic distribution of I atoms with relative initial separation r_1 after the light pulse at $t = 0$

$$S_1(r, t) = \delta(r - r_1)\delta(t)\ S_1(0)/4\pi r_1^2 \quad (5)$$

(2) indirect I atom formation at the relative separation r_2 from the collisional deactivation of a molecular iodine excited state, called I_2^*.

$$S_2(r, t) = \delta(r - r_2)\exp(-k_R t)\ S_2(0)/4\pi r_2^2 k_R \quad (5a)$$

$S_1(0)$ and $S_2(0)$ are the initial concentrations of the I_2 excited states which dissociate immediately and after a time delay, respectively, k_R is the rate constant for the first-order decay of I_2^*. The total source, $S(r, t)$, is the sum of the formation rates $S_1(r, t)$ and $S_2(r, t)$.

Denote the solution to eq 3, using the source function in eq 5, by $P_S(r, t)$. In terms of the Green's function, $P^0(r = a, r_0, t)$, $P_S(r = a, t)$ is given by

$$P_S(r = a, t) = \int_0^t dt_1 \int d\mathbf{r}\ S(r, t_1)\ P^0(r = a, \mathbf{r}, t - t_1) \quad (6)$$

The total concentration of I_2 resulting from I atom recombination will be denoted by $C_1(t)$ and is related to the time integral of eq 6, evaluated at a collisional separation, $r = a$

$$C_1(t) = \lambda \int_0^t dt'\ P_S(r = a, t') \quad (7)$$

The parameter, λ, represents the fraction of I atoms at $r = a$ which react to form molecular I_2. The origin of this parameter λ is clarified in the Appendix.

The concentration of the excited state of I_2, also detected by the probe pulses, is simply

$$C_2(t) = \exp(-k_r t)\ S_2(0) \quad (8)$$

The transmittance of the light beam, $T(t)$, follows from Beer's law

$$T(t) = \exp(-Q\{C_1(t) + C_2(t)\}) \quad (9)$$

where Q contains the path length of the cell and the extinction coefficient. From eq 6–9 the transmittance can be calculated as a function of time, $S_1(0)$, $S_2(0)$, k_r, Q, r_1, r_2, λ, and τ_a. The parameter, τ_a, can be estimated using the Stokes–Einstein relation for the iodine atom diffusion constant, D_0, and the iodine atom radius, r_I

$$\tau_a = 2r_I^2/D_0 = 12\pi r_I^3(\eta/kT)$$

Using $r_I = 1.35$ Å and $\eta = 0.89$ cP, we calculate $\tau_a = 20$ ps.

With Green's function, eq 4, and the expression for the source, eq 5, the integrals in eq 7 can be performed

$$C_1(t) = \lambda\{S_1(0) + S_2(0)\}\ h(x, \epsilon) - \lambda S_2(0) \int_0^x dx_1\ g(x_1, \epsilon)\exp(-\kappa(x - x_1)) \quad (10)$$

with

$$(1 + \epsilon)\ h(x, \epsilon) = \mathrm{erfc}\left\{\frac{1}{2}\epsilon/\sqrt{x}\right\} - \exp(x + \epsilon)\ \mathrm{erfc}\left\{\sqrt{x} + \frac{1}{2}\epsilon/\sqrt{x}\right\} \quad (11a)$$

$$(1 + \epsilon)\ g(x, \epsilon) = (1/\sqrt{\pi x})\exp(-\epsilon^2/4x) - \exp(x + \epsilon)\ \mathrm{erfc}\left\{\sqrt{x} + \frac{1}{2}\epsilon/\sqrt{x}\right\} \quad (11b)$$

and $x = t/\tau_a$; $\kappa = k_r\tau_a$; $\epsilon = (r_1 - a)/a = (r_2 - a)/a$. As a simplification, the initial separation of the iodine atom pairs, used in eq 5, have been chosen to be equal, $r_1 = r_2$.

The effect of the $C_2(t)$ part of $T(t)$ is to increase T for times of the order of k_r^{-1}. For times longer than k_r^{-1}, the C_2 contribution can be simply ignored. Equation 10 for $C_1(t)$ has contributions from a κ dependent and a κ independent part. For $\kappa \gg 1$, we can integrate eq 10 by parts generating an asymptotic expansion in κ^{-1},

$$C_1(t) = \lambda\{S_1(0) + S_2(0)\}\ h(t/\tau_a, \epsilon) - \lambda S_2(0)\ g(t/\tau_a, \epsilon)/\kappa + O(\kappa^{-2}) \quad (12)$$

Numerical computation indicates that for $\kappa > 4$ and for times $k_r t > 1$, the κ dependent corrections can be neglected. This arises because of the inverse κ dependence and, more importantly, the function g decreases much faster than h. For the case, $\kappa = 2$ ($k_r = 10^{11}\ s^{-1}$, $\tau_a = 20$ ps), a 3% error in underestimating T is obtained at 40 ps by neglecting the κ dependent part. The error rapidly diminishes with increasing time. Therefore, on the basis of these remarks, we can treat I atom recombination for times longer than 40 ps as if the source were a delta function in time and we are assured that the curvature in T is not due to the reaction kinetics.

For times long compared to k_r^{-1}, we have the result

$$T(t) = \exp(-\Phi h(t/\tau_a, \epsilon)) \quad (13)$$

T is a function of three variables: τ_a was calculated above; Φ is a collection of constants $\Phi = Q(S_1(0) + S_2(0))\lambda$; and ϵ, a dimensionless number which measures the deviation of the initial relative separation of the radicals from the case of tangent radicals.

In comparing the diffusion theory to Eisenthal's experimental results, we shall fit the 800-ps point in Figure 1, using Φ as the adjustable parameter, fixing τ_a at 20 ps. In Figure 1 we represent three cases: initially tangent radicals, $r_0 = 2r_I$ or $\epsilon = 0$; radicals having the separation, $r_0 = 4r_I$ or $\epsilon = 1$; and finally a 50–50 mixture of the two previous cases. All three cases required a different value of Φ to fit the long time asymptote. Clearly, the 50–50 mixture of initial conditions better accommodates the data. A closer fit could be achieved by further experimenting with the initial conditions, however, we think the plotted results serve to underline the physics involved in the iodine atom pair dynamics. We therefore forego detailed curve fitting owing to the equivocal nature of the distance distribution which would result from such a procedure. Alternatively, one could choose $\tau_a = 80$ ps and thereby fit the data assuming initially tangent radicals. It is apparent that there are enough parameters which may be varied within reasonable limits and accommodate the experimental results. One is forced to conclude that the data from this experiment does not mitigate against a simple diffusional description for iodine recombination.

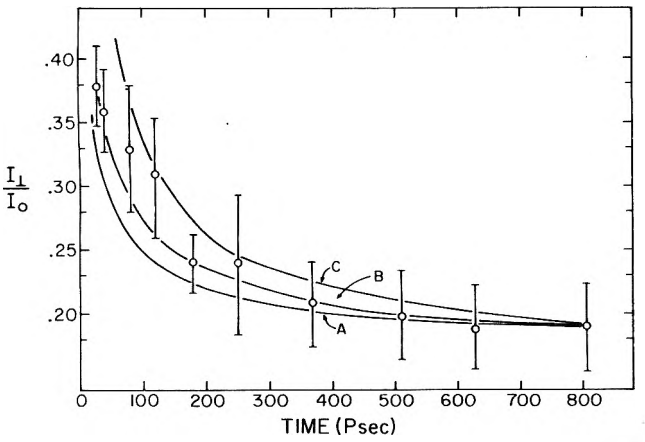

Figure 1. Probe transmission, $I_\perp/I_0$ for iodine in CCl_4. In all cases τ_a = 20 ps: (A) Φ = 1.81 and ϵ = 0; (B) Φ = 2.50 and a 50–50 mixture of ϵ = 0 and ϵ = 1; (C) Φ = 3.96 and ϵ = 1.

C. Refinements in the Theory of Recombination Dynamics

1. *General Considerations.* In picosecond experiments, it is possible that the direct temporal dependence of D is significant. Likewise, due to the shortness of the timescale, the distances probed by the translating radicals are the order of a few molecular diameters, and on this distance scale, the fluid will not appear continuous, as required by the simple diffusional models. It is appropriate to ask under what conditions will the spatial and temporal characteristics of D modify the simple model of Fick's law Brownian motion.

The criteria for the frequency breakdown of the diffusion equation for single particle motion is that the timescale be comparable to β^{-1} (= particle mass/friction constant). For times of the order of β^{-1}, the one particle distribution function or singlet density is coupled to the particle velocity and to higher moments of the velocity.[7] For I atoms in room temperature CCl_4, β^{-1} is very short (10^{-13} s) and, consequently, the momentum degrees of freedom relax essentially instantaneously on a timescale of a few picoseconds. The equation of motion for the momentum relaxed singlet density is just the ordinary diffusion equation. To sample the frequency dependent behavior of the diffusion process, the solvent viscosity would have to be increased by at least two orders of magnitude in order to shift β^{-1} into the tens of picosecond regime.

The situation is not nearly as clear regarding the spatial dependence of D. As a simple model, we will allow the I atoms to execute independent trajectories being correlated only by the initial conditions in the equation of motion for the two body distribution function. Because of the assumed independence of the particle trajectories, the two body distribution function can be derived from the equations of motion of the one particle function.

If the singlet density, $\sigma(r_1, t)$, is Markovian, it will obey a Chapman–Kolmogorov–Smoluchowski equation[8]

$$\sigma(\mathbf{r}_1, t + t_1) = \int d\mathbf{r}'\, \sigma(\mathbf{r}_1 - \mathbf{r}', t)\, \sigma(\mathbf{r}', t_1) \qquad (14a)$$

If $\sigma(r, t)$ evolves slowly in time and space, we can expand the left-hand side of eq 14 in a power series in time and the right-hand side in a power series in the spatial variable. Retaining the first-order time derivative and the second and fourth spatial derivatives (first and third vanish by symmetry) yields the equation

$$\partial\sigma/\partial t = D_0\nabla^2\sigma + D'\nabla^2(\nabla^2\sigma) \qquad (14b)$$

where D_0 is the one particle, Stokes–Einstein diffusion coefficient, and D', the super-Burnett coefficient,[9] is related to the fourth moment of the position variable. To fix the value of D', we shall consider the k-space single particle equation[10] generalized to include a wave vector dependent diffusion constant, $D(k)$.

$$\frac{\partial\sigma(k, t)}{\partial t} = -k^2 D(k)\sigma(k, t) \qquad (15)$$

$D(k)$ can be measured directly from the incoherent, inelastic scattering of thermal neutrons. From the neutron scattering experiments it is found that for large k, $O(1\ \text{Å}^{-1})$, $D(k)$ is explicitly wave vector dependent. A model for $D(k)$ proposed by Egelstaff[11] which has had considerable success in accommodating neutron scattering line widths is the so-called jump model,[11] wherein

$$D(k) = D_0/\{1 + D_0k^2\tau_0\} \qquad (16a)$$

In this version of a jump model, the time constant, τ_0, is interpreted as the time spent vibrating prior to a translation jump. For small k, $D(k)$ can be expanded

$$D(k) = D_0\{1 - D_0k^2\tau_0 \ldots\} \qquad (16b)$$

Inserting eq 16b into eq 15 and comparing this result with the k space analogue of eq 14 indicates that $D' = D_0^2\tau_0$. Therefore, for the case of independent particle diffusion, the effect of a spatially dependent diffusion constant is to recast eq 1 into the form

$$\partial P/\partial t = D_1\nabla^2 P + D_2\nabla^2(\nabla^2 P) \qquad (17)$$

where $D_1 = 2D_0$, and $D_2 = 2D_0^2\tau_0$. In the following section we shall solve eq 17 exactly and illustrate the effect of the correction term, D_2, on the time dependence of the relative translational motion.

2. *Solution of the Improved Diffusion Equation.* The equation of motion for the two particle density can be rewritten as

$$\partial P/\partial t = -\nabla \cdot \mathbf{J} \qquad (18)$$

where the flux, **J**, is

$$\mathbf{J} = -\{D_1\nabla P + D_2\nabla(\nabla^2 P)\} \qquad (19)$$

The reflecting sphere boundary condition, eq 2, restricts the flux on the spherical surface, $r = a$. The initial condition is a spherically symmetric point source at r_0.

$$P(r, t = 0) = \delta(r - r_0)/4\pi r_0^2 \qquad a \leq r_0 \qquad (20)$$

Since eq 17 is a fourth order differential equation, two additional boundary conditions are required. We shall use the constraints

$$\int \mathbf{r}^{2n} P(\mathbf{r}, t)\, d\mathbf{r} < \infty \qquad \text{for } n = 0, 1 \qquad (21)$$

These conditions restrict $P(r, t)$ to be volume normalizable and to have a finite second moment.

After performing the Laplace time transform of eq 17, defining $P(r, s)$ by

$$P(r, s) = \int_0^\infty dt\, \exp(-st)P(r, t) \qquad (22)$$

the resulting fourth-order linear differential equation with constant coefficients can be solved by standard means (taking the usual precautions regarding the continuity and appropriate discontinuity of $P(r, s)$ and its derivative across the position of the delta function source). In terms of the Laplace transform variable, the solution for $P(r, s)$ evaluated at the

collisional separation is

$$P(r = a, s) = \exp(-\Lambda(r_0 - a))/\{4\pi r_0 D_1(1 + a\Lambda)(1 + D_2\Lambda^2/D_1)\} \quad (23)$$

with

$$\Lambda = (D_1/2D_2)^{1/2}\{[1 + 4sD_2/D_1^2]^{1/2} - 1\}^{1/2} \quad (24)$$

As discussed in the end of section B.1, $4\pi aD_1$ can be factored from the denominator of eq 23. To simplify the following notation and execution of the inverse Laplace transform, set $\tau_0 = 2D_2/D_1^2$ and $r_0 = a$. The inverse transform can be reduced to a single real integral

$$(\tau_a + \tau_0/2)P(a, t) = (1/2)\exp(-t/2\tau_0)g(t/2\tau_0, \epsilon = 0) + \int_0^\infty dx(x/x_0)D(x - x_0)\, f(x) \quad (25)$$

with

$$f(x) = W_I(\sqrt{2x\tau_a/\tau_0}) - \exp(x)\,\mathrm{erfc}\,(\sqrt{x}) \quad (26)$$

$$W_I(y) = \mathrm{Im}\, W(iy) = \frac{2}{\sqrt{\pi}}\exp(-y^2)\int_0^y dy' \exp(y'^2) \quad (27)$$

$$D(x - x_0) = \exp(-(x - x_0)^2)/2\sigma_0)/[2\pi\sigma_0]^{1/2} \quad (28)$$

and

$$x_0 = t/\tau_a,\ \sigma_0 = (t/\tau_a)(\tau_0/\tau_a)$$

$g(x, \epsilon)$ is given by eq 11b and $W_I(y)$ has been tabulated for small arguments.[13] Although the integral in eq 25 could not be performed analytically for arbitrary τ_0 and τ_a it could be approximated in the limit of $\tau_0/\tau_a \ll 1$. In this limit, $D(x - x_0)$ is sharply peaked about x_0 and approaches the Gaussian representation of a delta function as $\tau_0/\tau_a \to 0$. If $D(x - x_0)$ is very narrow but not a delta function, we can expand the integrand in terms of products of its derivative and the moments of $D(x - x_0)$.

$$[\tau_a + 1/2\tau_0]P(a, t) = (1/2)\exp(-t/2\tau_0)\, g(t/2\tau_0, 0) + \sum_{n=0}^{\infty} M_n \frac{\partial^n}{\partial x^n}\{x\, f(x)/x_0\}_{x_0} \quad (29)$$

$$M_n = \frac{1}{n!}\int_0^\infty dx(x - x_0)^n D(x - x_0) \quad (30)$$

The physical content of eq 29 can be made more transparent if we consider the behavior of the leading term, $f(x_0)M_0$, temporarily neglecting the contribution from the higher moments. For comparison purposes, we reiterate the Fick's law solution given in Section B, $P^0(a, t)$, obtained using the same boundary and initial conditions as in the case of $P(a, t)$.

$$\tau_a P^0(a, t) = 1/\sqrt{\pi x_0} - \exp(x_0)\,\mathrm{erfc}\,(\sqrt{x_0})$$

In the limit of very short times, $t \ll \tau_0$, $P(a, t)$ behaves as

$$P(a, t) \simeq [\tau_0/2\pi t\tau_a^2]^{1/2}$$

which is to be compared with the more rapid growth of $P^0(a, t)$

$$P^0(a, t) \simeq [\pi t\tau_a]^{-1/2}$$

With increasing time, $\tau_0 \ll t \sim \tau_a$, $P(a, t)$ can be represented by the asymptotic expansion

$$P(a, t) = \left\{\tau_a P^0(a, t) + (\tau_a/\pi t)^{1/2} \times \sum_{n=1}^{\infty}(\tau_0/4t)^n 1.3 \ldots (2n - 1)\right\}/(\tau_a + 1/2\tau_0)$$

In this intermediate regime, $P(a, t)$ increases relative to $P^0(a, t)$, crosses $P^0(a, t)$ and, for longer times, bounds $P^0(a, t)$ from above. Finally, for very long times, $t \gg \tau_a$, both $P(a, t)$ and $P^0(a, t)$ decay as

$$P(a, t) = P^0(a, t) \simeq [\tau_a]^{1/2}/2[\pi t^3]^{1/2}$$

One would expect that the tail would be unaffected by the extra diffusion constant. Likewise, the role of the spatial dependence in D is to retard motion for small separations, whereupon, $P(a, t)$ will fall off more slowly than $P^0(a, t)$. In order to maintain time normalization, the $P(a, t)$ must lie below $P^0(a, t)$ for very short times. It is notable that the behavior in the intermediate range, $\tau_0 \ll t \sim \tau_a$, was precisely what the theory was to achieve, viz., retarded translational motion due to the microscopic structure of the fluid.

The correction terms due to the first and second moments are significant only for short times, $t < \tau_0$. Both the first and second moment are oscillatory functions of time which oscillate roughly out of phase with one another, and individually have a vanishing time integral. For times below τ_0, the moment expansion does not suffice as the zeroth, first, and second moments are of the same magnitude. Fortunately, the absolute magnitude of the first moment decreases exponentially for times longer than τ_0. Although the second moment decreases more slowly than the first, it does decay by an order of magnitude in going from $t = \tau_0$ to $t = 2\tau_0$, being negligible for longer times. In the long time limit, $t \gg \tau_0$, the second moment decays as $t^{-5/2}$ and therefore does not affect the $t^{-3/2}$ tail of the zeroth moment.

The moment calculation indicates that the analytic results are only accurate for times longer than about $t = \tau_0$. To extend the treatment to times less than this requires a more accurate calculation of the integral in eq 25.

$P(a, t)$ was calculated using eq 29 and 30, retaining terms up to the second moment using $\tau_0 = 0.2\tau_a$ and compared with $P^0(a, t)$. The maximum difference between $P(a, t)$ and $P^0(a, t)$ was 36% and that occurred at $t = 0.5\tau_a$. At $t = \tau_a$, the deviation is reduced to 12% and by $t = 3\tau_a$ drops further to 5%. It is apparent that the retardation of relative diffusion is significant and within the realm of detection provided the timescale is of the order $0.5 < t/\tau_a < 3$–4. Using τ_a of 20 ps indicates that τ_0 is 4 ps. From neutron scattering in neat liquid argon and pentane,[11] values of $\tau_0 \sim 1$–2 ps have been reported. The value of τ_0 used here (for the CCl_4–I_2 solution) was chosen to be slightly longer, although it is certainly a reasonable figure.

D. Summary

In this calculation we have presented a solution to the diffusion equation using reflecting sphere boundary condition and apply it to the analysis of Eisenthal's laser experiments. The experimental results can be fit using either a long correlation time ($\tau_a = 80$ ps) and initially tangent radicals, or a more reasonable time, $\tau_a = 20$ ps, and a distribution of initial conditions (i.e., a 50:50 mixture of initially tangent atoms and atoms with an intervening solvent molecule). In this context, initial denotes a description of the system at a time long compared with β^{-1} but short compared to τ_a. The requirement involving β ensures that the momentum released by the rupture of the I–I bond is dissipated by collisions with the fluid and that the atoms have attained a Maxwellian velocity distribution. As the dissipation of excess momentum will require several collisions, the resulting initial separation of the atoms will not in general correspond to tangency of the species.

Eisenthal's results are in agreement with this interpretation.

In section C of this paper it was demonstrated that the dynamical effects associated with breakdown of the continuum description of the fluid are not entirely negligible and are, *in principle, capable of detection on a picosecond* timescale.

Two difficulties arise concerning the iodine case: (1) The competing chemical kinetics of molecular iodine formation and dissipation, apart from the diffusion controlled contribution, occur on a timescale when the corrections to the diffusion model become important. Therefore, one is not sure if an apparent deviation from Fick's law is indicative of complicated kinetics or a true non-Fickian behavior. (2) The observable is the total concentration of molecular iodine and is a time integral of the solution to the appropriate diffusion equation. The integrated solutions are a much less sensitive function of the dynamics, than the integrand itself. It would *seem that the detection of the subtleties of the fluid, such as* a jump time, would force one to employ viscous media whereupon the timescale for the liquid dynamics is shifted out of the realm of the competing chemical kinetics.

Acknowledgment. This work was supported in part by the National Institutes of Health under Grant No. GM 13556.

Appendix A. Effect of the Delta Function Sink

To evaluate the effect of the sink term in eq 1, we shall solve eq 1a with Fick's law flux, reflecting sphere boundary condition at $r = a$; a delta function sink at $r = a'$, and initial condition at $r = r_0$ with $r_0 \geq a, a'$. Because we have employed a sink, the probability of forming a recombination *product is*[4a]

$$\mathrm{p}(t) = \int \mathrm{d}\mathbf{r}\, K(r)\mathrm{P}(r, t) \qquad \text{(A1)}$$

$K(r)$ is given by eq 1c and K is the rate density for loss of pairs. In terms of a first-order rate constant, K_0 (in units of s^{-1}), K is of the order $K_0 a'^3$. The solution to the boundary value *problem and appropriate calculation of p(t) gives the* intermediate result

$$\mathrm{p}(s) = (a/r_0)\exp(-q(r_0 - a))K_0\tau_a/\{1 + aq + K_0\tau_a\} \qquad \text{(A2)}$$

with

$$\mathrm{p}(s) = \int_0^\infty \mathrm{d}t\, \exp(-st)\mathrm{p}(t)$$

and

$$q = [s/D_1]^{1/2}$$

In the final stage of the solution we have allowed the chemical reaction or sink to operate at the separation corresponding to touching spheres and therefore a' was set equal to a from above. Equation A2 can be rearranged to give

$$\mathrm{p}(s) = (a/r_0)\lambda \exp(-q(r_0' - b))/(1 + bq) \qquad \text{(A3)}$$

with $\lambda = K_0\tau_a/(1 + K_0\tau_a)$, $b = a/(1 + K_0\tau_a)$, and $r_o' = r_0 - K_0\tau_a b$. Equation A3 consists of three parts. The factor, a/r_0, represents the fraction of atoms born at the relative separation r_0, which will eventually recombine with their original partners. The fraction, λ, inserted heuristically in eq 7 arises naturally in the current context and can be interpreted as the fraction of atoms which recombine on a collision. The remaining part, $\exp(-q(r_0' - b))/1 + bq)$, differs from the sink-free solution in that the distance b replaces a and r_0' replaces r_0. Thus, apart from a change of scale, the basic time dependent solutions are not modified by the use of a delta function sink.

References and Notes

(1) (a) M. Smoluchowski, *Ann. Phys.*, **48**, 1103 (1915); *Z. Phys. Chem.*, **92**, 129 (1917); (b) For a summary, see R. M. Noyes, *Prog. React. Kinet.*, **1**, 131 (1961).
(2) R. G. Lawler, *Prog. Nucl. Magn. Reson. Spectrosc.*, **9**, 3 (1973).
(3) T. J. Chuang, G. W. Hoffman, and K. B. Eisenthal, *Chem. Phys. Letts.*, **25**, 201 (1974).
(4) (a) G. T. Evans, P. D. Fleming, and R. G. Lawler, *J. Chem. Phys.*, **58**, 2071 (1973); (b) G. T. Evans and R. G. Lawler, *Mol. Phys.*, **30**, 1085 (1975); (c) G. T. Evans, *Mol. Phys.*, **31**, 777 (1976).
(5) G. Wilemski and M. Fixman, *J. Chem. Phys.*, **58**, 4009 (1973).
(6) A solution of a boundary value problem of this type can be found in several elementary texts, e.g., E. A. Kraut, "Fundamentals of Mathematical Physics", McGraw-Hill, New York, N.Y. 1967.
(7) S. A. Rice and P. Gray, "The Statistical Mechanics of Simple Liquids", Interscience, New York, N.Y., 1965, p 250.
(8) I. Oppenheim, K. E. Shuler, and G. H. Weiss, *Adv. Mol. Relaxation Processes*, **1**, 13 (1967).
(9) D. Burnett, *Proc. London Math. Soc.*, **40**, 382 (1935). For a more recent discussion of the Burnett coefficients, consult I. M. De Schepper, H. Van Beyeren, and M. H. Ernst, *Physica*, **75**, 1 (1974).
(10) B. J. Berne and G. D. Harp, *Adv. Chem. Phys.*, **17**, 63 (1970).
(11) P. A. Egelstaff, "An Introduction to the Liquid State", Academic Press, New York, N.Y., 1967, Chapter 10.
(12) T. Springer, "Quasielastic Neutron Scattering for the Investigation of Diffusive Motions in Solids and Liquids", Springer Tracts in Modern Physics, Vol. 64, Springer-Verlag, Berlin, 1972.
(13) W. Gautschi in "Handbook of Mathematical Functions", M. Abramowitz and I. A. Stegun, Ed., Dover Publications, New York, N.Y., 1965, p 325 ff.

Pulse Radiolysis of Aqueous Cyanide Solutions. Kinetics of the Transient OH and H Adducts and Subsequent Rearrangements

Hch. Büchler, R. E. Bühler,* and R. Cooper[1]

Laboratory for Physical Chemistry, Swiss Federal Institute of Technology, CH-8006 Zurich, Switzerland *(Received December 29, 1975)*

OH radical reactions with aqueous cyanide were studied by pulse radiolysis over the pH range 1.9–15. The reaction is characterized by three pH ranges: (A) In acid solution (up to pK(HCN/CN$^-$) = 9.3), OH adds to HCN with $k = (6 \pm 2) \times 10^7$ M^{-1} s^{-1}, forming HO–CH=N. This radical disappears by second-order kinetics with $2k = (2.8 \pm 0.5) \times 10^9$ M^{-1} s^{-1}. (B) In alkaline solutions (pH 9.3 to pK(OH/O$^-$) = 11.9) the OH radical adds to CN$^-$ with $k = (7.1 \pm 0.5) \times 10^9$ M^{-1} s^{-1}. Subsequently a fast protonation equilibrium occurs HO–Ċ=N$^-$ + H$^+$ ⇌ HO–Ċ=NH (pK = 10.2 ± 0.5), the product decaying by an H-atom transfer to the radical ·CONH$_2$ with $k = (4.0 \pm 1.0) \times 10^7$ s^{-1}. This latter radical disappears with $2k = (6.2 \pm 1.0) \times 10^9$ M^{-1} s^{-1}. (C) In very alkaline solutions (pH > pK(OH/O$^-$) = 11.9) the O$^-$ addition to CN$^-$ ($k = 2.6 \times 10^8$ M^{-1} s^{-2}) and the consecutive protonation and rearrangement to form ·CONH$^-$ are identical with the results published by Behar. Computer simulation techniques were used to determine the resolved spectra, extinction coefficients, and rate constants from the experimentally observed absorptions. The amount of contribution from remaining H-atom reactions has been analyzed separately. The H addition to HCN ($k = 3.6 \times 10^7$ M^{-1} s^{-1}) leads to the CH$_2$=N· radical showing an absorption band with λ_{max} 275 nm. This radical disappears by a second-order process with $2k = (2.6 \pm 0.8) \times 10^9$ M^{-1} s^{-1}. The results for the OH reactions have been corrected for the contribution from the small amount of H-atom reactions throughout the mechanism.

Introduction

In analogy to halogenide ions[2] and to the thiocyanide ion,[3] it was originally expected, that an aqueous solution of cyanide (a pseudo-halogenide) should also follow the usual reaction mechanism under OH radical attack:

$$OH + X^- \rightarrow HOX^- \quad (1)$$

$$HOX^- + X^- \rightarrow OH^- + X_2^- \quad (2)$$

During the present study this was shown not to be the case; no $(CN)_2^-$ or its protonated form $H(CN)_2$ could be found. This was also shown by Behar et al.,[4,5] whose work paralleled ours. Earlier work by others usually studied the initial OH-addition step or H-addition step only by competition experiments.[6-9] The present study, in general, supports the results by Behar et al. However, due to better time resolution and due to the application of a computer simulation, additional information on the mechanism, and new or improved transient spectra and rate data could be derived.

In relation to the pK values of the primary reaction species (pK(HCN/CN$^-$) = 9.31[10] and pK(OH/O$^-$) = 11.9[11]) three pH regions have been distinguished. Scheme I gives a survey of the mechanisms involved.

Experimental Section

The pulse radiolysis apparatus has been described elsewhere.[2,12] All solutions were prepared in triply distilled water, deoxygenated by argon bubbling for at least 30 min. The potassium cyanide, potassium hydroxide (Fluka puriss. p.a. = 99.9%) and perchloric acid (Merck puriss. p.a. = 99.99%) were used without further purification. When HCN was needed in the system, an aqueous cyanide solution was deoxygenated by bubbling with argon (and saturated with N_2O if desired) before the pH was adjusted by adding a separately degassed $HClO_4$ solution. Thus loss of HCN could be avoided.

For measurements at wavelengths below 280 nm appropriate interference filters were added (Barr & Stroud Ltd, Type UD1 and U2). Under these conditions the stray light was ≤1‰.

For the computer simulation each of the systems was selected in such a manner that only one or two parameters had a dominant influence on the observed experimental rate curves. The relative importance of the reactions was checked by comparing the actual calculated reaction rates.

Results and Discussion

1. *Reactions of the Hydroxyl Radicals and Hydrogen Atoms with Hydrogen Cyanide (pH ≪ pK(HCN/CN$^-$) = 9.31).* The reaction of OH with HCN and its subsequent processes were investigated in N_2O-saturated aqueous solutions of 10^{-2} M HCN at pH 3.5 (system 1, Table I) and 10^{-1} M HCN at pH 2.85 (system 2). For the former system an absorption spectrum with λ_{max} 240 nm was observed 250 ns after the end of the pulse. It is identical with the one detected by Behar[5] for comparable conditions. Behar attributed this to be the OH adduct radical HOCH=N·. From the upper limit of $k_3 \leq 5 \times 10^7$ M^{-1} s^{-1} given by Draganic et al.[9] an estimate indicates that only a few percent of the OH radicals should have reacted 250 ns after the pulse. The spectrum peaking at 240 nm therefore must contain a strong contribution from the well characterized OH radical absorption[13] (λ_{max} 230 nm; ϵ_{230} 543 M^{-1} cm^{-1}). For system 2, with a ten times larger HCN concentration, a similar estimate predicts that about 99% of the OH radicals will have reacted with HCN 1 μs after the pulse. Figure 1 clearly shows this difference in the two spectra. Except for a small contribution from the H-adduct radical (ca. 18% CH$_2$=N·), this spectrum is assigned to the OH-adduct radical HOCH=N·. By converting all hydrated electrons to hydrogen atoms in a very acid solution (system 3, pH 1.9) a band at 275 nm appears (Figure 2), which we assign to the H-adduct radical:

$$H + HCN \rightarrow CH_2{=}N\cdot \quad (15)$$

From competition experiments Draganic has already reported

Scheme I

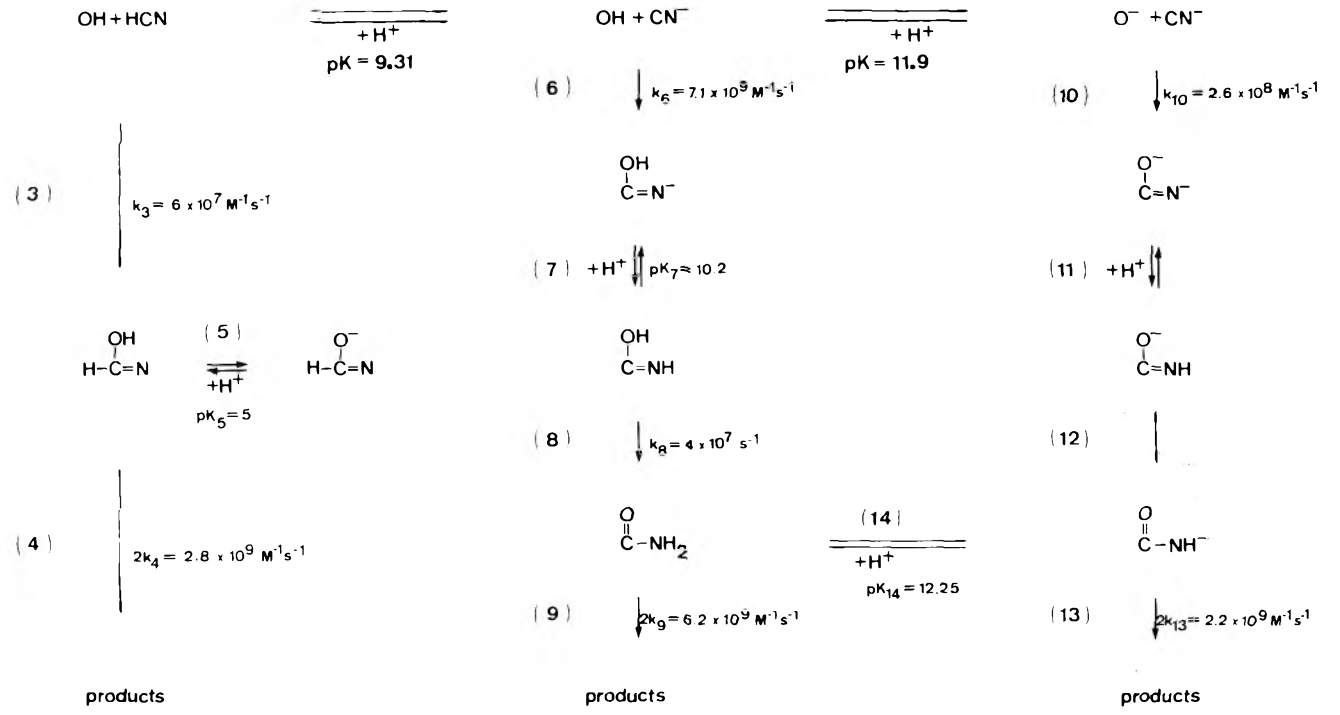

TABLE I

System no.	$[HCN]_{tot}$, M	pH ±0.1	$[N_2O]$, M	Dose, ±1.5 krads
1	10^{-2}	3.5	2.5×10^{-2}	29.4
2	10^{-1}	2.85	2.5×10^{-2}	34.8
3	10^{-1}	1.9		34.8
4	10^{-2}	9.85	2.5×10^{-2}	25.8
5	10^{-4}	10.6	2.5×10^{-2}	25.8
6	10^{-2}	10.7	2.5×10^{-2}	25.8
7	10^{-1}	11.4	2.5×10^{-2}	28.1
8	10^{-2}	11.5	2.5×10^{-2}	30.7
9	10^{-2}	11.1	2.5×10^{-2}	29.4
10	10^{-2}	10.2	2.5×10^{-2}	29.4
11	10^{-1}	10.2	2.5×10^{-2}	31.2
12	10^{-2}	15.0	2.5×10^{-2}	32.0

the rate constant to be $k_{15} = 3.6 \times 10^7\ M^{-1}\ s^{-1}$.[9] At very long times (>200 μs) the spectra of the products appear with $\lambda_{max} < 270$ nm in both systems 2 and 3. They most likely are due to the following radical combination reactions:

$$2HO\text{-}CH{=}N\cdot \rightarrow \text{products} \quad (4)$$

$$2CH_2{=}N\cdot \rightarrow \text{products} \quad (16)$$

$$CH_2{=}N\cdot + HO\text{-}CH{=}N\cdot \rightarrow \text{products} \quad (17)$$

Whether the spectra are due to the direct combination product or to some secondary products (e.g., by hydrolysis) cannot be resolved.

For this low pH region the reaction mechanism consists of reactions 3, 4, 15, 16, and 17, together with the complete set of reactions for water radiolysis (see description in ref 2). This mechanism can be simulated by numerical integration on a computer. The unknown rate data k_3, k_4, and k_{16} are parameters for the computer optimization (for details of a comparable computer optimization see ref 2). Since the extinction coefficients and spectrum of the OH radical is known,[13] and

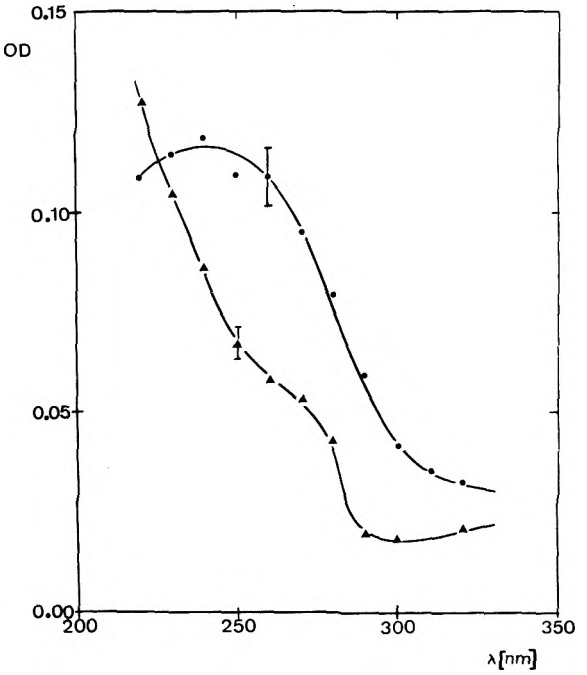

Figure 1. Spectra obtained in N_2O saturated aqueous solution of 10^{-1} M HCN at pH 2.85 (▲, 1 μs after pulse end) and of 10^{-2} M HCN at pH 3.5 (●, 0.25 μs after pulse end).

the one for the products can be derived from measurements at very long times, the computer calculated concentrations allow the determination of the extinction coefficient for the OH-adduct radical HO-CH=N· at any time of the experiment:

$$\epsilon(HO\text{-}CH{=}N\cdot) = \frac{OD(\text{expt}) - OD(OH) - OD(\text{products})}{l[HO\text{-}CH{=}N\cdot]} \quad (I)$$

ε must be constant at all times. This condition was used to

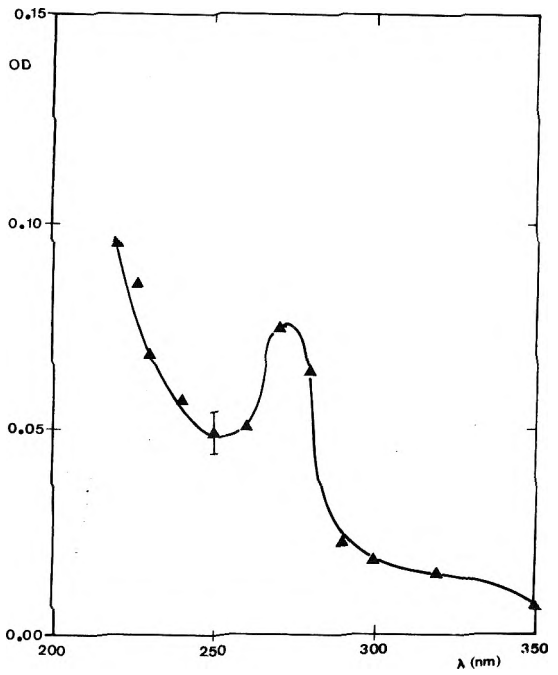

Figure 2. Spectrum obtained in aqueous 0.1 M HCN solution at pH 1.9: (▲) 1 μs after pulse end.

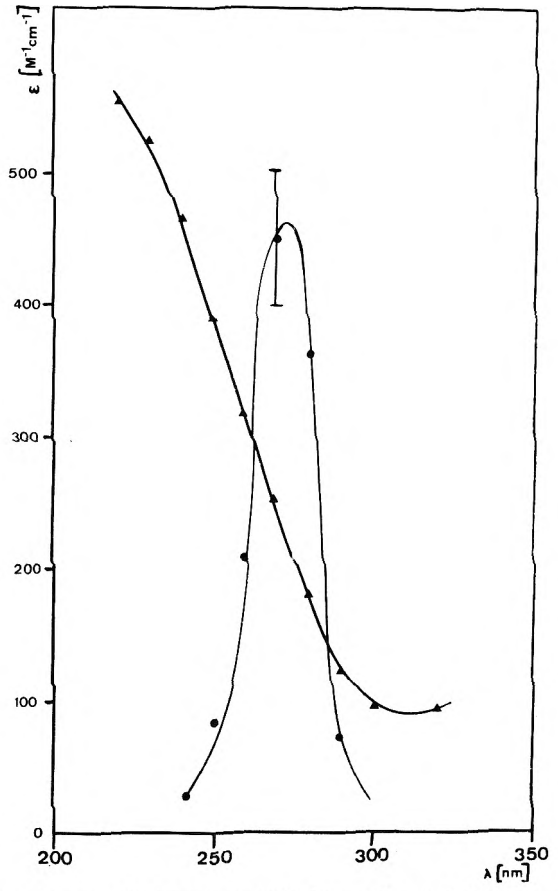

Figure 3. Spectra obtained by numerical computer analysis of the acid cyanide systems 1, 2 and 3: (▲) HOCH=N·, (●) H_2CN.

optimize the appearance rate constant k_3 and the disappearance rate constant k_4 for the OH-adduct radical in the computer simulation for $\lambda \leq 250$ nm in system 2 (Table I). In this wavelength region no H-adduct radical absorbs. The rate

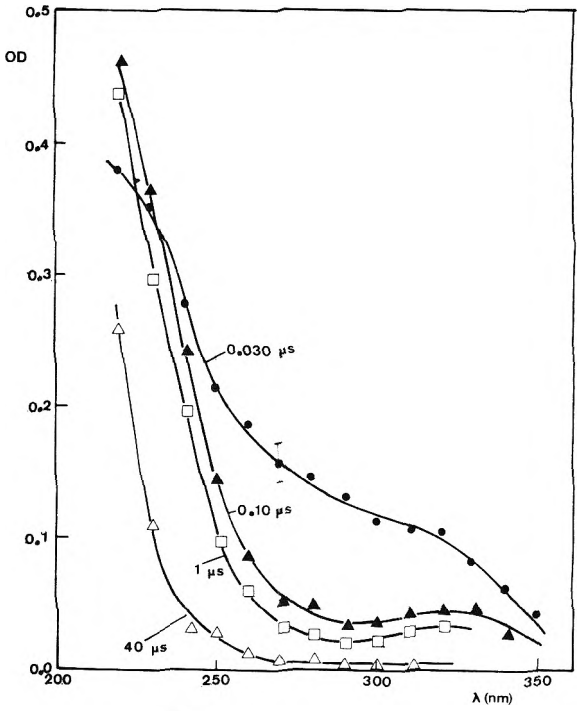

Figure 4. Spectrum obtained in aqueous, N_2O saturated, 10^{-2} M cyanide solution at pH 9.85 (●) 30 ns, (▲) 100 ns, (□) 1 μs, and (△) 40 μs after pulse end.

constants were determined to be $k_3 = (6 \pm 2) \times 10^7\ M^{-1}\ s^{-1}$ and $2k_4 = (2.8 \pm 0.5) \times 10^9\ M^{-1}\ s^{-1}$. In the range 250 nm $\leq \lambda \leq$ 300 nm both adduct radicals (HO-CH=N· and CH_2=N·) contribute to the absorption. Their extinction coefficients can be determined from the results from systems 2 and 3, together with the known value of k_{15} and the values for k_3 and k_4 derived above, by solving the following for the two systems (i = 2, 3):

$$\frac{OD_i(\text{expt}) - OD_i(OH) - OD_i(\text{products})}{l} = \epsilon(HO\text{-}CH{=}N\cdot)[HO\text{-}CH{=}N\cdot]_i + \epsilon(CH_2{=}N\cdot)[CH_2{=}N\cdot]_i \quad \text{(II)}$$

The criterion that for any wavelength between 250 and 300 nm and for any time of the experiment the extinction coefficients have to be constant is maintained. This approach leads to a value for the decay rate constant, k_{16}, of $2k_{16} = (2.6 \pm 0.8) \times 10^9\ M^{-1}\ s^{-1}$. The resulting spectra for the two adduct radicals HO-CH=N· and CH_2=N· are shown in Figure 3.

2. *Reactions of the Hydroxyl Radical with Cyanide Ions (9.31 ≪ pH ≪ 11.9).* Typical transient spectra due to OH radical reactions with the cyanide ions are given in Figure 4 (system 4, pH 9.85). Although this pH is very close to the pK(HCN/CN^-) value, the OH radicals react predominantly with the cyanide ion, $k_6 \gg k_5$. The spectrum at 1 μs has already been assigned by Behar[5] to the ·$CONH_2$ radical, in agreement with results from ESR measurements with in-situ radiolysis of a similar system.[4] The reaction sequence is initiated by OH addition to CN^- (reaction 6), most likely followed by a very fast protonation equilibrium (reaction 7) and an intramolecular hydrogen transfer (reaction 8) to form the identified ·$CONH_2$ radical. These intermediate steps 7 and 8 are responsible for the early transient spectra in Figure 4 (curves for 30 and 100 ns). With a small CN^- concentration (typically 10^{-4} M; system 5) the second-order build up reaction 6 becomes quite slow relative to the very fast succeeding

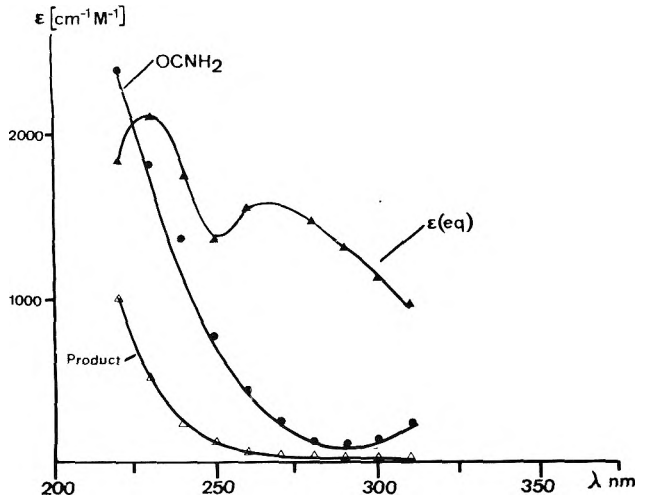

Figure 5. Spectra obtained in systems 4, 6, 8, 9, 10, and 11 by numerical computer analysis: (●) $OCNH_2$, (△) products, (▲) $\epsilon(eq)$, for the equilibrium HOCNH $\rightleftharpoons$ $HOCN^- + H^+$ at pH 9.85 (for details see text).

steps 7 and 8. In this case, reaction 6 is rate determining for the build up of the $\cdot CONH_2$ radical absorption. The resulting $k_6 = (7.1 \pm 0.5) \times 10^9\ M^{-1}\ s^{-1}$ is in good agreement with the published value.[5] In highly concentrated CN^- solutions (typically 10^{-2} M CN^-), however, reaction 6 (and also the protonation reaction 7) is very much faster than the hydrogen-transfer reaction 8. From solutions at pH 9.85, 10.7, and 11.4 (systems 4, 6, and 7) the rate constant $k_8 = (4.0 \pm 1.0) \times 10^7\ M^{-1}\ s^{-1}$ is derived. The final disappearance of the $\cdot CONH_2$ radical absorption has already been reported to be of second order with $k_9 = 6.2 \times 10^9\ M^{-1}\ s^{-1}$.[5] In changing the pH value from 9.85 to 11.4 it was found that the earliest transient spectra (the 30-ns spectrum in Figure 4) did change, although the 1-μs transient spectra were identical. This is clearly due to the shift in the protonation equilibrium 7. In order to separate the absorption spectra of the three transients involved (HO–Ċ=N^-, HO–Ċ=NH, and $\cdot CONH_2$) the reaction mechanism was again simulated by computer. In this case all rate constants were already known from the experiments. Under the assumption that equilibrium 7 be established faster then any other reaction step in this mechanism, the only unknown data were the values of pK_7, the extinction coefficients, and spectra of the transients. For all systems with 9.85 < pH < 11.5 the time profiles of all transient concentrations could be calculated by numerical integration. The optical densities at 1 and 10 μs after the pulse end were found to be due almost exclusively to the radical $\cdot CONH_2$ and the product, respectively. The spectra as shown in Figure 5 for $\cdot CONH_2$ and the products represent the average values of the extinction coefficients from the six systems 4, 6, 8, 9, 10, and 11 (Table I). The third curve in Figure 5 represents the composite spectrum of both species making up equilibrium 7 (system 4 only; pH 9.85). As long as pK_7 is not known, the computer calculates the sum of the concentrations [HO–Ċ=N^-] and [HO–Ċ=NH]. The composite extinction coefficient $\epsilon(eq)$ was therefore calculated by

$$\epsilon(eq) = \frac{OD(expt) - OD_{calcd}(OH) - OD_{calcd}(CONH_2) - OD_{calcd}(prod)}{l([HOCN^-] + [HOCNH])} \quad (III)$$

Actually $\epsilon(eq)$ is a concentration-weighted average of the true ϵ values:

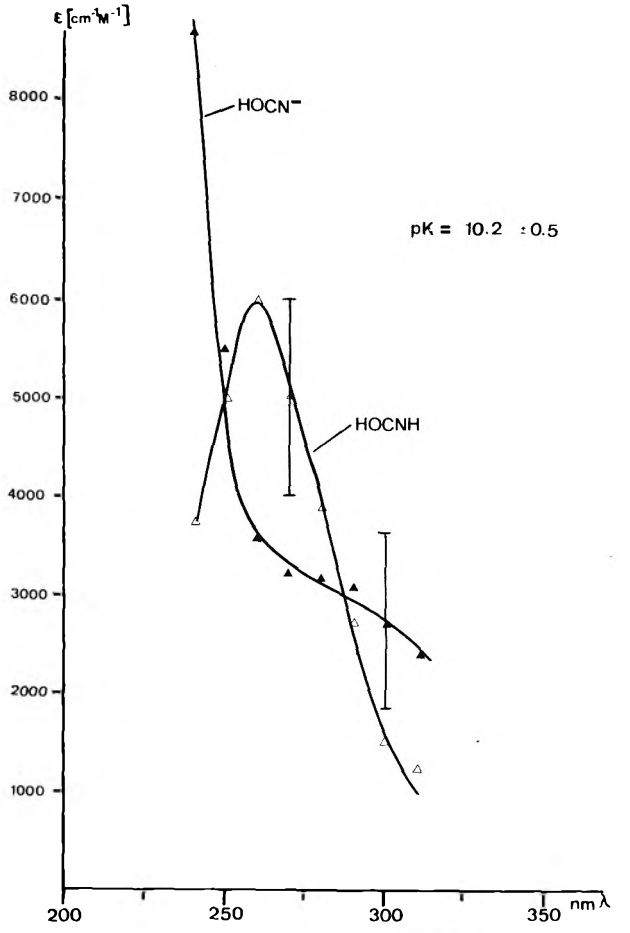

Figure 6. Spectra obtained for HOCNH and $HOCN^-$ in the numerical computer analysis using systems 4, 6, and 7 (Table I).

$$\epsilon(eq) = \frac{\epsilon(HOCN^-)[HOCN^-] + \epsilon(HOCNH)[HOCNH]}{([HOCN^-] + [HOCNH])} \quad (IV)$$

If the pH dependence of equilibrium 7 is introduced into eq IV we obtain

$$\epsilon(eq)(10^{pH} + 10^{pK_7}) = \epsilon(HOCN^-) \times 10^{pH} + \epsilon(HOCNH) \times 10^{pK_7} \quad (V)$$

The unknown quantities in this equation are pK_7, $\epsilon(HOCN^-)$, and $\epsilon(HOCNH)$. $\epsilon(eq)$ was determined for the three systems 4, 6, and 7 (i.e., pH 9.85, 10.7, and 11.4). From the resulting three equations of type (V), the three unknown quantities could be determined at each wavelength. Figure 6 shows the individual spectra of the radicals HO–Ċ=N^- and HO–Ċ=NH as determined by the method outlined above. At each wavelength an individual pK_7 value is calculated. The average of all values is $pK_7 = 10.2 \pm 0.5$.

3. *Reaction of O^- with Cyanide Ions ($pH \gg pK(OH/O^-) = 11.9$).* The transient absorption in an aqueous 10 M KOH solution of cyanide (system 12) is identical with the published spectrum at pH 14.[5] The spectrum is assigned to the radical anion $\cdot CONH^-$. The rate constants for reactions 10 and 13, determined in system 12, are again identical with the published data at pH 14. In an attempt to find the absorption of the precursor species of $\cdot CONH^-$, the dianion $^-OCN^-$, system 12 was studied at reduced temperature (213 K). No spectral change was observed.

Conclusions

A complete reaction mechanism for OH reactions with hydrogen cyanide in the pH range from 1.9 to 15 is presented (Scheme I). All major processes as proposed by Behar[5] have been confirmed, including the rate data k_6, k_9, k_{10}, k_{13}, and pK_{14}. Equilibrium 5 has not been rechecked, as the species $^-O\text{-}CH{=}N\cdot$ is only detectable by ESR.[4] Original rate data have been derived for k_3, k_4, k_8, k_{16}, and pK_7. The spectra and extinction coefficients of all transient species in this complete mechanism are now known. The only exception is the dianion $^-O\text{-}\dot{C}{=}N^-$ at pH >11.9, which seems to have a lifetime shorter than about 30 ns in all systems studied.

The reaction mechanism discussed in this paper represents one of the rare cases where a complete quantitative understanding could be achieved.

Acknowledgment. This work was supported by the Schweizerischer Nationalfonds zur Förderung der wissenschaftlichen Forschung.

References and Notes

(1) On leave from the University of Melbourne, Department of Physical Chemistry, Parkville, Victoria 3052, Australia.
(2) H. Büchler and R. E. Bühler, *Chem. Phys.*, in press.
(3) D. Behar, P. L. T. Bevan, and G. Scholes, *J. Phys. Chem.*, **76**, 1537 (1972).
(4) D. Behar and R. W. Fessenden, *J. Phys. Chem.*, **76**, 3945 (1972).
(5) D. Behar, *J. Phys. Chem.*, **78**, 2660 (1974).
(6) I. Kraljic and C. N. Trumbore, *J. Am. Chem. Soc.*, **87**, 2547 (1965).
(7) I. G. Draganic, Z. D. Draganic, and R. A. Holroyd, *J. Phys. Chem.*, **75**, 608 (1971).
(8) H. Ogura, T. Fujimura, S. Murozono, K. Hirano, and M. Kondo, *J. Nucl. Sci. Technol.*, **9**, 339 (1972).
(9) I. Draganic, Z. D. Draganic, Lj. Petkovic, and A. N. Kolic, *J. Am. Chem. Soc.*, **95**, 7193 (1973).
(10) "Handbook of Chemistry and Physics", 54th ed, The Chemical Rubber Co., Cleveland, Ohio, 1973–1974.
(11) G. V. Buxton, *Trans. Faraday Soc.*, **66**, 1656 (1970).
(12) B. Hurni, U. Brühlmann, and R. E. Bühler, *Int. J. Radiat. Phys. Chem.*, **7**, 499 (1975).
(13) P. Pagsberg, H. Christensen, J. Rabani, G. Nilsson, J. Fenger, and S. O. Nielson, *J. Phys. Chem.*, **73**, 1029 (1969).

Pulse Radiolysis of Ethyl Acetate and Its Solutions[1]

G. Ramanan

Chemistry Division, Bhabha Atomic Research Centre, Bombay 400085, India *(Received November 26, 1975)*

Pure ethyl acetate was subjected to electron pulse radiolysis in the liquid state and the absorption spectrum of the transient species produced was obtained between 280 and 650 nm. Two different species were produced, one with a short life of about 150 ns absorbing at longer wavelengths attributed to the solvated electron and a much longer lived radical absorbing at wavelengths less than 400 nm. The solute triplet yields were followed using anthracene and biphenyl at different concentrations. An upper limit for the yield of excited singlet anthracene was estimated from the study of fluorescence to be $G \simeq 0.1$. Anthracene singlet yields in the presence of benzene at different concentrations were measured and the contribution of ethyl acetate positive ions in forming the additional excited singlets are discussed. The free ion yield is $G = 0.25$. Yield of ethyl acetate positive ions scavengeable at high benzene concentrations is $G = 0.63$.

Introduction

In recent years pulse radiolysis has been extensively used as a complementary technique to steady state radiolysis in studying the radiation chemistry of different chemical systems. The excited states both singlet and triplet and the free ions produced during radiolysis have been conveniently investigated using submicrosecond and nanosecond pulse radiolysis. The presence of solvated electrons in irradiated water and alcohols has been established by this technique.[2] Both aliphatic and aromatic hydrocarbons having very low static dielectric constant are shown to contain free ions under irradiation by several investigators.[3–6] In this work, the radiation chemistry of ethyl acetate, whose dielectric constant is above those of the hydrocarbons and much below those of alcohols and water, has been studied using pulse radiolysis with 12-MeV electron pulses of 100-ns duration.

Very little work has been carried out on the radiolysis of esters in general and ethyl acetate in particular. The γ radiolysis of ethyl acetate has been studied[7,8] and the gaseous and liquid products have been analyzed. In the present study the main interest is not in the stable products of radiolysis but rather in the transient intermediates of ethyl acetate. The yields and behavior of ions and excited states in the intermediate dielectric constant region is interesting from the point of view of the general understanding of radiation chemical processes. Ethyl acetate in the presence and absence of suitable solutes has been pulse irradiated and the transient species have been analyzed by kinetic spectrophotometry.

Experimental Section

Materials. Ethyl Acetate. Wilkinsons AnalaR ethyl acetate was kept over anhydrous potassium carbonate for about 24 h with occasional shaking. The ethyl acetate was filtered and fractionated over a 4-ft vacuum-jacketed column packed with stainless steel mesh, under a nitrogen atmosphere. The middle cut boiling at 77 °C was collected and stored under a nitrogen atmosphere.

Biphenyl and Anthracene. BDH AnalaR grade biphenyl and anthracene were recrystallized from ethanol and used as such.

Benzene. BDH AnalaR grade benzene was fractionally crystallized three times rejecting one third of the volume each time. The benzene was dried over sodium and then used.

Nitrous Oxide. Anaesthetic quality nitrous oxide supplied by British Oxygen was used as received.

Sample Preparation, Irradiation, and Optical Measurements. Ethyl acetate and its solutions were deoxygenated by bubbling argon through the liquids for about 1 h. A quartz irradiation cell having a path length of 2.5 cm was used and was connected to a flow system described elsewhere.[9] The cell containing the liquid was irradiated with a beam of 12-MeV electrons from a linear accelerator at the Christie Hospital and Holt Radium Institute, Manchester. The transient species were monitored by kinetic spectrophotometry, employing a xenon light source, a monochromator, and a photomultiplier. The amplifier signals were displayed on a cathode ray oscilloscope, Tektronix-445. The optical densities were calculated from a knowledge of the initial light level and the photographed decay curve on the oscilloscope. Absorption spectra were obtained by setting the monochromator to a particular wavelength and finding the optical density at the end of pulse. The electron pulses employed in the experiments were of 100–500 ns duration which delivered a dose of about 3–15 krads. The absorbed doses were measured from a secondary emission chamber which had been precalibrated with modified Fricke dosimeter.[10]

The fluorescence intensities were obtained by reading off the top flat portion of the emission during the pulse for the solution under study and correcting for the Cerenkov emission at that particular wavelength for the solvent alone.

Results

Transient Absorptions. The end of pulse spectrum for a 100-ns pulse of 12-MeV electrons delivering 4 krads to pure ethyl acetate is given in Figure 1a. The spectrum shows an absorption maximum at about 310 nm and weak absorption bands in the 400–700-nm region. Kinetic analysis of the 310-nm absorption reveals that the growth period was over 200 ns and decays by second-order kinetics. The analysis of the decay plot gives a k/ϵ value, at 310 nm, of 7.6×10^7 cm s^{-1}, where k represents the second-order decay constant and ϵ the molar extinction coefficient of the absorbing species. The transient absorptions at 400 and 600 nm have approximate half-lives of about 150 ns. The 310-nm absorption was proportional to a dose absorbed between 0.2 and 3.6 krads and had a $G\epsilon$ value of 3.4×10^3 units.

Figure 1b gives the absorption spectrum at the end of a 100-ns pulse in ethyl acetate saturated with nitrous oxide (~40 mM). The absorption maximum is around 300 nm with a $G\epsilon$ value of 4.3×10^3 units. The absorption shows second-order decay with a k/ϵ value of 2.6×10^7 cm s^{-1}. The longer wavelength absorption is no longer present in this case.

Excited States and Their Yields. Singlets. Estimation of the yield of singlet excited ethyl acetate was made by measuring the emission intensities at 445 nm from excited singlet anthracene in pulse irradiated ethyl acetate containing anthracene. Table I shows the measured emission intensities in pure benzene, ethyl acetate, anthracene in benzene, and anthracene in ethyl acetate under the same geometry and absorbed dose conditions.

Table II summarises the emission intensities at various benzene concentrations along with the calculated $G(^1A)$.

TABLE I: Fluorescence Emissions at 445 nm with 0.2-μs Pulse, 0.71 krad

Description of system	Emission intensity, au	$G(^1A^*)$
Benzene	40	
Ethyl acetate	36	
Anthracene in benzene (20 mM)	620	1.62[a]
5 mM anthracene in ethyl acetate	72.6	0.102
15 mM anthracene in ethyl acetate	73.5	0.105
25 mM anthracene in ethyl acetate	74.0	0.106

[a] Reference 18.

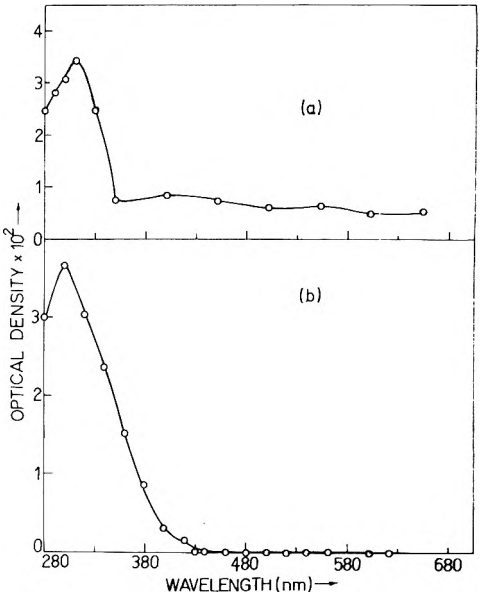

Figure 1. End of pulse spectrum in the pulse radiolysis of (a) pure ethyl acetate (3.92 krads, 0.1 μs) and (b) nitrous oxide saturated (40 mM) ethyl acetate (3.6 krads, 0.1 μs).

Triplet Yields. The absorption spectrum from a 0.2-μs electron pulse in ethyl acetate containing anthracene corresponds well with the anthracene triplet spectrum peaking at about 420 nm. Using the known ϵ value of 5.72×10^4 M^{-1} cm^{-1},[11] the triplet yields were calculated. Biphenyl solutions were also examined in an analogous way. Figure 2 gives the absorption spectrum immediately after the pulse in a 25 mM biphenyl solution. Two broad peaks in the region of 360 and 400 nm are observed. The absorption at 400 nm decays rapidly leaving the much longer-lived absorption at 360 nm shown in Figure 3a, which is the spectrum after 0.8 μs of the pulse. The spectrum is identical with the biphenyl triplet spectrum.[11] Using $\epsilon_{360\ nm}$ of 3.54×10^4 M^{-1} cm^{-1} for the triplet, the triplet yields were calculated and the results are given in Table III. Figure 5a gives the plot of G(triplet) vs. (anthracene) or biphenyl concentration.

Ion Yields. The scavengeable free ion yields were calculated from the absorptions at 700 and 410 nm for anthracene and biphenyl solutions, respectively, in pulse irradiated ethyl acetate solutions. Figure 3b gives the spectrum of the biphenylide ion obtained by subtracting the long-lived ab-

TABLE II: Emissions at 445 nm in the Pulse Radiolysis of Ethyl Acetate-Benzene-Anthracene System[a]

Benzene concn, M	Benzene electron fraction ϵ_B	Emission intensity, au	$G(^1A^*)$
11.3	1	860	1.62
0	0	56	0.105
0.015	0.001	56	0.105
0.068	0.006	63	0.108
0.367	0.032	120	0.226
0.688	0.060	168	0.317
1.035	0.089	207	0.390
1.80	0.155	272	0.513
2.59	0.224	364	0.686
3.41	0.296	460	0.866
4.23	0.368	532	1.00
5.10	0.443	585	1.10
7.85	0.692	659	1.24
9.60	0.849	740	1.37

[a] 0.2-μs pulse, 0.84 krad, 25 mM A.

TABLE III: Anthracene and Biphenyl Triplet Yields in the Pulse Radiolysis of Ethyl Acetate Solutions

A, mM	$G(^3A)$	D, mM	$G(^3D)$
1.5	0.07	5.0	0.15
3.0	0.11	6.7	0.15
7.6	0.17	11.0	0.15
9.0	0.19	18.0	0.21
11.5	0.17	35.0	0.34
17.5	0.23	52.0	0.46
25.4	0.26	88.0	0.61
		262.0	0.87

TABLE IV: Ion Yields in Pulse Irradiated Ethyl Acetate Solutions

A, mM	$G(A^+) + G(A^-)$	D, mM	$G(D^+)$
7.6	0.46	5	0.16
11.5	0.50	6.7	0.20
17.5	0.51	11.0	0.27
25.4	0.53	18.0	0.30
24.0	0.53	35.0	0.30
24.0	0.47	52.0	0.25

sorption from the end of pulse spectrum. Table IV summarises the yields at different concentrations of the solutes, making use of $\epsilon_{700\ nm}$ for the anthracene anion or cation as 10^4 M^{-1} cm^{-1} and $\epsilon_{410\ nm}$ for the biphenylide ion as 5.8×10^4 M^{-1} cm^{-1}.[12,13]

Discussion

The following reactions can be postulated in the radiolysis of ethyl acetate (EtAc):

$$EtAc \rightarrow EtAc^*, EtAc^+, e^- \quad (1)$$

$$EtAc + e^- \rightarrow e_s^-, EtAc^- \quad (2)$$

$$EtAc^+ + e_s^- \rightarrow EtAc^* \quad (3)$$

$$EtAc^* \rightarrow \text{radical products} \quad (4)$$

(e.g., CH_3CO, OC_2H_5, CH_3COO, etc.)

$$EtAc^+ \rightarrow CH_3COOCHCH_3 + H^+ \quad (5)$$

$$e_s^- \text{ or } EtAc^- \rightarrow \text{products} \quad (6)$$

(e.g., CH_3COO^-, C_2H_5, CH_3CO, and $C_2H_5O^-$)

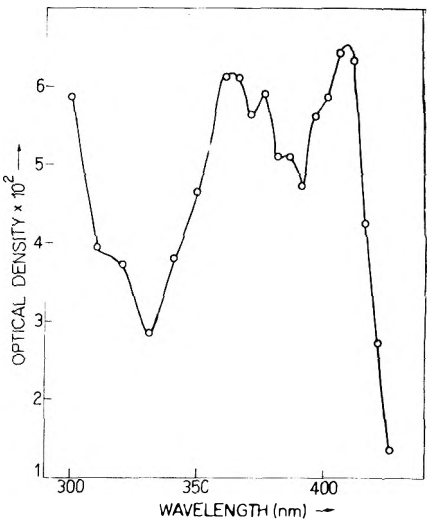

Figure 2. End of pulse spectrum of 25 mM biphenyl in ethyl acetate (0.1 μs, 2.63 krads).

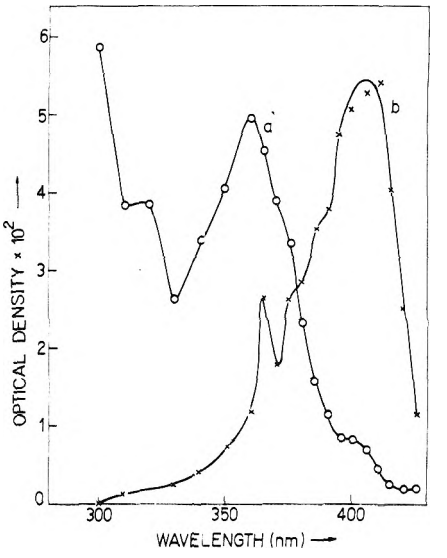

Figure 3. (a) Transient absorption spectrum after 0.8 μs of biphenyl in ethyl acetate (0.1 μs, 2.68 krads). (b) Spectrum of biphenyl cation obtained after subtraction of the long-lived absorption from end of pulse spectrum.

When nitrous oxide (N_2O) is also present in the system the following additional reactions can be postulated:

$$e_s^- + N_2O \rightarrow N_2 + O^- \quad (7)$$

$$O^- + EtAc \rightarrow OH^- + CH_3COOCHCH_3 \quad (8)$$

The absorbing species in the 300–400-nm region can be attributed to radicals such as CH_3CO, CH_3COO, and $CH_3COOCHCH_3$ though a definite assignment is not possible at this stage. The weak longer wavelength absorption found in pure ethyl acetate but eliminated completely in presence of N_2O can be attributed to either the solvated electron or $EtAc^-$. In the presence of N_2O the yield of cations should increase as otherwise some would have reacted with electrons or negative ions and hence radicals arising from $EtAc^+$ should also dominate over those arising from excited ethyl acetate. Thus one would expect to see a different absorption spectrum,

yields, and decay kinetics. This, indeed, was observed in our experiments for the 310-nm species where the $G\epsilon$ value increased by about 30%, the k/ϵ value decreased by a factor of 3, and the absorption maximum slightly shifted to the lower wavelength region, when nitrous oxide was present in the system. It will be interesting to note that the α-ethanol radical, i.e., the CH_3CHOH radical, has absorption maximum around 290 nm in ethanol[14] and the CH_2COCH_3 radical in aqueous acetone has absorption maximum around 295 nm.[15] The absorption maxima around 310 and 300 nm for the radicals obtained in ethyl acetate pulse radiolysis may indicate similar type of radicals such as $CH_3COOCHCH_3$ or $CH_2COOC_2H_5$ in the system. The acetyl radical CH_3CO in methyltetrahydrofuran (MTHF) matrix has been found[16] to have absorption maxima at 340, 500, and 540 nm and the very small absorptions in the 500–600-nm regions probably indicates that the CH_3CO radical yield is very small.

In the pulse radiolysis of pure ethyl acetate, the 310-nm transient absorption shows a grow-in time of about 200 ns. The explanation for this formation time can only be speculative with the present observations. The absorbing radical may be formed by the decomposition of ethyl acetate cation according to reaction 5. It is also probable that the radical is a result of the ethyl acetate cation radical abstracting an H atom from the neutral molecule through an ion–neutral molecule collision complex haveing a lifetime of the order of ~ 200 ns under the experimental conditions.

In the prsence of anthracene (A) or biphenyl (D) in ethyl acetate the solute excited states can arise through energy transfer reactions from both excited singlet (^{1}EtAc*) and the triplet (^{3}EtAc*) ethyl acetate or charge transfer and subsequent neutralization reactions. These reactions are shown as follows:

$$^1\text{EtAc}^* + \text{A (or D)} \rightarrow {}^1\text{A}^* \text{ (or } {}^1\text{D}^*)$$

$$^3\text{EtAc}^* + \text{A (or D)} \rightarrow {}^3\text{A}^* \text{ (or } {}^3\text{D}^*) \quad (9)$$

$$^1\text{A}^* \text{ (or } {}^1\text{D}^*) \rightarrow {}^3\text{A}^* \text{ (or } {}^3\text{D}^*) \quad \text{(intersystem crossing)} \quad (10)$$

$$\text{EtAc}^+ + \text{A} \rightarrow \text{A}^+ + \text{EtAc} \quad (11)$$

$$\text{EtAc}^+ + \text{D} \rightarrow \text{D}^+ + \text{EtAc} \quad (12)$$

$$\text{A}^+ + e_s^- \rightarrow {}^1\text{A}^* \text{ and } {}^3\text{A}^* \quad (13)$$

$$\text{D}^+ + e_s^- \rightarrow {}^1\text{D}^* \text{ and } {}^3\text{D}^* \quad (14)$$

Reactions 11 and 12 can occur as the ionization potentials of anthracene and biphenyl are lower than that of ethyl acetate.[17]

Solute Singlet Yields. As seen from Table I, the emissions at 445 nm in pure benzene and ethyl acetate are approximately equal, thus showing it to be from Cerenkov radiation which is less than 5% of the emission of anthracene in benzene. Anthracene solution in benzene was used as a monitor for the singlet yield since $G(^1\text{A}^*)$ in benzene is known to be about 1.62.[18] The yields of anthracene singlet have been calculated using this value since the geometry and absorbed dose were kept identical. The $G(^1\text{A}^*)$ in ethyl acetate was found to be very small (~0.1) and does not change between 5 and 20 mM of anthracene. This means that all the precursors to the excited solute singlet are scavenged even at 5 mM of anthracene. To confirm this, benzene was added to the system since excited benzene transfers energy to anthracene to give anthracene singlet. Table II shows that even at thrice the concentration of anthracene benzene does not increase the singlet yield indicating this to be a plateau value. In addition to reactions 1 and 3, where the directly excited ethyl acetate singlet and the one arising from the geminate recombination reaction are involved, the following reaction may also take place:

$$\text{EtAc}^+ \xrightarrow{k_{15}} \text{F}^+$$

$$\text{F}^+ + e_s^- \text{ or } \text{EtAc}^- \rightarrow \text{F}^* \quad (15)$$

Here F^+ represents the different cations formed from the excited ethyl acetate cation. Thus the yield of $G = 0.1$ is an upper limit of the lowest (fluorescent) singlet ethyl acetate.

At much higher concentrations of benzene, benzene intercepts the geminate ion recombination reaction more efficiently giving rise to the benzene cation which on neutralization can give ^{1}B*. The ionization potentials of ethyl acetate and benzene (10.2 and 9.6 eV, respectively) favor this mechanism:

$$\text{EtAc}^+ + \text{B} \rightarrow \text{B}^+ \text{ EtAc} \quad (16)$$

$$\text{B}^+ + e^- \rightarrow {}^1\text{B}^* \quad (17)$$

$$^1\text{B}^* + \text{A} \rightarrow {}^1\text{A}^* + \text{B} \quad (18)$$

Thus if G_0 is the yield of ^{1}A* formed at low concentrations of anthracene (= 0.1), ϵ_B the electron fraction of benzene in the system, and k_{15} the rate constant for formation of F^+ which cannot transfer charge to benzene, and $G_0(\text{EtAc}^+)$ is the yield of ethyl acetate cation formed initially then the observed yield of singlet anthracene can be given by

$$G(^1\text{A}^*) = 1.62\epsilon_B + (1 - \epsilon_B)G_0 + (1 - \epsilon_B)G^0(\text{EtAc}^+) \times [k_{16}(\text{B})]/[k_{15} + k_{16}(\text{B})] \quad (19)$$

In accordance with this mechanism the observed excited anthracene singlet does not show linearity with the benzene electron fraction as observed in Figure 4. From a reciprocal plot using this equation $G^0(\text{EtAc}^+)$ was found to be 0.63 and the rate constant ratio k_{15}/k_{16} to be 9.7 M^{-1}.

Solute Triplet Yields. Figure 5a gives the variation of the anthracene or biphenyl triplet yields as a function of the solute concentration in ethyl acetate. Both curves show similar behavior, with the triplet yield increasing with concentration. This suggests that the triplets arise from the singlet states produced by the neutralization of the anthracene or biphenyl cations. The efficiency of charge transfer reaction increases with increasing solute concentration as it has to compete with the geminate recombination. Similar behavior has been observed in cyclohexane.[11]

In order to investigate the formation of triplet biphenyl, i.e., whether it arises only through intersystem crossing of the singlet excited biphenyl, singlet and triplet biphenyl yields were measured in the presence of oxygen at different concentrations. A linear relation between the yields of the singlet and triplet passing through origin is to be expected if the triplet biphenyl is formed only through intersystem crossing. Figure 5b proves this to be the case where the biphenyl singlet emission intensity at 310 nm is plotted against the triplet yield obtained from 360-nm absorption at a particular oxygen concentration. Here the assumption made is that the triplet measurement is made before oxygen quenches the triplet biphenyl, which is much longer lived than the singlet.

Ion Yields. As has been postulated earlier, both ethyl acetate cations and anions and solvated electrons are formed during the radiolysis. As shown in reactions 11 and 12, the cations of anthracene and biphenyl are formed when they are also present in the system. The solute anions also are formed according to their electron affinity compared with the solvent. The ionization potentials of ethyl acetate, anthracene, and biphenyl are 10.2, 7.7, and 8.6 eV, respectively,[9] making re-

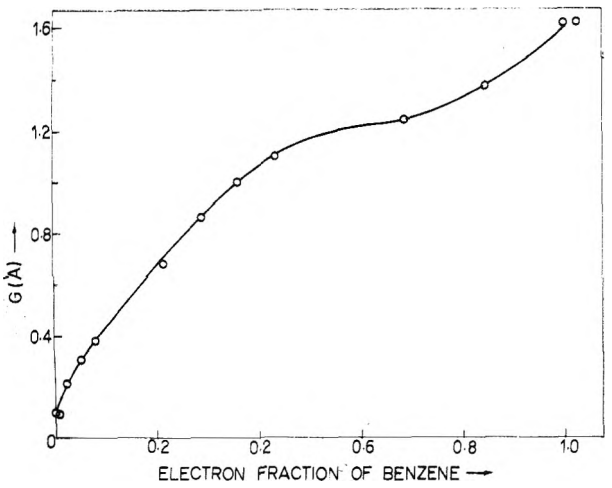

Figure 4. Variation of $G(^1A^*)$ as a function of benzene electron fraction in benzene–anthracene in ethyl acetate.

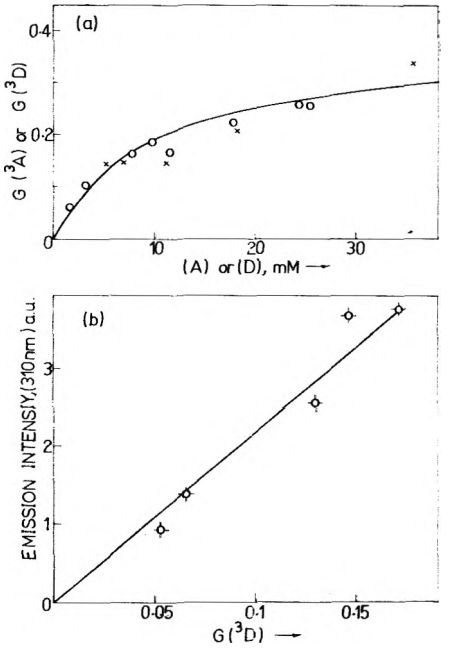

Figure 5. (a) Variation of solute triplet yields with concentration: (O) anthracene (3.9 krads); (X) biphenyl (0.9 krads). (b) Relation between biphenyl singlet emission at 310 nm with $G(^3D)$ in ethyl acetate–biphenyl in presence of different oxygen concentrations.

actions 11 and 12 possible. The observed ion yields can be attributed to the free ion yields which are scavengeable since the solute concentrations are kept below 50 mM, when the geminate recombination reaction is not interfered with.

It can be seen that the ion yield obtained from the biphenyl ion absorption is only half that obtained from the anthracene case. Since the absorption spectra of both cations and anions are observed to be similar[13,19] it is likely that both anthracene cations and anions are observed in the anthracene case while only the cation is observed in the biphenyl case. This is possible only if the electron affinity of biphenyl is much less than that of ethyl acetate and that of anthracene is much more than that of ethyl acetate.

In order to throw light on this point, anthracene and biphenyl solutions in 2-propanol were pulse irradiated (0.1 μs, 1.6 krads) and the absorptions at 700 and 575 nm for the anthracene anion and biphenyl anion were examined in the presence and absence of ethyl acetate. 2-Propanol was chosen as the solvent because of its efficiency for scavenging cations and the absorptions at these wavelengths can safely be assigned to the anions only. It was found that ethyl acetate did not affect the yield or the decay kinetics of the anthracene anion, but in the case of the biphenyl both the yields and the decay kinetics of the biphenylide anion absorption were profoundly affected by the presence of small amounts of ethyl acetate. Thus, in 7 mM anthracene, in the absence of ethyl acetate, in 2-propanol the $G\epsilon$ value was 9.4×10^3 at 700 nm. When ethyl acetate was added at concentrations of 0.065, 0.415, and 0.875 M, the $G\epsilon$ values were 9.6, 9.6, and 9.1×10^3, respectively. Further, the 700-nm absorption decays by first order with a rate constant of $(3.4 \pm 0.6) \times 10^5$ s^{-1} in all the cases. On the other hand, in a 9.7 mM biphenyl solution in 2-propanol the $G\epsilon$ values were 8.6×10^3 and 4.2×10^3 at 575 nm in the absence and presence (0.032 M) of ethyl acetate, respectively. Further the absorption decays by second-order kinetics in the absence of ethyl acetate with a k/ϵ value of 1.8×10^8 cm s^{-1} at 575 nm whereas in the presence of ethyl acetate the absorption shows a first-order decay with a rate constant of 2.3×10^6 s^{-1} at 0.082 M ethyl acetate. Thus there would be little chance of observing the biphenyl anion in pure ethyl acetate. It can be concluded that the free ion yields in the radiolysis of ethyl acetate is $G = 0.25$.

This yield for free ions is consistent with the static dielectric constant (viz. 6) of ethyl acetate. Schmidt and Allen[4,5] have found free ion yields (in terms of their G values) of 0.05, 0.13, and 0.15 in irradiated benzene, hexane, and cyclohexane with static dielectric constants of 2.3, 1.9, and 2.02, respectively. Holroyd has observed[20] that the yield of "free ions" increases with the static dielectric constant and has given a plot of variation of $G(e_s^-)$ with the dielectric constants of several liquids and has compared it with the theoretically expected curve.[3] The observed G(free ion) of 0.25 for ethyl acetate ($D = 6$) fits this curve reasonably well.

Acknowledgments. The author wishes to express his thanks to Dr. J. H. Baxendale under whose suggestion and guidance the above study was conducted at the University of Manchester, U.K.

The author is indebted to the personnel of the Peterson Laboratories, Manchester for the provision of the facilities used during the pulse radiolysis experiments.

The author is thankful to the British Government and the Indian Government for awarding the Colombo Plan Fellowship during which this study was carried out.

The author is grateful to Dr. K. N. Rao of Bhabha Atomic Research Centre for his helpful suggestions in the preparation of this paper.

References and Notes

(1) Based upon the Ph.D Thesis in Chemistry submitted to the University of Manchester, U.K., in Sept. 1970.
(2) (a) E. J. Hart and J. W. Boag, *J. Am. Chem. Soc.*, **84**, 4090 (1962); (b) I. A. Taub, M. C. Sauer, and L. M. Dorfman, *Discuss. Faraday Soc.*, **36**, 206 (1963).
(3) G. R. Freeman and J. M. Fayadh, *J. Chem. Phys.*, **43**, 86 (1965).
(4) W. F. Schmidt and A. O. Allen, *J. Phys. Chem.*, **72**, 3730 (1968).
(5) W. F. Schmidt and A. O. Allen, *J. Chem. Phys.*, **52**, 2345 (1970).
(6) M. G. Robinson, P. G. Fuochi, and G. R. Freeman, *Can. J. Chem.*, **49**, 3657 (1971).
(7) G. E. Adams, J. H. Baxendale, and R. D. Sedgwick, *J. Phys. Chem.*, **63**, 854 (1959).
(8) P. Y. Feng, W. A. Glasson, and S. A. Marshall, Contract No. AF 33, (616)-6141, 1960, Project No. 7360, p 64, WADD-TR-60-344.
(9) J. P. Keene, *J. Sci. Instrum.*, **41**, 493 (1964).
(10) J. K. Thomas and E. J. Hart, *Radiat. Res.*, **17**, 408 (1962).

(11) E. J. Land, *Proc. R. Soc. London, Ser. A*, **305**, 457 (1968).
(12) I. A. Taub, D. A. Hartner, M. C. Sauer, and L. M. Dorfman, *J. Chem. Phys.*, **41**, 979 (1964).
(13) S. Arai, H. Ueda, R. F. Firestone, and L. M. Dorfman, *J. Chem. Phys.*, **50**, 1072 (1969).
(14) I. A. Taub and L. M. Dorfman, *J. Am. Chem. Soc.*, **84**, 4053 (1962).
(15) M. Nakashima and E. Hayon, *J. Phys. Chem.*, **75**, 1910 (1971).
(16) S. Noda, K. Fueki, and Z. Kuri, *J. Chem. Phys.* **49**, 3287 (1968).
(17) J. L. Franklin et al., Ed., *Natl. Stand. Ref. Data Ser., Natl. Bur. Stand.*, **No. 26**, 60, 131, (1969).
(18) R. Cooper and J. K. Thomas, *J. Chem. Phys.*, **48**, 5097 (1968).
(19) Balk, Hoijtink, and Schreurs, *Recl. Trav. Chim., Pays-Bas*, **76**, 813 (1957).
(20) R. A. Holroyd, "Fundamental Processes in Radiation Chemistry", P. Ausloos, Ed., Interscience, New York, N.Y., 1968, p 433.

Pulse Radiolytic Investigations of Peroxy Radicals Produced from 2-Propanol and Methanol

Yael Ilan,[1] Joseph Rabani,*[2] and Arnim Henglein[3]

Bereich Strahlenchemie, Hahn-Meitner-Institut für Kernforschung, Berlin GmbH, 1 Berlin 39, West Germany and The Department of Physical Chemistry, The Hebrew University of Jerusalem, Jerusalem 91000, Israel *(Received May 7, 1975; Revised Manuscript Received October 28, 1975)*

Publication costs assisted by the Hahn-Meitner-Institut für Kernforschung

The reactions of peroxy radicals produced from 2-propanol and from methanol were investigated. At pH 3 the peroxy radicals were found to decay by both second- and first-order processes: $O_2CH_2OH \rightarrow HO_2 + CH_2O$, $k \cong 5 \times 10^2\ s^{-1}$; $O_2COH(CH_3)_2 \rightarrow HO_2 + (CH_3)_2CO$, $k = (700 \pm 150)\ s^{-1}$; $2O_2CH_2OH \rightarrow$ products, $2k = (3 \pm 1) \times 10^8\ M^{-1}\ s^{-1}$; $2O_2COH(CH_3)_2 \rightarrow$ products, $2k = (1.1 \pm 0.2) \times 10^7\ M^{-1}\ s^{-1}$. The reactivity of $O_2C(OH)(CH_3)_2$ toward OH^- and HPO_4^{2-} ions, resulting in the ionization of the peroxy radicals, and the subsequent formation of O_2^-, was studied. A rate constant $k_{((CH_3)_2C(OH)(O_2)+OH^- \rightarrow (CH_3)_2C(O^-)(O_2)+H_2O)} = (5.2 \pm 1) \times 10^9\ M^{-1}\ s^{-1}$ was measured. The similar reaction with HPO_4^{2-} was found to have a rate constant of $(1.07 \pm 0.15) \times 10^7\ M^{-1}\ s^{-1}$. All results are reported for an ionic strength of 0.1 M.

Introduction

Several papers have been published recently concerning the formation and decay kinetics of various peroxy radicals.[4-13] H atoms,[10] e_{aq}^-,[10] and CO_2^- [5,14] are known to reduce oxygen and form superoxide radicals. In general, when an organic solute, RH_2, is present in an irradiated N_2O-containing aqueous solutions, it reacts with the free radicals formed by irradiation according to

$$H_2O \longrightarrow e_{aq}^-, H, OH, H_2O_2, H_2, H_3O^+, OH^- \quad (1)$$

$$e_{aq}^- + N_2O \xrightarrow{H_2O} OH + OH^- + N_2 \quad (2)$$

$$OH + RH_2 \rightarrow RH + H_2O \quad (3)$$

$$H + RH_2 \rightarrow RH + H_2 \quad (4)$$

When O_2 is also present, peroxy radicals, RHO_2, are produced according to

$$RH + O_2 \rightarrow RHO_2 \quad (5)$$

Note that O_2 may compete with N_2O for e_{aq}^-, and with RH_2 for H, so that RHO_2 radicals are expected to form along with some quantities of HO_2 and O_2^-. (HO_2 has a pK at 4.9.[4,5]) Of the radicals RHO_2 studied so far, two groups have been observed: aliphatic radicals with no additional functional groups around the carbon atoms that add to the O_2 (such as cyclopentyl peroxyl radicals[11] ($C_5H_9O_2$)), decay away by a bimolecular reaction of the type

$$2RHO_2 \rightarrow 2R + H_2O_2 + O_2 \quad (6)$$

or

$$RHO_2H + R + O_2$$

On the other hand, α alcohol radicals, such as O_2CH_2OH[12] and $(CH_3)_2C(OH)(O_2)$ (which will be discussed in the present manuscript), are capable, under certain conditions, of producing HO_2 and O_2^- radicals according to

$$RHO_2 \rightarrow R + H^+ + O_2^- \quad (7)$$

or

$$RHO_2 \rightarrow R + HO_2$$

in competition with reaction 6.

In a previous paper,[12] the formation of O_2^- from O_2CH_2OH has been reported. It has been shown that the formation of O_2^- according to stoichiometric eq 7 is quite complicated, and is enhanced by bases (OH^-, HPO_4^{2-}). Evidence for a bimolecular process at the higher pulse intensities has been obtained, but no systematic study of this process has been carried out.

The purpose of this manuscript is to investigate the bimolecular decay of $(CH_3)_2C(OH)(O_2)$ and of O_2CH_2OH, and the first-order noncatalytic formation of HO_2. The effect of OH^- and HPO_4^{2-} on O_2^- formation in 2-propanol aqueous solutions is also measured, and the results support the idea that the ability to produce superoxide radicals is general to α peroxy radicals of alcohols. Previous work may now be better understood on the basis of our new findings.

Experimental Section

The linear accelerator at the Hahn-Meitner-Institute was used at 8–12 MeV, 1–3 A current, and 10–2000 ns pulse duration. Tektronix 549 and 7613 memory scopes with plug-in units 1A5 and 7A22, respectively, were employed. The light source was 450-W Xe–Hg lamp. A 4 cm long cell with one light path was used for the irradiations. Carl Zeiss M4QIII prism monochromator, with no scattered light under our conditions, was also employed. Each solution was pulse irradiated once, and then replaced. Mixtures of N_2O–O_2 were used unless otherwise stated. The solutions were in equilibrium with the same gas mixture while filling the irradiation cell. Equilibration with the gas was carried out by vigorous bubbling of the gas mixtures (total pressure, 1 atm) through 1-l flasks containing the solutions. The flasks were kept under gas mixture pressure until after use. The equilibration processes lasted 15–20 min, during which time 7–10 l. of gas were bubbled through the solution, above which the gas volume was about 200 cm^3. The temperature was 22.5 ± 1 °C. Unless otherwise stated, experiments were carried out at ionic strength 0.1 M, obtained by the addition of appropriate amounts of $NaClO_4$. Dosimetry was carried out by measuring the 248-nm extinction of O_2^- produced in 0.1 M sodium formate solution at pH 7 (phosphate buffer 10^{-2} M). The extinction coefficient ϵ of O_2^- is known as 2×10^3 M^{-1} cm^{-1}. Total radical yields in the test solutions were assumed to be the same as the O_2^- yield in the dosimeter solution.

Materials. Water, triply distilled after first being deionized with an ion exchanger, was used. Tetranitromethane (TNM, Fluka, puriss) was washed 15 times with water, and distilled at room temperature by means of a stream of air through a solution of bicarbonate. It was collected in a trap of liquid N_2. Avoiding the last step of distillation did not affect the results. All other materials, products of Merck (pro analysis), were used as received.

Results and Discussion

The 2-Propanol System. (a) *Spectrum of* $(CH_3)_2C(OH)O_2$. All the experiments were carried out in 0.5 M 2-propanol solutions. In Figure 1 we present a typical oscilloscope trace at pH 7.3. Under the conditions of Figure 1, reactions 2, 3, and 4 are very fast in comparison with the time resolution of the apparatus, and reaction 5 has a half-life of about 0.4 μs, as will be discussed later. Thus, 2 μs after the electron pulse, 5% of the radicals are present as O_2^- due to the competition of O_2 for e_{aq}^- and H (according to the known[15] rate constants of the competing solutes), while 95% of the radicals are present as $(CH_3)_2C(OH)(O_2)$ and $O_2CH_2CHOHCH_3$. Of these, about 11% are β radicals, and nearly 89% are α radicals (assuming that H produced α radicals only, while 15% of the OH produced β radicals[16]). Thus, the optical absorption at 2 μs after the electron pulse is mainly due to α and β peroxy radicals. The increase in optical density observed in Figure 1 was found to be strictly first order. The absorption increases are due to the formation of O_2^- according to reaction 7, catalyzed by HPO_4^{2-}.[12] The spectrum observed after 150 μs was taken and found to be in very good agreement with the known spectrum of O_2^-.[5] The initial spectrum (Table I) is due to the absorptions of the α and β peroxy radicals $(CH_3)_2C(OH)(O_2)$ and $O_2CH_2CHOHCH_3$. As we do not know the precise spectrum of the β radicals, we are unable to correct for this, and calculate a more exact spectrum of the α radicals, which form the great majority of the peroxy radicals. It is reasonable to assume that the β radicals absorb in the same range, and have perhaps an absorption similar to the $C_5H_9O_2$ radicals.[11]

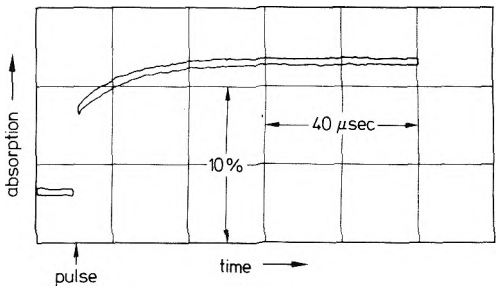

Figure 1. The formation of O_2^- from $(CH_3)_2C(OH)(O_2)$: 0.033 M Na_2HPO_4 at pH 7.3 (10^{-3} M NaH_2PO_4 added), at ionic strength 0.1 M. 67% N_2O and 33% O_2 (by partial pressure above the solution). Total radical concentration 1.00×10^{-5} M. The spectra were recorded at 248 nm.

TABLE I: Initial Absorption Spectra at pH 3 and 7.3[a]

λ, nm	10^2D^λ (pH 7.3)[b]	10^2D^λ (pH 3)[b]	D^λ/D^{248} (pH 7.3)[c,d]	D^λ/D^{248} (pH 3)[c,e]
232	4.45	4.7	1.08	1.02
240	4.3	4.7	1.04	1.03
248	4.15	4.55	1.00	1.00
260	3.4	3.6	0.83	0.81
270	3.35	3.3	0.82	0.77
280	2.6	2.7	0.64	0.63
290	1.9	1.9	0.50	0.44
302	1.3	1.25	0.33	0.30
313	0.9	0.87	0.22	0.21
325	0.6		0.15	
350	0.35		0.09	

[a] Each value is an average of at least two determinations. Experiments at pH 3 were carried out after equilibration with 1:1 (partial pressures) O_2:N_2O. Experiments at pH 7.3 were carried out in the presence of 3.3×10^{-3} M Na_2HPO_4 and 1×10^{-3} M NaH_2PO_4, after equilibration with 1:2 (partial pressures) O_2:N_2O. Total radical concentration 1.00×10^{-5} M. [b] Optical densities at wavelength λ, extrapolated to the end of the electron pulse. [c] Optical densities at wavelength λ, extrapolated to the end of the electron pulse and corrected for the absorptions of HO_2 (9% of the total radical concentration) at pH 3 and of O_2^- (5% of the total radical concentration) at pH 7.3. [d] Corrected optical density at 248 nm (see also footnote c) was 3.8×10^{-2}. [e] Corrected optical density at 248 nm (see also footnote c) was 4.2×10^{-2}.

The absorption of $(CH_3)_2C(OH)(O_2)$ at pH 7.3 was found to be the same as that observed at pH 3 (Table I). At pH 3, an optical absorption is produced soon after the electron pulse, as is the case for pH 7.3. However, this is not followed by an additional formation of absorbance. Instead, mixed second- and first-order decay kinetics are observed. The initial (extrapolated) absorbance at pH 3 is attributed mainly to α peroxy radicals, and some β radicals (~10% of the total radicals), and HO_2 (~9% of the total radicals). It can be seen that extinction coefficients in Table I are somewhat higher (up to 10%), at pH 3, but apart from this the spectra are identical and should be attributed to the same species. The results at pH 3 are more accurate, as the changes of D with time are much slower at pH 3 as compared with our results at pH 7.3. Therefore, the extrapolation to time zero is more accurate at pH 3. (In fact at pH 3 there is a negligible change of D with time on the microsecond time range, after 2 μs.) Average extinction coefficients $\epsilon^{248}_{(CH_3)_2C(OH)(O_2)}$ of 1100 ± 100 and $\epsilon^{290}_{(CH_3)_2C(OH)(O_2)}$ of 500 ± 50 M^{-1} cm^{-1} can be considered as the best values. Note that both the α and the β radicals have been assumed to have identical absorptions.

TABLE II: Reaction Rate Constant of $(CH_3)_2C(OH)(O_2)$ with HPO_4^{2-} [a]

pH	$[HPO_4^{2-}]$, M	μ,[b] M	$[H_2PO_4^-]$, M	$10^6 k_8$ M^{-1} s^{-1}
7.30[c]	3.3×10^{-3}	0.1	1.1×10^{-3}	10.5[e]
7.30[c]	1.0×10^{-2}	0.1	3.3×10^{-3}	10.8
6.65[d]	1.0×10^{-2}	0.7	5.0×10^{-3}	6.8[e]
6.65[d]	2.0×10^{-1}	0.7	1.0×10^{-1}	5.3
6.42[d]	2.0×10^{-1}	0.9	3.0×10^{-1}	4.6

[a] Total radical concentration 1.0×10^{-5} M. [2-propanol] = 0.5 M. Each value in the table is an average of at least two determinations. [b] Ionic strength. [c] 1:2 O_2/N_2O (partial pressure). [d] 1:0.82 O_2/N_2O (partial pressure). [e] Including 5% correction for the contribution of OH^- to the formation of O_2^- under the conditions of the experiment.

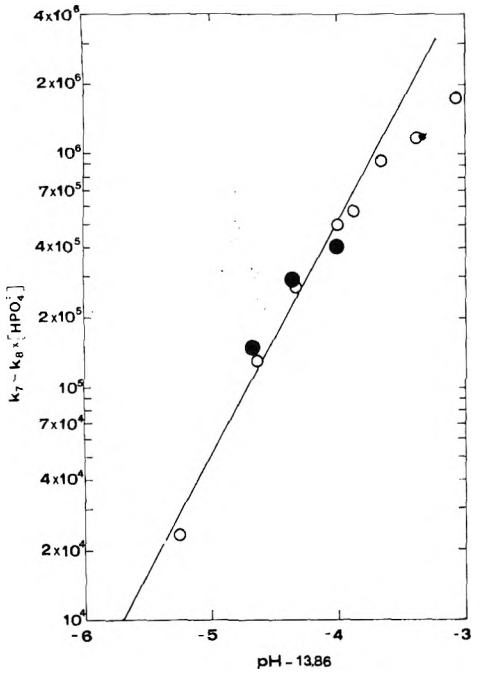

Figure 2. Effect on pH on the rate of formation of O_2^- from $(CH_3)_2C(OH)(O_2)$. The ionic strength μ was 0.1 M. Total radical concentration 10^{-5} M; 1:1 N_2O/O_2 (partial pressures). k_7 is the apparent rate constant for O_2^- builcup and is equals to the sum $k_8[HPO_4^{2-}] + k_{10}[OH^-]$: (O) 1×10^{-3} M HPO_4^{2-}; (●) 2×10^{-4} M HPO_4^{2-}. The line represents $k_{10} = 5.2 \times 10^9$ M^{-1} s^{-1}. The value of K_w under our conditions is 13.86.

(b) *Reaction of* $(CH_3)_2C(OH)(O_2)$. In the presence of HPO_4^{2-} ions, $(CH_3)_2C(OH)(O_2)$ reacts with it according to

$$(CH_3)_2C(OH)(O_2) + HPO_4^{2-} \rightarrow (CH_3)_2C(O^-)(O_2) + H_2PO_4^- \quad (8)$$

followed by

$$(CH_3)_2C(O^-)(O_2) \rightarrow (CH_3)_2CO + O_2^- \quad (9)$$

Previous work in the methanol system has shown a similar reaction pattern.[12] Under the conditions of Figure 1, by analogy with the methanol system[12] we assume that $(CH_3)_2C(O^-)(O_2)$ decomposes very quickly to O_2^-, and reaction 8 is the rate-determining step in the formation of O_2^-. From the formation kinetics observed in figures such as Figure 1, at various $[HPO_4^{2-}]$ and pulse intensities, we measured k_8. Some of the results are included in Table II. Changing the pulse intensity so that from 2 to 50 μM of $(CH_3)_2C(OH)(O_2)$ were produced did not affect the kinetics. This is in contrast with the results observed previously in the methanol system,[12] and, as will be discussed later, should be attributed to the relative slowness of reaction 6 in the 2-propanol system. The decrease in k_8 at high ionic strength is similar to the one observed in methanol.[12]

The reactivity of $(CH_3)_2C(OH)(O_2)$ toward OH^- has also been investigated.

$$(CH_3)_2C(OH)(O_2) + OH^- \rightarrow (CH_3)_2C(O^-)(O_2) + H_2O \quad (10)$$

The results are presented in Figure 2. We used $k_8 = 1.07 \times 10^7$ M^{-1} s^{-1}. The experimental data yield $k_{10} = 5.2 \times 10^9$ M^{-1} s^{-1}. The deviations from the straight line observed in the higher pH range can be accounted for if we assume that $k_5 \simeq 4 \times 10^9$ M^{-1} s^{-1}. Thus, at sufficiently high pH, reaction 5 is not well separated in time from (10), and (10) cannot be considered as rate determining.

The value $k_5 \simeq 4 \times 10^9$ M^{-1} s^{-1} agrees well with the values measured for methanol[12] and for cyclopenthyl[11] (C_5H_9) radicals.

(c) *Effect of Changing Pulse Intensity.* No effect of pulse intensity on the rate of buildup of optical absorption has been observed in solutions containing $>3 \times 10^{-3}$ M HPO_4^{2-} or $>5 \times 10^{-5}$ M OH^-. (Pulse intensities which produced 2–50 μM $(CH_3)_2C(OH)(O_2)$ have been tested.) The ratio $D_\infty^{248}/D_0^{248} = 1.65 \pm 0.05$ (see Figure 1 and related text) did not depend on the pulse intensity in solutions containing $>3 \times 10^{-3}$ M HPO_4^{2-} in the range studied. However, when no phosphate was present, at pH 3, no build up of absorbance could be observed after the formation of $(CH_3)_2C(OH)(O_2)$. Instead, the optical density decayed away by mixed first- and second-order kinetics. Typical results are presented in Figure 3 at 290 nm. The curves have been calculated with the aid of a Hewlett-Packard 9810 A calculator. A program based on the method described by Schmidt[17] was applied. Agreement with the data could be obtained taking $k_6 = 1.1 \times 10^7$ M^{-1} s^{-1} and $k_7 = 5.5 \times 10^2$ s^{-1}. This value for k_7 represents the spontaneous (noncatalytic) formation of HO_2 from $(CH_3)_2C(OH)(O_2)$. Curve fittings at 248 nm were also carried out, using identical solutions with similar pulse intensities. Best fits were obtained with the same values of k_6 and k_7, using $\epsilon^{248}_{HO_2} = 1050$, $\epsilon^{248}_{RO_2} = 1200$, $\epsilon^{248}_{\text{(bimolecular reaction product)}} = 250$, and $\epsilon^{248}_{H_2O_2} = 25$ M^{-1} cm^{-1}. Values of $k_{11} = (2.5\text{–}3.3) \times 10^6$ M^{-1} s^{-1}, which were used for the calculated curves, are higher than the value reported previously for the low ionic strength.[4,5]

$$\text{“}HO_2\text{”} + \text{“}HO_2\text{”} \rightarrow H_2O_2 + O_2 \quad (11)$$

(Note that k_{11} is an apparent reaction rate constant, related to the overall decay rate of $HO_2 + O_2^- \equiv$ “HO_2”.) Measurements at ionic strength 0.1 M at pH 3, in HCO_2H–HCO_2Na–O_2 solutions, where HO_2 and O_2^- are the only decaying products,[5] gave $k_{11} = 3.0 \times 10^6$ M^{-1} s^{-1}. The effect of ionic strength on k_{11} at pH 3 is expected, since at this pH the reaction of HO_2 with O_2^- still contributes to k_{11}. At higher ionic strengths more O_2^- is expected. As the reaction of HO_2 with O_2^- is relatively fast,[4,5] an increase in k_{11} can be expected, and is indeed observed.

Methanol Solutions. When 0.1 M methanol was substituted for 2-propanol, results which are in qualitative agreement with those presented in Figure 3 were obtained. Using pulse intensities corresponding to 10–50 μM radicals, best fits between the calculated curves and the experimental data were obtained at 290 nm (pH 3) with $k_6 = 3 \times 10^8$ M^{-1} s^{-1}. A first-order decay of O_2CH_2OH, $k = 5 \times 10^3$ s^{-1}, had to be included in the

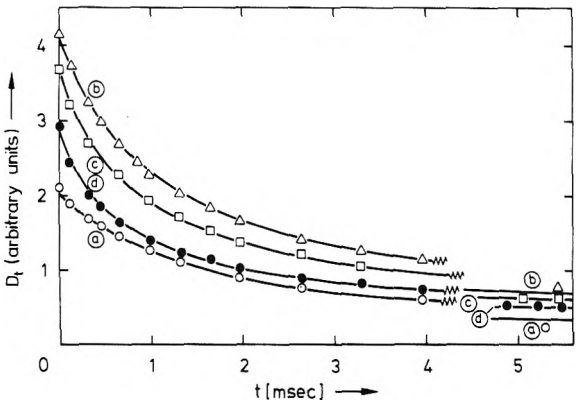

Figure 3. The effect of changing pulse intensity in 2-propanol solutions at pH 3; measured at 290 nm, 1:1 O_2/N_2O (partial pressure above the solution). Initially formed HO_2 was calculated to compose 9% of the initial total radical concentration. The ionic strength was 0.1 M. We assumed $k_{(e_{aq}^- + H^+)} = 1 \times 10^{10}$ M^{-1} s^{-1} for this ionic strength. $\epsilon^{290}_{RO_2} = 500$, $\epsilon^{290}_{(\text{bimolecular reaction product})} = 250$, and $\epsilon^{290}_{H_2O_2} = 10$ M^{-1} cm^{-1} were used for the calculations of the curves. The β peroxy radicals were disregarded (equivalent to assuming that the β radicals and the α radicals have identical absorptions and kinetics). $k_{(\text{"}HO_2\text{"} + \text{"}HO_2\text{"})} = 3.0 \times 10^6$ M^{-1} s^{-1} was used for all computations: (Δ, □, O, ●) experimental results. (a) Scale reads real optical densities if multiplied by 10^{-2}. Curve was computed taking $k_{(RO_2+RO_2)} = 1.0 \times 10^7$ M^{-1} s^{-1} and $k_{(RO_2 \rightarrow HO_2)} = 6.0 \times 10^2$ s^{-1}. Initial total radical concentration is 10.7 μM. Initial $[H_2O_2]$ assumed 1.2 μM. (b) Scale reads real optical densities if multiplied by 10^{-2}. Curve was computed taking $k_{(RO_2+RO_2)} = 1.3 \times 10^7$ M^{-1} s^{-1} and $k_{(RO_2 \rightarrow HO_2)} = 5.5 \times 10^2$ s^{-1}. Total initial radical concentration was 21.5 μM. Initial $[H_2O_2]$ assumed 2.5 μM. (c) Scale reads real optical densities if multiplied by 2×10^{-2}. Curve was computed taking $k_{(RO_2+RO_2)} = 1.2 \times 10^7$ M^{-1} s^{-1} and $k_{(RO_2 \rightarrow HO_2)} = 5.5 \times 10^2$ s^{-1}. Total initial radical concentration was 38.5 μM. Initial H_2O_2 assumed 4.5 μM. (d) Scale reads real optical densities if multiplied by 4×10^{-2}. Curve was computed taking $k_{(RO_2+RO_2)} = 1.1 \times 10^7$ M^{-1} and $k_{(RO_2 \rightarrow HO_2)} = 5.0 \times 10^2$ s^{-1}. Total initial radical concentration was 60 μM. Initial $[H_2O_2]$ assumed to be 7 μM.

reaction scheme. This decay, as will be shown later, is not due to reaction 7. In these calculations we had to assume an ϵ of 175 M^{-1} cm^{-1} for the product of reaction 6.

Solutions Containing Tetranitromethane. When tetranitromethane (TNM) is also present, in addition to the O_2, N_2O, and alcohol, it competes for e_{aq}^-, H, and RH radicals.[18,19] TNM does not react with peroxy radicals as will be shown later but reacts efficiently with O_2^-.[18,19] Therefore, TNM can be used to discriminate between peroxy radicals and superoxide radicals. The reactions of e_{aq}^-, H, RH, and O_2^- with TNM produce nitroform, NF^-, which strongly absorbs at 350 nm (ϵ 15 000 M^{-1} cm^{-1})

$$\text{TNM} + \text{X} \rightarrow \text{NO}_2 + \text{NF}^- + \text{X}^+ \qquad (12)$$

X represents a reducing radical and X^+ represents the product formed from X upon its reaction with TNM.

Solutions containing 0.1 M 2-propanol, saturated 0.5 atm of N_2O, and 0.5 atm of O_2 were pulse irradiated at pH 4 in the presence of 40 μM TNM. Pulse produced 0.7 μM radicals. An optical absorbance corresponding to the reactions of TNM with 30% of the radicals was built up within 100–200 μs. This was due to the reactions of TNM with e_{aq}^-, RH, and O_2^- (in equilibrium with HO_2. Some O_2^- is quickly formed by the reactions of e_{aq}^- and H with O_2). This relatively fast process was followed by an additional formation of absorbance which obeyed a first-order rate law, $k = 1100$ s^{-1}. We attribute the slower build-up process to the additional formation of O_2^- according to reaction 7.

Under our experimental conditions, the rate of NF^- formation is controlled by the rate of reaction 7. The optical absorption finally reached a constant value, which was stable for at least 100 ms, The final optical absorption was only 85% of that measured when total radical scavenging by TNM took place. From these results we conclude that a pseudo-first-order process was competing with reaction 7, presumably, a reaction of peroxy radicals with impurities. After correcting for this effect we obtained $k_7 = (700 \pm 150)$ s^{-1}. When the TNM concentration was doubled, the fast process became more important, as expected.

The kinectics of the slower build up of absorbance remained unaffected. This shows that the possible reaction of RHO_2 peroxy radicals with TNM was not important.

Similar experiments in methanol showed a higher sensitivity of this system to the effects of impurities. However, $k_6 \simeq 5 \times 10^2$ s^{-1} was measured, a value similar to that found in the 2-propanol system. The first-order rate constant of 5000 s^{-1}, which was used for the curve fittings in the absence of TNM (see previous section), represents mainly the reaction of O_2CH_2OH with impurities. The reliability of the TNM system for the measurements of k_6 was demonstrated when we used solutions containing phosphate buffer (10 μM) at pH 6.6 instead of $HClO_4$. The enhancement of reaction 7 by OH^- resulted in the formation of NF^-, the rate of which was still controlled by (7). Although the impurity effect could not be neglected, we were able to measure by this method $k_{(O_2CH_2OH + OH^-)} = 1.5 \times 10^{10}$ M^{-1} s^{-1} which is in agreement with the value published previously.[12]

The optical changes during the decay of the α peroxy radicals and especially the accompanying changes in conductivity of the solutions have previously been attributed to the formation of intermediate hydrotetroxides. However, a number of reasons against the existence of hydrotetroxides can now be given, the most prominent one being the postulate that tetroxides have extinction coefficients twice as large as the corresponding peroxy radicals (this postulate had to be made in the earlier investigations). The mechanism of eq 8–10 is able to describe not only the observed optical effects but also the conductivity changes described in the earlier work.

Acknowledgment. This work was supported in part by the U.S. Energy Research and Development Adminstration under Contract No. E(11-1-3221).

References and Notes

(1) In part fulfillment of the requirements toward a Ph.D. Degree at the Hebrew University.
(2) Department of Physical Chemistry, The Hebrew University, Jerusalem 91000, Israel.
(3) Sektor Strahlenchemie, Hahn-Meitner-Institut, 1 Berlin 39, Berlin, Germany.
(4) J. Rabani and S. O. Nielsen, *J. Phys. Chem.*, **73**, 3736 (1969).
(5) D. Behar, G. Czapski, L. M. Dorfman, J. Rabani, and H. A. Schwarz, *J. Phys. Chem.*, **74**, 3209 (1970).
(6) K. Stockhausen, A. Fojtik, and A. Henglein, *Ber. Bunsenges. Phys. Chem.*, **74**, 34 (1970).
(7) T. Eriksen, A. Henglein, and K. Stockhausen, *Trans. Faraday Soc.*, **69**, 337 (1973).
(8) E. Hayon and M. Simic, *J. Am. Chem. Soc.*, **95**, 6681 (1973).
(9) K. Stockhausen and A. Henglein, *Ber. Bunsenges. Phys. Chem.*, **75**, 833 (1971).
(10) G. Czapski, *Ann. Rev. Phys. Chem.*, 171 (1971).
(11) J. Rabani, M. Pick, and M. Simic, *J. Phys. Chem.*, **78**, 1049 (1974).
(12) J. Rabani, D. Klug-Roth, and A. Henglein, *J. Phys. Chem.*, **78**, 2089 (1974).
(13) M. Simic and E. Hayon, *J. Phys. Chem.*, **75**, 1677 (1971).
(14) A. Fojtik, G. Czapski, and A. Henglein, *J. Phys. Chem.*, **74**, 3204 (1970).
(15) (a) M. Anbar, M. Bambenek, and A. B. Ross, "Selected Specific Rates of Reactions of Transients from Water in Aqueous Solutions", National Bureau of Standards, U.S. Department of Commerce, Washington, D.C., 1973. (b) L. M. Dorfman and G. E. Adams, "Reactivity of the Hydroxyl Radical in

Aqueous Solutions", National Bureau of Standards, U.S. Department of Commerce, Washington, D.C., 1973.
(16) K. D. Asmus, M. Mockel, and A. Henglein, *J. Phys. Chem.*, **77**, 1218 (1973).
(17) K. H. Schmidt, ANL Report No. 7199, Argonne National Laboratory, Argonne, Ill., 1966.
(18) K. D. Asmus, A. Henglein, M. Ebert, and J. P. Keene, *Ber. Bunsenges. Phys. Chem.*, **68**, 657 (1964).
(19) J. Rabani, W. A. Mulac, and M. S. Matheson, *J. Phys. Chem.*, **69**, 53 (1965).

Pulse Radiolytic Investigations of Peroxy Radicals in Aqueous Solutions of Acetate and Glycine

Sara (Dinur) Abramovitch and Joseph Rabani*

Department of Physical Chemistry, The Hebrew University of Jerusalem, Jerusalem 91000, Israel *(Received January 7, 1976)*

Aqueous solutions of glycine and acetate have been pulse irradiated in the presence of O_2. Radicals produced from these compounds by H abstraction reacted with O_2 to form peroxy radicals. The reaction rate constants $k_{(RH+O_2)} = (2.1 \pm 0.3) \times 10^9$ and $\simeq 1 \times 10^9$ M^{-1} s^{-1} were measured for RH = acetate radicals and glycine radicals, at pH 8.2 and 7.9, respectively. The peroxyacetate radicals decay by a second-order reaction, $k = (6.5 \pm 1) \times 10^8$ M^{-1} s^{-1} at both pH 5.7 and 8.2. The peroxyglycine radicals produce O_2^- by a first-order process, $k = (1.5 \pm 0.3) \times 10^5$ s^{-1} at pH 7.9. Evidence for the formation of O_2^- from peroxy glycine radicals is presented.

Introduction

The suggestion made by McCord and Fridovich[1] that superoxide radicals may cause damage to living cells is relevant to irradiated biological system. As water consists the major part of living cells, reactions of the radiation primary species which are written on the right-hand side of eq 1 must be considered.

$$H_2O \text{ —}\sim\!\!\rightarrow e_{aq}^-, H, OH, H_2O_2, H_2, H_3O^+, OH^- \quad (1)$$

Of these species, e_{aq}^- is known to react efficiently with O_2 in the presence of air, according to

$$e_{aq}^- + O_2 \rightarrow O_2^- \quad k_2 = 2 \times 10^{10}\ M^{-1}\ s^{-1}\ [2] \quad (2)$$

The hydrated electron, e_{aq}^-, may also react with a variety of biomolecules to form reduction products and intermediates which may later transfer electrons to oxygen. At present, it is not known how e_{aq}^- is shared between the various scavengers. OH radicals are expected to react with organic molecules, usually according to

$$OH + RH_2 \rightarrow RH + H_2O \quad (3)$$

RH_2 and RH, respectively, represent organic molecules and radicals formed from them upon H abstraction. Many radicals of the type RH are known to react with O_2 and produce either peroxy radicals, RHO_2, or O_2^-. RH^+ can be obtained as R + H^+.

$$RH + O_2 \rightarrow RHO_2$$
$$\rightarrow RH^+ + O_2^- \quad (4)$$

Thus, cyclopentane,[3] methanol,[4] and 2-propanol[5] have been reported to belong to the RHO_2 forming group, while formate[6] forms the CO_2^- radical ion which transfers an electron to O_2. Of the RHO_2 forming compounds, the alcohol peroxy radicals were found[4,5] to decompose and form O_2^-, a process which is accelerated by bases

$$RHO_2 \text{ (alcohol)} \xrightarrow{\text{base}} R + H^+ + O_2^- \quad (5)$$

In order to obtain information concerning the possible role of O_2^- in the damage of irradiated cells, one has to know whether O_2^- forms at considerable yields. For that purpose it is necessary to investigate various peroxy organic and bioradicals, with respect to their ability to produce O_2^-. We have previously studied[3-5] very simple molecules such as $C_5H_9O_2$, O_2CH_2OH, and $(CH_3)_2(COH)O_2$. Now we report on more complicated molecules, which are also of greater biological significance.

Experimental Section

The experimental technique has been described previously.[6] 5 meV, 200 mA electrons were used. The light source was 150-W Xe, 200-W He–Hg, or 60-W D_2 lamps. The irradiation cell was 4 cm long with 1–3 light passes, so that the optical path was 4 or 12.3 cm. Bausch and Lomb grating monochromator with 32 nm/mm resolution was used with slits ranging from 1 to 2 mm. The monochromator was calibrated every time before use, with the aid of the mercury lines of Hg or Xe–Hg lamps. IP 28 photomultiplier and Tektronix 556 or 549 oscilloscopes were applied. Scattered light was less than 10%, for which corrections have been carried out, assuming no absorption of scattered light by the transients. The pH was determined by an El-Hamma pH meter. The temperature was 20 ± 1 °C unless otherwise stated.

Dosimetry was carried out using formate solutions, which contained O_2 or N_2O/O_2 mixtures. The formate dosimeter solutions were always at the same pH, and had the same $[O_2]$ and $[N_2O]$ as the test solutions of acetate and glycine. The

formate concentrations were chosen so that the efficiency of OH scavenging by the formate was similar to that by acetate and glycine in the appropriate test solutions.

Materials. Triply distilled water was used. Sodium acetate (Baker Analyzed) was recrystallized before use. Glycine (Fluka, purum) was used as received, except for a few test experiments, in which recrystallized glycine was used and showed identical results. Gas mixtures of N_2O and O_2 (Matheson's) were prepared before use. The gas mixture which was used for cell emptying, was the same which was used to saturate a given solution.

Sodium formate (Baker Analyzed), NaH_2PO_4, and Na_2HPO_4 (Mallinckrodt analytical) were used as received.

Results and Discussion

(a) *Acetate.* $CH_3CO_2^-$ is known to react with OH[7] and H,[8] and is inert[9] toward e_{aq}^-. The reaction of the $CH_2CO_2^-$ radical ion with O_2 was reported.[10] Unlike O_2^-, the peroxyacetate radicals do not transfer electrons to benzoquinone.[10] In the absence of O_2, the acetate radicals decay away with a bimolecular reaction rate constant of 5×10^8 M^{-1} s^{-1} at pH 10.[11]

$$CH_3CO_2^- + OH \rightarrow CH_2CO_2^- + H_2O \quad (6)$$
$$k_6{}^7 = 7.0 \times 10^7 \text{ M}^{-1} \text{ s}^{-1}$$

$$CH_3CO_2^- + H \rightarrow CH_2CO_2^- + H_2 \quad (7)$$
$$k_7{}^8 = 2.7 \times 10^5 \text{ M}^{-1} \text{ s}^{-1}$$

$$CH_2CO_2^- + O_2 \rightarrow O_2CH_2CO_2^- \quad (8)$$

$$2CH_2CO_2^- \rightarrow (CH_2CO_2^-)_2 \quad k_9{}^{11} = 5 \times 10^8 \text{ M}^{-1} \text{ s}^{-1} \quad (9)$$

We have measured the decay rate of $CH_2CO_2^-$ at 366 nm (pH 6.5) and found, in agreement with the previously published value, $k_9 = (5.5 \pm 1) \times 10^8$ M^{-1} s^{-1} (using the extinction coefficient of $CH_2CO_2^-$ at 366 nm, $\epsilon_{CH_2CO_2^-}^{366}$ 780[11] M^{-1} cm^{-1}). We measured $k_8 = (2.1 \pm 0.3) \times 10^9$ M^{-1} s^{-1} at 366 nm (pH 8.2) using $[O_2]$ ranging from 10^{-4} to 5×10^{-4} M, and (1–2) $\times$ 10^{-5} M total radical concentration. Corrections were carried out for reaction 9 and for O_2 depletion. A typical example is the pulse irradiation of near neutral solutions containing 0.01 M sodium acetate, saturated with a gas mixture of 24% O_2 and 76% N_2O (partial pressure). $O_2CH_2CO_2^-$ is produced along with some O_2^- within 5 μs after the electron pulse. According to the known reaction rate constants of H and e_{aq}^- one expects about 15% of the total radicals to be O_2^- and about 85% to be $O_2CH_2CO_2^-$. (About 5% of the $CH_2CO_2^-$ radicals are expected to disappear by radical–radical reactions under our conditions.) The absorption of $O_2CH_2CO_2^-$ peaks at 305 nm, ϵ 550 $\pm$ 30 M^{-1} cm^{-1}. The calculation of ϵ is based on comparison of the absorbance in the acetate solutions with that observed in 10 mM formate under similar conditions, taking $\epsilon_{O_2^-}^{236}$ 1920 M^{-1} cm^{-1}. The spectra of $O_2CH_2CO_2^-$ and of O_2^- obtained in this work are given in Figure 1. The decay of the 270-nm absorbance obtained in the acetate solutions described above takes place by two steps: about 80% of the absorbance decays away by a second-order process, attributed to

$$2O_2CH_2CO_2^- \rightarrow \text{products} \quad (10)$$

The second process is considerably slower (half-life at pH 8.2 is several hundred milliseconds) and is attributed to the decay of O_2^- which is expected to form from e_{aq}^- and H reactions with O_2. This is confirmed by measurements at 320–360 nm, where $O_2CH_2CO_2^-$ absorbs light and O_2^- absorption is negligible. Under these conditions only one decay process of all the absorption could be observed, the rate constant of which was found to be $k_{10} = (6.5 \pm 1.2) \times 10^8$ M^{-1} s^{-1} measured at

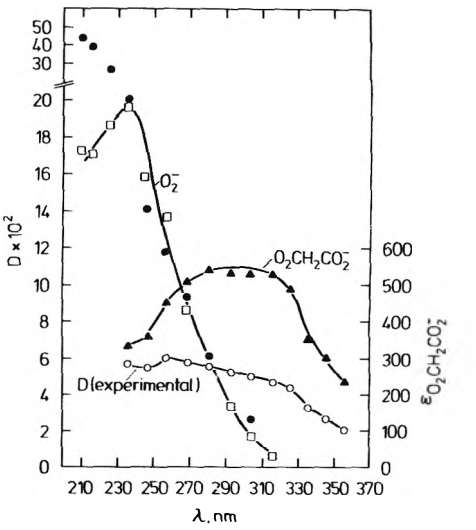

Figure 1. Spectra of $O_2CH_2CO_2^-$ and O_2^- taken in solutions of 0.01 M sodium acetate or sodium formate saturated with 1 atm gas mixture of 24% O_2 and 76% N_2O (partial pressures) at pH 8 (9.5×10^{-2} M phosphate buffer). 26 μM (total) radicals per pulse (C_{total}). Optical path l = 4 cm. Each point is an average of 1–3 determinations; 18 °C: (○) experimental absorbance, D_{expt}, in the acetate solutions, extrapolated to the middle of the 1.5-μs pulse (left scale); (▲) the spectrum of $O_2CH_2CO_2^-$ (right scale). $\epsilon_{O_2CH_2CO_2^-}$ was calculated from the relation $\epsilon_{O_2CH_2CO_2^-} = (D_{expt} - 0.14D_{formate})/0.86lC_{total}$; (□) the absorbance of O_2^- in the formate solutions ($D_{formate}$) (left scale); (●) the absorbance which remains after the decay of $O_2CH_2CO_2^-$, multiplied by 5 (left scale).

340 nm taking $\epsilon_{O_2CH_2CO_2^-}$ 360 M^{-1} cm^{-1}, at both pH 5.7 and 8.2, with total radical concentrations ranging from 2.6 to 11 μM. Measurements at pH 10.5 gave $k_{10} = (4 \pm 1.2) \times 10^8$ M^{-1} s^{-1}. Measurements at pH 8.2 at other wavelengths (270, 320–360 nm) gave similar results. The spectrum which remains after the decay of $O_2CH_2CO_2^-$, after normalization, agrees with that of O_2^- down to 235 nm (Figure 1). Below this wavelength, deviations are observed which may be attributed to a product of reaction 10. Indeed, in the wavelength range 210–230 nm, the initial formation of $O_2CH_2CO_2^-$ + O_2^- absorbances is followed by an additional increase of the absorbance with a half-life that corresponds to the decay of $O_2CH_2CO_2^-$. The absorptions observed at 240–300 nm at the end of reaction 10 agree with O_2^- being 19–22% of the total radicals. This value is perhaps somewhat higher, but within experimental error with the calculated value of 15%. We conclude that $O_2CH_2CO_2^-$ did not produce significant concentrations of O_2^- under our conditions. In this respect, $O_2CH_2CO_2^-$ reacts similarly to $O_2C_5H_9$.[3]

Glycine. Unless otherwise stated, the experiments in glycine solutions were carried out at 0.2 M glycine, in order to have sufficient buffer capacity at pH's not very close to the pK of glycine, and to guarantee total OH scavenging. Typical oscilloscope traces are shown in Figure 2 from which the time dependence of the absorbance can be obtained. Under the experimental conditions of this figure, the absorbance formed during the electron pulse decays away by three processes. A glycine radical,[12,13] "$NH_2CHCO_2^-$" ("$NH_2CHCO_2^-$" denotes all forms of glycine radicals at acid–base equilibrium) with a maximum absorption at 250–260 nm is formed during the electron pulse. The reactivity of the glycine zwitterion toward OH radicals is low, but the $NH_2CH_2CO_2^-$ form of glycine is relatively reactive,[14] so that practically all the OH radicals react with glycine during the electron pulse, under our conditions. The glycine radicals react with O_2 to form a peroxy radical, according to

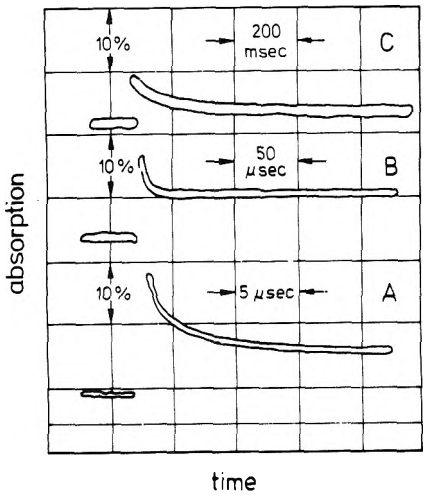

Figure 2. Oscilloscope traces in glycine solutions: 0.2 M glycine, saturated 1 atm of N_2O/O_2 mixture, 1:1 (partial pressures), pH 7.9 (2 mM NaOH added). Total radical concentration per pulse = 20 μM measured at 307 nm with a 12.3-cm light path.

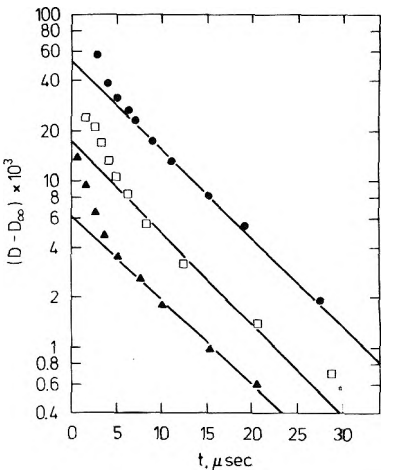

Figure 3. Decay kinetics for the measurements of k_{12}: 0.2 M glycine at pH 7.9. Measured at 313 nm, using 12.3-cm light path. Each point is an average of 2–4 determinations: (●) saturated at O_2/N_2O mixture 1:1 (partial pressures) 20 μM radicals (total); (□) 1:1 O_2/N_2O, 7.7 μM radicals; (△) 68% N_2O, 32% O_2 (partial pressures), 3.3 μM radicals.

$$\text{“}NH_2CHCO_2^-\text{”} + O_2 \rightarrow \text{“}NH_2CH(O_2)CO_2^-\text{”} \quad (11)$$

“$NH_2CH(O_2)CO_2^-$” denotes all forms of peroxyglycine radicals. We attribute the fast decay observed in Figure 2A to reaction 11. This is supported by the enhancement of this decay when higher O_2 concentrations are used, and by an independent measurement of $k_{11} \simeq 10^9$ M^{-1} s^{-1} (based on competition experiments with ferricyanide, using $k = 1 \times 10^9$ M^{-1} s^{-1} for the reaction of glycine radicals with ferricyanide. The reactivity of glycine radicals toward ferricyanide ions was measured directly at 420 nm). Reaction 11 is followed by a slower decay (slower decay in Figure 2A and decay in Figure 2B) which was found to obey first-order kinetics with an average $k_{12} = 1.5 \times 10^5$ s^{-1} at pH 7.9 (see Figure 3). The initial deviations are due to incompletion of reaction 11. The decay which we attribute to reaction 12 will be referred to as “process A”. The nature of the glycine oxidation products was not investigated. These products may be $NH{=}CH_2CO_2^-$ formed along with H^+ which may later hydrolyze to form $CHOCO_2^-$ and ammonia. Such reactions, upon the oxidation of glycine, have been previously proposed.[15] Finally, the remaining absorbance decays almost to zero with $\tau_{1/2} \sim 10^{-1}$ s (Figure 2C). This decay is attributed to the disappearance of O_2^- [6,16] (in the following: “process B”).

$$\text{“}NH_2CH_2(O_2)CO_2^-\text{”} \rightarrow O_2^- + \text{glycine oxidation products} \quad (12)$$

Evidence for the Formation of O_2^- According to Reaction 12. (a) *Spectrum.* Under our conditions, reaction 11 was usually well separated in time from process A. No accurate spectrum of the peroxyglycine radicals could be taken. At the end of process A, the absorption spectrum in 0.2 M glycine at pH 7.9, multiplied by 1.16, was identical with the spectrum observed in solutions of 0.01 M formate under the same conditions (25% O_2, 75% N_2O, 19 °C, total radical concentration 31 μM, pH 7.9 obtained with 9.5×10^{-2} M phosphate buffer in the formate solutions and with 2 mM NaOH in the glycine solutions). The normalization factor of 1.16 was necessary in order to obtain precisely the same absorbance. As the same factor had to be used at several test wavelengths also for considerably lower pulse intensities (e.g., total radical concentration 0.7 μM), we conclude that the factor 1.16 does not arise from bimolecular competing reactions. It is perhaps due to a form of glycine radical which does not react with O_2 to produce O_2^- by reaction 12 (e.g., $NHCH_2CO_2^-$ or $^+NH_2CH_2CO_2^-$).

(b) *Decay Kinetics.* At pH 6.8 the absorbance remaining at the end of process A decayed away with an apparent second-order rate law[2] yielding $2k = 1.7 \times 10^6$ M^{-1} s^{-1}. Identical results were obtained when formate was used instead of glycine, at the same pH and ionic strength. In another set of experiments, glycine was pulse irradiated using solutions saturated with either 1:1 (partial pressure) ratio of N_2O to O_2, or with O_2 alone.

In the first case, e_{aq}^- reacted mainly with N_2O so that most of the radiation induced radicals produced the peroxyglycine radicals. In the second case, namely, in O_2 saturated solutions, OH reacted with glycine while e_{aq}^- reacted with O_2. About 50% of the peroxy radicals were O_2^-, while the other 50% were peroxyglycine radicals. The decay kinetics in milliseconds measured at 255 nm in N_2O/O_2 solutions were identical to those observed in the O_2 saturated solutions (pH's 6.0, 6.8, 7.7 and 8.8). The dependence of O_2^- decay on pH is specific,[6,16] and therefore the identical decays observed for process B and for O_2^- produced from the reaction of e_{aq}^- with O_2 show that O_2^- is indeed a product of reaction 12. Moreover, in the O_2 saturated solutions, the decay of the absorbances after the termination of process A was all by one process, at the above mentioned pH's. Had the product of reaction 12 been different from O_2^-, separation between two decay processes would have been observed at least in some of the pH's.

Reaction with 1,4-Naphtoquinone-2-sulfonic Acid. Solutions containing 0.2 M glycine at pH 6.8 (10^{-2} M phosphate) were saturated N_2O/O_2 mixtures (2:1 by partial pressures). 200 or 400 μM of the quinone was added, and the absorbance changes following electron pulses (0.7 μM radicals per pulse) were measured. The formation of the semiquinone ions according to

$$O_2^- + Q \rightarrow O_2 + Q^- \quad (13)$$

was followed at 402 nm.[17,18] Q represents the quinone molecule. The pseudo-first-order plots gave $k_{13} = (2.5 \pm 0.3) \times 10^8$ M^{-1} s^{-1}. A reaction rate constant $k_{13} = (2.5 \pm 0.4) \times 10^8$ M^{-1} s^{-1} was obtained in similar solutions containing formate instead of glycine, supporting the proposed formation of O_2^- according to reaction 12.

Reaction with Cu(II). Cu(II) enhances the decay of O_2^- radical ions.[19,20] When we added 10^{-4} M $Cu(ClO_4)_2$ to a solution containing 5×10^{-2} M glycine at pH 8.0 (1 mM NaOH added) saturated with 1 atm gas mixture $N_2O/O_2 = 1.5$ (partial pressures), we observed an enhanced decay of the optical absorbance at 275 nm (20 μM radicals per pulse). The results agreed with $k_{14} = (4.1 \pm 0.6) \times 10^6$ M^{-1} s^{-1}.

$$O_2^- + Cu(II) \rightarrow O_2 + Cu(I)$$

or

$$O_2^- + Cu(II) \xrightarrow{2H^+} H_2O_2 + Cu(III) \qquad (14)$$

This result was the same as obtained under similar conditions, when 20 mM formate was added to the above solution. As the formate reacts very efficiently with OH radicals, it competed successfully for OH to form CO_2^- which eventually gave O_2^-. Again, these experiments confirm the identification of O_2^- as the product of reaction 12. Note that the relatively low reactivity of O_2^- with Cu(II) in these experiments results from the complexation of Cu(II) with glycine.[20]

Conclusions

The product of reaction 12 has properties identical with those of O_2^-: the absorption spectrum, decay kinetics and pH dependence, reactions with Cu(II) and with a quinone. This is unlike the results in the acetate system. It is possible that the peroxyglycine radicals form O_2^- by a mechanism similar to that proposed for peroxyalcohol radicals,[4,5] namely, an internal electron transfer from the nitrogen to the O_2^- group, followed by cleavage of the C–O bond and formation of a C=N bond.

$$\begin{aligned} NH_2CH(O_2)\,CO_2^- &\rightarrow {}^+NH_2CH(O_2^-)CO_2^- \\ &\rightarrow O_2^- + {}^+NH_2{=}CHCO_2^- \\ &\rightarrow O_2^- + H^+ + NH{=}CHCO_2^- \\ &\rightarrow O_2^- + NH_4^+ + CHOCO_2^- \qquad (15) \end{aligned}$$

We do not know which of the forms, $NH_2CH(O_2)CO_2^-$ or $NH_3^+CH(O_2)CO_2^-$ is the stable form of the peroxyglycine radical under our conditions. If it is the zwitterion peroxy radical, one may assume a similar mechanism, starting with H transfer from the $-NH_3^+$ group to the $-O_2$.

The carboxyl group, as observed in acetate, does not facilitate the formation of O_2^-, when $-O_2$ becomes attached to an adjacent C atom.

The formation of O_2^- from the peroxyglycine radical may depend on pH, as well as on the presence of acids and bases. Such dependence have been previously reported for peroxyalcohol radicals.[4,5] As glycine itself possesses acid–base character, the value that we reported for k_{12} must be considered good only for the conditions of its measurements. Due to the poor time separation between process A and reaction 11, we were unable to carry out a quantitative investigation on the possible catalysis of process A.

Qualitatively, however, we have found that the addition of phosphate buffer or the increase of glycine concentration beyond 0.2 M enhanced the rate of process A. Similarly, decreasing the glycine concentration to 0.01 M (at pH 8) slowed down process A. At such a low glycine concentration we cannot assume total radical scavenging. In addition, the expected half-life of reaction 3 is a few microseconds. No quantitative work was therefore carried out on process A under these conditions.

Acknowledgment. The authors are indebted to Y. Ogdan for careful linac operation and maintenance. This work was supported in part by USERDA under Contract No. E(11-1-3221).

References and Notes

(1) J. M. McCord and I. Fridovich, *J. Biol. Chem.*, **244**, 6049 (1969).
(2) (a) J. P. Keene, *Radiat. Res.*, **22**, 1 (1964); (b) S. Gordon, E. J. Hart, M. S. Matheson, J. Rabani, and J. K. Thomas, *J. Am. Chem. Soc.*, **85**, 1375 (1963).
(3) J. Rabani, M. Pick, and M. Simic, *J. Phys. Chem.*, **78**, 1049 (1974).
(4) J. Rabani, D. Klug-Roth, and A. Henglein, *J. Phys. Chem.*, **78**, 2089 (1974).
(5) Y. A. Ilan, J. Rabani, and A. Henglein, *J. Phys. Chem.*, preceding article in this issue.
(6) D. Behar, G. Czapski, L. M. Dorfman, J. Rabani, and H. A. Schwarz, *J. Phys. Chem.*, **74**, 3209 (1970).
(7) R. L. Willson, C. L. Greenstock, G. E. Adams, R. Wageman, and L. M. Dorfman, *Int. J. Radiat. Phys. Chem.*, **3**, 211 (1971).
(8) S. Nehari and J. Rabani, *J. Phys. Chem.*, **67**, 1609 (1963).
(9) J. Rabani, H. B. Steen, H. Bugge, and T. Brustad, *Chem. Commun.*, 1353 (1971).
(10) E. Hayon and M. Simic, *J. Am. Chem. Soc.*, **95**, 6681 (1973).
(11) P. Neta, M. Simic, and E. Hayon, *J. Phys. Chem.*, **73**, 4207 (1969).
(12) P. Neta, M. Simic, and E. Hayon, *J. Phys. Chem.*, **74**, 1214 (1970).
(13) J. V. Davies, M. Ebert, and A. J. Swallow, "Pulse Radiolysis", M. Ebert, J. P. Keene, A. J. Swallow, and J. H. Baxendale, Ed. Academic Press, New York, N.Y., 1965, p 165.
(14) L. M. Dorfman and G. E. Adams, Ed., *Natl. Stand. Ref. Data Ser., Natl. Bur. Stand.*, **No. 46** (1973).
(15) W. M. Garrison, *Curr. Top. Radiat. Res.*, 45 (1968).
(16) J. Rabani and S. O. Nielsen, *J. Phys. Chem.*, **73**, 3736 (1969).
(17) K. B. Patel and L. Wilson, *J. Chem. Soc., Faraday Trans. 1*, **69**, 814 (1973).
(18) Y. A. Ilan, D. Meisel, and G. Czapski, *Isr. J. Chem.*, **12**, 891 (1974).
(19) J. Rabani, D. Klug-Roth, and J. Lilie, *J. Phys. Chem.*, **77**, 1169 (1973).
(20) D. Klug-Roth and J. Rabani, *J. Phys. Chem.*, **80**, 588 (1976).

Partial Molal Volumes of HCl in Pure Ethylene and Propylene Glycols and in Their Aqueous Mixtures

Utpal Sen[1]

Physical Chemistry Division, Jadavpur University, Calcutta 700032, India *(Received March 11, 1975; Revised Manuscript Received March 22, 1976)*

Partial molal volumes at infinite dilution ($\bar{V}_2^0$) of HCl in pure ethylene and propylene glycols and in their aqueous mixtures have been determined at 25 °C from density measurements. The values of $\bar{V}_2^0$ of HCl in the pure glycols are much lower than in water. With gradual addition of water to the glycols, $\bar{V}_2^0$ increases and passes through a maximum around 50 and 45 wt % of ethylene glycol and propylene glycol, respectively. The results have been examined with respect to structural aspects of the solvent systems.

Introduction

Different methods[2,3] are used to obtain information about the nature of mixed solvents and the behavior of electrolytes in them. The determination of the partial molal volumes of electrolytes in different solvent mixtures has gained in importance recently and the need has been felt[4] to stimulate the use of this property to examine different interactions (ion–solvent, ion–ion, and solvent–solvent) in various solvent systems. Though a large amount of data on aqueous solutions is available, partial molal volumes studies on pure nonaqueous[5–19] and on mixed solvent media[17–26] are few.

The partial molal volume of an ion can, generally, be considered to be the combination of two component parts: (i) increase in volume of the system due to the intrinsic ionic volume and (ii) change in volume of the system due to the alteration of the solvent structure arising from ion–solvent interactions. The process becomes complicated when more than one kind of solvent molecule is available for these interactions. In such cases, while the behavior of the ions in the pure solvent has to be kept in the picture, the influence of the other kind of molecules, which modify the properties of the ion–solvent interaction, has to be taken into account also. Recently, an attempt to use the behavior of the partial molal volumes of salts and their component ions as a function of solvent composition as a probe to investigate the varying structure of the binary solvent system has been reported.[25] The partial molal volumes of tetraalkylammonium salts in aqueous mixtures of ethanol, acetone, and dimethyl sulfoxide (Me_2SO) (up to 0.5 mole fraction of the cosolvent) have been studied.[25,26] The work reported here involves the determination of the partial molal volumes of HCl in pure ethylene and propylene glycols and in their aqueous mixtures (from 0 to 1 mole fraction). The results have been used to make a comparative study of the nature of the mixed solvents and the various interactions in them. No partial molal volume study with HCl as the solute in any mixed solvent system has been reported so far.

Experimental Section

Purification of the solvents and preparation of the solutions have been described elsewhere.[27] A pycnometer[28] has been used for the density measurements in a temperature-controlled bath maintained at 25.00 ± 0.05 °C. For each solution the mean of four different density readings has been used. For the density of the solvent the mean of eight to ten readings, taken at the beginning and at the end of the experiment, has been used. The maximum uncertainty in the density readings is 0.000 02 unit. In the calculations the absolute density of water at 25 °C is taken as 0.997 08 g ml^{-1}.[29] Densities of pure ethylene glycol and pure propylene glycol obtained are 1.109 90 and 1.032 65 g ml^{-1} against the reported literature values,[30] 1.109 86 and 1.0326 g ml^{-1}, respectively.

Results

Apparent molal volumes (ϕ_v) have been calculated from the corresponding density values by the following equation[29]

$$\phi_v = \frac{1000}{cd_0}(d_0 - d) + \frac{M_2}{d_0} \tag{1}$$

where c is the molar concentration ($= md1000/(1000 + mM_2)$), d_0 and d are the densities of the solvent and the solution, respectively, M_2 is the molecular weight of the solute, and m is the molality. At present three major equations[17,29] have been available for the extrapolation of the apparent molal volumes. The simplest is the equation due to Masson[31] who found that ϕ_v varies linearly with $\sqrt{c}$ in dilute solutions and that this simple relationship often extends to concentrated solutions.[17,29,31] Thus

$$\phi_v = \phi_v^0 + S_v^*\sqrt{c} \tag{2}$$

where ϕ_v^0 is the apparent molal volume at infinite dilution and S_v^* is the experimental slope. It has been assumed that the Masson equation holds for hydrochloric acid in the glycolic and aquo–glycolic solvent systems. The calculated ϕ_v values at concentrations from 1 to 0.05 m have been plotted against $\sqrt{c}$, and, from the extrapolation of the data to zero concentration, apparent molal volumes at infinite dilution (ϕ_v^0), which are equal to the partial molal volumes at infinite dilution ($\bar{V}_2^0$), have been obtained. Figure 1 shows the plot of ϕ_v vs. $\sqrt{c}$ for ethylene glycol and its aqueous mixtures. The plots for propylene glycol and its aqueous mixtures are of the same nature and, hence, not shown in the figure. Due to the limitation of the pycnometer measurements, extrapolations have to be made from rather high concentrations. The minimum concentration attainable in the determination of the densities with all the different solvent mixtures is about 0.05 m. The uncertainty of 0.000 02 unit in density readings at 0.05 m will amount to uncertainty in ϕ_v of the order of 0.4 cm^3 as calculated from the relationship[29]

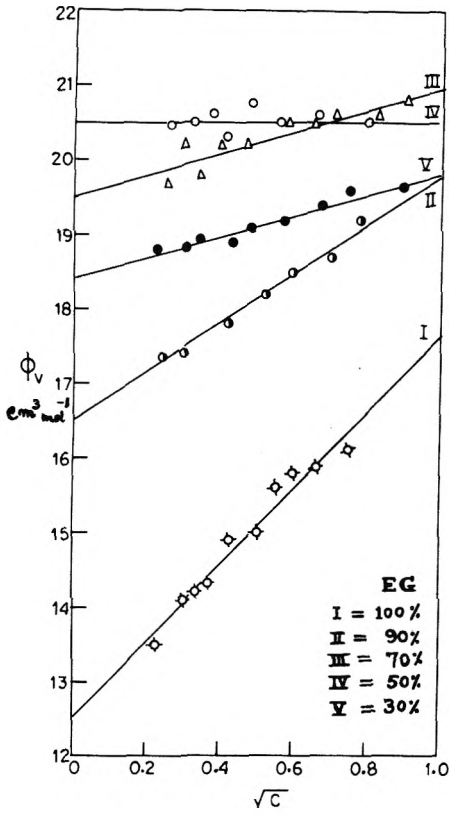

Figure 1. Plot of ϕ_v (in cm^3 mol^{-1}) vs. $\sqrt{c}$. Curves I to V represent 100, 90, 70, 50, and 30 wt % ethylene glycol, respectively.

$$\text{probable error in } \phi_v = -\frac{1000}{c}\frac{\partial d}{d} \qquad (3)$$

The limiting slope (S_v) can be calculated theoretically[29] when the compressibility (β) and the pressure differentiation of the dielectric constant ($\partial \ln D/\partial P$) of the solvents are known. For the solvents used in the present study these data are not available, and, hence, any attempt to have a comparison of the experimentally obtained values of S_v^* with the theoretically calculated values of the limiting slope cannot be made. The value of ϕ_v^0 (= $\bar{V}_2^0$) and S_v^* of HCl in ethylene glycol and in propylene glycol and in their different aqueous mixtures are recorded with their respective least-squares standard deviations in Table I (see the paragraph at the end of text regarding supplementary material). It is evident from the table that $\bar{V}_2^0$ of HCl in the pure glycols is much lower than it is in pure water, and, with the addition of water to the glycols, $\bar{V}_2^0$ increases, passes through a maximum around 50% ethylene glycol and 45% propylene glycol, and finally approaches closely its value in pure water in the water-rich solvent mixtures. It has been also noted that the value of S_v^* is the highest in the pure glycols and passes through a minimum ($\simeq 0$) around the composition of the glycol–water mixture where $\bar{V}_2^0$ values are at a maximum. Figure 2 shows the variation of $\bar{V}_2^0$ of HCl with mole fraction of the glycols in the solvent mixtures.

Discussion

When an ion is introduced into a solvent, the partial molal volume at infinite dilution ($\bar{V}_2^0$), which is thermodynamically defined as the actual change in the volume of the system, can be expressed as

$$\bar{V}_2^0 = V_{int} + \Delta V \qquad (4)$$

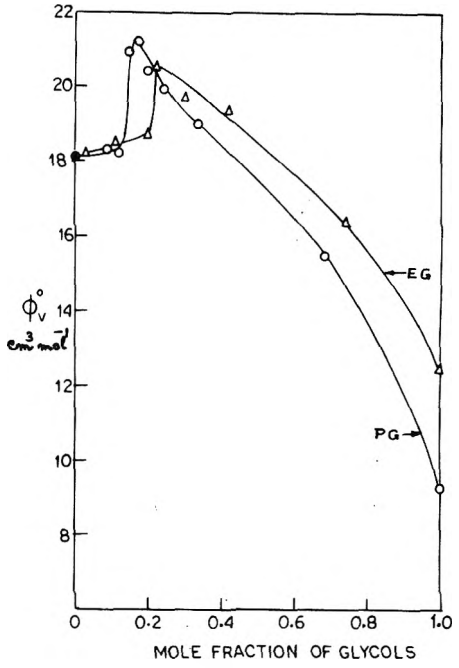

Figure 2. Variation of ϕ_v^0 (in cm^3 mol^{-1}) of HCl with mole fractions of the glycols: curve I for ethylene glycol; curve II for propylene glycol.

where V_{int} is the intrinsic volume of the ion and ΔV is the change in volume of the system due to ion–solvent interactions. The values of $\bar{V}_2^0$ of HCl in ethylene glycol (= 12.5) and in propylene glycol (= 9.8) are much lower than in water (= 18.1) (see Table I). From the observed minimum of the activity coefficients of some alkali metal halides and hydrochloric acid in ethylene glycol and in glycol–water mixtures, it has been suggested[28,32] that solvation is comparatively stronger in glycol and in glycol-rich water mixtures. A lower value of $\bar{V}_2^0$ of HCl in the glycols is, thus, expected and has been obtained. $\bar{V}_2^0$ of HCl is the sum of its ionic partial molal volumes, $\bar{V}^0_{H^+}$ and $\bar{V}^0_{Cl^-}$. It has been assumed by earlier authors[33,34] that in electrolytic solutions the anion solvation can be considered as negligible. They argued that the solvation number at infinite dilution is really a measure of the extent to which the cation is solvated. Extending these arguments in other media it can be assumed that in the case of hydrochloric acid solution the chloride ion, due to its large size and small surface charge density, has negligible solvation in comparison to a proton. The solvation of the proton of HCl will then take the most effective role in the volume change due to structural alteration arising from ion–solvent interactions. So the lower values of $\bar{V}_2^0$ of HCl in the glycols suggest that $\bar{V}^0_{H^+}$ is smaller in the glycols than it is in water. The absolute volume of the H^+ ion has a negative value in water. This means that there is some sort of a collapse among the solvent molecules in the vicinity of the incorporated hydrogen ion, or, in other words, a volume contraction in the system (electrostriction).[4,35] In the glycols, possibly $\bar{V}^0_{H^+}$ has still more negative values and the electrostrictive volume contraction is more pronounced. This gives the picture that relative to water, both propylene and ethylene glycols are prone to be held more compactly around the H^+ ion, thus suggesting that the glycols are more basic in nature than water (propylene glycol > ethylene glycol > water). A recent comparative study[16] of the ionic volumes in different solvent media shows that the volume of a proton ($\bar{V}^0_{H^+}$) in ethylene glycol is about -12 cm^3 mol^{-1} while in water it is -4.5 cm^3 mol^{-1}.[36] Larger negative values of $\bar{V}^0_{H^+}$ have also been

reported in methanol (-17.0 cm^3 mol^{-1}) and in ethanol (-15.5 cm^3 mol^{-1}) solutions.

In aquo–glycolic media the above structural arrangement is complicated by other associated factors such as (i) preferential solvation[37–39] of the ions by the different species present in the solvent system, and (ii) interactions between the molecules of water and those of the glycols. It has been observed that $\bar{V}_2^0{}_{(HCl)}$ has its maximum value at about 0.25 and 0.2 mole fractions of ethylene glycol and propylene glycol solutions, respectively (see Figure 2). The change of partial molal volumes with varying proportion of other solvents in water in the cases of electrolytes has been noted earlier by other workers.[20–26] Bateman[20] assigned this change of the partial molal volumes, $\bar{V}_2^0$, with composition of the mixed solvent to variable solvation of the ions. When solvation occurs, the ion complex may be assumed to be packed differently in different media and the greater the packing, the smaller the molal volumes. He found that around 50 wt % ethanol–water mixture $BaCl_2$ and $SrCl_2$ have maximum $\bar{V}_2^0$ values. The observation of Padova[21] and of Das et al.[22–24] are also of a similar nature when the partial molal volumes of some electrolytes have been studied in water with acetone, ethanol and dioxane as the cosolvents. Most recent studies of $\bar{V}_2^0$ in mixed solvents, however, are those of Hyne and co-workers.[25,26] They studied four tetraalkylammonium chlorides in ethanol–water, acetone–water, and Me_2SO–water mixtures. The ionic volumes of the tetraalkylammonium ions and the chloride ion have been determined by extrapolating the $\bar{V}_2^0$ values of the salts to the zero cation molecular weight, and the structural arrangements of these different mixtures and the influence of the ions on them have been discussed. However, due to the large size of the cations, the values of $\bar{V}_2^0$ of the tetraalkyl salts are determined mainly by the term V_{int} of eq 4, or, what they called the volume contribution due to the hole formation in the solvent to accommodate the large ions, and not determined primarily by the electrostriction caused by the ions as the case would be with HCl as the solute. Minimum and also maximum in the values of partial molal volume in tetraalkylammonium ions have been observed[25,26] at about 0.1 and 0.3 mole fractions of ethanol, respectively. Similar observations have also been reported[26] in acetone and to a lesser extent in Me_2SO–water mixtures. It has been suggested that around 0.1 mole fraction of alcohol the structure formation between the two kinds of the solvent molecules is the most enhanced, and, in this solvent arrangement, due to the preformed holes (or availability of solvent free volume) into which the cations may fit without the prerequisite of hole formation prior to dissolution, $\bar{V}_2^0$ becomes minimum. As the proportion of the nonaqueous cosolvent in the mixture increases the simple bulk effect of the cosolvent will begin to break down the characteristic water structure. At 0.3 mole fraction of ethanol where $\bar{V}_2^0$ of tetraalkylammonium ions becomes maximum, the competition between pure water and pure cosolvent structure results in the mixture having essentially a closed packed structure with consequent minimum free volume. Thus, there are no preformed holes in the binary solvent and dissolution of the third component solute requires maximum expansion of the solvent to accommodate the solute. The enhancement of the three dimensional order characteristic of pure water, reaching a maximum at a mole fraction between 0.1 and 0.3 of methanol and, thereafter, a structural breakdown due to the bulk effect has also been suggested from experimental observations.[39,40] Somewhat similar types of interactions between the solvent molecules have been assumed in some glycol–water mixtures also.[39–44]

The size of the solvent molecules and the degree of steric hindrance of the poles of the dipole of the solvent molecule are the other parameters (besides the electrostriction) which determine the ionic partial molal volumes, and, as we go from water to larger solvent molecules, these factors become more important.[15] The partial molal volumes of HCl in the glycol–water mixtures do not show any minimum in the region of lower percentage of the glycols. The decrease in the value of $\bar{V}_2^0$ of tetraalkylammonium salts to reach the minimum is about 4–5% of the total value. In HCl solutions (where $\bar{V}_2^0{}_{(HCl)} \simeq 18$) this 4–5% possible decrease may not be sufficient to detect distinctly within the accuracy of the present work. Moreover, the enhancement of water structure (iceberg[45]) with the addition of small amount of the glycols might also be a possibility as in the case of other alcohols.[44,46–49] Since, with a solute such as HCl, the hole formation has not been of primary importance to determine the value of $\bar{V}_2^0$, the more characteristic structure formation of water in the mixture might result in nearly the same partial molal volume of HCl in these solvent mixtures (as observed). In tetramethylammonium salts (the smallest of the tetraalkylammonium salts), however, the minimum around 0.1 mole fraction of the cosolvent has not been observed though it has been observed in the case of cations (separately), when the ionic contributions are split into parts. In this connection the variation of the partial molal volume of the chloride ion ($\bar{V}_2^0{}_{(Cl^-)}$) in different mixed solvents as reported by Hyne and coworkers[25,26] might deserve a closer look. It has been found that $\bar{V}^0{}_{Cl^-}$ increases with addition of Me_2SO and acetone in water and reaches a maximum around 0.2 mole fraction of the cosolvent. However in ethanol–water mixture $\bar{V}^0{}_{Cl^-}$ decreases and reaches a minimum value around 0.3 mole fraction of the ethanol. It has been suggested[25] that at that particular composition the ethanol–water solvent is "closest to close packed" and the chloride ion promotes the electrostriction of the solvent molecules to form solvation shells, since at this composition the soft-ice[45] promoting effect of the ion is no longer in competition with the hydrophobic iceberg[45] promoting effect of the alcohol cosolvent. It was also suggested that at 0.3 mole fraction of ethanol the binary solvent system is as unstructured as it can be and the solvent molecules are, relatively, most available for electrostriction around the ion. However, with this picture of the solvent–solvent interaction around 0.3 mole fraction of ethanol, it is difficult to explain the maximum value of the partial molal volume of $BaCl_2$ and $SrCl_2$ around 50–60 wt % alcohol (i.e., about 0.3 mole fraction of ethanol) which was assigned to the minimum solvation.[20] Both Ba^{2+} ($r = 1.35$) and Sr^{2+} ($r = 1.18$) have smaller volumes and greater surface charge densities in comparison to those of Cl^- ($r = 1.81$) and it may be expected that electrostriction involving these ions will be more pronounced leading, therefore, to a minimum partial molal volume around this particular composition of the solvent system. Thus, if around 0.3 mole fraction of ethanol, the solvent molecules are relatively most available for electrostriction around the ion, $BaCl_2$ and $SrCl_2$ should show the minimum value of the partial molal volume at this composition, but, the experimental observations have been otherwise and the values of $\bar{V}_2^0$ of $BaCl_2$ and of $SrCl_2$ are about maximum there.

In the present study the ionic parts of the partial molal volume of HCl could not be split at this stage, and the change of volume of the chloride ion ($\bar{V}^0{}_{Cl^-}$) with the solvent composition in the glycol–water systems could not be determined. The character of a proton in different media, however, is unique and draws much attention as such.[16] In water the

primary species is H_3^+O and in the glycols it is $HOROH_2^+$, but, how the proton is distributed among the molecules of a mixed solvent is not yet known. Without the knowledge of this distribution, structural arguments remain only conjectural. The present study can, on the other hand, show that the electrostriction is maximum in the pure glycols, and, when water is added to the glycols, the incorporated water molecules become somehow engaged with the glycol molecules making the process of electrostrictive volume decrease, caused by the proton, more and more difficult. Consequently, the value of $\bar{V}^0_{HCl}$ increases with the water content of the solvent mixtures. Around 50 wt % (i.e., three to four water molecules per one ethylene glycol molecule) and 45 wt % (i.e., five to six water molecules per one propylene glycol molecule) the involvement among the solvent molecules is maximum and the electrostriction minimum. Hence, from the solvent structural consideration, it might be said that the solvent composition in which HCl has the maximum partial molal volume becomes the minimum basic. Beyond this particular region of the solvent composition, the value of $\bar{V}^0_{HCl}$ sharply decreases and becomes nearly the same as it is in pure water (see Figure 2). This is because after the region of maximum partial molal volume, water molecules, free from any significant interaction with the glycol molecules, are available and H^+ ions, being preferentially solvated by them, makes the value of $\bar{V}^0_{HCl}$ approach that in pure water.

The apparent molal volume concentration dependence constant (S_v^*), though an empirical quantity, can give some indication of ion–ion interactions in solution. Interionic attraction is undoubtedly higher in the glycols than in water because of the lower dielectric constants ($D_{PG} = 31.1$, $D_{EG} = 37.7$, $D_W = 78.5$). It has been observed that the value of S_v^* becomes maximum in the pure glycols and decreases with the increasing amount of water in the solvent composition, but rises again after reaching a minimum. Considering that ion–ion interactions can be affected by the influence of ions on the structure of the solvent,[7,50–52] the apparent coincidence of the maximum ϕ_v^0 and minimum S_v^* can be noted with interest.

It has been found from the structural consideration of the solute–solvent system that the value of the partial molal volume of HCl ($\bar{V}^0_{HCl}$) has some relation to the basic character of the aquo–glycolic solvents, and $\bar{V}^0_{HCl}$ is maximum in the solvent composition where the basic character is the minimum. This simple method may prove useful in determining the minimum basic compositions for other aquo–organic solvent mixtures. The knowledge of the ionic partial molal volumes, however, are necessary to have a better understanding of the observations, and further works in this direction may be worthwhile.

Acknowledgment. Thanks are due to Professor S. P. Moulik for interesting discussions and Professor M. N. Das, Head of the Physical Chemistry Division, Jadavpur University, Calcutta, for laboratory facilities.

Supplementary Material Available: Table I, containing values of $\bar{V}_2^0$ and S_v^* of HCl in glycols and in their aqueous mixtures (1 page). Ordering information is available on any current masthead page.

References and Notes

(1) Present address: Central Electro-Chemical Research Institute, Karaikudi 623006, Tamil Nadu, India.
(2) H. Schneider, "Solute-Solvent Interactions", J. F. Coetzee and C. D. Ritche, Ed., Marcel Dekker, New York, N.Y., 1969, p 30; R. G. Bates, *ibid.*, p 45.
(3) R. L. Kay, G. P. Cunningham, and D. F. Evans, "Hydrogen-Bonded Solvent System", A. K. Covington and P. Jones, Ed., Taylor and Francis, London, 1968, p 249; R. G. Bates, *ibid.*, p 49.
(4) F. J. Millero, "Water and Aqueous Solutions", R. A. Horne, Ed., Wiley, New York, N.Y., 1972, p 519.
(5) R. E. Gibson and J. F. Kincaid, *J. Am. Chem. Soc.*, **59**, 579 (1937).
(6) S. D. Hamann and S. C. Lim, *Aust. J. Chem.*, **7**, 329 (1954).
(7) R. W. Gurney, "Ionic Processes in Solution", McGraw-Hill, New York, N.Y., 1953, p 193.
(8) R. M. Gopal and R. K. Srivastaba, *J. Phys. Chem.*, **66**, 2704 (1962); *J. Ind. Chem. Soc.*, **40**, 99 (1963).
(9) R. M. Gopal and M. A. Siddique, *J. Phys. Chem.*, **73**, 3390 (1969).
(10) F. J. Millero, *J. Phys. Chem.*, **72**, 3209 (1968).
(11) F. C. Schmidt, W. E. Hoffman, and W. B. Schaap, *Proc. Indiana Acad. Sci.*, **72**, 127 (1962).
(12) V. N. Fesenko, E. F. Ivanova, and G. P. Kottyarova, *Russ. J. Phys. Chem.*, **42**, 416 (1968).
(13) J. Padova in ref 4, p 129.
(14) F. Kawaizumi and R. Zana, *J. Phys. Chem.*, **78**, 627 (1974).
(15) F. Kawaizumi and R. Zana, *J. Phys. Chem.*, **78**, 1099 (1974).
(16) U. Sen, *J. Phys. Chem.*, submitted for publication.
(17) F. J. Millero, *Chem. Rev.*, **71**, 147 (1971).
(18) O. Redlich and D. M. Meyer, *Chem. Rev.*, **64**, 221 (1964).
(19) N. M. Baron, *Tr. Leningr. Tekhnol. Inst. im. Lensoveta*, **37**, 10 (1957); *Chem. Abstr.*, **53**, 2751*a* (1959).
(20) R. L. Bateman, *J. Am. Chem. Soc.*, **71**, 2291 (1949); **74**, 5516 (1952).
(21) J. Padova, *J. Chem. Phys.*, **39**, 2599 (1963).
(22) S. Devi and P. B. Das, *J. Ind. Chem. Soc.*, **42**, 501 (1965).
(23) H. Mohapatra and P. B. Das, *J. Ind. Chem. Soc.*, **44**, 573 (1967).
(24) N. C. Das, H. Mohapatra, and P. B. Das, *J. Ind. Chem. Soc.*, **43**, 373 (1966).
(25) I. Lee and J. B. Hyne, *Can. J. Chem.*, **46**, 2333 (1968).
(26) D. D. Macdonald and J. B. Hyne, *Can. J. Chem.*, **48**, 2416 (1970).
(27) U. Sen, K. K. Kundu, and M. N. Das, *J. Phys. Chem.*, **71**, 3665 (1967).
(28) U. Sen, *J. Chem. Soc., Faraday Trans. 1*, **69**, 2006 (1973).
(29) H. S. Harned and B. B. Owen, "The Physical Chemistry of Electrolytic Solutions", 3d ed, Reinhold, New York, N.Y., 1958.
(30) G. O. Crume and F. Johnstone, "Glycols", Reinhold, New York, N.Y., 1952.
(31) D. O. Masson, *Phil Mag.* (7), **8**, 218 (1929).
(32) U. Sen, *J. Chem. Eng. Data*, 20, 151 (1975).
(33) J. Bernal and R. Fowler, *J. Chem. Phys.*, **1**, 515 (1933).
(34) R. H. Stokes and R. A. Robinson, *J. Am. Chem. Soc.*, **70**, 1870 (1948).
(35) M. H. Panckhurst, *Rev. Pure Appl. Chem.*, **19**, 45 (1969).
(36) P. Mukerjee, *J. Phys. Chem.*, **65**, 740 (1961).
(37) J. E. Desnoyers and C. Jolicoeur, "Modern Aspects of Electro-Chemistry", Vol. 5, B. E. Conway and J. O'M. Bockris, Ed., Butterworth, London, 1969, Chapter 1.
(38) H. Strehlow and H. Schneider, *J. Pure Appl. Chem.*, **25**, 327 (1971).
(39) J. Padova, in ref 37, Vol. 7, 1971, Chapter 1.
(40) F. Franks and D. J. G. Ives, *Quart. Rev., Chem. Soc.*, **20**, 1 (1966).
(41) J. H. Stern and J. Nobilione, *J. Phys. Chem.*, **72**, 3937 (1968).
(42) K. Crickard and J. F. Skinner, *J. Phys. Chem.*, **73**, 2060 (1969).
(43) A. Z. Golik, A. V. Oritschenko, and O. G. Artenchenko, *Dopov. Akad. Nauk. Ukr. RSR*, 457 (1954).
(44) O. Ya. Samoilov, *Discuss. Faraday Soc.*, **24**, 141 (1957).
(45) J. L. Kavanau, "Water and Solute-Water Interactions", Holden-Day, San Francisco, Calif., 1964.
(46) A. Roy and G. Nemethy, *J. Chem. Eng. Data*, **18**, 309 (1973).
(47) S. N. Timashoff and H. Inone, *Biochemistry*, **7**, 2501 (1966).
(48) K. Nakanishi, *Bull. Chem. Soc. Jpn.*, **33**, 793 (1960).
(49) K. Nakanishi, N. Kato, and M. Murayama, *J. Phys. Chem.*, **71**, 814 (1967).
(50) H. S. Frank and A. L. Robinson, *J. Chem. Phys.*, **8**, 953 (1940).
(51) H. S. Frank, *J. Phys. Chem.*, **67**, 1554 (1963).
(52) H. S. Frank, *Z. Phys. Chem. (Leipzig)*, **228**, 364 (1965).

Osmotic Effects Near the Critical Point

Peter G. Wolynes*

Department of Chemistry, Harvard University, Cambridge, Massachusetts 02138 *(Received March 3, 1976)*

Publication costs assisted by Harvard University

Near the critical mixing point of binary solutions, anomalous osmotic effects can occur. These effects involve the interaction of the microscopic structure of the mixture near a wall and the nonlinear coupling of the composition and momentum of the fluid. The Onsager principle relating the osmotic and inverse osmotic effects is verified. Diffusion through a capillary, which has a contribution from the same causes as the osmotic effects, is shown to provide a particularly simple example of mode–mode coupling theory.

I. Introduction

Hydrodynamic quantities which by symmetry are uncoupled in a bulk fluid may be coupled together in the presence of a boundary. In a fluid in which there are no pressure gradients, concentration gradients cannot linearly couple with the momentum.[1] Near a wall, however, concentration gradients can force fluid motion. This phenomenon in dilute gas mixtures is referred to as diffusion slip (or creep).[2] It is an effect which becomes noticeable when the characteristic dimension of the fluid flow becomes comparable to a mean free path. This phenomenon in solutions is very familiar as osmosis.[3] If two solutions of different composition are connected by a thin capillary or porous plate, fluid will flow between them until the osmotic pressures are equalized.

An inverse coupling exists. If a dilute gas mixture is bled through a small opening demixing results. The composition of a fluid forced through a porous plate changes. This is inverse osmosis.

In measurements of viscosity near the critical point of binary mixtures by the capillary method, hysteresis has been observed.[4] Also Leister and co-workers have noted separation of the mixture when forced through a capillary near the critical point.[5]

In this paper we discuss a simple theory of osmotic effects near the critical consolute point of binary mixtures. This theory is analogous to the theory of electroosmosis of dilute electrolyte solutions.[3] Its essential features involve the microscopic structure of the solution near the capillary walls and the nonlinear couplings of the momentum and concentration which are thought to give rise to the anomalous behavior of the viscosity and diffusion constant near the critical point. This theory does not seem to be sufficient to explain the observation of Leister et al., but is of at least pedagogic value. We examine explicitly the Onsager relation of the osmotic and inverse osmotic effect and will see how a relation between the nonlinear coupling coefficients and the equilibrium properties of the system is implied by the Onsager symmetry. This relation is exactly that predicted from microscopic theories of the nonlinear coupling coefficients. Also diffusion through a capillary (or porous plate) is considered and will be seen to be a particularly simple manifestation of mode–mode coupling theory.

* Present address: Department of Chemistry, Massachusetts Institute of Technology, Cambridge, Mass. 02139.

II. Theory

To simplify the calculations we consider the following geometry (Figure 1). Two very large vessels are connected by a rectangular capillary of large length l. The capillary has a width w which is much larger than its depth d. In the following we will consider the case where d is larger than the correlation length $\xi = \kappa^{-1}$.

We assume that one component is preferentially adsorbed on the glass walls of the capillary. Let us define the concentration variable $c(\mathbf{X})$ as the difference in concentration of one of the components from its average value in the bulk medium. The concentration at the wall is determined by the difference in the standard chemical potential of the substance adsorbed on the wall and the standard chemical potential in the bulk medium. Since the standard chemical potential in the bulk medium is nonsingular at the critical point we take $c(\mathbf{X})$ at the wall to be a constant $c_0 \neq 0$.

Theories of inhomogeneous systems near the critical point, such as the van der Waals theory of surface tension,[6] indicate that $c(\mathbf{X})$ satisfies the Ornstein–Zernike equation:

$$\nabla^2 c = \kappa^2 c \tag{1}$$

Since we are neglecting end effects the concentration profile satisfies the equation

$$d^2c/dz^2 = \kappa^2 c \tag{2}$$

with the boundary conditions $c(0) = c(d) = c_0$ the concentration profile is therefore

$$c(z) = c_0 \frac{\cosh \kappa(z - d/2)}{\cosh \kappa d/2} \tag{3}$$

If fluid is forced through the capillary this concentration profile will be convected along. The material emerging from the capillary will be of a different composition than the bulk medium. This is an inverse osmotic effect. A pressure gradient along the capillary will induce fluid motion. At steady state the velocity will satisfy the steady Navier–Stokes equation for an incompressible fluid.

$$\eta \nabla^2 \mathbf{v} = \frac{\Delta p}{l} \hat{x} \tag{4a}$$

$$\nabla \cdot \mathbf{v} = 0 \tag{4b}$$

Assuming stick boundary conditions on the capillary walls $v(0) = v(d) = 0$ the velocity profile[7] is

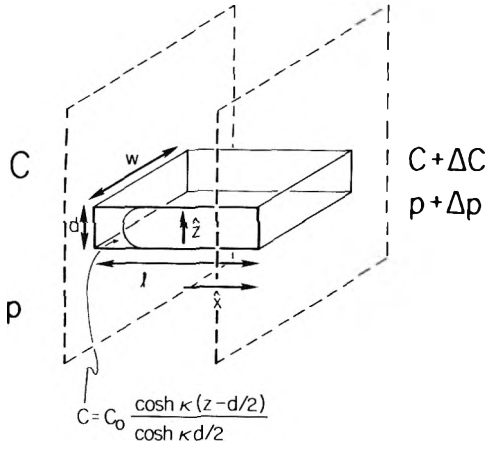

Figure 1. Diagram of hypothetical capillary for measuring osmotic effects.

$$v(z) = \frac{\Delta p}{l}\frac{1}{2\eta}\left[\left(z-\frac{d}{2}\right)^2 - \frac{d^2}{4}\right] \tag{5}$$

The total flow through the capillary is the integral of this velocity over the cross section of the capillary

$$I = \int v \, d\Omega = \frac{wd^3}{12\eta}\frac{\Delta p}{l} \tag{6}$$

This is Poiseuille's formula for flow through a rectangular capillary.

The concentration current j is the product of the velocity and the concentration C. The concentration flux through the capillary is

$$J = \int cv \, d\Omega = w \int_0^d dz \times c_0 \frac{\cosh \kappa(z-d/2)}{\cosh \kappa d2}\frac{\Delta p}{l}\frac{1}{2\eta}\left[\left(z-\frac{d}{2}\right)^2 - \frac{d^2}{4}\right] \tag{7}$$

If d is much greater than the correlation length the concentration profile decays exponentially away from the wall at $z = 0$ and we can replace c and v by the approximate form

$$c = c_0 e^{-\kappa z} \tag{8a}$$

$$v(z) = -\frac{zd}{2\eta}\frac{\Delta p}{l} \tag{8b}$$

for z near 0 and analogous formulae when $z \simeq d$. Thus J is approximately

$$J = 2w \int_0^\infty dz \, c_0 e^{-\kappa z}\left(-\frac{zd}{2\eta}\frac{\Delta p}{l}\right) = -wdc_0\frac{\kappa^{-2}}{\eta}\frac{\Delta p}{l} \equiv \Lambda_{cv}\frac{\Delta p}{l} \tag{9}$$

This concentration current diverges quite strongly near the critical point. However, we should recall that the derivation only holds when d is greater than a correlation length. When d is less than a correlation length the concentration current should level off to a constant value. The change in concentration of the emerging fluid is

$$\delta c = \frac{J}{I} = 12c_0(\kappa d)^{-2} \tag{10}$$

Thus demixing can become quite large when the diameter of the capillary is comparable to the correlation length. Since this inverse osmotic effect exists, nonequilibrium thermodynamics requires that a concentration gradient along the capillary must cause the fluid to flow. This osmotic effect is due to a nonlinear concentration dependent stress tensor for the fluid. While symmetry requires that the velocity cannot linearly couple to the concentration it is possible to have nonlinear stresses proportional to the products of the concentration gradients:

$$\sigma = \alpha(\nabla c)(\nabla c) \tag{11}$$

This type of stress tensor was first introduced by Korteweg in his theory of hydrodynamic capillary phenomena.[8] It is also used in mode–mode coupling theories of the anomalies in transport coefficients of critical mixtures.[9,10] Because of the concentration profile in the capillary, a concentration gradient along the capillary can force the fluid motion by this nonlinear stress. The Navier–Stokes equations with this nonlinear stress are:

$$\eta\nabla^2\mathbf{v} = -\nabla p - \alpha(\nabla^2 c)\nabla c \tag{12a}$$

$$\nabla \cdot \mathbf{v} = 0 \tag{12b}$$

Considering the case without a pressure gradient the flow is described by the equation

$$\eta\frac{d^2v}{dz^2} = -\alpha\left(\frac{d^2c}{dz^2}\right)\frac{\Delta c}{l} \tag{13}$$

where $\Delta c/l$ is the concentration gradient along the capillary. Imposing stick boundary conditions on the walls of the capillary the velocity profile is

$$v = -\frac{\alpha}{\eta}\frac{\Delta c}{l}[c(z) - c_0] \tag{14}$$

Using the concentration profile (3), we find that the total fluid flux due to the concentration gradient is

$$I = \int v \, d\Omega = \frac{\alpha}{\eta}c_0 wd\left(1 - \frac{2}{\kappa d}\tanh\frac{\kappa d}{2}\right)\frac{\Delta c}{l} \tag{15}$$

When the capillary diameter is greater than the correlation length, this is

$$I = \frac{\alpha}{\eta}c_0 wd\left(\frac{\Delta c}{l}\right) \tag{16}$$

It is useful to rewrite this expression in terms of the thermodynamic force, the chemical potential gradient:

$$I = \frac{\alpha}{\eta}c_0 wd\left(\frac{\partial c}{\partial \mu}\right)\frac{\Delta \mu}{l} \equiv \Lambda_{vc}\frac{\Delta \mu}{l} \tag{17}$$

The Onsager reciprocal principle then requires the equality coefficients in eq 9 and eq 17:[3]

$$\Lambda_{cv} = \Lambda_{vc} \tag{18}$$

This is true only if the nonlinear stress tensor coefficient α satisfies the relation:

$$\kappa^{-2} = \alpha\left(\frac{\partial c}{\partial \mu}\right) \tag{19}$$

This relation is in fact satisfied. Kawasaki has shown by microscopic calculations that α is related to the k dependent susceptibility χ_k:[10]

$$\alpha = k_B T\frac{\partial \chi_k^{-1}}{\partial (k^2)^h}\bigg|_{k=0} \tag{20}$$

We also know that $k_B T\chi_{k=0}^{-1}$ is the thermodynamic derivative $\partial\mu/\partial C$. Thus

$$\alpha = \frac{\partial \mu}{\partial c}\frac{\partial}{\partial (k^2)}\left(\frac{\chi_0}{\chi_k}\right)\bigg|_{k=0} \tag{21}$$

If the spatial correlations are of Ornstein–Zeinike form, as we have assumed in the derivation of the transport coefficients, χ_k is proportional to $(k^2 + k^2)^{-1}$. Thus we have

$$\alpha = \frac{\partial \mu}{\partial c} k^{-2} \tag{22}$$

which is the same as eq 19. Thus we see that the Onsager relation is satisfied in a fairly nontrivial manner.

If there is a concentration gradient along the capillary a concentration flux will be established. One contribution to the flux will be due to diffusion. The diffusive flux will be

$$J_D = Dwd \frac{\Delta c}{l} \tag{23}$$

The diffusion constant vanishes at the critical point. Mode–mode coupling theory indicates that it vanishes much more slowly than the conventional theory of critical slowing down would indicate and gives the relation[10]

$$D = \frac{k_B T}{6\pi\eta} \kappa \tag{24}$$

In addition to the diffusive flux there is a convective contribution. As we have seen, a concentration gradient interacting with the concentration profile of the capillary can force fluid motion. The moving fluid can then convect the concentration profile, leading to a net transport of concentration. This process is directly analogous to the mode–mode coupling process which leads to the breakdown of the conventional theory of the vanishing near the critical point of diffusion constant. In the bulk fluid, an imposed concentration gradient interacts with a concentration fluctuations to give rise to fluid motion through the nonlinear stress tensor. The resulting fluid flow transports the concentration fluctuation and causes the net concentration flux to be larger than in the absence of these nonlinear processes. In the transport through a capillary the concentration profile plays the same role as the concentration fluctuation does in the case of diffusion in the bulk fluid.

To find the convective flux we use eq 3 for the concentration profile and eq 14 for the velocity profile due to a concentration gradient:

$$J_c = \int cv \, dl = w \int_{-d/2}^{d/2} dz - \frac{\alpha}{\eta} c_0^2 \frac{\Delta c}{l} \frac{\{\cosh^2 \kappa z - \cosh \kappa z\}}{\cosh^2 \kappa d/2}$$

$$= -w \frac{\alpha}{\eta} c_0^2 \frac{1}{\cosh^2 \kappa d/2} \left\{ \frac{d}{2} + \frac{1}{2\kappa} \sinh \kappa d - \frac{2}{\kappa} \sinh \frac{\kappa d}{2} \right\} \frac{\Delta c}{l} \tag{25}$$

When d is much greater than the correlation length this becomes

$$J_c = +w \frac{\alpha}{\eta} c_0^2 \kappa^{-1} \frac{\Delta c}{l} \tag{26}$$

This "surface" contribution to the flux through the capillary diverges near the critical point.

When d is much less than the correlation length the convective contribution to the flux vanishes:

$$J_c \simeq +wd \frac{\alpha}{\eta} c_0^2 \frac{1}{24} (\kappa d)^2 \frac{\Delta c}{l} \tag{27}$$

The total flux through the capillary is the sum of the diffusive flux and the convective flux. It is clear that when d is much less than ξ the diffusive contribution will not be correctly given by eq 23 with the diffusion constant from eq 24. The diffusion constant will be in error both because the markedly noncritical composition throughout the capillary and because the mode–mode coupling processes in such a small capillary will be different from those in a bulk fluid because the fluctuations must satisfy boundary conditions on the capillary walls. For these reasons we cannot trust our derivation for the total concentration flux through a capillary when it is smaller than a correlation length.

When d is greater than ξ the convective contribution is only a "surface" term but it can be comparable to the diffusive flux:

$$\frac{J_c}{J_0} = 6\pi \frac{\alpha c_0^2}{h_B T} \frac{\xi^2}{d} \tag{28}$$

To estimate this ratio we use eq 22 for α and use the Ornstein–Zernike relation between the correlation length ξ and the short-range correlation length l_0 which is of the order of an intermolecular distance:[9]

$$\xi = l_0 \sqrt{c_c h_B T / (\partial \mu / \partial c)} \tag{29}$$

where c_c is the critical concentration in particles per unit volume. If c_0 is of the order of c_c which is of the order of one particle per l_0^3 we obtain

$$J_c / J_D \sim \xi^2 / l_0 d \tag{30}$$

Thus the ratio of convective to diffusive flow depends on the ratio of the correlation length to the geometric mean of the capillary diameter and the short-range correlation length. This ratio can be large even when d is larger than ξ.

The osmotic effects discussed in this paper do not explain the demixing phenomena observed by Leister et al. In their experiments the capillary diameter is about .2 mm and in their measurements closest to the critical point the correlation length is about 10^{-4} mm. Equation 10 indicates that the change in concentration of the fluid is only about a ten thousandth of a percent. This is too small to explain the observed demixing. Leister notes that the demixing is a nonlinear effect, increasing with the rate of fluid flow.[5] This is of course not indicated by the linear theory considered here, but extensions of the basic effects, which we have studied, to include nonlinear phenomena and treating the critical fluctuations may perhaps lead to a better explanation of the experimental observations.

We should note also that the linear effects considered here are quite observable. Order of magnitude calculations indicate that osmosis through porous media, such as millipore filters, can be quite considerable and that the convective contribution to concentration flow can be comparable to that due to diffusion.

Acknowledgment. I thank Professors J. M. Deutch and Roy G. Gordon for support.

References and Notes

(1) R. H. Trimble and J. M. Deutch, *J. Stat. Phys.*, **3**, 149 (1971).
(2) H. A. Kramers and J. Kistemaker, *Physica*, **10**, 699 (1943).
(3) S. R. de Groot and P. Mazur, "Non-equilibrium Thermodynamics", North Holland Publishing Co., Amsterdam, 1962.
(4) J. V. Sengers in "Proceedings of the International Summer School of Physics Enrico Fermi", Varenna, Italy, 1970, M. S. Green, Ed., Academic Press, New York, N.Y., 1971; J. Brunet and K. E. Gubbins, *Trans. Faraday Soc.*, **65**, 1255 (1969).
(5) H. M. Leister, J. C. Allegra, and G. F. Allen, *J. Chem. Phys.*, **51**, 3701 (1969).
(6) B. Widom in "Phase Transitions and Critical Phenomena", Vol. 2, C. Domb and M. S. Green, Ed., Academic Press, New York, N.Y., 1972.
(7) L. D. Landau and I. M. Lifshitz, "Fluid Mechanics", Addison Wesley, Reading, Mass., 1959.
(8) C. Truesdell and W. Noll, "Handbuch der Physik", Vol. III/3, S. Flugge, Ed., Springer-Verlag, Berlin, 1965, p 513; D. J. Korteweg, *Arch. Neerl. Sci. Exactes Nat., Ser. 2*, **6**, 1 (1901).
(9) M. Fixman, *J. Chem. Phys.*, **47**, 2808 (1967).
(10) K. Kawasaki, *Ann. Phys. (N.Y.)*, **61**, 1 (1970).

Adsorption Kinetics during the Flow of a Constant Electric Current through a Nitrobenzene/Water Interface

P. Joos* and M. Van Bockstaele

Department of Cell Biology, Universitaire Instelling Antwerpen, Wilrijk, Belgium *(Received November 21, 1975)*

The interface between a water and a nitrobenzene phase is considered. In both phases some surface active electrolyte, cetyltrimethylammonium bromide, is dissolved and both phases are in equilibrium. When a constant electric current flows through that interface the interfacial tension changes. This variation in interfacial tension is explained by a difference in transport numbers of the cation in both phases. A mathematical analysis is given. For depletion experiments good agreement between experiments and theory is observed; for accumulation experiments good agreement occurs only for high concentrations or for short times.

Introduction

When an electric potential difference is applied across a liquid–liquid interface, the concentration of ions at that interface may change. This change of interfacial composition, hence of interfacial tension, may be due to two entirely different mechanisms; this problem is discussed in detail by Blank and Feigl.[1] One of these mechanisms, known as electrocapillarity, is a pure thermodynamic phenomenon. For the other mechanism, which is considered here, the cations and anions are not confined to one bulk phase, but they can freely move across the interface, which is therefore said to be nonpolarizable. In this case changes in interfacial composition are due to a difference in transport number of the cations (or the anions) in both phases. We considered the following system: two liquid phases are brought in contact with each other, water and a polar oil such as nitrobenzene. In both phases a surface active electrolyte is dissolved, e.g., cetyltrimethylammonium bromide (CTAB), and the system is in thermodynamic equilibrium. Two electrodes one in each phase, are mounted parallel to the interface in such a way as to extend over its whole area. A potential difference is applied causing a current, I, to flow through the interface. The flux of cations migrating from the aqueous solution to the interface is $In_1^+/F\Omega$ (n_1^+ is the transport number of the cation in the aqueous phase, F the Faraday number, Ω, the area of the interface). At the same time the flux of cations transported from the interface to the nitrobenzene phase is $In_2^+/F\Omega$ (n_2^+ is the transport number of the cation in nitrobenzene). Hence the net change of cations at the interface is $I(n_1^+ - n_2^+)/F\Omega$. Depending on the direction of the current cations are accumulated or depleted at the interface. Similarly the amount of anions accumulated or depleted at the interface is $-I(n_1^- - n_2^-)/F\Omega$ (n_1^- and n_2^- are the transport numbers of the anion in water and nitrobenzene, respectively). Since the sum of the transport numbers in each phase equals one ($n_1^- + n_1^- = 1; n_2^+ + n_2^- = 1$) it is seen that the same amount of anions and cations accumulate at the interface, hence the interface remains electrically neutral.

At the beginning of this century concentration changes due to interfacial electrical transference were studied by Nernst and Riesenfeld[2] using common salts such as KCl in a phenol/water system. These experiments were repeated by Guastalla[3] and Blank[4] with surface active electrolytes. These authors[5–7] also studied the effect obtained with a second common salt added to the system. The situation with a supporting electrolyte will, however, not be considered here, because the supporting electrolyte is confined to one phase only and a quantitative treatment is more complicated.

Theory

As outlined above, the passage of an electric current causes CTAB to be accumulated or depleted at the nitrobenzene/water interface. This interface remains electrically neutral. We will assume that the current, I, through the interface is constant. The transport by electric migration is partly balanced by diffusion, to or from the interface depending on the direction of the current. The diffusion process is ruled by the ordinary diffusion equations, since the interface and the bulk phases are electrically neutral it is not the diffusion of each ion (electrodiffusion) which must be taken into account, but the diffusion of the electrolyte as a whole. This fact is particularly well discussed in Newman's book.[8] The diffusion equations are:

for phase 1 ($z < 0$)

$$\frac{\partial C_1}{\partial t} = D_1 \frac{\partial^2 C_1}{\partial z^2} \tag{1}$$

for phase 2 ($z > 0$)

$$\frac{\partial C_2}{\partial t} = D_2 \frac{\partial^2 C_2}{\partial z^2}$$

The z coordinate has its origin in the interface and points from the water phase (subscripts 1) to the nitrobenzene phase (subscript 2). The above diffusion equations must be integrated taking into account the appropriate boundary and initial conditions. These boundary conditions can be found assuming local equilibrium between the two subsurfaces and the interface, and the conservation of mass at the interface.[9] The condition of thermodynamical equilibrium in the subsurfaces is expressed by

$$KC_1(0, t) = C_2(0, t) \tag{2}$$

K being the distribution coefficient. The distribution coefficient of CTAB between water and nitrobenzene was experimentally determined by Blank[5] and equals 1.6.

The second boundary condition deals with the conservation of mass at the interface. The amount of surface active electrolyte transported by migration from or to the interface is $I\Delta n/F\Omega$ ($\Delta n = n_1^+ - n_2^+$). Part of this amount is used to change the adsorption $d\Gamma/dt$ and the remaining part is transported by diffusion, whence

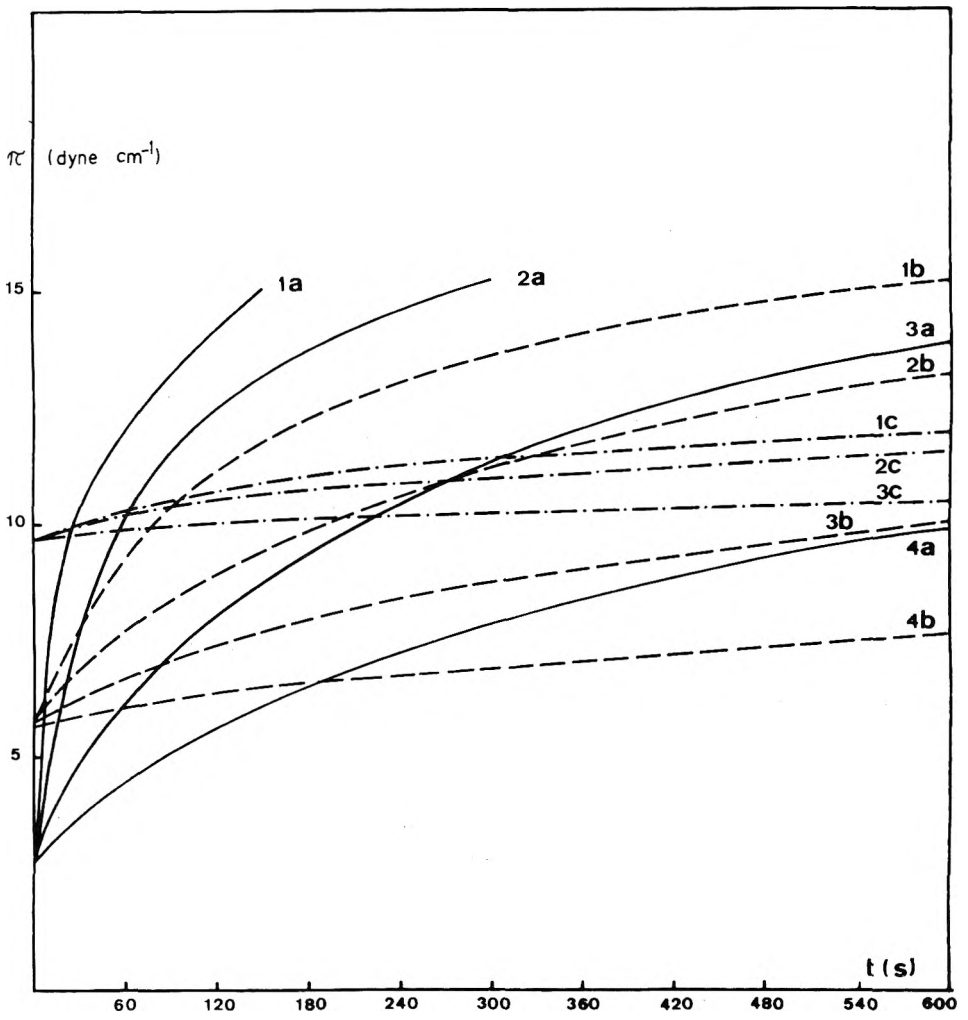

Figure 1. Ion accumulation experiments. Increase of interfacial pressure, π, as a function of time t (in seconds) for constant currents flowing through the interface. Solid line (a): concentration of CTAB in water 3×10^{-8} mol cm^{-3}; (1a) 300 μA; (2a) 200 μA; (3a) 100 μA; (4a) 50 μA. Broken line (b): concentration of CTAB in water 10^{-7} mol cm^{-3}; (1b) 300 μA; (2b) 200 μA; (3b) 100 μA; (4b) 50 μA. Dotted line (C): concentration of CTAB in water 3×10^{-7} mol cm^{-3}; (1c) 300 μA; (2c) 200 μA; (3b) 100 μA; (4c) 50 μA.

$$\frac{I\Delta n}{F\Omega} = \frac{d\Gamma}{dt} + D_1\left(\frac{\partial C_1}{\partial z}\right)_0 - D_2\left(\frac{\partial C_2}{\partial z}\right)_0 \tag{3}$$

This equation without the source or sink term $I\Delta n/F\Omega$ is discussed by Levich[10] who also considered interfacial diffusion and convection. These terms are omitted here because the interface remains uniform. Equation 3 without the term $d\Gamma/dt$ was already used by Nernst and Riesenfeld.[2] In the cases studied by Nernst and Riesenfeld neglection of the term $d\Gamma/dt$ is certainly justified since they studied common inorganic electrolytes which are not surface active. The two remaining boundary conditions state that far away from the interface the concentrations do not change

$$\begin{aligned} C_1 &= C_1^0 \quad z \to -\infty \\ C_2 &= C_2^0 \quad z \to +\infty \end{aligned} \tag{4}$$

The initial conditions are at $t = 0$

$$\begin{aligned} C_1 &= C_1^0 \quad z < 0 \\ C_2 &= C_2^0 \quad z > 0 \\ \Gamma &= \Gamma_0;\ KC_1^0 = C_2^0 \quad z = 0 \end{aligned} \tag{5}$$

The last condition in eq 5 follows from the fact that initially both phases are in equilibrium. With the above boundary and initial conditions the diffusion equations are integrated. As pointed out by Hansen[11] such a problem can conveniently be solved by the Laplace transform method. The result is (see Appendix)

$$\Gamma = \Gamma_0 + \frac{I\Delta n}{F\Omega}t + \frac{2[\sqrt{D_1} + K\sqrt{D_2}]}{\sqrt{\pi}} \times \left| C_1^0\sqrt{t} - \int_0^{\sqrt{t}} C_1(0, t-\zeta)\, d\sqrt{\zeta} \right| \tag{6}$$

where ζ is an auxiliary variable.

This result bears some similarity with that of Ward and Tordai,[12] who studied simple diffusion controlled adsorption kinetics. In fact we made the same assumption of Ward and Tordai: no adsorption barrier. We will denote

$$\mathcal{J}(t) = C_1^0\sqrt{t} - \int_0^{\sqrt{t}} C_1(0, t-\zeta)\, d\sqrt{\zeta} \tag{7}$$

The convolution integral may be evaluated graphically and in this paper the method of Lange[13] will be followed. By introducing numerical values of Δn and $(\sqrt{D_1} + K\sqrt{D_2})$ in eq 6 it turns out that $\Gamma - \Gamma_0$ can be neglected, whence

$$\mathcal{J}(t) = -\frac{\sqrt{\pi}}{2F\Omega}\frac{\Delta nI}{[\sqrt{D_1} + K\sqrt{D_2}]}t \tag{8}$$

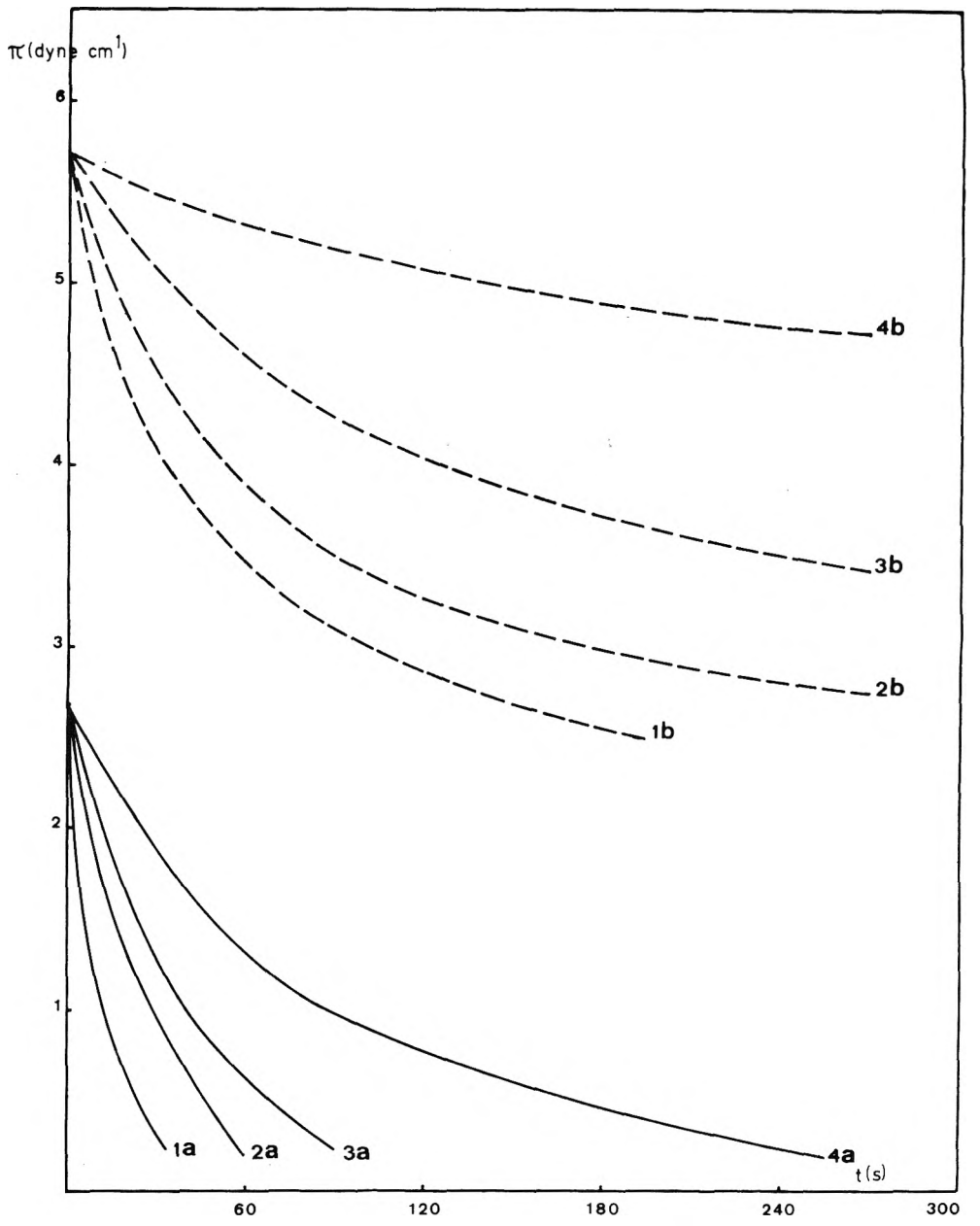

Figure 2. Ion depletion experiments. Decrease of interfacial pressure, π, as a function of time t (in seconds) for constant current flowing through the interface. Full line (a): concentration of CTAB in water 3×10^{-8} mol cm^{-3}; (1a) 300 μA; (2a) 200 μA; (3a) 100 μA; (4a) 50 μA. Broken line (b): concentration of CTAB in water 10^{-7} mol cm^{-3}; (1b) 300 μA; (2b) 200 μA; (3b) 100 μA; (4b) 50 μA.

From this expression it follows that the plot of $\mathcal{F}(t)$ as a function of time should yield a straight line and from its slope $\Delta n/[\sqrt{D_1} + K\sqrt{D_2}]$ is obtained. In eq 8 the term $\Gamma - \Gamma_0$ is neglected, hence one should expect that an equivalent expression should be obtained by assessing $d\Gamma/dt = 0$ in eq 3. Integration with the same boundary and initial conditions yields Sand's equation[14]

$$C_1^s = C_1^0 + \frac{I\Delta n}{F\Omega[\sqrt{D_1} + K\sqrt{D_2}]}\sqrt{t} \qquad (9)$$

However we have some doubt about the application of this equation to our system because small changes in adsorption correspond with rather important changes in the subsurface concentration C_1^s. Therefore we prefer the rather tedious graphical integration for calculating C_1^s.

Experimental Section

The materials used in this investigation were nitrobenzene (grade puriss) obtained from U.C.B. and a pure CTAB purchased from Baker. Clean glassware and double distilled water was used throughout. The interfacial tension between pure nitrobenzene and water was 24.4 dyn cm^{-1}. Interfacial tensions were measured by the Wilhelmy plate method using a Cahn electrobalance. The Wilhelmy plate was siliconized. The measuring cell was similar to that described by Blank.[4] The area of the interface was 42 cm^2. The potential difference between the electrodes was obtained by means of a constant current source. Generally the following intensities were used: 300, 200, 100, and 50 μA. The output of the balance was connected to a recorder enabling us to follow the variations of interfacial tension with time.

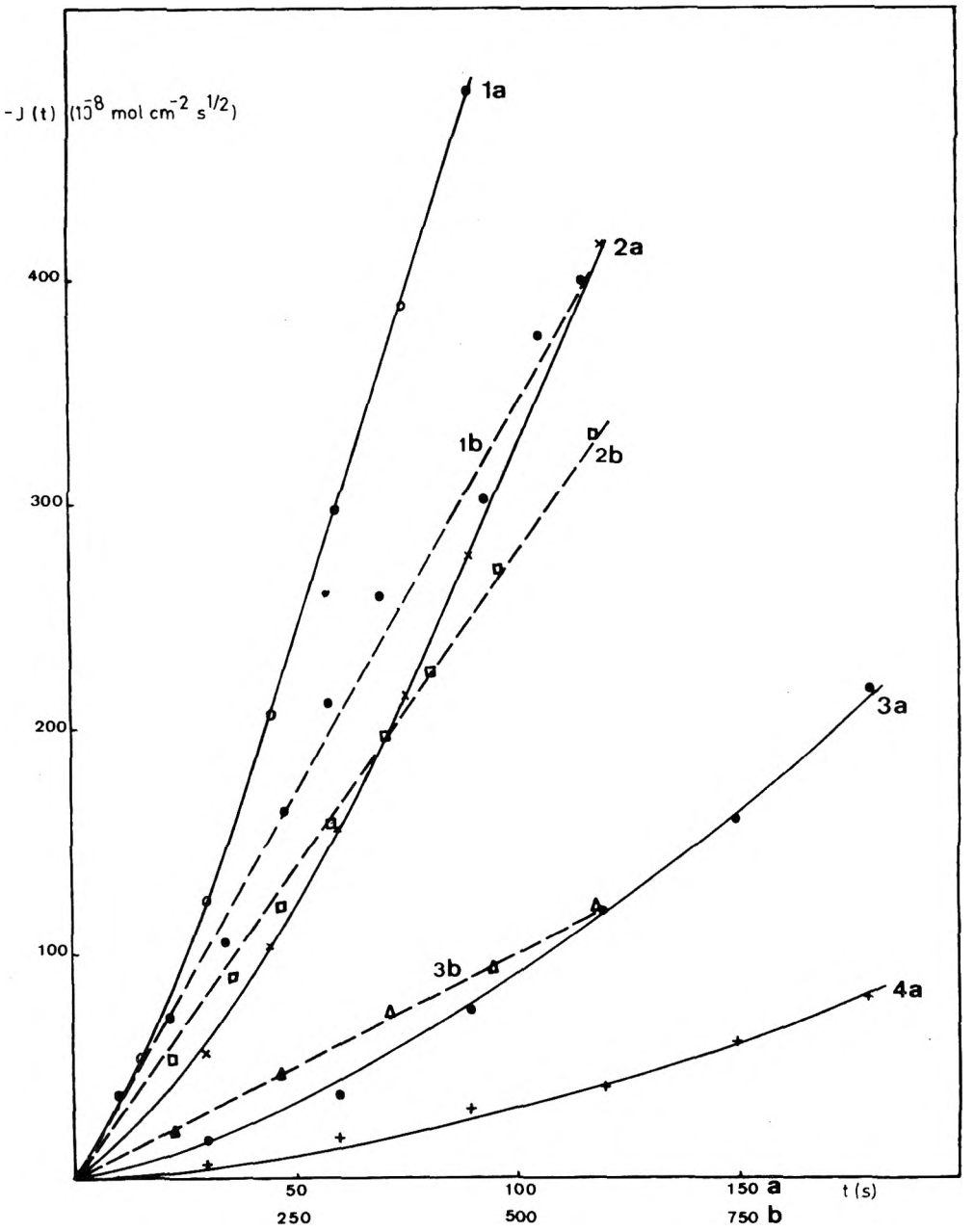

Figure 3. The function J(*t*) as defined in text for accumulation experiments. Full line (a): concentration of CTAB in water 3×10^{-8} mol cm^{-3}; (1a) 300 μA; (2a) 200 μA; (3a) 100 μA; (4a) 50 μA. Broken line (b): concentration of CTAB in water 3×10^{-7} mol cm^{-3}; (1b) 300 μA; (2b) 200 μA; (3b) 100 μA; (4b) 50 μA.

Results

The interfacial pressure, π, i.e., the lowering of the interfacial tension as a function of the CTAB concentration in water, was measured. As argued before the concentration in nitrobenzene was 1.6 times higher. Since no indifferent electrolyte was added the Gibbs equation reads:

$$\Gamma = \frac{1}{2RT} \frac{d\pi}{d \ln C_1} \tag{10}$$

The experimental $\pi - C$ curve could be fitted by the von Szyszkowski equation[15]

$$\pi = 2RT\Gamma^{\infty} \ln \left(1 + \frac{C_1}{a}\right) \tag{11}$$

where Γ^{∞} is the saturation adsorption ($\Gamma^{\infty} = 8.7 \times 10^{-11}$ mol cm^{-2}) and a is the Langmuir constant ($a = 3.5 \times 10^{-8}$ mol cm^{-3}). The other symbols have their usual meaning.

From the von Szyszkowski equation, the Langmuir equation is obtained using the Gibbs equation

$$\Gamma = \Gamma^{\infty} \frac{C_1}{a + C_1} \tag{12}$$

Three CTAB concentrations were investigated: 3×10^{-8}, 10^{-7}, and 3×10^{-7} mol cm^{-3}. In experiments where the current flows from the nitrobenzene phase to the water phase the interfacial tension decreases and the adsorption increases (accumulation experiments), when the current flows in the inverse direction the interfacial tension increases (depletion experiments). Accumulation experiments are summarized in Figure 1, depletion experiments in Figure 2. No experiments were carried out when the interfacial pressure attains a value of about 15 dyn cm^{-1} because this pressure corresponds with

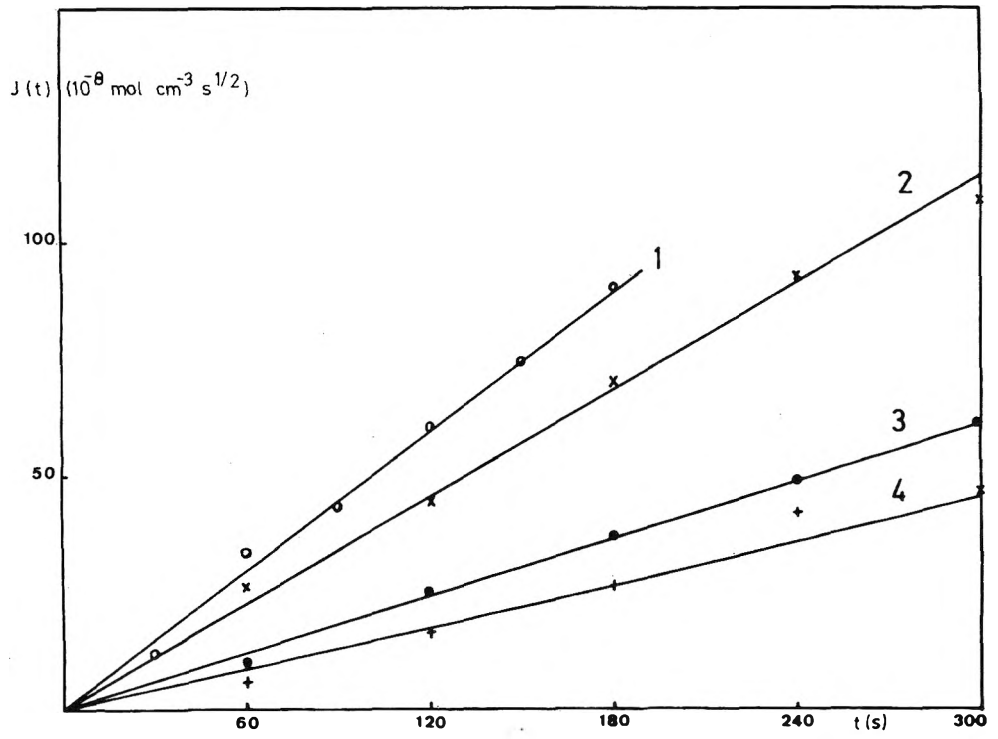

Figure 4. The function J(*t*) as defined in text for depletion experiments for a CTAB concentration in water of 10^{-7} mol cm^{-3}: (1) 300 μA; (2) 200 μA; (3) 100 μA; (4) 50 μA.

TABLE I: Values of the Parameter $\Delta n/[\sqrt{D_1} + K\sqrt{D_2}]$ and Δn Obtained from the Slopes of the J(t) Curves [a]

C_1^0, mol cm^{-3}	I, μA	$\Delta n/(\sqrt{D_1} + K\sqrt{D_2})$	Δn
3×10^{-8}	+300	0.57[b]	1.20[c]
	+200	0.33[b]	0.70[c]
	+100	0.15[b]	0.31
	+50	0.21[b]	0.44
	−300	0.06	0.13
	−200	0.07	0.14
	−100	0.12	0.25
	−50	0.15	0.32
10^{-7}	+300	0.21[b]	0.47
	+200	0.11[b]	0.25
	+100	0.09[b]	0.19
	+50	0.09[b]	0.19
	−300	0.08	0.16
	−200	0.09	0.19
	−100	0.09	0.19
	−50	0.16	0.32
3×10^{-7}	+300	0.10	0.21
	+200	0.12	0.26
	+500	0.09	0.19
		Mean Δn = 0.255	

[a] Accumulation experiments are noted by + before the current and depletion experiments by −. [b] Extrapolated from initial slope of J(t). [c] Not considered for calculating the mean value of Δn.

a subsurface concentration of about 10^{-6} mol cm^{-3} and at this concentration micel formation sets in.[16]

Discussion

Starting from the experimental $\pi - t$ curves (Figures 1 and 2) the subsurface concentration in the aqueous phase was calculated as a function of time by means of eq 11 and the adsorption using eq 12. Assuming reasonable values of D_1, D_2, and Δn it appeared that the contribution of $\Delta\Gamma$ in eq 6 could be safely neglected, hence eq 6 may be simplified to eq 8. Knowing the subsurface concentration as a function of time the back diffusion integral of Ward and Tordai can be evaluated and also the function $\mathcal{F}(t)$ as defined in eq 7. Some typical $\mathcal{F}(t) - t$ curves are given in Figures 3 and 4. It appears that, for both depletion and accumulation experiments at $C = 3 \times 10^{-7}$ mol cm^{-3}, $\mathcal{F}(t)$ is indeed a linear function of t as expected from eq 8. From these data the value of $\Delta n/[\sqrt{D_1} + K\sqrt{D_2}]$ and assuming values for D_1 (= 10^{-6} cm^2 s^{-1}), D_2 (= 5×10^{-7} cm^2 s^{-1}), and K (= 1.6) the difference in transport number of the cation in water and nitrobenzene can be estimated. Although there is some scatter, the experimental values for Δn seem quite reasonable. However, for accumulation experiments at concentrations of 3×10^{-8} and 10^{-7} mol cm^{-3} no linear relation for $\mathcal{F}(t) - t$ is obtained. At present we can offer no explanation for this deviation, but probably double layer effects become operative which are neglected in our theory. The more important the deviation becomes the higher the current and the lower the concentration. Describing his experiments with Sand's equation, Blank[4] also observed some deviations, without assessing numerical values, however. We assume our theory is correct as long as the deviations from the initial state are not too large. Therefore we calculated the parameter $\Delta n/[\sqrt{D_1} + K\sqrt{D_2}]$ from the initial slope of $\mathcal{F}(t)$ at $t \to 0$: this procedure yields more consistent results.

We have also carried out experiments with alternating current which will be published elsewhere.[17] In this case the oscillations around the equilibrium state were extremely small. These experiments yielded a value for $\Delta n = 0.25$. The mean value from our present experiments is also 0.25 (see Table I). Not too much importance should, however, be given to this agreement in view of the scatter of values for Δn. This scatter is mainly due to experimental and computing errors, since the determination of the initial slope is rather inaccurate.

Finally we plotted in Figure 5 the variation of adsorption,

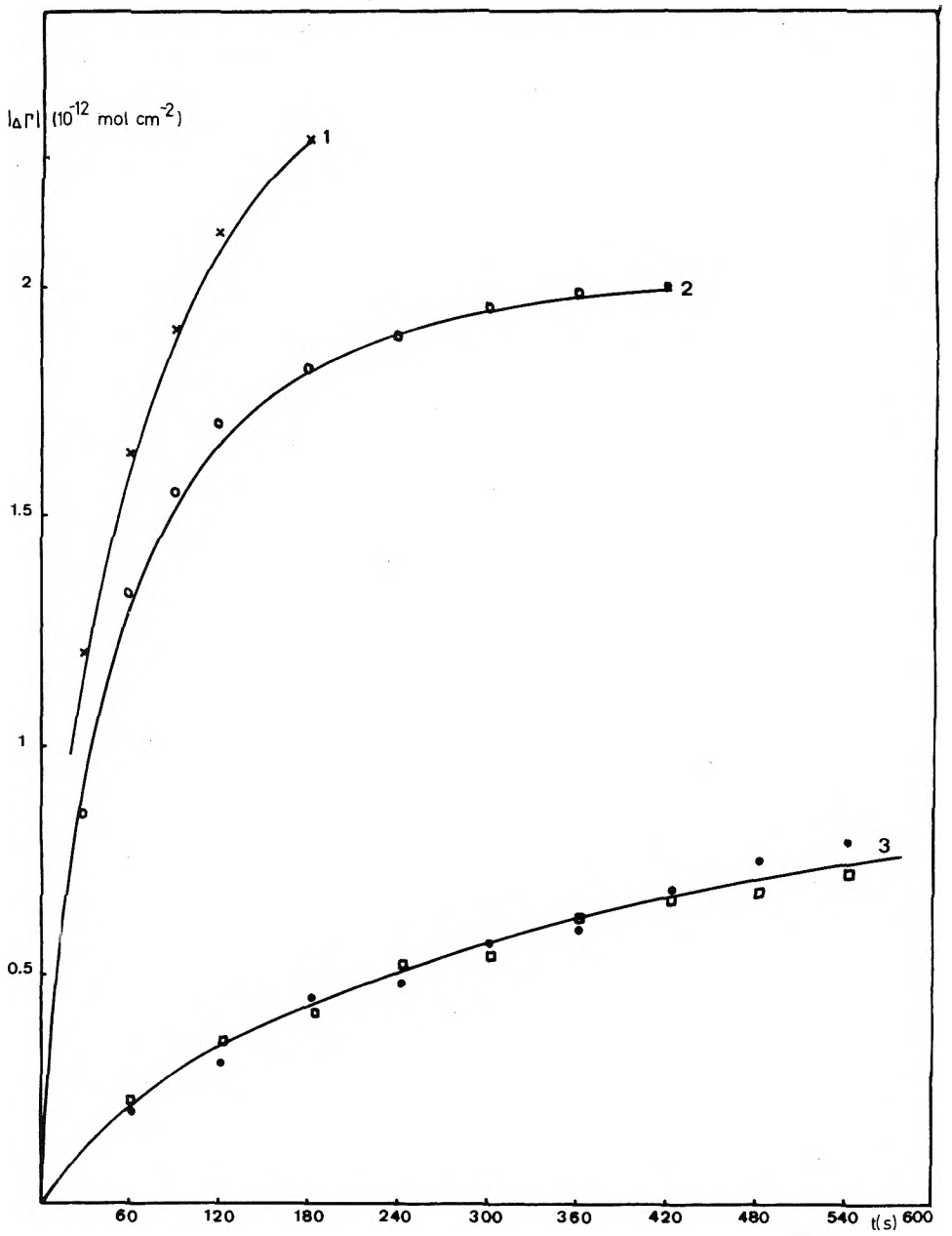

Figure 5. Absolute value of adsorption variation as a function of time for a CTAB concentration in water of 10^{-7} mol cm^{-3}: (1) $I = 300$ μA accumulation; (2) $I = 300$ μA depletion; (3) $I = 50$ μA accumulation and depletion.

calculated from the Langmuir equation, as a function of time. It is seen that for high concentrations ($C = 10^{-7}$ mol cm^{-2}) and small deviations from the equilibrium state (small currents) the same value of $\Delta\Gamma$ was found for depletion and accumulation experiments. For higher currents, however, this is not longer true.

Appendix

Integration of Diffusion Eq 2 with the Boundary and Initial Conditions (Eq 1-4). Making use of the Laplace transform the diffusion equations are transformed to

$$D_1 \frac{d^2\bar{C}_1}{dz^2} = s\bar{C}_1 - C_1^0 \quad z < 0 \tag{A1}$$

$$D_2 \frac{d^2\bar{C}_2}{dz^2} = s\bar{C}_2 - C_2^0 \quad z > 0 \tag{A2}$$

($\bar{C}$ is the Laplace transform of c). Solutions of (A1) and (A2) are

$$\bar{C}_1 = A_1 \exp\left(\sqrt{\frac{s}{D_1}}z\right) + \frac{C_1^0}{s} \tag{A3}$$

$$\bar{C}_2 = A_2 \exp\left(-\sqrt{\frac{s}{D_2}}z\right) + \frac{C_2^0}{s} \tag{A4}$$

where A_1 and A_2 are integration constants. In view of *boundary condition 3 one has*

$$K\bar{C}_1(0) = \bar{C}_2(0) \tag{A5}$$

yielding

$$A_2 = KA_1 \tag{A6}$$

The Laplace transform applied to the boundary condition for conservation of mass at the interface yields

$$\frac{I\Delta n}{F\Omega s} = s\gamma - \Gamma_0 + A_1\sqrt{sD_1} + A_2\sqrt{sD_2} \qquad \text{(A7)}$$

(γ being the Laplace transform of Γ). Substitution of eq A6 and A7 in A3 yields for the concentration in the subsurface at $z = 0$

$$\bar{C}_1(0) = \frac{\Gamma_0 - s\gamma + (I\Delta n/F\Omega s)}{\sqrt{s}[\sqrt{D_1} + K\sqrt{D_2}]} + \frac{C_1^0}{s} \qquad \text{(A8)}$$

whence

$$\gamma = \frac{\Gamma_0}{s} + \frac{I\Delta n}{F\Omega}\frac{1}{s^2} - \frac{\bar{C}_1(0)}{\sqrt{s}}[\sqrt{D_1} + K\sqrt{D_2}] + \frac{C_1^0[\sqrt{D_1} + K\sqrt{D_2}]}{\sqrt{s^3}} \qquad \text{(A9)}$$

Taking now the inverse transform of eq A9 and considering the convolution theorem

$$\mathcal{L}^{-1}\left\{\frac{\bar{C}_1(0)}{\sqrt{s}}\right\} = \frac{2}{\sqrt{\pi}}\int_0^{\sqrt{t}} C_1(0, t - \zeta)\, d\sqrt{\gamma}$$

yields eq 5.

References and Notes

(1) M. Blank and S. Feigl, *Science*, **141**, 1173 (1963).
(2) W. Nernst and E. H. Riesenfeld, *Ann. Phys.*, **8**, 600 (1902).
(3) J. Guastalla, *Proc. Int. Congr. Surf. Act., 2nd*, **3**, III, 122 (1957).
(4) M. Blank, *Proc. Int. Congr. Surf. Act., 4th*, B II/10 (1964).
(5) M. Blank, *J. Colloid Sci.*, **22**, 51 (1966).
(6) Cl. Gavach and F. Henry, *Electr. Chem. Interface Electrochem.*, **54**, 361 (1974).
(7) Cl. Gavach and B. d'Epinoux, *Electr. Chem. Interface Electrochem.*, **55**, 59 (1974).
(8) J. Newman, "Electrochemical Systems", Prentice Hall, Englewoods Cliffs, N.J., 1973, Section 69.
(9) J. C. Crank, "The Mathematics of Diffusion", Clarendon Press, Oxford, 1963.
(10) V. Levich, "Physicochemical Hydrodynamics", Prentice Hall, Englewood Cliffs, N.J., 1962, p 591.
(11) R. S. Hansen, *J. Colloid Sci.*, **16**, 549 (1961).
(12) A. F. H. Ward and L. Tordai, *J. Chem. Phys.*, **14**, 453 (1946).
(13) H. Lange, *J. Colloid Sci.*, **20**, 50 (1965).
(14) H. J. S. Sand, *Phil. Mag.*, **1**, 45 (1900).
(15) E. H. Lucassen-Reynders, *J. Phys. Chem.*, **70**, 1777 (1966).
(16) J. Lucassen and M. van den Tempel, *Chem. Eng. Sci.*, **27**, 1283 (1972).
(17) P. Joos and R. van den Bogaert, *J. Colloid Interface Sci.*, accepted for publication.

Mechanism of the Exchange of Chloride Ions in Colloidal Suspension of Silver Chloride

Tadao Sugimoto* and Goro Yamaguchi

Department of Industrial Chemistry, Faculty of Engineering, University of Tokyo, Hongo, Bunkyo-ku, Tokyo, Japan

(Received September 10, 1975; Revised Manuscript Received March 29, 1976)

Publication costs assisted by Tokyo University

The exchange of chloride ions in a colloidal suspension of silver chloride at 25 °C was investigated by means of the radioactive chloride ion, and quantitative relationships were obtained between the degree of exchange and the change in the specific surface area or in the average particle volume. It has thus been shown that there are two steps in the halide ion exchange between a solid and a solution in a colloidal suspension of silver chloride. The first step is an instantaneous process due to the exchange in the surface layer of a solid less than 2 atomic layers deep, as derived from the linear relationship between the degree of exchange extrapolated to $t = 0$ and the specific surface area. The second one is a relatively slow process ascribed to the Ostwald ripening of microcrystals, in which no self-diffusion was found to be involved even at the early stage of aging, for the following three reasons: (1) the minimum amount of inhibitor needed to stop the exchange agreed with that for stopping the particle growth; (2) some inhibitors of particle growth adsorbed on the surface of silver halide particles freely allowed the surface exchange, but they did not permit any further exchange at all; and (3) the degree of exchange was a function of only the change in the average particle volume and was independent of time.

Introduction

Silver halide is a well-known material for conventional photographic emulsions; it has wide industrial uses and, at the same time, very interesting properties for scientific investigation.

However, despite its technological importance, the details of the mechanism of nucleation and recrystallization process during the preparation of the emulsion are still not clear enough probably because of its complexity. In the present work, radioactive halide ions have been used to study mainly the recrystallization process in colloidal suspensions of silver chloride, for it appears to be one of the most excellent techniques for this kind of investigation.

In relation to the halide ion exchange in silver halide suspension, Kolthoff and his coworkers[1-5] reported an extremely rapid exchange of bromide ions in freshly prepared silver bromide suspensions. They attributed it to the great thermal mobility of bromide in the extremely imperfect structure of solid, or to the Schottky defects which were supposed to cause high mobility of silver and bromide. They appear to have assumed an instantaneous diffusion for the bromide ion exchange.

Pitts[6] suggested, from his quantitative analyses, that the bromide exchange in a silver bromide suspension might occur by recrystallization, though he did not refer to the question whether a self-diffusion process was involved in the recrystallization. Mirnik and Vlatković[7] pointed out that fresh silver

chloride suspensions completed homogeneous exchange in a few minutes. They ascribed it mainly to a rapid recrystallization.

However, Conti and Cammarata,[8] assuming a diffusion process, have recently estimated the value of the diffusion coefficient of bromide in fresh silver bromide solid on the order of 10^{-14} cm^2 s^{-1}, which is 12 orders of magnitude higher than the intrinsic diffusion coefficient at 25 °C extrapolated from the high temperature data of Tannhauser.[9] They accounted for this great discrepancy in the magnitude of the diffusion coefficients in terms of the imperfections or the disorders of the solid structure of freshly prepared silver bromide.

As has been shown in this survey, there are mainly two different interpretations of the mechanism of the halide ion exchange between solid and solution in a silver halide suspension; the recrystallization process by way of solution, and the direct self-diffusion process into solid. It has been generally accepted that the two processes occur simultaneously, though opinions are divided as to the relative importance of the two processes. These inconsistencies among authors are considered to be due to the nonquantitative studies, or to the lack of close observations of the states of the particles.

In the present work, by making clear the causes of the above inconsistencies, the mechanism of chloride ion exchange in a colloidal suspension of silver chloride is described in connection with the problem of whether the self-diffusion process is involved in the exchange. Also, the explanation of the extremely rapid exchange cited above will be attempted from a different point of view, and finally the aging effect upon the activity of recrystallization will be discussed. For these purposes, the exchange was followed together with the changes in specific surface area and in average particle volume in the suspensions, and an occasional observation of the states of the particles was made using an electron microscope.

Experimental Section

Preparation of Colloidal Suspensions of Silver Halide. Two kinds of silver chloride suspension and one silver bromide suspension were used in the present work. The silver bromide was used for reference in this paper.

AgCl(A). Silver nitrate (200 ml of 0.02 N) was added continuously to 200 ml of a well-stirred 0.03 N potassium chloride contained in a 500-ml polyethylene (PE) flask over a period of 200 s at 25 ± 0.1 °C. The experiments of the exchange for this suspension were carried out on 50 ml of the samples in a 100-ml PE flask transferred from the original suspensions in the 500-ml PE flask.

AgCl(B). The procedure used to prepare this suspension was similar to that used for AgCl(A), but smaller in scale. Silver nitrate (25 ml) was added continuously to 25 ml of a well-stirred 0.03 N potassium chloride in a 100-ml PE flask over a period of 30 s at 25 ± 0.1 °C. This suspension was used only for determining the relationship between the degree of exchange and the average particle volume (Figures 8–11). In the case of this suspension, the exchange was performed directly. The other experiments involving silver chloride suspensions were carried out in AgCl(A).

AgBr(A). The procedure of preparation was identical with that of AgCl(B) except that 25 ml of 0.03 N potassium bromide was used in place of the potassium chloride solution.

Halide Ion Exchange. The ratio of the specific radioactivity of the solid phase to that of the solution phase was adopted as the degree of exchange. This has been frequently used since its definition by Kolthoff and Rosenblum.[10]

$$r = \left(\frac{A_0 - A_t}{M_s}\right) \Big/ \left(\frac{A_t}{M_l}\right) \quad (1)$$

where A_0 is the total radioactivity of the suspension and A_t is the radioactivity of the solution phase at time t. M_s and M_l are the number of moles of the halide in solid and in solution, respectively. As can be readily derived from the preparation procedure of the suspensions, M_s and M_l were kept at 0.01 and 0.005 M, respectively, in the present work.

The radioactive chloride ion $^{36}Cl^-$ for AgCl or the bromide $^{82}Br^-$ for AgBr, in the form of a solution of sodium salt, was added by means of a hypodermic syringe to suspensions after certain periods of aging. Then the exchange was followed by sampling each 1.5 ml of the suspension with a pipet into a test tube already containing 0.04 ml of a solution of 4-hydroxy-6-methyl-1,3,3a,7-tetraazaindene (Aza); at the same time, the tube was subjected to enough shaking to mix them in order to stop any further exchange. As is well known, Aza is one of the most popular stabilizers for photographic emulsions.[11] A 1.0-ml portion of each sample containing Aza was filtered with a Millipore ultrafiltration filter (VMWP 29325) by suction 5 min after the addition of Aza. The filtration time was about 30–60 s. The concentration of the Aza solution was 0.005 M for AgCl(A) and AgCl(B), and 0.1 M for AgBr(A), enough to stop completely the exchange and particle growth. These amounts are also of the order of 10^2 for AgCl and 10^4 for AgBr, below the range at which the silver halide begins to be etched by formation of an insoluble salt of Aza.[12] In the case of ^{36}Cl (β ray), the radioactivity of the solid on a filter was counted with a Geiger-Mueller counter (Rikenkeiki BIN type); in the case of ^{82}Br (γ ray), where the correction for the decay time was made, the radioactivity of the filtrate was counted with a scintillation counter (Rikagaku Kenkyusho No. 59017). From these results, the values of A_s (= $A_0 - A_t$) or A_t were determined by calibration curves. The relative experimental error of A_s in the 95% confidence limit was ±9.8%.[32] Each A_0 value used was the arithmetic average of three samples which were prepared by precipitating all chloride ions in sample suspensions with $AgNO_3$.

Incidentally, we found a great difference in the degree of exchange between the samples filtered with Aza and those filtered without it (Figure 1). This phenomenon may be explained in terms of a drastic recrystallization of microcrystals without Aza during filtration, as is clearly shown in the electron micrographs of direct replicas of the precipitates on the filters after filtration (Figure 2). The detailed mechanism of this phenomenon is now under investigation. At any rate, it has been confirmed in our preliminary examination that Aza instantly stops not only the ordinary exchange and particle growth but also the tremendous recrystallization during filtration.

The filtration efficiency was checked by filtering a suspension containing radioactive silver ^{110m}Ag in an excess of halide. The portion of the precipitate passing through the filter was less than 0.1% throughout this work.

The radioactive ^{36}Cl and ^{82}Br used in the present work were furnished by The Radiochemical Centre (England) and by The Isotope Institution of Japan, respectively.

Measurement of the Specific Surface Area of the Precipitate. The specific surface area of the silver halide precipitate was measured with a cyanine dye, 1,1′-diethyl-2,2′-cyanine (DEC), according to the method of Peacock and Kragh.[13] The values used for the molecular area of the adsorbed dye were 83 Å^2 for silver chloride[14] and 58 Å^2 for silver bromide.[13]

Measurement of Average Particle Volume. The turbidi-

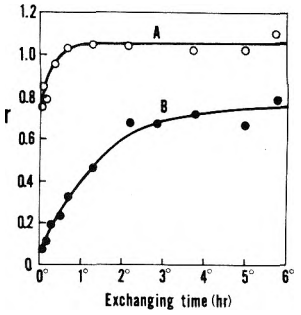

Figure 1. Effect of Aza added before filtering on the exchanging curve. Curve A is that of AgCl(A) without Aza added, while Curve B is that with Aza added immediately after every sampling. Both exchanges were started in AgCl(A)'s at the age of 15 min.

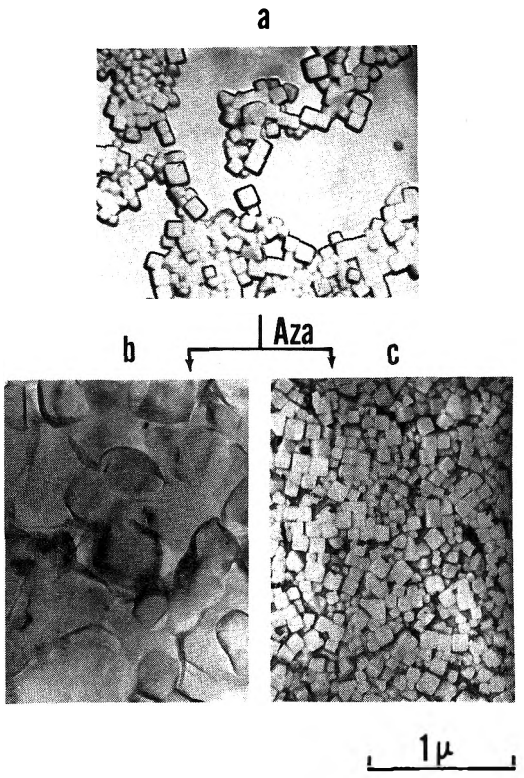

Figure 2. Electron micrographs of AgCl(A) filtered at the age of 15 min with and without Aza: (a) original particle centrifuged with Aza; (b) filtered sample without Aza added; (c) filtered sample with Aza added.

metry based on the Mie theory[15-19] was used for this purpose. The measurements of the specific turbidity were performed at 570 nm for AgCl suspensions, where the relative refractive index, m, is 1.55, and at 452 nm for AgBr, where m is 1.75, with a MPS-50L spectrophotometer (Shimadzu Seisakusho). The particle growth of the samples was stopped by Aza every time immediately after sampling; the amount of Aza used for this purpose was the same as that used for stopping the exchange. The average particle volumes as spheres were calculated with the aid of the scattering coefficients in the NBS table.[20]

All operations in the present study were carried out in photographically inactive light.

Results

The effect of aging on the rate of exchange in the AgCl(A) suspension is shown in Figure 3, where r is the degree of exchange as defined in the Experimental Section. As Mirnik and

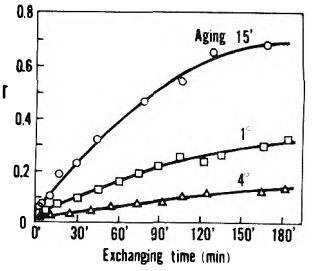

Figure 3. Aging effect on the exchange of AgCl(A). The exchanges started after the agings of the indicated times.

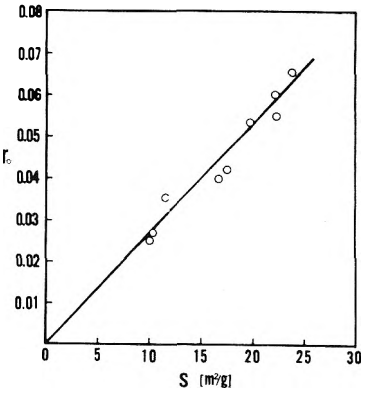

Figure 4. Relationship between r_0 and S in AgCl(A).

Vlatković[7] have already indicated, a decrease in the exchanging rate with aging is observed in this figure. However, it should be noted that the extrapolations of r to $t = 0$ are not zero, but have certain small positive values which decrease with aging. Therefore, it is evident that there are two essential steps in the exchange of chloride ions in a colloidal suspension of AgCl; the first step is an instantaneous process, probably due to a surface exchange, while the second one is a relatively slow process due to the Ostwald ripening and/or a self-diffusion of chloride ions into the solid. When each extrapolated value of r for the each aging time, r_0, was plotted against the corresponding specific surface, S, a linear relationship was obtained, as is shown in Figure 4. Since the experimental errors including the sampling and the statistical ones in the measurements of the specific radioactivities were limited within ±10%, as has been stated in the Experimental Section, 95% confidence limits of the relative error of r_0 were approximately ±10% of each r_0 value (see ref 33). In this case the aging periods ranged from 6 min to 4 h.

If the exchange is limited to the surface layer of solid in radioactive equilibrium with the solution, we obtain

$$\frac{A_0 - A_t}{M_s^*} = \frac{A_t}{M_l} \tag{2}$$

where M_s^* is the number of moles of hypothetical homogeneous surface layer in radioactive equilibrium with the solution. In this case, r_0 is expressed from eq 1 as follows:

$$r_0 = \frac{A_0 - A_t}{A_t}\frac{M_l}{M_s} \tag{3}$$

Thus, the combination of eq 2 and 3 gives

$$r_0 = M_s^*/M_s \tag{4}$$

Hence, the proportionality of r_0 to S in Figure 4 is considered to support strongly the assumption of the surface exchange;

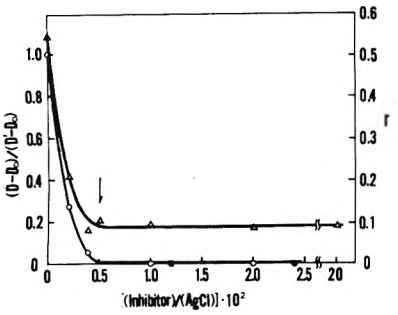

Figure 5. Inhibiting effect of Aza or DEC on the particle growth and the exchange. (O) and (●) are the effects of Aza and DEC, respectively, on the particle growth. (Δ) is the effect of Aza added 5 min after the start of exchange upon the degree of exchange.

at the same time, the constant reactivity of the instantaneous exchange at the surface throughout the aging range from 6 min to 4 h. On the other hand, the following equation generally holds:

$$M_s^*/M_s = S\delta d \tag{5}$$

where δ is the thickness of the hypothetical homogeneous surface layer, and d is the density of the solid. By substituting r_0 for M_s^*/M_s in eq 5

$$\delta = \frac{r_0}{S}\frac{1}{d} \tag{6}$$

From the slope of the straight line (r_0/S), which is determined by $\Sigma_i S_i r_{0i}/\Sigma_i S_i^2$ from least squares, in the Figure 4, we obtain $\delta = 4.69 \pm 1.13$ Å in the 95% confidence limit,[34] which is equivalent to 1.69 ± 0.41 atomic layers, assuming that the thickness of one atomic layer is equal to half of the lattice parameter.

Next, the relatively slow exchange of the second step must be described. If the particles in a colloidal suspension reveal some growth, it is undoubted that the exchange by the Ostwald ripening must have taken place. However, it is still in question whether a self-diffusion process is simultaneously involved in the exchange. In order to answer this question, the following experiments were made.

First, the amount of Aza required to stop the exchange was compared with that needed to inhibit the particle growth. The results are shown in Figure 5, where the exchange was performed by adding a radioactive chloride solution to 50 ml of the AgCl(A) at the age of 15 min, adding Aza solution at the age of 20 min, and filtering the sample 5 min after the addition of Aza; for the particle growth, D_0 is the specular density at 400 nm of the AgCl(A) at the age of 15 min, while D and D' are those after standing for 5 h at 25 °C, with and without Aza or DEC added at the age of 15 min, respectively. All these measurements of turbidity were carried out with samples diluted to 5 times their initial volume with distilled water just before the measurements. From Figure 5 the apparent degree of exchange without Aza reaches 0.55. It rapidly falls with increase in the amount of Aza to 0.09 at 0.5 mol % and is kept constant at 0.09 over 0.5 mol %. The constancy of r over the critical value 0.5 mol % means a complete inhibition of the exchange, and that this value of r is the real extent of the exchange from 15 to 20 min. On the other hand, the particle growth indicated by $(D - D_0)/(D' - D_0)$ is not either observed over 0.5 mol %. DEC is also found to be an excellent stopper of particle growth. It is now obvious that the minimum amount of Aza to stop the exchange is in agreement with that for inhibiting the particle growth due to the Ostwald ripening.

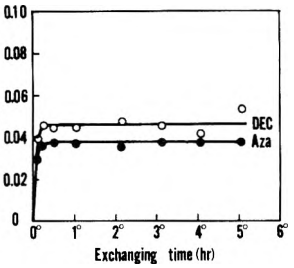

Figure 6. Exchange in AgCl(A) previously adsorbed with Aza (●) or DEC (O).

This means that the exchange can be stopped by inhibiting the particle growth; therefore, it implies that the exchange is ruled only by Ostwald ripening, or at least that the minimum amount of Aza for stopping a self-diffusion, if any, would be not more than the minimum for inhibiting Ostwald ripening.

Second, it was found that, when radioactive chloride was added at the age of 20 min to an AgCl(A) suspension whose particles had already been covered with Aza or DEC at the age of 15 min, a rapid exchange in the surface layer occurred, but the exchange did not proceed further at all, as is shown in Figure 6. If an appreciable self-diffusion were to occur, the direct penetration of chloride ions into the solid could not be prevented by the adsorptives which are supposed to be adsorbed to some silver atoms of the surface, once the exchange in the surface layer has been allowed. In fact, Langer[21,22] found that a variety of adsorptives did not affect the diffusion of the Ag^+ ions which have been proved by many workers[6,21-25] to diffuse readily into the solid in silver halide suspensions. Therefore, this finding in Figure 6 also suggests that there is originally no self-diffusion of chloride at 25 °C. However, if an appreciable self-diffusion should exist and if, at the same time, both Aza and DEC should strongly interact with halide to stop completely any self-diffusion of halide ions into a solid, this evidence might not hold. These apprehensions appear, however, very improbable, since the adsorptives on the surface of the silver halide have no influence on the diffusion coefficient of silver ions which ought to interact much more strongly with the adsorptives than halide ions, and since Aza is widely known to cause little change in the general photographic properties of practical emulsions, which are generally quite sensitive to a slight change in solid properties.[11]

When the degree of exchange, r, in AgCl(A) adsorbed with Aza or DEC in advance was plotted against the specific surface area, a linear relationship such as in Figure 4 was obtained, as is shown in Figure 7. The thickness of the surface layer undergoing exchange is 2.44 ± 0.41 Å or 0.88 ± 0.15 atomic layers with Aza, and 3.52 ± 1.01 Å or 1.27 ± 0.36 atomic layers with DEC.[34] The amount of Aza used was 1.3 mol % of AgCl, which was equal to that for inhibiting the exchange of the particle growth in AgCl suspensions in the present work; the amount of DEC used for this purpose was 1.2 mol % of AgCl(A), which is enough to obtain saturated coverage in monolayer.

It may be desirable to confirm the absence of the self-diffusion by a different method which is independent of the effect of the adsorptives. If the exchange in a given system is dominated only by Ostwald ripening in the second slower step, the differential change in r, dr, is caused only by the dissolution (or growth) of the individual particles, dv_i, and not directly affected by the change either in time, dt, or in temperature, dT (i.e., $(\partial r/\partial t)_{v_i} = 0$ and $(\partial r/\partial T)_{v_i} = 0$). Therefore, we can generally write it as

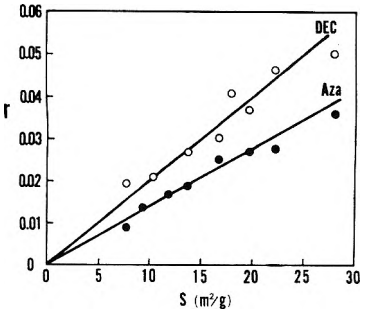

Figure 7. Relationship between r and S in AgCl(A) previously adsorbed with Aza (●) and DEC (O).

$$dr = g(\Phi, r)\, d\Phi \tag{7}$$

where Φ is a function describing the physical (not radiochemical) state of the particle system, as determined by the particle-volume distribution, $f(v_i)$; v_i is a particle volume of the ith class. Since the $f(v_i)$ is a one-valued function of the average particle volume, $\bar{v}$, in a given system, Φ is finally also a one-valued function of $\bar{v}$; that is

$$\Phi = \Phi(\bar{v}) \tag{8}$$

By combining eq 7 with eq 8, the general solution of the differential eq 7 is obtained in the following form:

$$r = F(\bar{v}, \bar{v}_0, r_0) \tag{9}$$

where $\bar{v}_0$ and r_0 are the initial values of $\bar{v}$ and r, respectively.

On the other hand, if self-diffusion besides Ostwald ripening is responsible for the exchange, r is a function not only of $\bar{v}$, $\bar{v}_0$, and r_0, but also of the independent variables, t and T. Thus

$$r = F(\bar{v}, \bar{v}_0, r_0, t, T) \tag{10}$$

Accordingly, if the initial conditions, $\bar{v}_0$ and r_0, are fixed, r becomes a function of only $\bar{v}$ in the case of pure Ostwald ripening. Therefore, when there are two suspensions which start to exchange under the same initial conditions of $\bar{v}_0$ and r_0 and then follow different paths, for instance, at different temperatures or upon the addition of a recrystallization accelerator, such as ammonia, the two curves of $\bar{v}$ vs. t of these suspensions and those of r vs. t may be greatly separated, but those of r vs. $\bar{v}$ can be expected to coincide completely. On the other hand, in case considerable self-diffusion is included, the two curves of r vs. $\bar{v}$ must be separated by the difference in the diffusion components.

According to this theory, two AgCl(B) suspensions were prepared and 0.5 ml of a radioactive chloride solution was added to each of them 1 min after the preparation. Then 1 ml of 0.1 N ammonia was added to one of them 1 min after the addition of the radioactive chloride, after which the exchange was continued to be followed. On the other hand, the exchange in the other suspension was followed after adding 1 ml of distilled water instead of ammonia. The particle growth was followed analogously, but without radioisotope. As is shown in Figures 8–10, despite the marked discrepancies between the two suspensions in $\bar{v}$ vs. t and in r vs. t, the curves of r vs. $\bar{v}$ completely coincide within the limits of experimental error. In this case, however, it must be confirmed that the dependence of the distribution function $f(v_i)$ upon $\bar{v}$ is identical in both suspensions. In fact, though, this requirement is fully satisfied, because the relationships between the specific turbidity at 750 nm and that at 450 nm with the particle growth were identical for the two suspensions, as is shown in Figure 11, and a suspension with a different distribution of particles

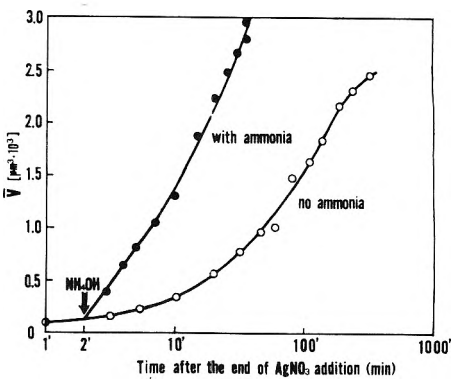

Figure 8. Acceleration of particle growth by ammonia: (O) without ammonia; (●) with 0.002 N ammonia.

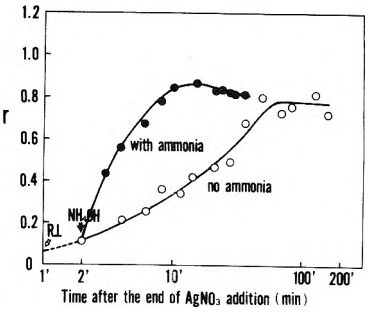

Figure 9. Acceleration of exchange by ammonia: (O) without ammonia; (●) with 0.002 N ammonia.

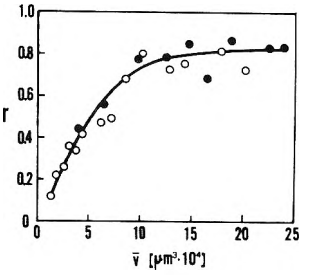

Figure 10. Relationship between r and $\bar{v}$: (O) without ammonia; (●) with 0.002 N ammonia.

generally shows a different dependence of the turbidity upon wavelength.[15]

Consequently, the contribution of the self-diffusion process to the exchange of chloride ions in a silver chloride suspension, even at the age of 1 min at 25 °C, is absent or, at least, negligible. Similar results were obtained for AgBr(A) as well.[31]

In relation to the drastic changes in the degree of exchange and in the forms of the microcrystals during the filtration (Figures 1 and 2), we examined the effect of the coagulating electrolyte, KNO_3, on the exchange of AgCl(A) and AgBr(A) suspensions. KNO_3 (10 ml of 1 N) was added to 40 ml of each suspension at certain times during the exchange. The exchange in AgCl(A) was started at the age of 15 min and KNO_3 was added at 21 min, while the exchange in AgBr(A) was started at the age of 1 min and KNO_3 was added at 8 min. They were flocculated instantaneously and showed drastically different exchanges at the same time (Figure 12). The abrupt rising of the curves over unity and the gradual decrease to unity are known to be characteristic of recrystallization.[26] The electron micrographs of the particles of AgCl(A) before and after the flocculation are shown in Figure 13, where the

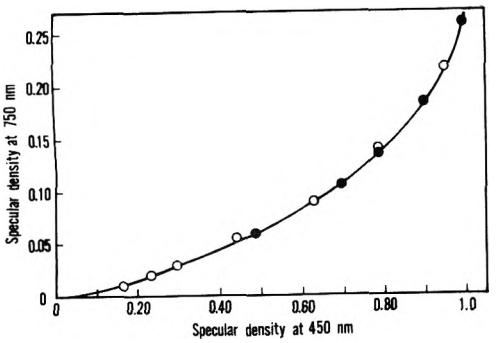

Figure 11. Relationship between the specular density at 750 and 450 nm of the AgCl(B) suspensions with and without ammonia: (O) without ammonia; (●) with 0.002 N ammonia.

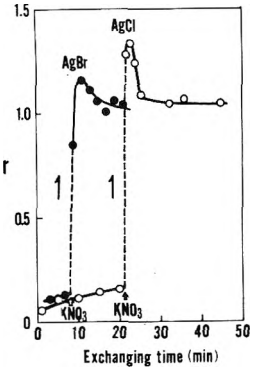

Figure 12. Effect of KNO_3 on the exchange in AgCl(A) (O) and AgBr(A) (●). The concentration in KNO_3 is 0.2 N.

strikingly enlarged and well-formed crystals with sharp edges and smooth surfaces demonstrate evidence of recrystallization. We have obtained, of course, quite similar photographs of AgBr(A) as well.[31] The detailed mechanism of this behavior in suspension is now under investigation in connection with the filtration process. At any rate, though, it is evident that the particles of silver halide in suspension undergo a drastic recrystallization and an exceedingly rapid exchange of halide ions, when they are filtered or coagulated. This strikingly rapid recrystallization appears to be essentially different from Ostwald ripening, though both of them are assumed to be a kind of recrystallization caused mainly by the difference in the surface energy of particles. Therefore, recrystallization in the colloidal state (Ostwald ripening) should be strictly distinguished from that in the coagulated state.

However, few workers have paid any attention to these two states. Kolthoff and Bowers[4,5] discussed separately the exchange in silver bromide suspension in two different states described above; they have reported that an extremely rapid exchange took place in a colloidal suspension as well as in a flocculated one. They did not, though, find the essential difference between them because they applied the flocculation method to the colloidal suspension to separate the supernatant liquid from the precipitate. Despotović and Subotić[27] found an enhancement of the iodide ion exchange in a colloidal suspension of silver iodide by coagulating electrolyte. They tried to interpret this phenomenon in terms of an acceleration of the perfect lattice formation in the individual crystals by electrolyte, accompanied by an enhancement of the exchange. However, no evidence substantiating such an electrolyte effect is so far known, so it seems more reasonable to explain it in terms of the recrystallization essential to the particles coalesced as has been stated above.

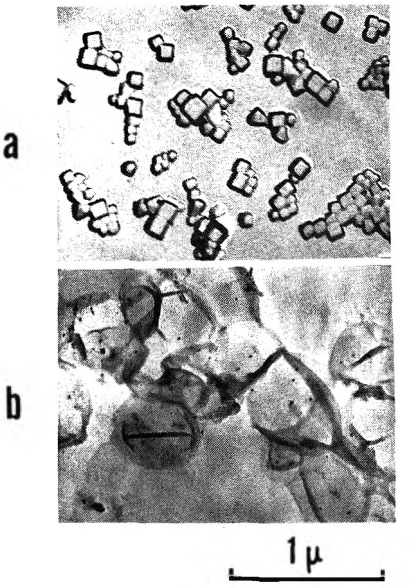

Figure 13. Electron micrographs of AgCl(A) flocculated with 0.2 N KNO_3: (a) particles before flocculation; (b) particles after flocculation.

Discussion

It is now evident from the above experimental results that there are two essential steps in halide ion exchange in a colloidal suspension of silver chloride and probably in other silver halide as well. In fact, we have obtained similar results also for silver bromide suspension.[31] That is, the first step is an instantaneous exchange within the surface layer of the solid, while the second one is a relatively slow process due to Ostwald ripening, in which no self-diffusion was found to be included.

On the other hand, the difference of the two kinds of recrystallization process described above has been generally ignored, and it seems to be widely accepted that fresh microcrystals of silver halide in a suspension with an extremely imperfect structure undergo a striking exchange due to a sort of instantaneous diffusion through the imperfect structure of the solid, or due to an exceedingly rapid recrystallization caused by their quite unstable structure. Kolthoff and Bowers pointed out in a report cited above[4] that fresh silver bromide in a colloidal suspension completed its homogeneous exchange within a few seconds. They ascribed the rapid exchange to the Schottky defects, which might cause a high silver and bromide mobility. Mirnik and Vlatković[7] reported that a silver chloride suspension aged for less than 10 min completed its homogeneous exchange in a few minutes. They attributed this mainly to the recrystallization by the extremely active microcrystals freshly prepared, and suggested also some possibility of a diffusion process. However, the microcrystals in their experiments were subjected to the coagulation. Conti and Cammarata[8] have recently reported that fresh silver bromide particles completed the exchange within about 1 h. They attributed the exchange in their suspension to a self-diffusion of bromide ions into the imperfect crystal structure. According to their experimental condition, the suspensions must be in a flocculated state. The concentration of bromide in the solution phase of their suspension was ca. 10^{-3} M. With this concentration of bromide, recrystallization is thought to be fairly limited, but, at least, some recrystallization appears to take place, for Kolthoff and O'Brien[2] have shown a considerable decrease in the specific surface of the AgBr precipitate with aging under similar conditions, and for an appreciable

crystal growth was observed even in a colloidal suspension of silver bromide with 10^{-3} M bromide solution in our experiment as well.[31] By the way, their proposal of a diffusion process is based on the apparent observation that the degree of exchange $\bar{W}/\bar{W}_\infty$ ($= r'$) used by them reached unity in about 1 h. The r' has been used as frequently as r, and it is defined as follows:

$$r' = \left(\frac{A_0 - A_t}{M_s}\right) \Big/ \left(\frac{A_0}{M_s + M_l}\right) \tag{11}$$

Therefore, the two definitions differ in the denominator, and there is the following relationship between them:

$$r' = \frac{r(1+m)}{r+m} \tag{12}$$

where $m = M_l/M_s$. According to their experimental conditions, where $m \simeq 1/250$, the r' value abruptly rises to over 0.98 when the r value is still as low as 0.2; this means that the system is far from being in equilibrium between solid and solution. In other words, in the case where $m \ll 1$, when $r' \simeq 1 - A_t/A_0$, A_t/A_0 practically reaches zero, even by merely a partial recrystallization of the solid. Moreover, if $m = 1/250$, eq 11 shows that r' cannot finally exceed 1.004 by any exchanging mechanism. Therefore, $r' \to 1$ is not necessarily a good criterion of diffusion, especially when m is extremely small. In this connection, it seems to be indispensable for the precise analysis of experimental curves of the exchange to establish a general and theoretical relationship between the extent of the exchange and the recrystallization as well as the diffusion. This is a future problem.

Now, it is thought that all the strikingly rapid exchanges at room temperature cited above may be also accounted for in terms of recrystallization by coagulation.

Aside from the discrimination between the two essentially different recrystallization processes, many authors[6,7,28,29] have already tried to interpret the exchange principally in terms of recrystallization. However, it has never been answered whether or not a self-diffusion process is included in recrystallization especially in the early stage of aging. This problem is of essential importance because proof of the lack of the self-diffusion would open the way for the use of the exchange technique in getting direct information on recrystallization or on crystal growth in suspensions. This is one of the reasons why we placed special stress upon it.

We have maintained that the crystal imperfections in fresh silver halides have been too exaggerated, but their effect on the recrystallization rate is nevertheless important. Berry and Skillman[17] suggested an aging effect, independent of the specific surface change, upon the rate of Ostwald ripening in AgBr emulsions; they have shown the possibility that the activity of Ostwald ripening is affected not only by the specific surface area and its energy in the sense of surface tension, but also by the so-called "thermal aging",[2-5,30] i.e., the improvement in the structural perfection of individual crystals by thermal agitation. Taking into account their results, it seems to us that point defects (e.g., Schottky defects) and/or structural imperfections (e.g., dislocation and grain boundary), which are reduced by thermal agitation or some other mechanism, accelerate the dissolution of the solid surface by acting as active sites on the surface, which appear anew by the dissolution, but that the absolute rates of their migration and/or their effective concentration may not be enough to contribute to the exchange by self-diffusion. Therefore, our concept of thermal aging, if any, is a little different from that of Kolthoff et al., who defined this term mainly in relation to diffusion.

Finally, no evidence of coagulation was found in colloidal suspensions of AgCl(A), AgCl(B), and AgBr(A), as far as our experiments were concerned. However, there is as yet no positive reason either to deny the possibility of the cementing or the recrystallization by coagulation in a usual stable colloidal suspension of silver halide in the very early stage of aging when the sizes of the particles are extremely small (<50 mμ) and when, therefore, the specific surface energy is very high.

Acknowledgments. The authors are indebted to Fuji Photo Film, Ltd., for the supply of chemicals and for other cooperation. Special thanks are due to Messrs. S. Takagi and M. Saito for their technical advice concerning the operation of the electron microscope. The authors are also particularly grateful to Professor Y. Ujihira for his helpful suggestions regarding the radiochemical analyses.

References and Notes

(1) I. M. Kolthoff and A. S. O'Brien, *J. Am. Chem. Soc.*, **61**, 3409 (1939).
(2) I. M. Kolthoff and A. S. O'Brien, *J. Am. Chem. Soc.*, **61**, 3414 (1939).
(3) I. M. Kolthoff and A. S. O'Brien, *J. Chem. Phys.*, **7**, 401 (1939).
(4) I. M. Kolthoff and R. C. Bowers, *J. Am. Chem. Soc.*, **76**, 1503 (1954).
(5) I. M. Kolthoff and R. C. Bowers, *J. Am. Chem. Soc.*, **76**, 1510 (1954).
(6) E. J. Pitts, *J. Chem. Phys.*, **22**, 56 (1954).
(7) M. Mirnik and M. Vlatković, *Kolloid-Z.*, **163**, 32 (1959).
(8) L. G. Conti and S. Cammarata, *J. Phys. Chem. Solids*, **35**, 125 (1974).
(9) D. S. Tannhauser, *J. Phys. Chem Solids*, **5**, 224 (1958).
(10) I. M. Kolthoff and C. Rosenblum, *J. Am. Chem. Soc.*, **56**, 1658 (1934).
(11) C. E. Mees and T. H James, "The Theory of the Photographic Process", 3d ed, Macmillan, New York, N.Y., 1966.
(12) E. J. Birr, "Stabilization of Photographic Silver Halide Emulsions", The Focal Press, London, 1974, p 181.
(13) R. Peacock and A. M. Kragh, *J. Photogr. Sci.*, **16**, 229 (1968).
(14) T. Tani, S. Kikuchi, and K. Hayamizu, *J. Chem. Soc. Jpn.*, **70**, 1288 (1967).
(15) E. J. Meehan and W. H. Beattie, *J. Phys. Chem.*, **64**, 1006 (1960).
(16) E. J. Meehan and W. H. Beattie, *J. Opt. Soc. Am.*, **49**, 735 (1959).
(17) C. Berry and D. C. Skillman, *J. Phys. Chem.*, **70**, 1871 (1966).
(18) E. Moisar, "Die Grundlagen der Photographischen Prozesse mit Silberhalogeniden", Akademische Verlagsgesellschaft, Frankfurt am Main, 1968, p 609.
(19) L. E. Oppenheimer, T. H. James, and A. H. Herz, "Particle Growth in Suspensions", A. L. Smith, Ed., Academic Press, London, 1973, p 159.
(20) A. N. Lowan, "Tables of Scattering Functions for Spherical Particles", National Bureau of Standards, Washington, D.C., 1948, AMS-4.
(21) A. Langer, *J. Chem. Phys.*, **10**, 321 (1942).
(22) A. Langer, *J. Chem. Phys.*, **11**, 11 (1943).
(23) A. M. Venet and J. Pouradier, *J. Chim. Phys.*, **52**, 779 (1955).
(24) M. Mirnik and R. Despotović, *Kolloid-Z.*, **180**, 51 (1962).
(25) R. Despotović and M. Mirnik, *Croat. Chem. Acta*, **37**, 163 (1965).
(26) I. M. Kolthoff and F. T. Eggertsen, *J. Am. Chem. Soc.*, **63**, 1412 (1941).
(27) R. Despotović and B. Subotić, *Croat. Chem. Acta*, **43**, 153 (1971).
(28) K. E. Zimmen, "Fundamental Mechanism of Photographic Sensitivity", Butterworths Scientific Publications, London, 1951, p 53.
(29) R. Despotović and M. Mirnik, *Croat. Chem. Acta*, **38**, 83 (1966).
(30) H. A. Laitinen, "Chemical Analysis", McGraw-Hill, New York, N.Y., 1960, p 160.
(31) T. Sugimoto, unpublished data.
(32) The experimental error of the radioactivity measurements is mainly composed of sampling and filtering errors, and geometric error in the counting position of specimen. The statistic error is able to be small enough by accumulating a number of counts. Thus, the standard deviation (σ_s) of specific radioactivities of solid (A_s) is considered proportional to the expected value of A_s; i.e., the coefficient of variance (C_s) of A_s, which is equal to σ_s/μ_s where μ_s is the expected value of A_s, is constant. C_s was found to be 4.98% in the present work; therefore, 95% confidence limits of the relative error of A_s were ±9.76% (= ±1.96 × 4.98%). Since A_0 is an average of three samples, the coefficient of variance of $\bar{A}_0$ was 2.88% (= 4.98/$\sqrt{3}$%).
(33) Since $r = (A_s/(A_0 - A_s))(M_l/M_s)$, the variance of r, σ_r^2, can be derived as follows:

$$\sigma_r^2 \simeq \left(\frac{\partial r}{\partial A_s}\right)^2 V(A_s) + \left(\frac{\partial r}{\partial \bar{A}_0}\right)^2 V(\bar{A}_0) \simeq \frac{m^2(\mu_0^2\sigma_s^2 + \mu_s^2\sigma_0^2/3)}{(\mu_0 - \mu_s)^4}$$

$$\therefore \frac{\sigma_r}{\mu_r} \simeq \left(1 + \frac{r}{m}\right)\sqrt{\left(\frac{\sigma_s}{\mu_s}\right)^2 + \frac{1}{3}\left(\frac{\sigma_0}{\mu_0}\right)^2} = \frac{2}{\sqrt{3}}\left(1 + \frac{r}{m}\right)C_s$$

where $V(A_s)$ and $V(\bar{A}_0)$ are the variances of A_s and $\bar{A}_0$, and are equal to σ_0^2 and $\sigma_0^2/3$, respectively;[32] σ_0^2 is the variance of A_0; $m = M_l/M_s$; μ_r, μ_0, and μ_s are the expected values of r, A_0, and A_s, respectively; σ_r/μ_r is the coefficient of variance of r, which is a measure of the relative error of r. When r is as small as $r \ll m$, 95% confidence limits of r approach

$\pm 1.96 \times (2/\sqrt{3}) \times 4.98\% = \pm 11.3\%$. In the case of r_0, however, the limits of relative error can be theoretically reduced further to $\pm 1.96 \times (1/\sqrt{3}) \times 4.98\% = 5.64\%$ as follows. Since r_0 is generally small

$$\frac{\sigma_r^*}{\mu_r^*} \simeq \sqrt{\left(\frac{\sigma_s^*}{\mu_s^*}\right)^2 + \frac{1}{3}\left(\frac{\sigma_0}{\mu_0}\right)^2}$$

where the asterisk means extrapolated value to $t = 0$. Assuming the exchanging curve near $t = 0$ to be linear, the coefficient of variance of A_s^*, σ_s^*/μ_s^*, can be readily derived from statistical theory concerning the regression in the case where C_s (= σ_s/μ_s) is constant. That is

$$\frac{\sigma_s^*}{\mu_s^*} \simeq \frac{1}{\mu_s^*}\sqrt{\frac{\Sigma\sigma_{si}^2}{n^2} + \frac{\Sigma(t_i - \bar{t})^2\sigma_{si}^2}{\{\Sigma(t_i - \bar{t})^2\}^2}\bar{t}^2} = C_s\sqrt{\frac{\Sigma\mu_{si}^2}{n^2\mu_s^{*2}} + \frac{\Sigma\mu_{si}^2(t_i - \bar{t})^2}{\mu_s^{*2}\{\Sigma(t_i - \bar{t})^2\}^2}\bar{t}^2}$$

where t_i is the exchanging time of the ith time of the ith sampling n is the number of samplings, and $\bar{t}$ is the average of t_i. If μ_{si}^2 near $t = 0$ is assumed approximately equal to μ_s^{*2}, this equation is reduced to

$$\frac{\sigma_s^*}{\mu_s^*} \simeq C_s\sqrt{\frac{1}{n} + \frac{\bar{t}^2}{\Sigma(t_i - \bar{t})^2}} = \frac{C_s}{\sqrt{n}}\sqrt{1 + \frac{\bar{t}^2}{V(t_i)}}$$

where $V(t_i)$ is a function of t_i's in the form of variance. When n and $V(t_i)$ are taken large enough near $t = 0$, σ_s^*/μ_s^* converges to zero. However practically σ_s^*/μ_s^* was taken about $2C_s/3$ in the present work. Therefore, σ_r^*/μ_r^* was nearly equal to C_s.

(34) The 95% confidence limits of the expected values of δ's were calculated from the variances of the data shown in Figures 4 and 7 by using the t-distribution table. The comparatively wide confidence limits are due to the relatively narrow ranges of S and due to the small number of samplings.

Spectroscopic Studies of Surfactant Solubility. 2. Solubilization in Carbon Tetrachloride by Complex Formation with Chloroform

Mitsuyo Okazaki, Ichiro Hara,

Laboratory of Chemistry, The Department of General Education, Tokyo Medical and Dental University, Ichikawa, Japan

and Tsunetake Fujiyama*

Department of Chemistry, Faculty of Science, Tokyo Metropolitan University, Setagaya, Tokyo, Japan *(Received December 3, 1975)*

Publication costs assisted by The Department of General Education

Infrared spectra of water soluble surfactants were studied with respect to their solubility in carbon tetrachloride. The ternary solution of carbon tetrachloride–chloroform–surfactant showed by quantitative analysis of the C–D stretching vibration bands of chloroform-*d* that the surfactants dissolved in these solvents by forming a complex consisting of several chloroform molecules to one surfactant molecule. The number of chloroform molecules which form a complex with a surfactant decreases as the mole ratio of carbon tetrachloride to chloroform increases. At the mole ratio corresponding to the solubilization limit, a (1:1) complex of chloroform and surfactant is formed. The surfactants studied are dodecyldimethylamine oxide and cetyltrimethylammonium chloride. Pyridine is also studied as a reference system.

Introduction

In a previous publication, the infrared spectra of some water soluble surfactants have been reported. From quantitative analysis of the absorption intensity, it had been shown that molecules that dissolve in chloroform form a complex with several solvent chloroform molecules. The bonding between a surfactant and solvent chloroform had been shown to be of hydrogen bond type.[1]

The present study concerns itself with a further study of solubilities of some surfactants in chloroform by the use of infrared spectra. The surfactants being studied are widely known to be insoluble in carbon tetrachloride, but can be made soluble in carbon tetrachloride by adding a small amount of chloroform. Focusing our attention on the infrared absorption band of chloroform-*d*, the effect on dilution with carbon tetrachloride on the hydrogen bonding between surfactants and chloroform can be seen. The surfactants studied were dodecyldimethylamine oxide ($C_{12}AO$) and cetyltrimethylammonium chloride (CTACl).

Many spectroscopic studies on ternary solutions have been performed and are well documented in the literatures.[2-22]

Experimental Section

Materials. Chloroform-*d* was purchased from Merck and Co., Ltd. and used without further purification. Carbon tetrachloride was purchased from Tokyo Kasei Co., Ltd. and used after distillation.

An aqueous solution of dodecydimethylamine oxide was supplied from Kao Atras Co., Ltd. and was used after recrystallization from acetone. Cetyltrimethylammonium chloride was purchased from Tokyo Kasei Co., Ltd. and purified by recrystallization from acetone. The purities of these samples were checked by thin layer chromatography. Pyridine was purchased from Tokyo Kasei Co., Ltd. and was used without further purification.

Infrared Absorption Measurements. The absorption spectra were obtained from a JASCO IR-G grating spectrometer with a resolution of 1 cm^{-1}. KBr cells of various thicknesses 0.1, 0.5, 1.0, and 2.0 mm were used to obtain the spectra of the ternary solutions of chloroform-*d*–carbon tetrachloride with a surfactant at various concentrations. The thickness of the sample cells were determined by the interference fringe method.

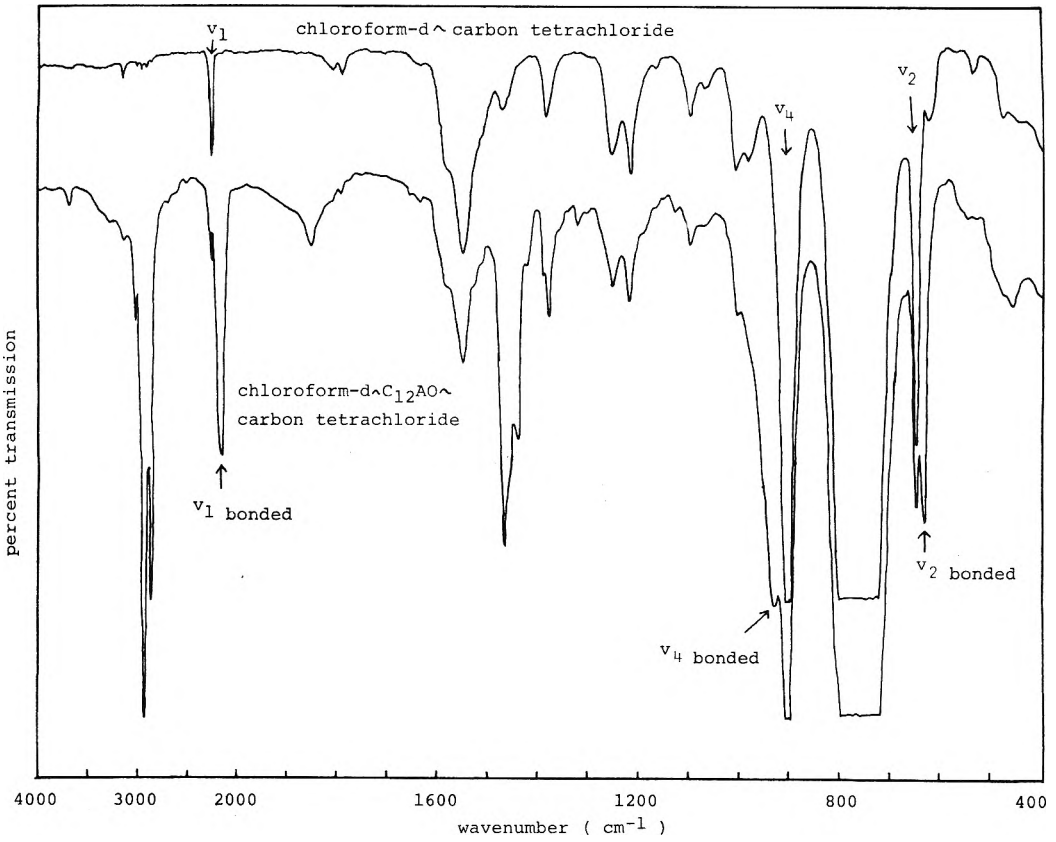

Figure 1. Infrared spectra for binary (chloroform-*d*–carbon tetrachloride) and ternary (chloroform-*d*–C_{12}AO–carbon tetrachloride) solutions.

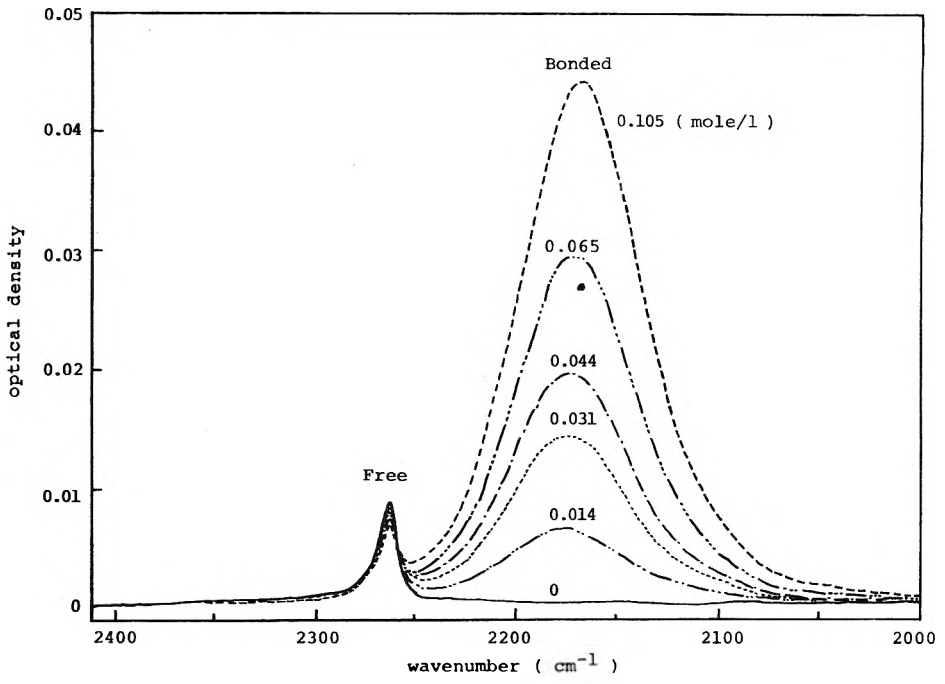

Figure 2. Concentration dependence of the C–D stretching vibration of chloroform-*d* for ternary solution (chloroform-*d*–C_{12}AO–carbon tetrachloride). $C^0_{CCl_4}/C^0_{CDCl_3}$ = 36.6. The numerical values on the peaks show molar concentration of C_{12}AO.

Ternary solutions containing varying concentrations of solute in the solvents were prepared before measurement by weighing the surfactant and solvents in the sample flask. Since the solutes are very hygroscopic, they were dried thoroughly to an anhydrous condition before each measurement. The elimination of water from the sample solution was confirmed by observing the infrared spectra in the region of 4000–2000 cm^{-1}.

The refractive index, n_D^{20}, and the specific gravity of the solution were measured with an Abbe refractometer and a

TABLE I: Relative Intensities of the C–D Stretching Vibration and Calculation of the Solvation Number, *n*, for the Chloroform-*d*–$C_{12}AO$–Carbon Tetrachloride System

$C^0_{CCl_4}/C^0_{CDCl_3}$	10^3C_{AO}, mol/cm^3	n_D	d	I_b^*, cm^{-1}	I_f^*, cm^{-1}	10^3C_b, mol/cm^3	n	$-(\nu - \nu_0)$, cm^{-1}	$\Delta\nu_{1/2}$, cm^{-1}
0	0	1.4470	1.48	0	1.302	0			
	0.017	1.4471	1.478	0.186	1.279	0.107	6.29	79	69
	0.065	1.4472	1.472	0.629	1.262	0.358	5.51	79	69
	0.090	1.4473	1.469	0.886	1.252	0.501	5.57	79.5	68
	0.114	1.4474	1.465	1.064	1.216	0.599	5.25	80	68
	0.182	1.4476	1.457	1.709	1.209	0.946	5.20	80.5	67
	0.182	1.4476	1.457	1.647	1.189	0.912	5.01	80.5	68
	0.329	1.4481	1.438	2.943	1.120	1.569	4.77	81.5	67.5
	0.405	1.4484	1.428	3.610	1.068	1.886	4.66	82	68
	0.538	1.4488	1.411	5.029	1.010	2.534	4.71	82.5	68
0.97	0	1.4540	1.529	0	0.484	0			
	0.050	1.4542	1.520	0.438	0.459	0.197	3.94	79.5	67
	0.100	1.4545	1.513	0.935	0.448	0.419	4.19	80	67
	0.200	1.4547	1.497	1.686	0.417	0.731	3.66	82.5	66
	0.400	1.4550	1.465	3.359	0.359	1.373	3.43	85	67
	0.800	1.4560	1.401	6.595	0.266	2.398	3.00	88	68
3.62	0	1.4571	1.554	0	0.171	0			
	0.018	1.4572	1.551	0.118	0.167	0.052	2.89	80	62
	0.035	1.4573	1.548	0.234	0.164	0.102	2.91	81	62
	0.058	1.4573	1.544	0.371	0.158	0.162	2.79	82	62
	0.090	1.4574	1.539	0.584	0.151	0.252	2.80	82.5	63
	0.111	1.4580	1.535	0.707	0.148	0.304	2.74	83.5	63.5
11.09	0	1.4590	1.567	0	0.0565	0			
	0.0172	1.4594	1.565	0.089	0.0542	0.033	1.92	84	64
	0.0311	1.4594	1.562	0.159	0.0521	0.060	1.93	84.5	64
	0.0471	1.4595	1.559	0.249	0.0504	0.092	1.95	85	64
	0.0848	1.4596	1.553	0.450	0.0460	0.165	1.95	87.5	65
	0.1004	1.4598	1.550	0.522	0.0435	0.191	1.90	88	66
36.60	0	1.4603	1.568	0	0.0161	0			
	0.0094	1.4604	1.566	0.0282	0.0155	0.0082	0.87	85.5	72
	0.0138	1.4604	1.566	0.0458	0.0153	0.0133	0.96	85.5	71
	0.0314	1.4603	1.563	0.0977	0.0142	0.0283	0.90	88.5	71
	0.0439	1.4602	1.561	0.1321	0.0138	0.0383	0.87	90	71
	0.0647	1.4602	1.557	0.1965	0.0130	0.0569	0.88	94	71
	0.1054	1.4603	1.550	0.2991	0.0110	0.0871	0.83	94.5	71

picnometer, respectively, at the same time as the absorption measurements.

All the measurements were taken at 20 ± 2 °C and the absorption spectra of the C–D stretching vibrations in the frequency region of 2500–2000 cm^{-1} were measured carefully with a resolution of 1 cm^{-1} and scanning speed of 33.3 cm^{-1} min^{-1}. The absorption due to carbon tetrachloride was eliminated by use of a variable pathlength cell in the reference side. The thickness of the variable cell was adjusted so that the absorption band of carbon tetrachloride in the region of 2350–2250 cm^{-1} was completely eliminated.

Results and Discussion

Infrared Spectra and Intensity Analysis. In Figure 1 the infrared spectra for a binary solution of CCl_4–$CDCl_3$ and for a ternary solution of CCl_4–$CDCl_3$–$C_{12}AO$ are shown. It is seen from the figure that the infrared spectra originating from $CDCl_3$ show remarkable changes in the fundamental bands of chloroform-*d;* the C–D stretching (ν(C–D)), the C–D bending (δ(C–D)), and the C–Cl_3 symmetric stretching (ν(C–Cl)) vibrations. As is discussed in a previous report,[1] these are certainly due to hydrogen bond formation between $CDCl_3$ and $C_{12}AO$. In the case of the spectra in Figure 1, the frequency shifts of these fundamental bands due to hydrogen bonding are observed to be −84, +28, and −16 cm^{-1}, respectively. The absorption spectra for the ternary solution of CCl_4–$CDCl_3$–$C_{12}AO$ in the frequency region from 2400 to 2000 cm^{-1} are shown in Figure 2. The bands of the C–D stretching vibration corresponding to the free and the bonded states are observed separately. As the concentration of $C_{12}AO$ increases, the intensity of the bonded band increases remarkably, while that of the free band decreases.

The procedure for the intensity measurements of ν(C–D) for ternary solution of CCl_4–$CDCl_3$–surfactant is the following. We first make a binary mixture of CCl_4–$CDCl_3$, the molecular concentrations of which are $C^0_{CCl_4}$ and $C^0_{CDCl_3}$. The ratio, $C^0_{CCl_4}/C^0_{CDCl_3}$, is called a dilution ratio hereafter. For a binary solution of a given dilution ratio, we observed the intensity change of ν(C–D) by dissolving various amounts of surfactant. We repeat these procedures for various dilution ratios. The molar concentrations of the resultant ternary mixture, C_{CDCl_3}, C_{CCl_4}, and C_s, are determined from the observed weight concentration and the density of the solution.

The definition of intensities are retained as those described in the previous report.[1] The relative intensity, I, of an absorption band is defined as

$$I = \frac{1}{l}\int_{band} \ln (I_0/I)\, d \ln (\nu) \qquad (1)$$

TABLE II: Relative Intensities of the C–D Stretching Vibration and Calculation of the Solvation Number, *n*, for the Chloroform-*d*–CTACl–Carbon Tetrachloride System

$C^0_{CCl_4}/C^0_{CDCl_3}$	10^3C_{CT}, mol/cm^3	n_D	d	I_b^*, cm^{-1}	I_f^*, cm^{-1}	10^3C_b, mol/cm^3	n	$-(\nu - \nu_0)$, cm^{-1}	$\Delta\nu_{1/2}$, cm^{-1}
0	0	1.4470	1.48	0	1.311	0			
	0.048	1.4480	1.465	0.428	1.278	0.218	4.54	56	42.5
	0.096	1.4489	1.463	0.810	1.269	0.406	4.23	57	42
	0.127	1.4493	1.458	1.070	1.255	0.530	4.17	57	42
	0.157	1.4499	1.453	1.331	1.234	0.654	4.17	57.5	42.5
	0.195	1.4507	1.446	1.594	1.223	0.772	3.96	58	42.5
	0.283	1.4514	1.431	2.475	1.169	1.160	4.10	58	42
	0.366	1.4529	1.416	3.126	1.141	1.421	3.88	58.5	42.5
1.25	0	1.4550	1.536	0	0.386	0			
	0.034	1.4553	1.529	0.200	0.373	0.087	2.56	62	41
	0.101	1.4560	1.517	0.622	0.369	0.264	2.61	61.5	42
	0.159	1.4567	1.499	1.222	0.356	0.505	3.18	64	41.5
	0.283	1.4570	1.482	2.018	0.318	0.807	2.85	64	41.5
	0.379	1.4574	1.486	2.590	0.281	0.856	2.25	65	41
3.33	0	1.4577	1.555	0	0.179	0			
	0.021	1.4578	1.549	0.089	0.176	0.036	1.71	63	41
	0.026	1.4578	1.550	0.151	0.170	0.060	2.31	64	40
	0.051	1.4579	1.545	0.280	0.171	0.111	2.18	65	41
	0.099	1.4580	1.540	0.451	0.164	0.176	1.78	65	41
	0.101	1.4583	1.535	0.533	0.161	0.208	2.06	66	41
	0.195	1.4584	1.517	0.904	0.157	0.340	1.74	66	41
	0.283	1.4590	1.499	1.451	0.137	0.523	1.85	67	40.5
7.49	0	1.4591	1.565	0	0.0769	0			
	0.010	1.4591	1.563	0.033	0.0760	0.012	1.20	66	41
	0.016	1.4591	1.562	0.053	0.0758	0.020	1.25	67	41
	0.025	1.4593	1.560	0.080	0.0746	0.030	1.20	67	40
	0.028	1.4592	1.560	0.095	0.0748	0.035	1.25	67	40

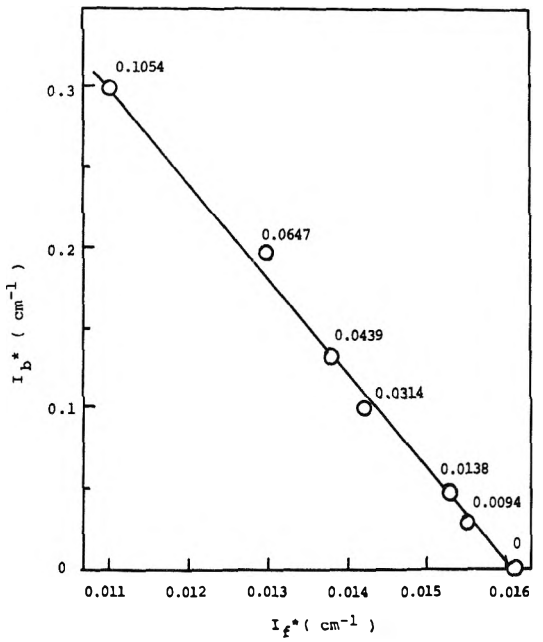

Figure 3. $I_b^* - I_f^*$ plot at $C^0_{CCl_4}/C^0_{CDCl_3} = 36.6$ for a ternary solution (chloroform-*d*–C_{12}AO–carbon tetrachloride). Numerical values on the circles show the molar concentration C_{12}AO.

in the unit of cm^{-1}, where l is a thickness of sample, I_0 the energy of incident light, I the energy of transmitted light, and ν the frequency of light.

The molar concentration of $CDCl_3$ is expressed as

$$C_{CDCl_3} = C_f + C_b \tag{2}$$

where C_f and C_b are molar concentrations of free and bonded $CDCl_3$, respectively. Then the absolute intensities of the ν(C–D) band for the bonded and free $CDCl_3$ are, respectively

$$\Gamma_b = \frac{1}{C_b} I_b$$
$$\Gamma_f = \frac{1}{C_f} I_f \tag{3}$$

in the unit of cm^2/mol. In order to determine both Γ_f and Γ_b simultaneously, we define a new form of a relative intensity, I^*

$$I^* = f_d f_c I \tag{4}$$

The factor, f_d, corresponds to the correction factor for the local field effect[23]

$$f_d = \frac{9n_D}{(n_D^2 + 2)^2} \tag{5}$$

where n_D is the refractive index of the solution. The factor, f_c, is introduced so that the relative intensity, I, can be compared at the same molar concentration for a given dilution ratio. Thus

$$f_c = C^0_{CDCl_3}/C_{CDCl_3} \tag{6}$$

together with the relations

$$C_f^* = f_c C_f \qquad C_b^* = f_c C_b$$
$$C_f^* + C_b^* = C^0_{CDCl_3} \tag{7}$$

Typical examples of the observed results are summarized in Table I for C_{12}AO and in Table II for CTACl. From Eq 3 and 7, the relation

$$\frac{I_f^*}{\Gamma_f} + \frac{I_b^*}{\Gamma_b} = C^0_{CDCl_3} \tag{8}$$

TABLE III: Final Results of the Intensity Data for the Chloroform-*d*-C_{12}AO-Carbon Tetrachloride System (A) and the Chloroform-*d*-CTACl-Carbon Tetrachloride System (B)

$C^0_{CCl_4}/C^0_{CDCl_3}$	$10^3C^0_{CDCl_3}$, mol/cm^3	Γ_f, cm^2/mol	Γ_b, cm^2/mol	Γ_b/Γ_f	$\bar{n}$	$(\Gamma_b/\Gamma_f)\bar{n}$
		A				
0	12.30	106	1726	16.3	5.2	85
0.97	5.66	86	2191	25.6	3.6	92
3.62	2.296	75	2268	30.4	2.8	85
11.09	0.858	66	2666	40.4	1.9	77
36.60	0.273	59	3422	58	0.9	52
		B				
0	12.30	107	1930	18	4.2	77
1.25	4.92	78	2262	29	2.7	78
3.33	2.46	73	2482	34	2.0	68
7.49	1.23	63	2709	43	1.2	52

TABLE IV: Results of the Intensity Data for the Chloroform-*d*-Pyridine-Carbon Tetrachloride System

$C^0_{CCl_4}/C^0_{CDCl_3}$	$10^3C^0_{CDCl_3}$, mol/cm^3	Γ_f, cm^2/mol	Γ_b, cm^2/mol	Γ_b/Γ_f	$-(\nu - \nu_0)$, cm^{-1}	$\Delta\nu_{1/2}$, cm^{-1}
0	12.30	107	1780	16.6	30.5	40.5
4.15	2.049	66	1175	17.8	30	35

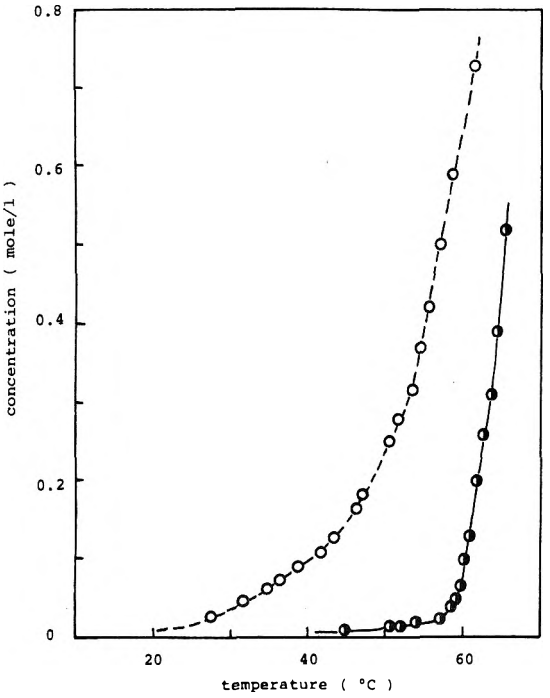

Figure 4. Solubilities of C_{12}AO (O) and CTACl (●) in carbon tetrachloride.

is obtained, which indicates that both Γ_f and Γ_b are obtained simultaneously for a given dilution ratio, when a plot of I_b^* against I_f^* for a series of concentration of a surfactant is made.[24,25] In Figure 3, a typical example of a $I_b^* - I_f^*$ plot for a ternary solution of CCl_4–$CDCl_3$–C_{12}AO at $(C^0_{CCl_4}/C^0_{CDCl_3})$ = 36.6 is shown. It is evident from the figure that a linear relationship is obtained between I_b^* and I_f^*. Consequently, Γ_f and Γ_b do not change their magnitude in this concentration range and at this dilution ratio. Linear behavior was obtained for all the systems studied in the present study.

The Γ_f and Γ_b values thus obtained are summarized in Table III. From the trend in Table III it can be seen that Γ_f decreases in magnitude as the dilution ratio increases. This corresponds to the fact that the hydrogen bonding between solvent $CDCl_3$ is broken as the concentration of CCl_4 increases. Therefore, even in the ternary solution of CCl_4–$CDCl_3$–surfactant, most of the $CDCl_3$ molecules are dissolved in CCl_4 when the dilution ratio is large. On the other hand, Γ_b increases in magnitude as the dilution ratio increases. This probably corresponds to the fact that the strength of hydrogen bond between $CDCl_3$ and a surfactant increases as the dilution ratio increases. The frequency shift of the ν(C–D) due to hydrogen bond formation increases as the dilution ratio increases (see Tables I and II), which is consistent with the increase of Γ_b.

Determination of Solvation Number. Figure 4 shows the observed temperature dependency of the solubility of C_{12}AO and CTACl in CCl_4. At room temperature, both C_{12}AO and CTACl are hardly soluble in CCl_4.[26] Therefore, the solvation number, n, can be determined exactly by method described previously. Using the observed Γ_b value, C_b is determined as

$$C_b = f_d I_b/\Gamma_b \tag{9}$$

and the solvation number is determined as

$$n = C_b/C_s \tag{10}$$

In Tables I and II, the C_b and n values calculated from eq 9 and 10 are summarized. The tables show that almost constant n values are obtained for a given dilution ratio and that the n value changes in magnitude as the dilution ratio changes. As the n value correspond to the number of chloroform-*d* molecules which forms a complex with one surfactant molecule, the above results indicate that the structure and nature of a complex of $CDCl_3$–surfactant are strongly related to the dilution ratio. The averaged n values, $\bar{n}$, at various dilution ratio are summarized in Table III for both C_{12}AO and CTACl systems.

Spectroscopic Information and Solubilization. The intensity data of the preceding sections show that a complex consisting of several $CDCl_3$ molecules and one surfactant is

formed in the ternary solution of CCl_4–$CDCl_3$–$C_{12}AO$ and of CCl_4–$CDCl_3$–CTACl. It is important to emphasize that the solvation number, n, decreases in magnitude as the dilution ratio increases for both $C_{12}AO$ and CTACl systems. The n value approaches unity almost as the dilution ratio approaches the solubilization limit. This suggests that the surfactants can dissolve in CCl_4 only when they form complexes with $CDCl_3$ molecules. In the case of $C_{12}AO$, for example, a complex is formed with about five $CDCl_3$ molecules for a binary mixture of $CDCl_3$–$C_{12}AO$. On adding CCl_4 to the binary solution, almost all $CDCl_3$ molecules are dissolved in the CCl_4. Moreover, the $CDCl_3$ molecules which formed a complex with the $C_{12}AO$ molecule are taken from the complex one by one, until there is no $CDCl_3$ molecule which can make a complex with the $C_{12}AO$ molecule. This may be the microscopic situation corresponding to the precipitation of $C_{12}AO$ from the ternary solution.

Table III shows that the absolute intensity of hydrogen bonded $CDCl_3$, Γ_b, increases as the dilution ratio, $C^0_{CCl_4}/C^0_{CDCl_3}$, increases. On the other hand, the number of $CDCl_3$ molecule decreases with the increase of the dilution ratio. If the strength of a hydrogen bond can be represented by the intensity ratio, Γ_b/Γ_f, the product of the intensity ratio and the solvation number, n, is an appropriate estimate of the stabilization energy of one surfactant molecule through hydrogen bond formation in the solution. The last column of Table III shows the calculated $\bar{n}(\Gamma_b/\Gamma_f)$ products. The result indicates that the product takes roughly the same value for all dilution ratios. This may correspond to the fact that the stabilization energy necessary for the surfactants to be dissolved is almost the same for all the dilution ratios. The decrease of the number of hydrogen bonding $CDCl_3$ is properly compensated by the increase of the strength of the remaining hydrogen bonds. If we give a little too much meaning to the $\bar{n}(\Gamma_b/\Gamma_f)$ value, its gradual decrease in magnitude with the increase of dilution ratio would be attributed either to the increase of an entropy term or to the decrease of intermolecular interactions between complexes, although we are not certain of the existence of such interactions yet. This certainly suggests future work into the problem.

Supplementary Results and Discussion. In the previous report,[1] the binary solution of pyridine and $CDCl_3$ was discussed as a reference system, because pyridine is known to form a (1:1) complex with $CDCl_3$. The results of the present study for the ternary solution of CCl_4–$CDCl_3$–pyridine are summarized in Table IV. For this system, the observed values for Γ_b and $\Delta\nu$(C–D) are constant on passing from the binary solution to ternary solution. This corresponds to the fact that the strength of the hydrogen bond between chloroform and pyridine does not change by dilution with CCl_4. Because pyridine is soluble in CCl_4, a complex such as this dissociates into pyridine and chloroform on dilution with CCl_4. Therefore, it is not necessary to form a different type of hydrogen bond on dilution in order to be stabilized in the ternary solution. Incidentally, it is of no meaning to calculate the solvation number, n, using eq 10 for the ternary solution of pyridine, although a (1:1) complex between chloroform and pyridine is formed even in the ternary solution.

Acknowledgment. The authors are pleased to express their sincere thanks to all the members of Fujiyama Laboratory and Tokyo Metropolitan University for their stimulating and helpful discussions. Helpful discussions and encouragement from Miss Yumiko Katayanagi are also deeply appreciated.

References and Notes

(1) M. Okazaki, I. Hara, and T. Fujiyama, *J. Phys. Chem.*, **80**, 64 (1976).
(2) C. J. Creswell and A. L. Allred, *J. Am. Chem. Soc.*, **85**, 1723 (1963).
(3) Soon Ng, *Spectrochim. Acta, Part A*, **28**, 321 (1972).
(4) T. Gramstad and O. Vikane, *Spectrochim. Acta, Part A*, **28**, 2131 (1972).
(5) K. B. Whetsel and R. E. Kagarise, *Spectrochim. Acta*, **18**, 329 (1962).
(6) K. B. Whetsel and J. H. Lady, *J. Phys. Chem.*, **68**, 1010 (1964).
(7) B. B. Howard, C. F. Jumper, and M. T. Emerson, *J. Mol. Spectrosc.*, **10**, 117 (1963).
(8) M. L. Josien, J. P. Leicknam, and N. Fuson, *Bull. Soc. Chim. Fr.*, 188 (1958).
(9) R. D. Green and J. S. Martin, *J. Am. Chem. Soc.*, **90**, 3659 (1968).
(10) A. Allerhand and P. R. Schleyer, *J. Am. Chem. Soc.*, **85**, 1233 (1963).
(11) G. R. Wiley and S. L. Miller, *J. Am. Chem. Soc.*, **94**, 3287 (1972).
(12) F. L. Sleiko, R. S. Drago, and D. G. Brown, *J. Am. Chem. Soc.*, **94**, 9210 (1972).
(13) A. Allerhand and P. v. R. Schleyer, *J. Am. Chem. Soc.*, **85**, 1715 (1963).
(14) R. E. Kagarise, *Spectrochim. Acta*, **19**, 629 (1963).
(15) V. A. Gushchin, *Opt. Spektrosk.*, **17**, 385 (1964).
(16) K. Kurosaki, *Nippon Kagaku Zasshi*, **83**, 655 (1962).
(17) G. S. Denisov, *Opt. Spektrosk.*, **6**, 426 (1964).
(18) M. F. Pushlenkov and E. V. Komarov, *Radiokhimiya*, **6**, 426 (1964).
(19) J. T. Bilmer and H. F. Shurvell, *J. Phys. Chem.*, **77**, 2085 (1973).
(20) V. F. Bystriv, V. P. Lezina, and S. M. Shostakovskii, *Opt. Spektrosk.*, **3**, 339 (1967).
(21) S. Nishimura, C. H. Ke, and N. C. Li, *J. Phys. Chem.*, **72**, 1297 (1968).
(22) O. Torbjoern, *Acta Chem. Scand.*, **24**, 3081 (1970).
(23) S. R. Polo and M. K. Wilson, *J. Chem. Phys.*, **23**, 2376 (1955); A. C. Gilby, J. Burr, and B. Crawford, Jr., *J. Phys. Chem.*, **70**, 1520 (1966); T. Fujiyama, J. Herrin, and B. L. Crawford, Jr., *Appl. Spectrosc.*, **24**, 9 (1970).
(24) T. Fujiyama and M. Kakimoto, *Bull. Chem. Soc. Jpn.*, in press.
(25) K. O. Hartman, G. L. Carlson, W. G. Fately, and R. E. Witowski, *Spectrochim. Acta, Part A*, **24**, 157 (1968).
(26) The results in Figure 4 were observed in the present study. The references to previous work are: C. W. Hoerr and H. J. Harwood, *J. Am. Chem. Soc.*, **74**, 4290 (1952); R. A. Reck, H. J. Harwood, and A. W. Ralston, *J. Org. Chem.*, **12**, 517 (1947); S. H. Shapiro, "Fatty Acids and Their Industrial Applications", New York, N.Y., pp 109–119.

A Method of Studying the Rate of the Photochemical Reaction of a Powdered Sample from Reflectance Measurements

E. L. Simmons

Department of Chemistry, University of Natal, Durban, South Africa *(Received September 15, 1975)*

Publication costs assisted by the University of Natal

An equation is derived which describes the rate of the photochemical reaction of a powdered sample in terms of its diffuse reflectance. For short reaction times, the equation reduces to a form which is much simpler than the previously reported rate equation for such a reaction. The equation is tested by the use of previously reported experimental results for the photochemical reaction of $K_3[Mn(C_2O_4)_3]\cdot 3H_2O$ and by studying the photochemical reaction of powdered $K_3[Fe(C_2O_4)_3]\cdot 3H_2O$.

Introduction

A number of attempts have been made to describe theoretically the rates of photochemical reactions of solid samples. Rate equations for the photochemical reaction of a solid sample with slab geometry have been derived by several authors for various special cases.[1-10] Photochemical reactions of powdered layers have also been treated theoretically and equations were obtained from which quantum yield values can be determined from rate data.[11-13] However, many solid samples are most easily obtained and handled in the form of bulk powdered samples. The theoretical treatment of the rate of the photochemical reaction of a bulk powdered sample is complicated by the complexity of the interaction of light with such a sample. Undoubtedly the most convenient experimental method of following the extent of the photochemical reaction of a powdered sample is the technique of reflectance spectroscopy.[14,15]

Recently, through the use of a model introduced by Melamed[16] which treats a powdered sample as a collection of uniformly sized rough-surfaced spherical particles, an equation was derived which relates the diffuse reflectance of a powdered sample to the fundamental optical parameters in a very simple manner.[17] Although a number of assumptions and approximations were made in the derivation of the equation, it agreed well with experimental measurements for powdered dydimium glass[17] and comparison[18,19] with more elaborate theories[20] indicates that the equation gives good approximate values for the diffuse reflectance over the relative index of refraction range of 1.5–2.5. The equation has been applied to the description of the luminescent properties of powdered samples[21] and, more recently,[22] to the description of the rate of the photochemical reaction of a bulk powdered sample. In the latter investigation, an approximate equation was obtained which describes the rate of the photochemical reaction of a powdered sample in terms of its diffuse reflectance in a somewhat complicated manner. Further investigation has revealed that the same model may be used to obtain a simpler, more easily applied, and probably more accurate rate equation. The purpose of this report is to describe the derivation of this equation which is tested using experimental results for the photochemical reactions of $K_3[Mn(C_2O_4)_3]\cdot 3H_2O$ and $K_3[Fe(C_2O_4)_3]\cdot 3H_2O$.

Theoretical Considerations

Background. Using a model representing a powdered sample as a collection of uniformly sized rough-surfaced spherical particles, the diffuse reflectance, R, for an infinitely thick sample, has been related to the fundamental optical parameters by the following equation:[17]

$$R = \frac{1 - (2A - A^2)^{1/2}}{1 - A} \tag{1}$$

where A is the fraction of incident light absorbed by a particle and is given by

$$A = \frac{(1 - \bar{m}_e)(1 - \exp[-2kd/3])}{1 - \bar{m}_i \exp[-2kd/3]} \tag{2}$$

where d is the average particle diameter, k the absorption coefficient, $\bar{m}_e$ the fraction of externally incident radiation reflected by a particle surface, and $\bar{m}_i$ the fraction of internally incident radiation reflected by a particle surface ($\bar{m}_e$ and $\bar{m}_i$ are related to Fresnel's equation and the Lambert cosine law and have been calculated for relative index of refraction values from one to five).[16]

By making two approximations for weakly absorbing powdered samples, it has been shown that eq 1 and 2 may be expressed in the form of a very simple equation.[17] Approximation 1 involved carrying out the indicated division in eq 1 to obtain ($A^2 \ll 2A$)

$$R = 1 - (2A)^{1/2} + A \ldots \simeq \exp[-(2A)^{1/2}] \tag{3}$$

while approximation 2 involved considering the exponential term in eq 2 as near unity for weakly absorbing powders and hence

$$1 - \bar{m}_i \exp[-2kd/3] \simeq 1 - \bar{m}_i \tag{4}$$

and

$$1 - \exp[-2kd/3] \simeq 2kd/3 \tag{5}$$

therefore

$$A \simeq \frac{1 - \bar{m}_e}{1 - \bar{m}_i}(2kd/3) = n^2 2kd/3 \tag{6}$$

since it has previously[17] been shown that the relative index of refraction, n, is related to $\bar{m}_i$ and $\bar{m}_e$ by $n^2 = (1 - \bar{m}_e)/(1 - \bar{m}_i)$. Therefore

$$R \simeq \exp[-2n(kd/3)^{1/2}] \tag{7}$$

A curious feature concerning the two approximations is that they tend to cancel each other.[17] While R values calculated using either approximation individually begin to deviate from those calculated using eq 1 and 2 at rather high R values, those

calculated using eq 7 which involve both approximations agree with eq 1 and 2 reasonably well even for low R values. Hence, a weakness of the previously derived[22] equation which describes the rate of the photochemical reaction of a powdered sample is that it is based on eq 1 and 6 and therefore involves only approximation 2. The equation derived here is based on eq 7 which involves both approximation and should therefore be more accurate.

The previously obtained equation describing the rate of the photochemical reaction of a bulk powdered sample in terms of its diffuse reflectance is[22]

$$g(R) - g(R_c) = \phi\epsilon n^2 I_0 t \tag{8}$$

where

$$g(R) = -\frac{1}{1+R^2} + (1 - A_P)\tan^{-1} R + \tfrac{1}{2}\ln\left[\frac{1+R^2}{(1-A_P)(1+R^2) - 2R}\right] + \tfrac{1}{2}(2A_P - A_P^2)^{1/2} \times \ln\left[\frac{(1-A_P)R - 1 - (2A_P - A_P^2)^{1/2}}{(1-A_P)R - 1 + (2A_P - A_P^2)^{1/2}}\right] \tag{9}$$

where ϕ is the quantum yield, I_0 the radiation intensity at the sample surface, ϵ the absorption coefficient given by

$$\epsilon = Mk/\rho \tag{10}$$

where M is the molecular mass of the reactant and ρ its density, and A_P the fraction of incident radiation absorbed by a particle of pure product.

Use of eq 8 therefore involves the lengthy calculations of $g(R)$ values. Another advantage of the equation derived in this investigation is that it is simpler in form and hence more easily applied.

The Derivation. The assumptions made in the following derivation are those made in the derivation of eq 7 based on the particle model and two other assumptions. Hence, the treatment is only valid for a powdered sample which (i) can be considered infinitely thick, (ii) is made up of particles whose diameters are large compared to the wavelength of the reacting radiation (so that Rayleigh scattering can be ignored), (iii) is made up of particles which are ideally diffusing (scatter radiation in all directions with equal intensity), (iv) for which adjacent particle layers may be considered to have similar reflectance values during the reaction, and (v) for which the index of refraction remains constant throughout the reaction.

Consider an infinitely thick powdered sample composed of substance, A, which conforms to the above assumptions and which undergoes a photochemical reaction to give product, P:

$$A \xrightarrow{h\nu} P \tag{11}$$

The sample is illuminated with monochromatic radiation of intensity, I_0, at the sample surface. It has previously been shown that if assumptions (i)–(v) are valid, then the rate of disappearance of A in the ith particle below the sample surface is given by[22]

$$dC_i/dt = -\phi\epsilon n^2 C_i I_i (1 + R_i^2) \tag{12}$$

where C_i is the concentration of A in the ith particle, $I_i(1 + R_i^2)$ the total radiation intensity on the ith particle, and R_i the reflectance of the ith particle.

From eq 7, the reflectance of a particle containing a mixture of two components, A and P, is given by

$$R_i = \exp\left[-2n(d/3)^{1/2}\left(k\frac{C_i}{C_0} + k_P\frac{C_{P_i}}{C_0}\right)^{1/2}\right] \tag{13}$$

where the subscript, P, refers to the product and C_0 is the concentration of A in pure A. Equation 13 may be rearranged and solved for C_i making use of the relation

$$C_0 = C_i + C_{P_i} \tag{14}$$

to give

$$C_i = C_0\frac{(\ln R_i)^2 - 4n^2k_P/3d}{(4n^2k_P/3d)(k - k_P)} \tag{15}$$

or

$$C_i = C_0\frac{(\ln R_i)^2 - (\ln R_P)^2}{(\ln R_A)^2 - (\ln R_P)^2} \tag{16}$$

where R_A is the reflectance of pure A and R_P that of pure P. Differentiating eq 16 with respect to time gives

$$\frac{dC_i}{dt} = C_0\frac{2\ln R_i}{(\ln R_i)^2 - (\ln R_P)^2}\frac{d\ln R_i}{dt} \tag{17}$$

Substituting eq 16 and 17 into eq 12 and rearranging for integration making use of the condition that at $t = 0$, $R_i = R_A$, gives

$$\int_{R_A}^{R_i}\frac{2\ln R_i\, d\ln R_i}{(1+R_i^2)[(\ln R)^2 - (\ln R_P)^2]} = -\int_0^t \phi\epsilon n^2 I_i\, dt \tag{18}$$

Finally, recognizing that only the reflectance, R, of the surface particles is experimentally measurable, eq 18 may be written for the surface particles as

$$\int_{R_A}^{R}\frac{2\ln R\, d\ln R}{(1+R^2)[(\ln R)^2 - (\ln R_P)^2]} = -\phi\epsilon n^2 I_0 t \tag{19}$$

For experimental applications, the reflectance of a powdered sample undergoing a photochemical reaction can be measured as a function of time, the integral in eq 19 could be numerically evaluated, and a plot of the integral values vs. time should give a straight line with a slope of $-\phi\epsilon n^2 I_0$. Hence, from such a plot, if ϵ, n, and I_0 are known, ϕ could be determined. However, one of the purposes of this investigation is to obtain a simpler, more easily applied rate equation. This can be done for short reaction times in the manner described below.

First, it can be seen that the integral may be written as

$$\int_{R_A}^{R}\frac{2\ln R\, d\ln R}{(1+R^2)[(\ln R)^2 - (\ln R_P)^2]} = \frac{1}{1+R^2}\ln\left[\frac{(\ln R)^2 - (\ln R_P)^2}{(\ln R_A)^2 - (\ln R_P)^2}\right] + \int_{R_A}^{R}\frac{2R^2}{(1+R^2)^2}\ln\left[\frac{(\ln R)^2 - (\ln R_P)^2}{(\ln R_A)^2 - (\ln R_P)^2}\right] d\ln R \tag{20}$$

which can be rearranged and the two integrals combined to give

$$\frac{1}{1+R^2}\ln\left[\frac{(\ln R)^2 - (\ln R_P)^2}{(\ln R_i)^2 - (\ln R_P)^2}\right] = \int_{R_A}^{R}\left[\frac{\ln R}{(\ln R)^2 - (\ln R_P)^2} - \frac{R^2}{1+R^2} \times \ln\left[\frac{(\ln R)^2 - (\ln R_P)^2}{(\ln R_A)^2 - (\ln R_P)^2}\right]\right]\frac{2d\ln R}{(1+R^2)} \tag{21}$$

Finally, noticing that for short reaction times for which $R_A \sim R$

$$\left|\frac{\ln R}{(\ln R)^2 - (\ln R_P)^2}\right| \gg \left|\frac{R^2}{1+R^2} \times \ln\left[\frac{(\ln R)^2 - (\ln R_P)^2}{(\ln R_A)^2 - (\ln R_P)^2}\right]\right| \quad (22)$$

the following equation can be written:

$$\frac{1}{1+R^2}\ln\frac{(\ln R) - (\ln R_P)}{(\ln R_A)^2 - (\ln R_P)^2} \simeq \int_{R_A}^{R}\frac{2\ln R\, d\ln R}{(1+R^2)[(\ln R)^2 - (\ln R_P)^2]} \quad (23)$$

and hence, for small conversion

$$\frac{1}{1+R^2}\ln\frac{(\ln R)^2 - (\ln R_P)^2}{(\ln R_A)^2 - (\ln R_P)^2} \simeq -\phi\epsilon n^2 I_0 t \quad (24)$$

Therefore, plots of values of the simple function in eq 24 vs. t should give straight lines for small conversion from which ϕ values can be calculated. In practice, for any given reaction, tests should be made to determine to what values of R the inequality in eq 22 holds.

It is of interest to note that by making use of eq 16 for surface particles, eq 24 may be written as

$$\ln\frac{C}{C_0} \simeq -\phi\epsilon n^2 I_0 t(1+R^2) \quad (25)$$

or

$$C \simeq C_0 \exp[-\phi\epsilon n^2 I_0 t(1+R^2)] \quad (26)$$

Hence, for small conversion, the concentration change of A in the surface particles approximately follows first-order kinetics analogous to simple fluid phase photochemical reactions.

Another point which may be of importance for experimental applications is that if ϵ and n are unknown but the average particle diameter, d, is known, then by making use of eq 7 and 10, values of ϵn^2 can be determined from reflectance measurements

$$\epsilon n^2 = \frac{3M(\ln R_A)^2}{4d\rho} = \frac{3(\ln R_A)^2}{4C_0 d} \quad (27)$$

Experimental Procedures

The compound, $K_3[Fe(C_2O_4)_3]\cdot 3H_2O$, which undergoes an oxidation–reduction reaction in the solid state when irradiated with ultraviolet light, was prepared as previously described.[23] Samples with particle sizes between 45–70 and 75–90 μm were obtained by sieving finely ground samples of the compound. The photochemical reactions were studies in a manner similar to that described previously.[22] Powdered samples were packed into a holder and photolyzed with light from a Bausch and Lomb high-intensity monochromator with a mercury lamp source. The radiation intensity was measured with a Ysi Kettering Radiometer and the diffuse reflectance of the sample was obtained after timed intervals of irradiation. A wavelength of 450 nm was chosen for these studies because the diffuse reflectance of the sample does not change enough during the reaction at shorter wavelengths to allow reasonably accurate measurements.

Comparison of Theory with Experiment

In order to apply eq 24 it is first necessary to establish whether or not the validity of the inequality given by eq 22 holds. For the reflectance changes of $K_3[Fe(C_2O_4)_3]\cdot 3H_2O$ at 450 nm, the smaller function never exceeded 5% of the larger function over the time ranges used in the investigation and therefore the inequality was assumed valid. Figure 1 illustrates rate plots using eq 24 for the reaction of $K_3[Fe(C_2O_4)_3]\cdot 3H_2O$ at 450 nm for the two different particle sizes and different radiation intensities. As can be seen, reasonably linear curves were obtained.

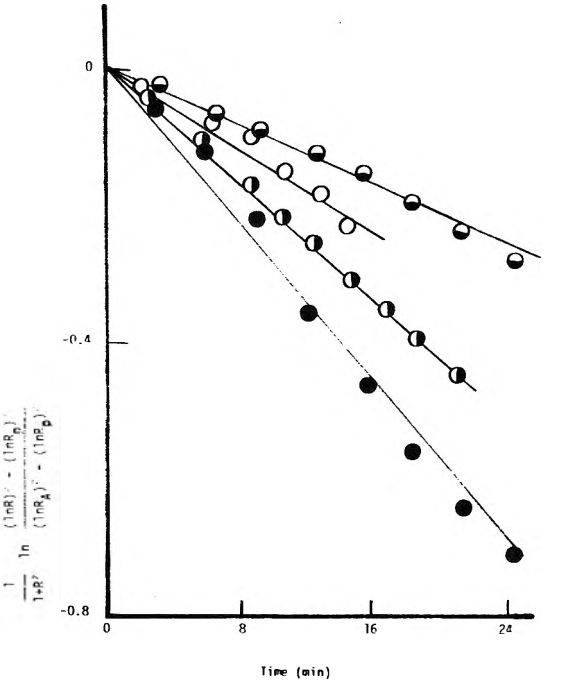

Figure 1. Rate plots for the photochemical reaction for $K_3[Fe(C_2O_4)_3]\cdot 3H_2O$ at 450 nm: (◒) $45 < d < 75$, $I_0 = 0.98 \times 10^{-8}$; (○) $75 < d < 90$, $I_0 = 1.32 \times 10^{-8}$; (◑) $75 < d < 90$, $I_0 = 2.24 \times 10^{-8}$; (●) $45 < d < 75$, $I_0 = 2.41 \times 10^{-8}$.

TABLE I: Quantum Yields for the Solid-State Photochemical Reaction of $K_3[Fe(C_2O_4)_3]\cdot 3H_2O$

I, einstein $cm^{-2}\ s^{-1}$	d, μm	Slope, s^{-1}	ϕ, einstein mol^{-1}
0.98×10^{-8}	45–75	1.60×10^{-4}	1.27
2.41×10^{-8}	45–75	4.42×10^{-4}	1.43
1.32×10^{-8}	75–90	2.36×10^{-4}	1.40
2.24×10^{-8}	75–90	3.47×10^{-4}	1.21

Using eq 7 and 10 along with the known values of the density and index of refraction values of the compound (from the Handbook of Chemistry and Physics) and measured values of R_A, the value of ϵn^2 was estimated to be 1.28×10^4 cm^2 mol^{-1} for $K_3[Fe(C_2O_4)_3]\cdot 3H_2O$. Therefore quantum yield values could be calculated from the slopes of the curves in Figure 1. Table I summarizes the values obtained. As can be seen, the average value of the quantum yield for the reaction obtained by this method is about 1.3. This value is in good agreement with one value (1.3)[24] previously obtained for 334-nm radiation but is in poor agreement with other values less than unity which have been obtained (0.07–0.9 in the 250–400-nm wavelength region[25–27]). The causes for the disagreements are unknown although it must be pointed out that because of the assumptions and approximations made in this theoretical investigation the value obtained here can only be considered a rough estimate. It is interesting to note, however,

TABLE II: Test of the Validity of the Inequality Given by Eq 22 for $K_3[Mn(C_2O_4)_3]\cdot 3H_2O$

$$\left|\frac{\ln R}{(\ln R)^2 - (\ln R_P)^2}\right| \gg \left|\frac{R}{1+R^2}\ln\left[\frac{(\ln R)^2 - (\ln R_P)^2}{(\ln R_A)^2 - (\ln R_P)^2}\right]\right|$$

I II

R	I	II	%
		λ 400 nm	
0.30	−0.892	−0.020	2.9
0.35	−1.048	−0.067	6.4
0.40	−1.239	−0.126	10.2
0.45	−1.485	−0.208	14.0
0.50	−1.822	−0.316	17.3
0.55	−3.174	−0.646	20.5
0.60	−5.034	−0.912	18.1
0.65	−13.105	−1.386	10.6
		λ 350 nm	
0.10	−0.447	−0.003	0.7
0.15	−0.550	−0.016	2.9
0.20	−0.680	−0.041	6.0
0.25	−0.782	−0.081	10.4
0.30	−0.926	−0.140	15.1
0.35	−1.103	−0.182	16.5
0.40	−1.329	−0.321	24.2
0.45	−1.638	−0.451	27.5
0.50	−2.100	−0.613	29.2
0.55	−2.880	−0.820	28.5
0.60	−4.601	−1.100	23.9
0.65	−12.110	−1.571	12.9

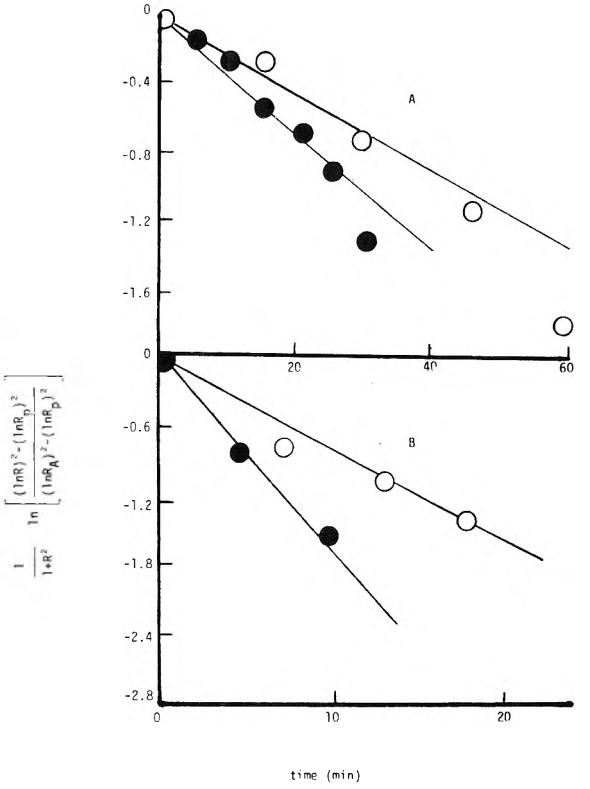

Figure 2. Plots of g(R) vs. t for the photochemical reaction of $K_3[Mn(C_2O_4)_3]\cdot 3H_2O$: (A) 400 nm, (O) $I_0 = 1.04 \times 10^{-8}$, (●) $I_0 = 1.64 \times 10^{-8}$; (B) 350 nm (O) $I_0 = 1.11 \times 10^{-8}$, (●) $I_0 = 1.67 \times 10^{-8}$.

that the value is very close to the value of about 1.2 obtained for the corresponding reaction in aqueous solutions for a wide wavelength range.[28]

Equation 24 was also tested using the previously obtained data for the photochemical reaction of $K_3[Mn(C_2O_4)_3]\cdot 3H_2O$. Inequality 22 was first tested and Table II lists calculated values of each function and the percent difference for reflectance values of a reacting sample of $K_3[Mn(C_2O_4)_3]\cdot 3H_2O$ at 400 nm ($R_A = 0.25$, $R_P = 0.73$) and at 350 nm ($R_A = 0.07$, $R_P = 0.68$). As can be seen, if quantum yield estimates within 15% are to be obtained, only R values less than about 0.45 should be used at 400 nm and those less than about 0.30 should be used at 350 nm. For the reaction at 400 nm, most of the reflectance values previously obtained[22] were less than 0.45. However, for the reaction at 350-nm reflectance values up to 0.54 were obtained; these are in the error range of almost 30%. Hence, all reflectance values of over 0.30 were not used to prepare the rate plots.

The rate plots based on eq 24 are illustrated in Figure 2 for the photochemical reaction of $K_3[Mn(C_2O_4)_3]\cdot 3H_2O$ at 350 and 400 nm for different radiation intensities. All of the reflectance values at 400 nm were less than 0.45 except for that represented by the last point on the steepest curve ($R = 0.49$) and the last two on the other curve ($R = 0.485$ and $R = 0.599$). As expected, these points deviate from the linear curves. Table II lists the slopes of the curves along with the previously obtained[22] values for ϵn^2 and the calculated quantum yield values. The quantum yield values obtained in this investigation are essentially the same as those previously obtained.[22] For the reaction at 400 nm, the values obtained agree reasonably well with previously obtained values[12] for the reaction of thin powdered layers ($\phi = 0.52 \pm 0.09$). Again, for this reaction, the quantum yield values are close to those obtained in aqueous solution (0.5 at 400 nm and 0.3 at 350 nm).[29]

TABLE III: Quantum Yield Values for the Photochemical Reaction of Powdered $K_3[Mn(C_2O_4)_3]\cdot 3H_2O$

I_0, einstein $cm^{-2}\ s^{-1}$	Slope, s^{-1}	ϵn^2, $cm^2\ mol^{-1}$	ϕ, mol einstein^{-1}
	λ 400 nm		
1.04×10^{-8}	4.2×10^{-4}	1.0×10^5	0.40
1.64×10^{-8}	7.6×10^{-4}	1.0×10^5	0.46
	λ 350 nm		
1.11×10^{-8}	1.3×10^{-3}	4.9×10^5	0.24
1.67×10^{-8}	2.2×10^{-3}	4.9×10^5	0.27

Discussion

Because of the large number of assumptions and approximations made in the derivation of eq 24, quantum yield values obtained by its use can only be considered as rough estimates. Obtaining estimates of quantum yield values for solid-state photochemical reactions is, however, important because of the increasing interest of solid-state photochemistry.[14,15] Considerably more theoretical work in this field is necessary before accurate quantum yield values can be obtained using reflectance measurements, but hopefully the equation derived in this investigation can serve as a starting point.

The main advantage of the equation derived in this investigation over the other[22] rate equation which has been derived for a powdered sample is that it is simpler and more easily applied. There are, however, other reasons for believing that it is also more nearly correct. These are: (1) the equation is based on both previously described approximations which tend to cancel each other out (rather than only a single approximation), and (2) the equation predicts the expected

approximately exponential decrease in concentration of the reactant (eq 26). Equation 24 is only valid for small reaction times. However, it is for short reaction times that approximation (iv) is most nearly valid. In any case, using reflectance data for short reaction times present no great experimental difficulties.

Undoubtedly, the most bothersome assumption made in the derivation of eq 24 is that the relative index of refraction remains approximately constant throughout the reaction. There is actually no assurance that the indices of refractions of the reactant and the photoproduct(s) are the same. However, for small conversion, only small amounts of the photoproduct(s) build up within the particles and, hence, should not greatly affect the index of refraction.

References and Notes

(1) P. G. Barker, M. P. Halstead, and J. H. Purnell, *Trans. Faraday Soc.*, **65**, 2404 (1969).
(2) C. E. Herrick, Jr., *IBM J. Res. Dev.*, **10**, 2 (1966).
(3) C. E. Herrick, Jr., *J. Opt. Soc. Am.*, **42**, 904 (1952).
(4) C. T. Slack, *Opt. Acta*, **17**, 47 (1970).
(5) H. Mauser, *Z. Naturforsch.*, **225**, 569 (1967).
(6) T. R. Sliker, *J. Opt. Soc. Am.*, **53**, 454 (1963).
(7) E. L. Simmons, *J. Phys. Chem.*, **75**, 588 (1971).
(8) P. Douzou and C. Whippler, *J. Chem. Phys.*, **60**, 1409 (1963).
(9) A. A. Burr, E. J. Llewellyn, and G. F. Lothian, *Trans. Faraday Soc.*, **60**, 2177 (1964).
(10) E. Mohn, *Appl. Opt.*, **7**, 1570 (1973).
(11) H. E. Spencer and M. W. Schmidt, *J. Phys. Chem.*, **74**, 3472 (1970).
(12) E. L. Simmons and W. W. Wendlandt, *Anal. Chim. Acta*, **53**, 81 (1971).
(13) E. L. Simmons, *J. Phys. Chem.*, **78**, 1265 (1974).
(14) E. L. Simmons and W. W. Wendlandt, *Coord. Chem. Rev.*, **7**, 11 (1971).
(15) E. L. Simmons, *Coord. Chem. Rev.*, **14**, 181 (1974).
(16) N. T. Melamed, *J. Appl. Phys.*, **34**, 560 (1963).
(17) E. L. Simmons, *Opt. Acta*, **18**, 59 (1971).
(18) E. L. Simmons, *Opt. Acta*, **19**, 845 (1972).
(19) E. L. Simmons, *Appl. Opt.*, **14**, 1380 (1975).
(20) E. L. Simmons, *J. Appl. Phys.*, **46**, 344 (1975).
(21) E. L. Simmons, *Opt. Acta*, **21**, 315 (1974).
(22) E. L. Simmons and W. W. Wendlandt, *J. Phys. Chem.*, **79**, 1158 (1975).
(23) W. W. Wendlandt and E. L. Simmons, *J. Inorg. Nucl. Chem.*, **28**, 2420 (1966).
(24) J. W. Pitts, Jr., J. K. S. Wan, and E. A. Shuck, *J. Am. Chem. Soc.*, **86**, 3606 (1964).
(25) R. Ballardini, M. T. Gandolfi, and V. Balzini, V. Atti de II Convegno Nationale di Chimica Inorganica, Bressanone, July 1969, p 109.
(26) H. E. Spencer, *J. Phys. Chem.*, **73**, 2316 (1969).
(27) H. E. Spencer and M. W. Schmidt, *J. Phys. Chem.*, **75**, 2986 (1971).
(28) C. G. Hatchard and C. A. Parker, *Proc. R. Soc. London, Ser. A*, **235**, 518 (1956).
(29) G. B. Porter, J. G. W. Poering, and S. Karanka, *J. Am. Chem. Soc.*, **84**, 4027 (1962).
(30) C. A. Parker, *Trans. Faraday Soc.*, **50**, 1213 (1954).

Infrared Emission of Low Pressure Gases Induced by Carbon Dioxide Laser Radiation

R. T. Bailey and F. R. Cruickshank*

Department of Pure and Applied Chemistry, University of Strathclyde, Glasgow G1 1XL, Scotland *(Received October 10, 1975)*

From an examination of the decay lifetimes of the ir emission of CO_2, C_2H_4, and C_2H_5Cl (2–35 Torr) excited by CO_2 laser pulses of widths 200 μs–15 ms in cells of 8–24 mm bore at duty cycles of 1:1 to 1:55, it is concluded that, at 16.6-Hz excitation frequency, the emission spectra of these gases arise from hot C_2H_4 and C_2H_5Cl, but that the CO_2 is essentially only vibrationally "hot". It is shown that the decomposition of C_2H_4 and C_2H_5Cl is consistent with a thermal process and that ir excited states need not be involved.

Introduction

A considerable body of information is currently available[1,2] on the relaxation processes of some gases subjected to relatively short (1–2 μs) pulses of moderate (1–10 kW) power ir laser radiation. At longer pulse lengths (typically 15 ms) or with the laser on continuously (CW) the ir emission of all compounds absorbing the laser radiation, occurring at characteristic frequencies, is used to obtain spectra for qualitative analysis. This technique is more sensitive[3] than absorption spectroscopy and has been used to monitor air pollution. Some compounds react chemically[4] when the pulse width is sufficiently great and some of these reactions have been described as ir laser sensitized processes, implying that ir excited states are involved. Such is the range of processes which occurs under these conditions, that we feel it is necessary to reserve the term "ir laser sensitized reaction" for one in which the *reacting species* is not in Boltzmann equilibrium in all three degrees of freedom of vibration, rotation, and translation. Thus we exclude systems where rotational, vibrational, and translational temperatures are identical, even although such systems often contain severe thermal gradients (e.g., between the laser irradiated zone and the gas at the cell walls). Such systems frequently yield products not observed in the isothermal reaction and thus the appearance of novel products is *not* proof of a laser sensitized reaction in terms of our definition above, but may simply be the consequence of the thermal gradients.

Some gases "pumped" by long (~1–2 ms) ir laser pulses of lower power (2–15 W) are known[5,6] to yield inverted rotational populations in the ground vibrational state and can even be made to lase in the far ir. Such gases are confined to quartz or metal waveguides, and the relaxation processes, at these long excitation pulse widths, leading to the inverted populations are of prime importance in determining the mechanism of the laser action.

It is the purpose of the present paper to examine the relaxation of some model gases CO_2, C_2H_4, and C_2H_5Cl under long pulse, low power excitation at two duty cycles (ratio of pulse width to time between pulses) 1:1 and 1:55. From these relaxation times the nature of the emitting gas will be deduced. CO_2 is chosen because it is very well characterized and is a

TABLE I[a]

								8-mm Cell Bore								
P, Torr	2.9	2.9	2.9	2.9	8.2	8.2	8.2	8.2	19.7	19.7	19.7	19.7	34.4	34.4	34.4	34.4
τ, μs		218	177	266	184	208	178	169	80	104	101		71	59	55	
Power, W	1.5	3.8	7.5	15	1.5	3.8	7.5	15	1.5	3.8	7.5	15	1.5	3.8	7.5	15
								12-mm Cell Bore								
P, Torr	2.2	2.2	2.2	2.2	8.0	8.0	8.0	8.0	20	20	20	20	34	34	34	34
τ, μs	322	390	421	424	218	252	205	210	105	117	133	132	65	74	74	70
Power, W	1.5	3.8	7.5	15	1.5	3.8	7.5	15	1.5	3.8	7.5	15	1.5	3.8	7.5	15
								24-mm Cell Bore								
P, Torr	2.9	2.9	2.9	2.9	8.2	8.2	8.2	8.2	19.7	19.7	19.7	19.7	34.4	34.4	34.4	34.4
τ, μs	425	280	400	552	250	304	303	314	142	125	141	127	77.4	71.4	72.3	68.2
Power, W	1.5	3.8	7.5	15	1.5	3.8	7.5	15	1.5	3.8	7.5	15	1.5	3.8	7.5	15

[a] Chopper duty cycle 1:55 throughout.

simple molecule. C_2H_4 and C_2H_5Cl are known to react when the laser is CW and of high power. Reaction products under these conditions are not typical of the isothermal system, and it is proposed to extrapolate from the long pulse high duty cycle data to the CW limit in deciding if ir excited states are involved, i.e., to discover whether these decompositions are ir laser sensitized in terms of the definition above.

Experimental Section

The gases used were CO_2 (B.O.C. X grade), C_2H_4 (B.O.C. X grade), and C_2H_5Cl (BDH). All were fractionated in vacuo and were >99.99% pure as estimated by GLC.

The cell consisted of a stainless steel block (5 cm cube) with an interchangeable aluminum liner determining the effective working diameter. The liner had a horizontal slit cross path (3 mm × 28 mm) to allow observation of ir emission. A NaCl "light pipe" filled the space between output slit and emission observation window in order to reduce self-absorption effects. NaCl windows were used throughout. The laser path through the liner was circular in cross section and the three diameters 8 mm, 1.2 cm, and 2.4 cm were used.

The laser was a Ferranti 200 W, 4 m, CW, multimode device with a resistance-capacity smoothed power supply. The output was confined to the 945.8-cm^{-1} line (P(18) of the 00°1 → 10°0 transition) irrespective of power. Power was varied by adjustment of CO_2, N_2, and He flow rates as well as applied voltage. The 1-in. diameter beam was reduced to 10 mm diameter by means of a 1-in. thick asbestos brick and aluminum sheet collimator, focussed at a chopper wheel with a variable duty cycle and again just outside the cell, so that the beam diameter varied from 1 to 3 mm diverging toward the cell laser output window.

Two detectors were used. A SBRC high-speed gold-doped Ge device cooled to 77 K and biased at 180 V with a 1.2-kΩ load resistor was used to detect the laser pulse and generate a reference pulse for the detector electronics. Its amplified output was used as a laser power monitor.

A Spectronics In–Sb detector with automatic bias preamplifier was used to detect the fluorescence. The sapphire window limits the detector bandpass to a lower frequency bound at 2000 cm^{-1}. The preamplified signal was further amplified by a Tektronix 7A22 amplifier (dc to 1-MHz band width) and this signal, averaged on a Brookdeal boxcar integrator, was displayed on an X–Y plotter.

Results

Carbon Dioxide. This gas was investigated at four pressures and laser power levels for the three cell diameters at a 200-μs laser pulse width and chopper duty cycle of 1:55. The data are shown in Table I. Laser power varied by up to 15%, the variations being greatest at the lowest powers. This gave increased apparent noise on the final fluorescence trace and seemed to arise from cavity instabilities. A high frequency noise component was also present in laser power and was due to such instabilities.

From Table I it is clear that there is no variation in lifetime with laser power within experimental error (±15%) and such variations as are observed are random. The lowest pressure data were usually poorest, the signal being weakest.

Most of the signal-averaged decay traces were of high S/N ratio (>100) and yielded excellent linear first-order plots (Figure 1). Averaged lifetime data are plotted in Figure 2 and show a shortening of τ in the small bore cell, as expected, with the introduction of a significant cell wall quenching effect at the lowest pressures (i.e., τ decreases slightly below about 4 Torr). The line shown in Figure 2 is that of Flynn et al.[8] for short pulse, high power data. Our data reproduce his $p\tau$ product of 2597 μs Torr for V → T relaxation of the 00°1 → 00°0, CO_2 transition centered on 2350 cm^{-1}. Since heating effects were absent in Flynn's study we interpret this as an indication that virtually no gas heating occurs in CO_2 (≤150 K temperature rise) at 200-μs laser pulse lengths and 1:55 duty cycle.

At greater pulse lengths, e.g., 5 ms (8 W), apparently good first-order decay curves are obtained (Figure 3). The Guggenheim treatment[9] was used, under these circumstances, to analyze the data, since the baseline between pulses may not have been the true zero signal point. The time interval selected always exceeded two half-lives of the decay. The $p\tau$ product calculated from these data is 3516 μs Torr (Figure 4).

It was expected that CO_2 molecules, relaxing in a hot bath of thermalized CO_2, would be responsible for this different $p\tau$ value at long laser pulse excitation. However, the $p\tau$ values should *decrease* under these conditions contrary to our observation. Closer examination of the fluorescence traces reveals that they are composed of a steep gradient (arising from the chopper cutoff time) and a slower subsequent decay with τ in the millisecond region. The latter is presumably the controlling factor in the appearance of Figure 4 and the quality of the first-order plots, e.g., Figure 3, is fortuitous. The logarithmic first-order plot is clearly insensitive to this distortion. In the case of the short pulse data (Table I) the chopper cutoff time was *not* significant in comparison with the decay times observed and did not distort the decay curve.

Increased pressure reduces the significance of the slow decay, at 5-ms laser pulse excitation, giving the positive slope of Figure 4.

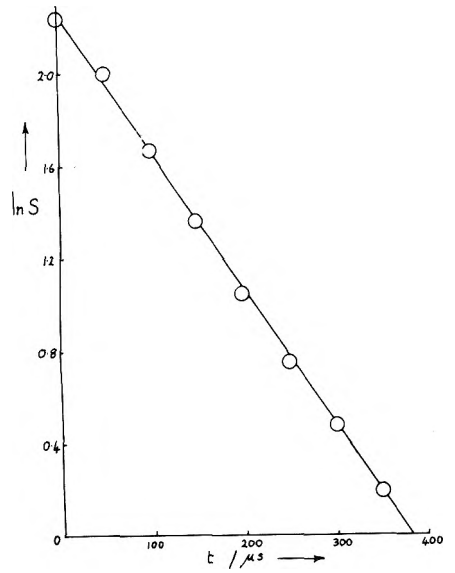

Figure 1. First-order plot of ln s (log signal in volts) vs. time in microseconds for 15-W laser power in 200-μs pulse on 8 Torr of CO_2 in the 8-mm bore cell.

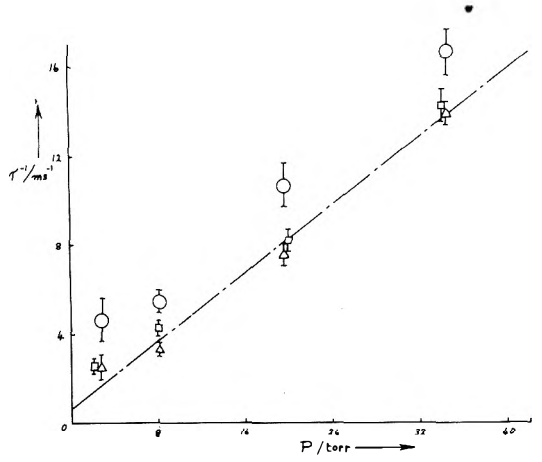

Figure 2. Averaged $1/T$ values (in ms^{-1}) against pressure (P, Torr). The chain line is that of Flynn et al. for the high pressure linear region: (⊙) 8 mm, (□) 12 mm, (△) 24 mm bore cell. Laser pulse width 200 μs.

With 15-ms laser pulses, the CO_2 absorption saturates, giving square wave emission pulses with some slow decay on the trailing edge of the pulse. Increasing the duty cycle of the chopper to 1:1 from 1:55 results in decay curves which are less and less exponential, ultimately becoming nearly linear. The baseline between pulses is then not the zero signal point and the decay is so slow that the slow component on the pulse trailing edge has grown in significance and is now controlling the decay observed. These are the conditions under which spectra have frequently been run, and it is meaningless to measure lifetimes from these curves, insufficient trace being available to enable accurate analysis. Since the observed waveform is not exponential, our previous model[3] is invalid for CO_2, although the interpretation for ethylene is correct as outlined below.

The variation of ir emission signal strength with laser power and CO_2 pressure is shown in Figure 5 for a 200-μs pulse width, 1:55 duty cycle, and 12 mm cell bore. At the highest power level and 2.2 Torr pressure the drop in amplitude is attributed to the approach of saturation. At higher pressures the curvature of the plot is less pronounced and this is consistent with

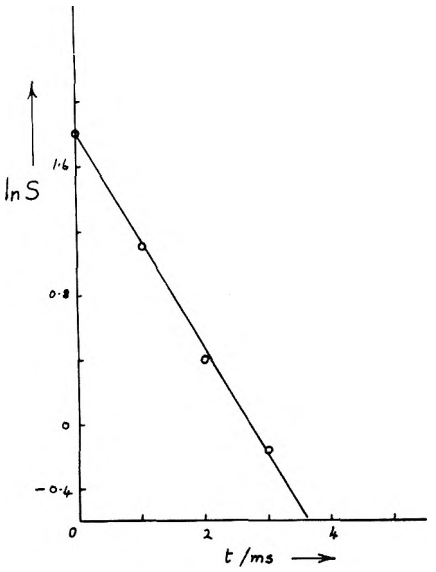

Figure 3. First-order plot of ln s (S is the Guggenheim ordinate ln volts, Δt = 3 ms, τ = 1.5 ms) vs. time in millisecond. Laser power 8 W in 5-ms pulse, 12-mm bore cell.

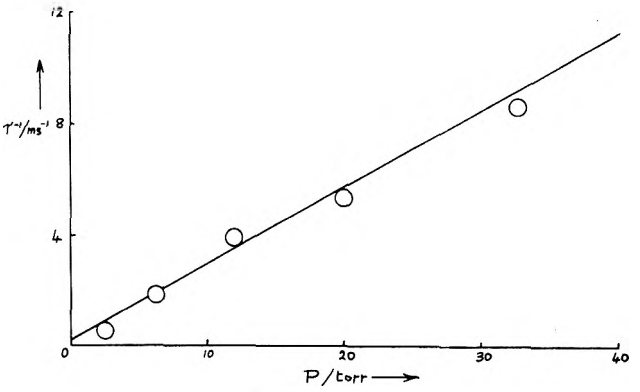

Figure 4. $1/T$ value (in ms^{-1}) vs. pressure (Torr). Laser power 8 W in 5-ms pulse, 12-mm bore cell.

the above interpretation. We have observed saturation at the higher duty cycle under these conditions. Less expected is the 34 Torr result with a dramatic drop in signal amplitude at laser powers above 8 W. Saturation cannot account for this phenomenon and it may arise from slight gas heating leading to a slightly divergent laser beam and thus an emission which is far less efficiently collected by our system. Such thermal lensing effects are well-known and also explain the overall drop in fluorescence intensity at this highest pressure.

Ethyl Chloride and Ethylene. Since both gases exhibited similar time dependent behavior in emission, only ethylene will be discussed in detail.

At the longest laser pulses (15 ms) and 1:1 duty cycle accurate first-order plots were obtained in the 12-mm cell (Figure 6). The lifetimes calculated from these passed through a maximum (Figure 7) of 7.5 ms at 80–90 Torr. The emission decay curves were far noisier than the CO_2 data. The occurrence of the maximum and its value are supported by our earlier work[3] where exponential decay was assumed, although the larger cell diameter in the earlier work resulted in a maximum in τ at a lower pressure (~20 Torr).

We interpret the reason for this maximum in τ as being a mass transport toward the cell walls. Diffusion of ir excited states to the walls typically is significant at far lower pressures

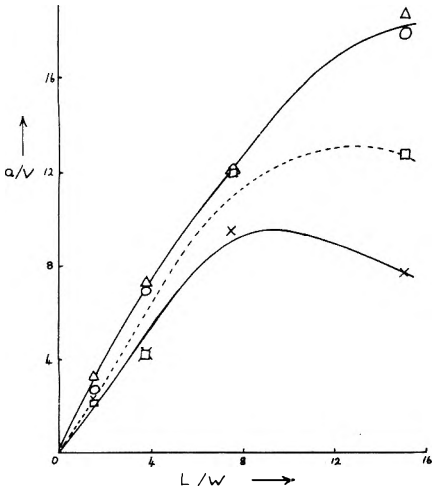

Figure 5. Amplitude of CO_2 fluorescence signal (a, volts), normalized to a common amplifier gain, vs. laser power, L (watts): (□) 2.2 Torr, (△) 8 Torr, (○) 20 Torr, (×) 34 Torr 200 μs laser pulse, 12-mm bore cell.

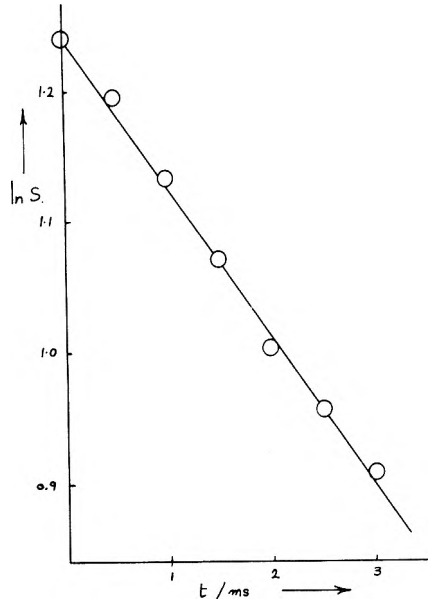

Figure 6. First-order decay plot for 30 Torr of ethylene fluorescence in the 12-mm bore cell. (S is the Guggenheim ordinate, t the time in milliseconds.) Laser power 15 W in 15-ms pulses at 1:1 duty cycle.

and is not reported at these higher pressures of C_2H_4. Most likely is the creation of a surrounding bath of hot, thermalized, molecules, in the cell, and their slow cooling at the cell wall. This is further supported by the observation that adding argon *lengthens* the lifetime until over 30 Torr are added. With shorter laser pulses (5 ms) and/or reduced duty cycle, the exponential nature of the decay signal is lost until at 5-ms pulses, 1:55 duty cycle the sharp decay, its observations now limited by the chopper cutoff time, is followed by a residual slow decay as seen in similar CO_2 runs. This residual decay has already been attributed to gas heating in the case of CO_2 and is consistent with the 1:1 duty cycle ethylene data. At 200 μs long, 1:55 duty cycle laser pulses very low amplitude ir emission signals are observed and only by careful boxcar averaging can the very noisy traces be recovered. Again laser power variation seemed to have little effect on the above phenomena. Under CW laser irradiation, the temperature of C_2H_4 and CO_2

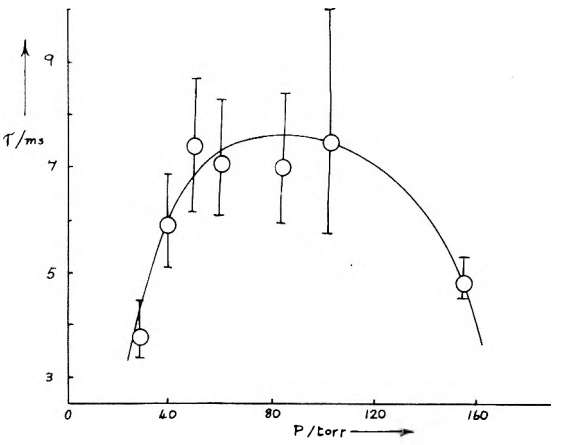

Figure 7. Variation of fluorescence lifetime (τ, millisecond) with pressure (P, Torr) for C_2H_4, 15-W laser in 15-ms pulses at 1:1 duty cycle. Maximum possible error estimates are shown and are rather large due to the noisy nature of some of the fluorescence traces (see text).

was measured by a thermocouple scanned across the 12-mm bore cell diameter (Figure 8). As the thermocouple nears the center of the cell the temperature should rise only at the 4.5-mm value of d as the laser impinges on the thermocouple. This behavior was observed approximately for CO_2 and the empty cell. For ethylene, however, the temperature never exceeded 420 K even at the center of the cell, indicating that in this case the laser beam must be highly divergent within the cell. This is consistent with strong absorption of laser radiation immediately behind the laser input window, followed by gas heating and thermal (divergent) lensing. We attribute the very slow decay of ir emission at long laser pulses and high duty cycles to the cooling of this heated volume of gas.

Laser radiation scattered from an 0.5 mm diameter pocket drilled in the laser entry window produced extremely noisy traces with the cell evacuated. A relatively insignificant amount of emission present in these traces is presumably due to scattered laser radiation heating some part of the apparatus. This test was performed to see if scattered laser radiation produced any significant fluorescence signal.

Ethyl chloride and ethylene differ in that the latter decomposes under prolonged irradiation at laser powers of 50–100 W 15-ms laser pulses and 1:1 duty cycle whereas ethyl chloride does not. This is contrary to the ratio of their thermal decomposition rate constants at a given temperature. However, ethylene has the greater extinction coefficient at 945.8 cm^{-1} and is thus expected to be at a higher temperature than the ethyl chloride for the same laser power. Thus a thermal explanation of the decomposition behavior is consistent with both this variation between ethylene and ethyl chloride and with their similar time dependent ir emission.

All lifetime measurements were carried out under conditions where no decomposition occurred.

Figure 9 shows the emission and absorption spectra of C_2H_4. By taking the ratio of the transmittance of the bands centered at 1450 cm^{-1} (see footnote 10) it is possible to calculate an approximate temperature for the ethylene of 900 ± 150 K which at a duty cycle of 1:1, 15 ms pulses is lower than the 1300 K previously observed[4] for CW laser irradiation. Temperature calculations from the band contour of the 1890-cm^{-1} band give 570 ± 150 K and for the ν_2 band 670 ± 150 K. Given the difficulty of calculating exact temperatures from these emission bands, we interpret these results as implying a single temperature of 750 K for C_2H_4 under pulsed irradiation.

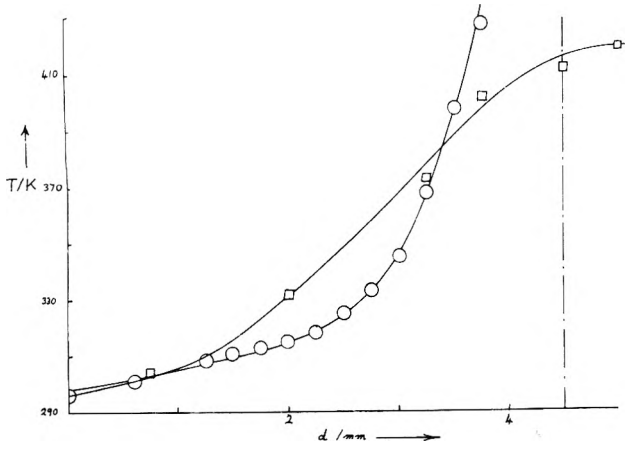

Figure 8. Temperature (T, K) vs. distance from the cell wall (12-mm bore cell) for C_2H_4 (60 Torr, □) and CO_2 (8 Torr, O) CW laser at 15 W. The vertical chain line represents the position of the edge of the laser beam. In the case of C_2H_4 the other half of the diameter gave an identical temperature profile. In the case of CO_2 the temperature became extremely high beyond the point shown.

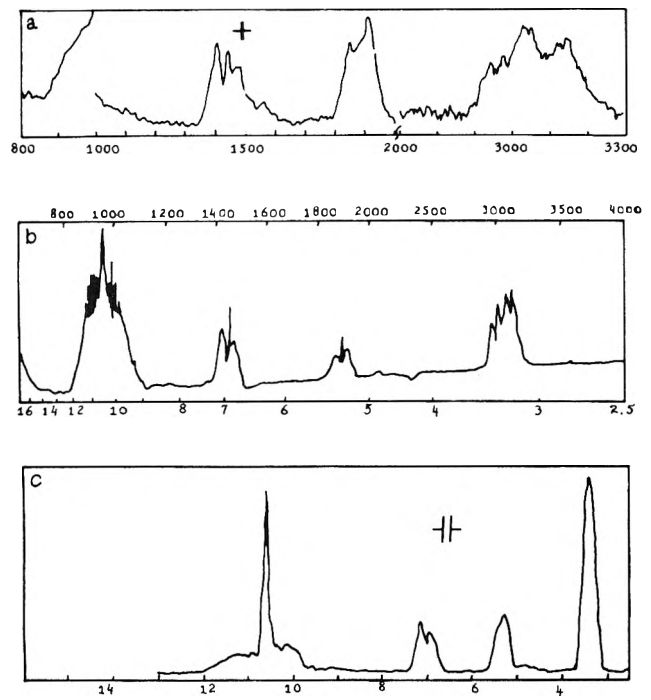

Figure 9. (a) Emission spectrum of 50 Torr of C_2H_4 on PE: E1 grating monochromator, 15 W laser, SW 6.5mm, SSW 14.3 cm^{-1} (1500 cm^{-1}); (b) absorption spectrum on P.E. 257; (c) emission spectrum on Grubb Parsons S-1 prism monochromator SW 0.7 mm, SSW 42 cm^{-1} (6.7 μ). Grating scattering of laser radiation is seen in (a) at the 1000-cm^{-1} grating change-over point. This scatter is also evident in (c). For all emission spectra a 16.6-Hz, 1:1 duty cycle laser chopper was used.

Conclusions

We find that the state of the gas subjected to pulsed CO_2 laser radiation depends on the gas, pressure, cell geometry, laser pulse width, and laser pulse duty cycle in a predictable way.

Carbon dioxide gas with laser pulse widths of 200 μs and 1:55 duty cycle is vibrationally hot with less than 150 K of translational temperature rise irrespective of laser power (with up to 15 W in the pulse). When the laser pulse width is increased to 5 ms and beyond, some element of the significant translational temperature rise is detected in the laser zone, by means of the long emission lifetime. With 15 ms long laser pulses the CO_2 absorption saturates and a quasi-steady-state translational temperature is produced which increases as the duty cycle is increased from 1:55 to 1:1. Thus when CO_2 laser induced ir emission spectra are obtained (1:1 chopper duty cycle, pulse width 15–60 ms) the CO_2 absorption is saturated, and a quasi-steady-state elevated translational temperature exists. It is also clearly possible to obtain CO_2 emission spectra with 200-μs laser pulses and 1:55 duty cycle at 15 W laser power, when no significant translational temperature rise occurs and the gas is only vibrationally hot.

Ethylene and ethyl chloride follow a similar pattern. The initial vibrational relaxation is so fast that the emission, when it is observed under our conditions and under conditions where laser induced emission spectra have been recorded, is almost entirely due to translationally hot gas cooling by interaction with the cell walls and colder molecules surrounding the laser irradiated zone. In larger bore cells the heating is more severe and in the case of gases with large extinction coefficients (e.g., C_2H_4) decomposition occurs. The more labile C_2H_5Cl with a lower extinction coefficient is not heated sufficiently to react at a significant rate. Powerful thermal lensing effects, in strongly absorbing gases, diverge the laser beam and give rise to noisy fluorescence signals which vary in intensity in a complex fashion with pressure due to varying efficiencies of fluorescence collection. We thus conclude, using Occam's razor, that C_2H_5Cl decomposition under CW CO_2 laser irradiation is unlikely to involve vibrationally exacted states, i.e., ethyl chloride decomposition,[4] under these conditions is *not* laser sensitized in terms of our definition above.

NOTE ADDED IN PROOF: It seems likely that ethyl iodide reacts similarly. (J. C. Bellows and F. K. Fong, *J. Chem. Phys.*, **63**, 3035 (1975).)

Acknowledgments. The authors wish to acknowledge the assistance of the Science Research Council in providing research apparatus, Dr. A. H. Brittain for commissioning the E-1 monochromator and running the emission spectrum of C_2H_4, and Messrs. M. Riddoch and F. Martinelli for preliminary work on CO_2 and ethylene carried out as part of their final degree course.

References and Notes

(1) R. T. Bailey and F. R. Cruickshank, *Mol. Spectrosc.*, **2**, 262 (1974).
(2) R. T. Bailey and F. R. Cruickshank, *Appl. Spectrosc. Rev.*, **10**, 1 (1975).
(3) R. T. Bailey, F. R. Cruickshank, and T. R. Jones, *Nature (London), Phys. Sci.*, **234**, 92 (1971).
(4) R. T. Bailey, F. R. Cruickshank, J. Farrell, D. S. Horne, A. M. North, P. B. Wilmot, and U. Tin Win, *J. Chem. Phys.*, **60**, 1699 (1974), and the appropriate sections of ref 1 or 2 above.
(5) T. Y. Chang, T. J. Bridges, and E. G. Burkhardt, *Appl. Phys. Lett.*, **17**, 249 (1970).
(6) D. T. Hodges and T. S. Hartwick, *Appl. Phys. Lett.*, **23**, 252 (1973).
(7) M. Margottin-Maclou, L. Doyenette, and L. Henry, *Appl. Opt.*, **10**, 1768 (1971).
(8) L. O. Hocker, M. A. Kovacs, C. K. Rhodes, G. W. Flynn, and A. Javan, *Phys. Rev. Lett.*, **17**, 233 (1966).
(9) E. A. Guggenheim, *Phil. Mag.*, **1**, 538 (1926).
(10) Let the transmittance of the 3100-cm^{-1} band be T_3 and the 1450-cm^{-1} band be T_1. We find

$$1.07 = \frac{\int T_1 \, d\nu}{\int T_3 \, d\nu} = \frac{\int [1 - \epsilon_1(\nu)] \, d\nu}{\int [1 - \epsilon_3(\nu)] \, d\nu} \quad (1)$$

(assuming zero reflectance) where $\epsilon_n(\nu)$ is emissivity at frequency ν of band n, defined as (energy emitted by line of frequency ν)/(energy emitted by black body at frequency ν)

$$= E_n(\nu)/E_{B_n}(\nu)$$

(1) becomes

$$1.07 = \frac{\Delta\nu_1 - \int \epsilon_1(\nu)\,d\nu}{\Delta\nu_3 - \int \epsilon_3(\nu)\,d\nu}$$

where $\Delta\nu_n$ is the frequency band width of band n.

$$= \frac{320 - \int \epsilon_1(\nu)\,d\nu}{370 - \int \epsilon_3(\nu)\,d\nu} = \frac{320 - \int \frac{E_1(\nu)}{E_{B_1}(\nu)}\,d\nu}{370 - \int \frac{E_3(\nu)}{E_{B_3}(\nu)}\,d\nu}$$

If we assume that the band widths are equal, the transmittance ratio is unity, and the black body emission over the band width is independent of frequency, we have

$$\frac{\int E_1(\nu)\,d\nu}{\int E_3(\nu)\,d\nu} = \frac{E_{B_1}(\nu)}{E_{B_3}(\nu)}$$

and the left-hand side is 0.34 ± 10% from either emission spectrum. Thus the ratio of the black body energy at 1450 and 3100 cm^{-1} must be ~0.34 and this occurs at 900 ± 100 K. Wide though the error limits are, the emission spectrum, taken while the C_2H_4 was under continuous irradiation, is indicative of a temperature consistent with its thermal decomposition rate.

Electron Spin Relaxation Mechanisms and Solvent Coordination in Bis(dithiooxalato)nitrosyliron(I) Solutions

Robert G. Kooser

Department of Chemistry, Knox College, Galesburg, Illinois 61401 *(Received November 17, 1975)*

Publication costs assisted by Cottrell College Science Grant, Research Corporation, and Dupont College Science Grant in Chemistry

Isotropic g values and hyperfine splitting constants for ^{14}N of bis(dithiooxalato)nitrosyliron(I) ($FeNO(dto)_2$) have been determined in 16 solvents. Plots of these electron spin resonance parameters vs. the solvent parameter Z showed that solvent coordination was occurring at the vacant sixth site of the iron complex. Similar results were found for bis(*cis*-1,2-dicyanoethylene-1,2-dithiolene)nitrosyliron(I). The splitting constant for $FeNO(dto)_2$ was studied as a function of temperature and this dependence was interpreted in terms of an equilibrium between the solvated and unsolvated radical. The widths of the three hyperfine lines of $FeNO(dto)_2$ were measured in six solvents as a function of temperature. They were found to depend on solvent, temperature, and the spectral index number $\tilde{m}$ of the line. The widths were fitted to the equation $\delta(\tilde{m}) = \alpha + \beta\tilde{m} + \gamma\tilde{m}^2$. In the strongly coordinating solvents (pyridine, dimethylformamide, and acetone), the spectral index number dependence was due to rotational modulation of the anisotropic g and dipolar tensors. The rotational correlation time in these solvents was obtained from the β term. This correlation time was used to subtract from the α term the contribution due to anisotropic g dipolar and spin–rotational interactions. A large, temperature-dependent residual component remained which was solvent independent and of an intramolecular nature. This residual width has not been seen in other transition metal complexes. In the weakly coordinating solvents ($CHCl_3$, CH_2Cl_2, and CH_3OH), an additional residual line width remained after subtraction of the anisotropic g dipolar, spin–rotational, and intramolecular components. This portion of the line width depended on solvent, temperature, and spectral index number. This relaxation arose from the two-jump equilibrium between the radical and its solvated form.

I. Introduction

Iron–nitrosyl complexes with sulfur containing ligands have been widely investigated by electron spin resonance (ESR) and other techniques. The pentacoordinate class ($Fe(NO)S_4$) of these complexes is particularly interesting and is divided into the dithiocarbamates ($Fe(NO)(S_2CNR_2)_2$),[1-4] the dithiolenes ($Fe(NO)(S_2C_2R_2)_2$),[4-7] and dithiooxalate ($Fe(NO)(S_2C_2O_2)_2$).[8,9] The dianionic form of these complexes is a spin doublet with an ESR spectrum of three hyperfine lines from the interaction with ^{14}NO.[1-8] Investigators have established the values of the **g** and hyperfine tensors for many of these complexes.[1,2,6,9]

All of these pentacoordinate compounds show similar ESR behavior but the isotropic g and hyperfine (a_N) values vary slightly with ligand substituent,[4-8] the ligand metal ring size being the major factor.[4] A marked solvent dependency has been found in g and a_N[3,7,9] and, in the case of the dithiocarbamates, this has been attributed to vacant sixth site solvent coordination.[3] These same resonance parameters also exhibit a temperature dependence.[3,9]

Besides characterizing the ESR behavior, several investigators have sought structural and dynamic information by studying the infrared spectra (principally the NO stretch),[3,7,8] the electronic spectrum,[7,8] and the electrochemistry[7] of these complexes. These findings are consistent with the information gathered by ESR. The similar chemical and dynamic behavior of this class of compounds suggests an identical electronic structure but none of the investigators has been able to establish the exact nature of the molecular orbital containing the unpaired electron.[2,7,8] There seems to be sufficient evidence to point to either a d_{z^2} or $d_{x^2-y^2}$ type orbital (a_1 symmetry in C_{2v}).[2,9]

While we know a great deal about the pentacoordinate iron–nitrosyls, we have found no systematic attempt to understand the electron spin relaxation processes of these mol-

ecules in solution. There is some evidence to suggest that iron–nitrosyls in the d^7 configuration have anomalously broad ESR lines when compared to other nitrosyl complexes. A study of the widths as function of solvent and temperature should elucidate what relaxation pathways are available and tell us about the solution dynamics of these compounds. We have used the bis(dithiooxalato)nitrosyliron(I) dianion ($FeNO(dto)_2$) as the model complex because there is only one magnetic nucleus in appreciable abundance (^{14}N), making the ESR lines undistorted by unresolved hyperfine structure. We will show that the solvent interacts at the vacant sixth site and, under certain conditions, this yields a contribution to the spin relaxation. We also will demonstrate that relaxation due to the reorientation of the anisotropic **g** and hyperfine tensors and spin–rotational coupling are present but cannot account for all of the line width in this complex.

II. Experimental Section

The benzyltriphenylphosphonium salt of $FeNO(dto)_2$ was prepared by the literature method.[8] The tetramethylammonium salt of the bis(*cis*-1,2-dicyanoethylene-1,2-dithiolene)-nitrosyliron(I) dianion ($FeNO(S_2C_2CN_2)_2$) was made by McCleverty's method I.[7a] Solvents were all reagent grade and were used without further purification except to dry them over $CaSO_4$. Oxygen was removed from solution either by degassing on a vacuum line by the freeze–pump method or by bubbling dry nitrogen through the solution for at least 0.5 h. No differences in the spectra were noticed between the two techniques. All solutions of the iron salt were 1×10^{-3} M or less to ensure no exchange broadening contribution to the line width.

The ESR spectra were taken on a Varian VA-4500-10A spectrometer system with 100-kHz modulation. Temperatures were controlled with a Varian variable temperature unit and are accurate to about ±1 °C. The usual precautions were taken with the modulation amplitude and microwave power to avoid distortion of the resonance line. All sweeps were calibrated from the known splittings of peroxylaminedisulfonate.[10] The g values were measured using a Varian V-4532 dual sample cavity and standard procedure[11] with magnet cycling to yield a reproducible field shape. Peroxylaminedisulfonate was used as the standard.[12]

The variation of the line widths within a given spectrum was measured by using the relationship

$$\delta_i h_i = C \tag{1}$$

where δ_i is the derivative line width of the ith hyperfine line and h_i is its amplitude. C is a constant for all lines in a spectrum if their line shapes are the same. The line shape of the central component is Lorentzian out to limits of measurement (four derivative half-widths). The value of C is the same for all hyperfine lines to better than 5%. The relative amplitudes of the lines and the width of the central component were carefully measured. Use of eq 1 then allows the determination of the remaining widths. Computer simulation was used to correct line widths where overlap caused errors exceeding experimental error.

All errors quoted are standard deviations for at least five trials. The g values are reproducible to ±0.0002 except in the solvents sulfolane, propylene carbonate, and acetonitrile where the error is ±0.0004. The error in the splitting constants is ±0.05 G. The absolute error in the line widths is ± 10 mG with a relative error among the widths in a spectrum of 5 mG.

III. Results and Discussion

A. *Isotropic g Values and Hyperfine Splitting Constants.* We have noted a solvent dependence in the isotropic g values of $FeNO(dto)_2$ and $FeNO(S_2C_2CN_2)_2$. Prior work with $FeNO(S_2CNEt_2)_2^{2-}$ [3] and vanadyl acetylacetonate ($VO(acac)_2$)[13] has shown that plots of the g values vs. the solvent parameter Z[14] (or its closely allied value E_t[14]) can discriminate between solvent interaction at the oxygen of the NO (or VO) and the vacant sixth site in these complexes. Our results, displayed in Table I and Figures 1 and 2, show behavior analogous to the $FeNO(S_2CNEt_2)_2^{2-}$ case of Guzy et al.[3] and are taken to be an indication of sixth site solvent coordination. If coordination occurred at the oxygen, a smooth correlation between the ESR parameter and the Z value should be observed since Z is a measure of the solvent's ability to solvate anions or negative dipoles. We do not have this correlation, instead the protic solvents (1–5) show a weak effect compared to their high Z values. The aprotic solvents (6–16), on the other hand, show a relatively smooth variation of g with the solvent parameter. The fact that the protic solvents are weakly coordinating probably arises from their known poor performance as Lewis basis in complexes.

The isotropic splitting constant a_N from the ^{14}N nucleus in $FeNO(dto)_2$ also shows some solvent sensitivity. As Table I demonstrates, there are two distinct groupings of a_N values, characterized by the protic and aprotic solvents. There appears to be only a random variation of a_N with Z within each group because the effect is small compared to experimental error. The mean of a_N for the protic group is 13.66 ± 0.06 G while the aprotic solvents have 13.87 ± 0.05 G. Within the limits of 95% confidence, these are two distinct values. Thus a_N behaves analogously to the g value and in the same manner as the a for $FeNO(S_2CNEt_2)_2^{2-}$.[3] This is taken as further indication of sixth site coordination.

In addition to solvent sensitivity a_N for $FeNO(dto)_2$ varies with temperature. This variation is very close to linear with a_N increasing as the temperature decreases. Least-squares fit to a linear relationship of a_N with temperature for various solvents are given in Table II. The variation of a_N with temperature is expected when an equilibrium in the limit of rapid change occurs

$$R + S \rightleftharpoons RS \tag{2}$$

R is the unsolvated radical and S is the solvent molecule. When the exchange is rapid, only a single, average value of a is observed. Gendell et al.[15] have worked out the theory of the solvent dependence of the hyperfine splitting constant when it results from the rapid exchange equilibrium 2. The mean splitting constant in this case should be temperature dependent because of the temperature variation in the equilibrium constant for reaction 2. Our observation of an increase in a_N with decreasing temperature shows that the equilibrium constant for (2) is increasing with decreasing temperature, favoring the solvent–radical complex. This follows qualitatively from theory[15] because the shift in the observed splitting is in the same direction as if the solvent were replaced by another in which the radical–solvent complex is more stable. Prior discussion has shown that the aprotic, more interacting solvents have a larger value of a_N than the more weakly interacting, protic solvents.

B. *Line Width Studies.* Additional information about the dynamic behavior of $FeNO(dto)_2$ in solution can be obtained from studying the ESR line widths as a function of solvent and temperature. The spectra of $FeNO(dto)_2$ show a dependence

TABLE I: ESR and Solvent Parameters for Solutions of $Fe(NO)(dto)_2$ and $Fe(NO)(S_2C_2(CN)_2)^{2-}$ at Room Temperature

	Solvent	Z^a	$Fe(NO)(dto)_2^{2-}$ g value	$Fe(NO)(dto)_2^{2-}$ $a_N{}^a$	$Fe(NO)(S_2C_2(CN)_2)_2^{2-}$ g value	$Fe(NO)(S_2C_2(CN)_2)_2^{2-}$ $a_N{}^a$
1	MeOH	83.6	2.0334	13.67	2.0278	15.77
2	HCONHMe	82.0	2.0336	13.75		
3	EtOH	79.6	2.0336	13.59	2.0277	15.70
4	*n*-PrOH	78.3	2.0335	13.68	2.0277	15.78
5	*n*-BuOH	77.7	2.0335	13.61		
6	$C_4H_8O_2S$	77.4	2.0331	13.88		
7	$MeNO_2$	72.0	2.0331	13.80	2.0274	15.69
8	Me_2SO	71.2	2.0331	13.86		
9	$PrCO_3$[b]	70.9	2.0331			
10	CH_3CN	71.3	2.0335	13.83		
11	DMF	68.5	2.0330	13.86	2.0273	15.66
12	$PhNO_2$	65.7	2.0331	13.86		
13	Acetone	65.7	2.0332	13.98	2.0273	15.74
14	Pyridine	64.0	2.0329	13.93	2.0273	15.63
15	CH_2Cl_2	64.2	2.0334	13.87	2.0276	15.57
16	$CHCl_3$	63.3	2.0336	13.86	2.0275	15.48

[a] Units of Z, kcal/mol; a_N, G. [b] Propylene carbonate.

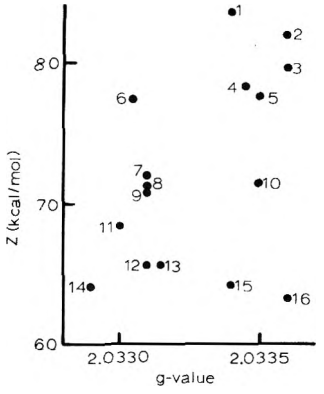

Figure 1. Plot of the g value for $FeNO(dto)_2$ as measured in various solvents at room temperature vs. the solvent Z parameter. See Table I for solvent key.

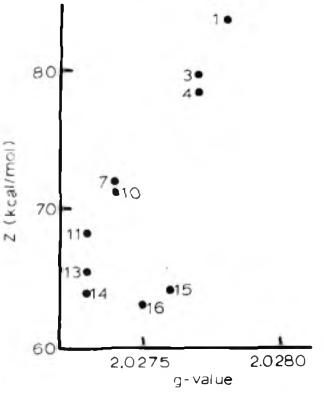

Figure 2. Plot of the g value for $FeNO(S_2C_2(CN)_2)_2$ as measured in various solvents at room temperature vs. the solvent Z parameter. See Table I for solvent key.

of the line width on spectral index number $\tilde{m}$[16] and theoretical considerations[17,18] suggest that the derivative line width should be given by

$$\delta(\tilde{m}) = \alpha + \beta\tilde{m} + \gamma\tilde{m}^2 \qquad (3)$$

This ignores small correction terms in $\tilde{m}^3$ [17,19] which will be justified later. The line widths of $FeNO(dto)_2$ in various solvents at various temperatures have been fitted to eq 3. The results are given in Table III. The γ term in eq 3 oscillated randomly about zero (±6 mG) because it is small compared to experimental error. That value is not included in Table III.

TABLE II: Linear Least-Squares Fits of the ^{14}N Hyperfine Splitting in $FeNO(dto)_2$ with Temperature for Various Solvents

Solvent	m^a	b^a	No. of points	Corrln coeff
Acetone	−0.0039	14.09	21	−0.96
DMF	−0.0041	14.03	5	−0.93
CH_2Cl_2	−0.0043	13.96	18	−0.95
Pyridine	−0.0066	13.85	5	−0.99
$CHCl_3$	−0.0049	13.84	7	−0.98
CH_3OH	−0.0040	13.77	14	−0.90

[a] $a_N = mT + b$; a_N in G, T in °C

Rotational modulation by Brownian motion of the anisotropic **g** and dipolar tensors has been shown to be an important relaxation mechanism in transition metal complexes.[17b,20-22] We expect a similar effect here. Since the ESR hyperfine lines of $FeNO(dto)_2$ are nondegenerate, we can use the more approximate theory of Kivelson[17] rather than the more detailed Freed–Fraenkel result[18] to describe the anisotropic contribution to the line width. The equation for the derivative line width in gauss for a radical with axial symmetry is[17]

$$\delta(\tilde{m}) = \left(\frac{8}{45\sqrt{3}}\gamma_e\frac{\Delta g^2}{g^2}B_0^2 + \frac{\gamma_e}{15\sqrt{3}}I(I+1)\Delta a^2\right)\tau_r + \alpha'' + \alpha_0 + \left(\frac{16}{45\sqrt{3}}\gamma_e\frac{\Delta g}{g}\Delta a B_0\tau_r\right)\tilde{m} + \left(\frac{\gamma_e}{9\sqrt{3}}\Delta a^2\tau_r\right)\tilde{m}^2 \qquad (4)$$

where $\Delta g = g_\parallel - g_\perp$, g is the isotropic value, $\Delta a = a_\parallel - a_\perp$ (in gauss), B_0 is the resonance field in gauss, γ_e is the gyromagnetic ratio for the electron, I is the nuclear spin quantum number, and τ_r is the rotational correlation time. The terms α'' and α_0 give the line width contribution from spin–rotational coupling and undefined residual mechanisms, respectively. This equation neglects the nonsecular terms which contribute as $[1 + (\omega_0\tau_r)^2]^{-1}$ where $\omega_0 = \gamma_e B_0$. For usual cor-

TABLE III: First Derivative ESR Line Widths for $FeNO(dto)_2$ in Various Solvents as a Function of Temperature[a]

T, °C	α	β	α′ [b]	α″ [b]	α_0 [b]
		Acetone			
−63	1.91	0.022	0.10	0.25	1.56
−65	1.90	0.024	0.11	0.23	1.56
−67	1.79	0.023	0.11	0.24	1.45
−73	1.73	0.028	0.13	0.19	1.40
−76	1.67	0.030	0.14	0.18	1.35
−81	1.61	0.034	0.16	0.16	1.29
−85	1.58	0.038	0.18	0.14	1.26
−87	1.35	0.045	0.21	0.12	1.23
−89	1.41	0.047	0.22	0.12	1.15
		DMF			
+3	2.79	0.013	0.06	0.42	2.31
−17.5	2.40	0.020	0.09	0.28	2.02
−38	2.12	0.028	0.13	0.20	1.80
−42	2.00	0.033	0.16	0.16	1.68
		Pyridine			
−6	2.48	0.015	0.07	0.37	2.04
−18	2.23	0.022	0.10	0.25	1.88
−28	2.06	0.033	0.15	0.17	1.74
−39.5	1.92	0.057	0.27	0.09	1.56
		CH_2Cl_2 [c]			
−15	2.36	0.025	0.052	0.501	1.81
−34	2.01	0.033	0.076	0.339	1.60
−43	1.89	0.044	0.092	0.278	1.52
−54	1.80	0.066	0.119	0.216	1.46
−59	1.80	0.070	0.135	0.192	1.47
−65	1.80	0.083	0.156	0.165	1.48
−70	1.84	0.102	0.178	0.145	1.52
−74	1.92	0.124	0.197	0.130	1.59
−85	2.24	0.196	0.270	0.095	1.88
		$CHCl_3$ [c]			
+4.5	3.01	0.031	0.046	0.560	2.40
−5	2.82	0.040	0.055	0.470	2.30
−15	2.59	0.051	0.066	0.389	2.14
−24	2.43	00065	0.079	0.325	2.03
−34	2.36	0.087	0.097	0.265	2.00
−44	2.37	0.115	0.120	0.214	2.04
−54	2.46	0.165	0.152	0.170	2.14
−59	2.68	0.209	0.171	0.150	2.36
		CH_3OH [c]			
−4.5	2.70	0.007	0.092	0.278	2.33
−15.5	2.44	0.021	0.123	0.208	2.11
−23.5	2.15	0.023	0.152	0.168	1.83
−32.5	2.02	0.030	0.198	0.131	1.69
−34	2.06	0.037	0.203	0.126	1.73
−43	1.95	0.054	0.263	0.098	1.59
−47.5	1.92	0.052	0.309	0.083	1.53
−54	1.95	0.076	0.370	0.070	1.51
−58	1.92	0.073	0.436	0.059	1.43
−60	2.17	0.093	0.450	0.057	1.66
−65	2.03	0.111	0.535	0.048	1.45
−69	2.30	0.148	0.617	0.042	1.64
−74	2.39	0.194	0.742	0.035	1.61
−77	2.66	0.216	0.831	0.031	1.80
−81	2.80	0.243	0.973	0.027	1.80
−83	2.92	0.262	1.055	0.025	1.84
−85	3.00	0.302	1.146	0.023	1.83
−88	3.53	0.369	1.299	0.020	2.21

[a] Fitted to $\delta(\tilde{m}) = \alpha + \beta\tilde{m} + \gamma\tilde{m}^2$, in G. γ is zero to within experimental error. [b] $\alpha = \alpha' + \alpha'' + \alpha_0$; α' = reorientation of anisotropic **g** and dipolar tensors, α'' = spin–rotational, α_0 = residual. α', α'' calculated values. See text. [c] Values of α', α'' calculated using acetone data. See text.

TABLE IV: Viscosity Formulas for Various Solvents[a]

	A, cP	B, K
CH_2Cl_2	0.0264	822
CH_3OH [b]	0.00800	1262
$CHCl_3$	0.0311	854
Acetone	0.0171	862
Pyridine	0.00482	1555
DMF [c]	0.0218	1110

[a] Based on least-squares fit of available data to $\ln \eta = \ln A + B/T$. Data from "Handbook of Chemistry and Physics", 41st ed, Chemical Rubber Publishing Co., Cleveland, Ohio, 1959, pp 2182–2187. [b] K. K. Innes, *J. Phys. Chem.*, **60**, 817 (1956). [c] A. Reis and J. Miller, *Klin. Wochenschr.*, 199 (1956).

relation times of 10^{-11} s at X-band frequencies, these terms are about 10% of the secular and pseudosecular contributions.

The anisotropic values of g and a_N for $FeNO(dto)_2$ have been determined in rigid glass[9] and show the complex to have axial symmetry. Equation 4 can be evaluated, except for τ_r, using these anisotropic values, the isotropic g value in acetone, and the appropriate resonant field. For studies in methanol, acetone, CH_2Cl_2, and $CHCl_3$, the resonant field was 3248.6 G yielding

$$\delta(\tilde{m}) = 1.582 \times 10^9\tau_r + \alpha'' + \alpha_0 + (3.327 \times 10^8\tau_r)\tilde{m} + (1.102 \times 10^7\tau_r)\tilde{m}^2 \quad (5a)$$

In pyridine and DMF solutions, B_0 equalled 3284 G to give

$$\delta(\tilde{m}) = 1.617 \times 10^9\tau_r + \alpha'' + \alpha_0 + (3.363 \times 10^8\tau_r)\tilde{m} + (1.102 \times 10^7\tau_r)\tilde{m}^2 \quad (5b)$$

The equation for the correlation time is

$$\tau_r = \frac{(4\pi r_0^3)}{3k}\frac{\eta}{T}\kappa \quad (6)$$

where k is the Boltzmann constant, T the absolute temperature, η the solvent viscosity, r_0 the effective solute radius, and κ is an adjustable factor called the anisotropic interaction parameter. For a spherical molecule, κ equals unity and this becomes the familiar Debye expression.[23] The value of κ is independent of temperature, pressure, and density but varies with the solute and solvent.[20-22] Hwang et al.[22] discovered considerable κ variation among solvents, so that it must be accounted for in careful work.

If the rotational modulation of **g** and the hyperfine tensors is the cause of the $\tilde{m}$ dependence in the line width, then as eq 5 and 6 indicate, the β term should be linear in η/T. Solvent viscosity values at temperatures of interest were taken from the literature and extrapolated by means of a least-squares fit to $\ln \eta = \ln A + B/T$. The results are given in Table IV. Figure 3 examines the η/T behavior of the β term in eq 3. Pyridine and DMF solvents give the expected linear behavior while acetone also is linear to near its freezing point but with a slightly larger slope. The other solvents are nonlinear in η/T. The essential correctness of the theory has been well enough established[20-22] to lead us to conclude that some other $\tilde{m}$ dependent mechanism is also operative in these solvents besides the anisotropic interaction.

The results in section IIIA show that solvent coordination occurs and that it is in the form of an equilibrium $R + S \rightleftharpoons RS$. This two-jump model might contribute to spin relaxation. However, basic solvents such as pyridine and DMF would be expected to form a strong coordination with the vacant sixth site. The equilibrium would lie far to the side of the radical-

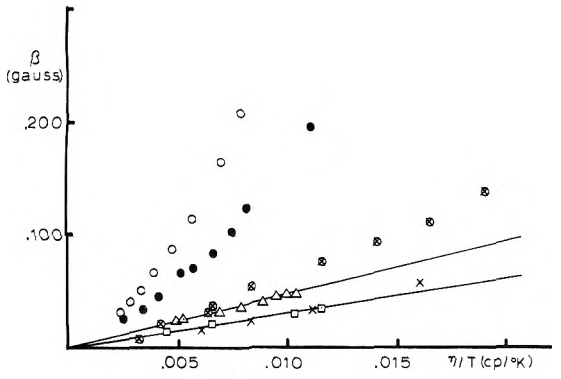

Figure 3. Variation of the $\tilde{m}$ dependent term β in the line width of $FeNO(dto)_2$ as a function of η/T in the solvents $CHCl_3$ (O), CH_2Cl_2 (●), CH_3OH (⊗), acetone (△), pyridine (X), and DMF (□).

solvent complex and would play only a minor role in relaxation. The derivative line width contribution (secular and pseudosecular) from the two-jump model which modulates both g and a_N is[16]

$$\delta_j(\tilde{m}) = \frac{2}{\sqrt{3}\gamma_e} j^{Go}(0)B_0^2 + j^{IGo}(0)2B_0\tilde{m} + j^{I}(0)\tilde{m}^2 \quad (7)$$

The j's are the spectral densities at zero frequency for isotropic **g** tensor (Go), isotropic **g** dipolar tensor (IGo), and isotropic dipolar (I) interactions. The spectral densities are proportional to $\tau P_r P_{rs}$[24] where P_r and P_{rs} are the probabilities of R and RS. $\tau = \tau_r\tau_{rs}/(\tau_r + \tau_{rs})$ where τ_r and τ_{rs} are the mean lifetimes of the species. This relaxation contribution becomes small in the limit of stable radical–solvent complex RS. In addition, the temperature dependence of $\delta_j(\tilde{m})$ is not expected in general to be linear in η/T. We therefore assign the β contribution in pyridine and DMF to anisotropic interactions. The data in Figure 3 show that β terms in the two solvents are nearly coincident and so we will treat them together. A linear least-squares fit gives

$$\beta = 3.654\eta/T - 0.0068 \quad (8)$$

with η in centipoise (correlation coefficient is 0.98). The intercept is zero to within experimental error as expected.

Data in section III A also show that acetone is strongly coordinating with $FeNO(dto)_2$. The anisotropic interaction should also dominate here and the linearity of β in Figure 3 confirms this. A least-squares fit to the β term in acetone gives

$$\beta = 4.763\eta/T - 0.0021 \quad (9)$$

The slope here is larger than in eq 8 and the differences can be analyzed in terms of κ in eq 6. Using eq 5 and 8, we find a correlation time of 0.88×10^{-10} s at a η/T value of 1.0×10^{-2} cP K^{-1}. In acetone solution, τ_r is 1.37×10^{-10} s at the same η/T. These values compare favorably with correlation times found in $VO(acac)_2$ and $Cu(acac)_2$ solutions.[20,21] Equation 6 can be used to evaluate κ for these solvents if r_0 is known. Since we are interested only in relative κ values, we can fix r_0 at the arbitrary value of 3.045 Å.[20] Then κ becomes 1.0 in pyridine and DMF and 1.6 in acetone.

In order to treat the $\tilde{m}$ term in the remaining solvents, we must have a means of calculating the anisotropic contribution so that the residual effect can be examined separately. This requires that values of τ_r be known at the appropriate η/T values so that eq 5 can be used. We need κ's for these solvents. An examination of Figure 3 shows that the line width contribution from effects other than the anisotropic interaction approaches zero at low η/T. The limiting slope as η/T approaches zero should be the result of anisotropic effects. This can be approximated by a fit of β to a polynomial in η/T. The coefficients for a regression analysis are given in Table V. In all cases, the best fit was achieved by a second-order polynomial. The B terms in Table V along with the slope in eq 9 and the known κ for acetone can be used to estimate κ values for the solvents by simple proportion. We find κ is 1.76, 2.30, and 1.60 for CH_2Cl_2, CH_3OH, and $CHCl_3$, respectively. The anisotropic contribution follows

TABLE V: Polynomial Regression Analysis for β as a Function of η/T in Various Solvents[a]

Solvent	A	B	C
CH_2Cl_2	0.0045	5.343	1074
$CHCl_3$	0.0055	4.857	2614
CH_3OH	−0.0116	6.968	60.46

[a] Fit to $\beta = A + B(\eta/T) + C(\eta/T)^2$.

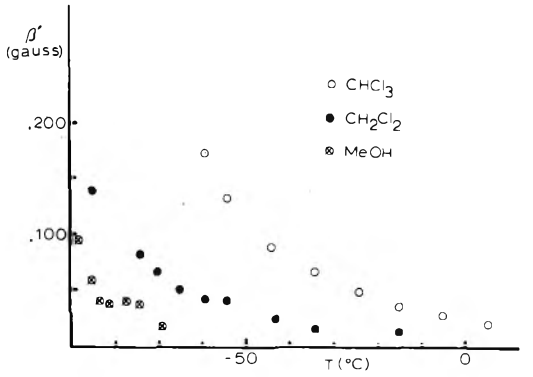

Figure 4. Variation of the residual $\tilde{m}$ line width dependence after removal of the anisotropic g and hyperfine contribution as a function of temperature for $FeNO(dto)_2$.

$$\beta' = 3.327 \times 10^8 \frac{\kappa'}{1.57}\tau_r \quad (10)$$

where κ' is the appropriate number for the solvent used, τ_r is the correlation time from acetone solutions at the appropriate η/T, and 1.57 is κ for acetone solutions. The residual portion of β after subtraction of the anisotropic part from the experimental β is displayed in Figure 4 as a function of temperature. The residual portion β_0 grows larger as the temperature decreases as expected for relaxation induced by the rapid jump mechanism in eq 7. At higher temperatures, there would be a more rapid exchange and consequent shortening of the species' lifetimes. This makes the $\tau P_r P_{rs}$ term small and the contribution to relaxation negligible at high temperatures. This is consistent with the analysis of the temperature dependence of the hyperfine splitting constant.

The α portion of the line width in eq 3 has contributions from several sources. Rotational modulation of the anisotropic **g** and dipolar tensors gives a contribution specified by eq 4 and 5. It is known that spin–rotational coupling is an important factor in relaxation[19-21] giving a term[19]

$$\alpha'' = \frac{2}{\sqrt{3}\gamma_e}\frac{(\Delta g_\parallel^2 + 2\Delta g_\perp^2)}{9\tau_r} \quad (11)$$

where $\Delta g_\parallel = g_\parallel - g_e$, $\Delta g_\perp = g_\perp - g_e$, and g_e is the g value of the free electron. Using the reported values[9] for $g_\parallel$ and $g_\perp$, we find

$$\alpha'' = \frac{1.626 \times 10^{-11}}{\tau_r} \quad (12)$$

In pyridine, DMF, and acetone solutions where the $\tilde{m}$ term is dominated by anisotropic relaxation, values for τ_r from β can be used to estimate the magnitude of anisotropic **g** and dipolar tensor modulation and spin–rotational interactions. These are given in Table III. The portion of the width remaining α_0 is due to other relaxation mechanisms. This residual width is plotted vs. temperature for the three solvents in Figure 5. The α_0 term is nearly linear in temperature and the results for the three solvents are colinear. Solvent nuclear spin–solute electron spin dipole–dipole interactions could be responsible for part of the residual width. As a check on the presence of this mechanism, we examined the width of the central hyperfine in $FeNO(dto)_2$ in deuterated acetone with the following results: 1.57, 1.70, and 1.88 G at −87, −74, and −65 °C. This compares with the width in undeuterated acetone of 1.56, 1.70, and 1.90 G at the same temperatures. We conclude there is no measurable contribution from this dipole–dipole coupling. The above results suggest that the relaxation mechanism for the electron spin in $FeNO(dto)_2$ responsible for the residual width is intramolecular.

This residual portion is not present in other transition metal complexes in which the electron spin relaxation mechanisms have been studied in detail.[20–22] Indeed, there is some evidence that iron–nitrosyls in the d^7 configuration have anomalously large widths. We have found $Cr(CN)_5NO^{3-}$ (d^5) to have widths of about 1.1 G at room temperature in aqueous solution while $Fe(CN)_5NO^{3-}$ (d^7) has a width of 2.9 G in DMF.[25] It is unlikely, given the similarity between $FeNO(dto)_2$ and $VO(acac)_2$,[20,22] that anisotropic rotational diffusion effects[22,26] not considered here could cause this anomalous relaxation. Kivelson[27] has proposed an Orbach mechanism but in the original analysis it depended on solvent-induced electrical field fluctuations. The solvent independence of our results suggest that this is not the mechanism at work here. Anomalous relaxation in highly symmetric aromatic hydrocarbon radicals has been studied[28,29] and attributed to spin–orbit interactions.[29] Such mechanisms may be at work here if the electronic structure of these d^7 complexes is characterized by nearly degenerate levels. Insufficient knowledge of the electronic states of $FeNO(dto)_2$ prevent further speculation.

The anisotropic **g** dipolar tensors and spin–rotational relaxation in CH_2Cl_2, $CHCl_3$, and CH_3OH can be estimated by using τ_r values obtained by the previously outlined method. Using these τ_r values and eq 5 and 12, we can arrive at the width contributions found in Table III. A graphical examination of α_0 as a function of temperature is contained in Figure 6. At high temperatures all solvents give approximately the same behavior as the first, strongly coordinating group. This indicates that the same intramolecular mechanism is operable in all solvents. As the temperature drops, marked deviation from the linear temperature dependence is noted. This "break" occurs at about the same temperature that the residual $\tilde{m}$ term (Figure 4) becomes appreciable showing that the same relaxation process causes both the α and β contributions to the width.

Data from the study of g and a_N as a function of temperature and solvent demonstrate the importance of solvent interaction in the solution dynamics of $FeNO(dto)_2$. The effect is expected to be modeled by a simple two-jump process R + S ⇌ RS. Under those conditions where the equilibrium constant is small enough and the radical lifetimes long enough, this process should effect the relaxation of the electron spin. In those solvents that are weakly coordinating ($CHCl_3$, CH_2Cl_2, and CH_3OH), these conditions are met as shown by the residual contribution to the line width (Figures 4 and 6).

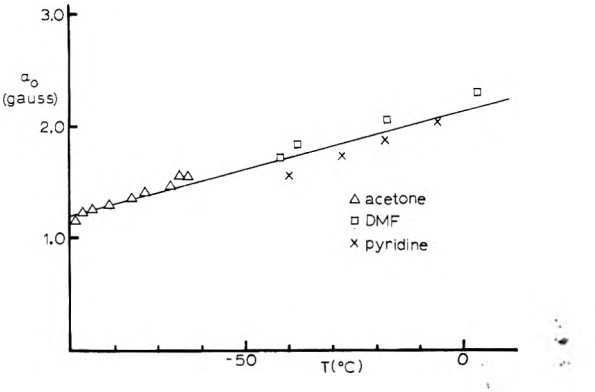

Figure 5. Residual line width contribution to $FeNO(dto)_2$ after subtraction of the spin–rotational and anisotropic g and hyperfine components as a function of temperature in various strongly coordinating solvents.

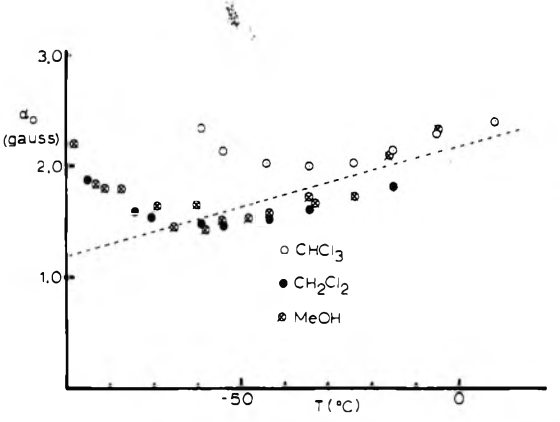

Figure 6. Residual line width contribution to $FeNO(dto)_2$ after subtraction of the spin–rotational and anisotropic g and hyperfine components as a function of temperature in various weakly coordinating solvents. The line indicates the best fit to the strongly coordinating solvent group data in Figure 5.

Equation 7 describing the contribution to the line width from the jump mechanism can be evaluated as[16]

$$\delta_j(\tilde{m}) = \frac{2}{\sqrt{3}}\gamma_e\left[\frac{\delta g^2 B_0^2}{g^2} + \frac{2B_0\delta a\,\delta g\tilde{m}_j}{g} + (\delta a)^2\tilde{m}_j^2\right]\tau P_r P_{rs} \quad (13)$$

where δg and δa are the differences in the isotropic g and a (in gauss) values between the two radical forms. Data are presently lacking which would allow quantitative checks between theory and experiment since the magnitudes of δg and δa are not known and the behavior of $\tau P_r P_{rs}$ is difficult to characterize. Sweeney and Coffman[9] noted the appearance of a small percentage of a second radical in the rigid glass spectrum of $FeNO(dto)_2$ but they gave no analysis of resonance parameters.

The ratio of the $\tilde{m}$ independent term α''' in eq 13 to the $\tilde{m}$ term β_0 gives

$$\frac{\alpha'''}{\beta_0} = \frac{\delta g B_0}{\delta a 2g} \quad (14)$$

The $CHCl_3$ data can be used to calculate this ratio by subtracting off the intramolecular contribution to α_0 from a least-squares fit to the pyridine, DMF, and acetone data (Figure 5) and then using the β_0 values displayed in Figure 4. This ratio should be independent of temperature. For $CHCl_3$ solutions, α'''/β_0 is 3.9 ± 0.6 with a random fluctuation for the

five lowest temperature points. This gives a $\delta g/\delta a$ ratio of 5×10^{-3} G^{-1}. The extremes of the isotropic g and a_N values in various solvents (Table I) should give an estimate of the order of magnitude of δg and δa. Using these values, we calculate $\delta g/\delta a$ equals approximately 2×10^{-3} G^{-1}, giving reasonable agreement with the line width results.

In analyzing the experimental data, we found the $\bar{m}^2$ term to be zero within experimental error. Using eq 5, we can check the consistency of the data by calculating its magnitude with a typical τ_r of 1.0×10^{-11} s. The γ term then has a magnitude of 1×10^{-4} G, well below experimental error. The $\bar{m}^3$ term ignored in the data analysis is of order or magnitude γ/B_0[17b] and is also negligible in this experiment.

Summary

Studies of the variation with solvent of the isotropic g and a_N values of $FeNO(dto)_2$ demonstrate a dependence which indicates solvent coordination at the vacant sixth site on the molecule. The temperature variation of a is consistent with a temperature-dependent equilibrium between the solvated and unsolvated radical. Similar behavior is exhibited by $FeNO(S_2C_2CN_2)_2$.

An examination of the line widths of $FeNO(dto)_2$ as a function of solvent and temperature show that several relaxation mechanisms are operable. Studies on other transition metal complexes have demonstrated that rotational modulation of the anisotropic **g** and dipolar tensors and spin rotational interactions should be present in this system. When these are accounted by the proper theoretical treatment, we find a considerable residual contribution to the line width. In solutions of strongly coordinating solvents this residual portion is independent of the solvent and spectral index number and is therefore of an intramolecular nature. This anomalous contribution to the width has not been seen in other systems and may well arise from some intramolecular spin–orbit type mechanism.

In the more weakly coordinating solvents, there is a line width contribution which cannot be accounted for by anisotropic **g** dipolar tensor, spin–rotational coupling, or intramolecular interactions. It is spectral index number, solvent, and temperature dependent. The behavior of this component to the line width is consistent with a two-jump process between the solvated and unsolvated radical modulating both g and a_N.

Acknowledgments. We wish to thank Dr. R. E. Coffman of the University of Iowa for stimulating our interest in iron–nitrosyl complexes. Several Knox students have contributed to this work with primary acknowledgment going to James Rybka. Gloria Pyrka and Michael Cinquegrani also did significant work. Major financial support came from a Cottrell College Science Grant given by the Research Corporation. Support was also received from institutional grants to Knox College from the Sloan Foundation, The National Science Foundation, and the Richter Trusts.

References and Notes

(1) (a) J. Gibson, *Nature (London)*, **64**, 96 (1962); (b) H. B. Gray, I. Bernal, and E. Billig, *J. Am. Chem. Soc.*, **84**, 3403 (1962).
(2) B. A. Goodman, J. B. Raynor, and M. C. R. Symons, *J. Chem. Soc. A*, 2572 (1969).
(3) C. M. Guzy, J. B. Raynor, and M. C. R. Symons, *J. Chem. Soc. A*, 2987 (1969).
(4) C. C. McDonald, W. D. Phillips, and H. F. Mower, *J. Am. Chem. Soc.*, **87**, 3319 (1965).
(5) L. Burlamacchi, G. Martini, and E. Tiezzi, *Magn. Resonance Biol. Res., Rep. Int. Conf., 3rd., 1969*, 137–153 (1971).
(6) N. S. Garif'yanov and S. A. Luchkina, *Dokl. Akad. Nauk. SSSR*, **189**, 779 (1969).
(7) (a) J. A. McCleverty, N. M. Atherten, J. Locke, E. J. Wharton, and C. J. Winscom, *J. Am. Chem. Soc.*, **89**, 6082 (1967); (b) J. A. McCleverty and B. Ratcliff, *J. Chem. Soc. A*, 1627 (1970).
(8) D. Coucovanis, R. E. Coffman, and D. Piltingsrud, *J. Am. Chem. Soc.*, **92**, 5004 (1970).
(9) W. V. Sweeney and R. E. Coffman, *J. Phys. Chem.*, **76**, 49 (1972).
(10) R. J. Farber and G. K. Fraenkel, *J. Chem. Phys.*, **47**, 2462 (1967).
(11) "Operational Considerations with the V-4532 Dual Sample Cavity", Varian Associates, Palo Alto, Calif, Publication No. 87-214-002.
(12) "EPR at Work Series" No. 28, Varian Associates, Palo Alto, Calif.
(13) C. M. Guzy, J. B. Raynor, and M. C. R. Symons, *J. Chem. Soc. A*, 2791 (1969).
(14) E. M. Kosower, "Introduction to Physical Organic Chemistry", Wiley, New York, N.Y., 1968, pp 293–333.
(15) J. Gendell, J. H. Freed, and G. K. Fraenkel, *J. Chem. Phys.*, **37**, 2832 (1962).
(16) J. H. Freed and G. K. Fraenkel, *J. Chem. Phys.*, **40**, 1815 (1964).
(17) (a) D. Kivelson, *J. Chem. Phys.*, **33**, 1094 (1960); (b) R. Wilson and D. Kivelson, *ibid.*, **44**, 154 (1966).
(18) J. H. Freed and G. K. Fraenkel, *J. Chem. Phys.*, **39**, 326 (1966).
(19) P. W. Atkins and D. Kivelson, *J. Chem. Phys.*, **44**, 169 (1966).
(20) R. Wilson and D. Kivelson, *J. Chem. Phys.*, **44**, 4440 (1966).
(21) R. Wilson and D. Kivelson, *J. Chem. Phys.*, **44**, 4445 (1966).
(22) J. Hwang, D. Kivelson, and W. Plachy, *J. Chem. Phys.*, **58**, 1753 (1973).
(23) N. Bloembergen, E. M. Purcell, and R. V. Pound, *Phys. Rev.*, **73**, 679 (1948).
(24) G. K. Fraenkel, *J. Phys. Chem.*, **71**, 139 (1967).
(25) W. B. Lewis and L. O. Morgan, "Paramagnetic Relaxation in Solution", "Transition Metal Chemistry", Vol. 4., R. L. Carlin, Ed., Marcel Dekker, New York, N.Y., 1968.
(26) R. E. D. McClung and D. Kivelson, *J. Chem. Phys.*, **49**, 3380 (1968).
(27) D. Kivelson, *J. Chem. Phys.*, **45**, 751 (1966).
(28) R. G. Kooser, V. W. Volland, and J. H. Freed, *J. Chem. Phys.*, **50**, 5243 (1969).
(29) M. R. Das, S. B. Wagner, and J. H. Freed, *J. Chem. Phys.*, **52**, 5404 (1970).

Multipole Expansion of the Madelung Parameter for Salts with the Potassium Hexachloroplatinate Structure

P. Herzig, H. D. B. Jenkins,* and A. Neckel

Institut für Technische Elektrochemie, Technische Universität, Vienna, Austria *(Received November 13, 1975)*

Two general expressions for the Madelung parameter M_{elec} for salts M'_2MX_6 with K_2PtCl_6 structure as a function of the cell constant a and the M–X distance d in the complex ion MX_6^{2-} are derived. Both equations are based on a multipole expansion of the electrostatic lattice potential. The charge distribution of the MX_6^{2-} ion is represented by a system of point charges, which are located at the sites of the atoms. The expansions of the Madelung parameter have the following form: $M_{elec} = \alpha_0 + [\Sigma_{n=2,\,even}^{\infty}\alpha_n(d/a)^n]q_X + [\Sigma_{n=2,\,even}^{\infty}\beta_n(d/a)^n]q_X^2$ and $M_{elec} = A_0 + \{B_0 + \Sigma_{m=1}^{\infty} B_m[(d - 0.24a)/a]^m\}\, q_X + \{C_0 + \Sigma_{m=1}^{\infty} C_m[(d - 0.24a)/a]^m\}\, q_X^2$, where q_X is the charge of the terminal X atom of the MX_6^{2-} ion. The values for the coefficients α_n and β_n up to $n = 32$ and for the coefficients A_0, B_m, and C_m up to $m = 8$ are given in this paper. ($\alpha_0 = A_0$.) For K_2PtCl_6 the results obtained are compared with the general quadratic expansion $M_{elec} = \Sigma_{i=0}^{2} D_i q_{Cl}{}^i$, which has been evaluated by using Bertaut's method for the calculation of electrostatic lattice sums of point charges.

Introduction

Potassium hexachloroplatinate, K_2PtCl_6, crystallizes in cubic form with a cell constant, $a_0 = 9.755$ Å.[1,2] There are two parameters involved in this salt: the external parameter a_0 and an internal distance, d, corresponding to the Pt–Cl distance in the complex $PtCl_6^{2-}$ ion ($d = 2.3412$ Å). On formation of the crystal, the total lattice potential energy is minimized with respect to the cell parameter a (which is equal to a_0 at the minimum) while the internal distance d remains practically constant. The ratio $d/a = u$ has the value 0.24 in the K_2PtCl_6 crystal.

The expansion of the Madelung parameter M_{elec} as a function of the two parameters a and d is valid for all salts with the K_2PtCl_6 structure. This form of the Madelung constant is also of special importance for studies on direct minimization equations[3,4] and offers a method of testing such equations by comparing the calculated total lattice potential energy with the result obtained by the term-by-term calculation.

Neckel, Vinek, and Kuzmany[5-10] have developed a technique for calculating Madelung parameters, which is based on a multipole expansion of the interaction energy of two cylindrical symmetrical charge distributions. The total electrostatic interaction energy of an ionic crystal is obtained by summing the contributions of all lattice points. This step requires the evaluation of multipole lattice sums. For the calculation of these lattice sums Ewald's method[11] for the calculation of lattice sums of point charges (monopoles) has been extended to multipoles.

In this work we are using the multipole expansion method, which has been successfully applied to crystals with complex ions, such as CaC_2,[5,8] KHF_2,[10,12] or $CaCO_3$.[7] We expand the Madelung parameter, M_{elec}, for salts M'_2MX_6 with K_2PtCl_6 structure, in terms of the multipole moments using: (i) the center of mass of the MX_6^{2-} ion as the origin, thus obtaining

$$M_{elec} = \alpha_0 + \left(\sum_{n=2}^{\infty}\alpha_n\left(\frac{d}{a}\right)^n\right)q_X + \left(\sum_{n=2}^{\infty}\beta_n\left(\frac{d}{a}\right)^n\right)q_X^2 \quad (1)$$

or (ii) the point $u = 0.24$ as the origin, thus obtaining

$$M_{elec} = A_0 + \left[B_0 + \sum_{m=1}^{\infty} B_m\left(\frac{d - 0.24a}{a}\right)^m\right]q_X + \left[C_0 + \sum_{m=1}^{\infty} C_m\left(\frac{d - 0.24a}{a}\right)^m\right]q_X^2 \quad (2)$$

where q_X is the charge assigned to a terminal X atom of the MX_6^{2-} ion. A charge q_M is assigned to the atom M such that

$$q_M + 6q_X = -2 \quad (3)$$

The results obtained by the multipole expansion method can be checked by comparing the coefficients of $q_X{}^i$ ($i = 0, 1, 2$) in (1) and (2) with the coefficients of the equation

$$M_{elec} = \sum_{i=0}^{2} D_i q_X{}^i \quad (4)$$

calculated by Bertaut's method[13] (see, for example, Jenkins and Smith[14]). Such a comparison for K_2PtCl_6 will be made in this paper.

For K_2PtCl_6 the Madelung energy, U_M, for the process

$$K_2PtCl_6(c) \rightarrow 2K^+(g) + Pt(g)^{q_{Pt}} + 6Cl(g)^{q_{Cl}}$$

which, in kJ mol^{-1}, we calculate to be

$$U_M = 1657.27 + 7522.33q_{Cl} + 15\,336.75q_{Cl}^2 \quad (5)$$

The associated Madelung constants take the form

$$M \text{ (based on } a_0) = 11.636\,579 + 52.818\,308q_{Cl} + 107.687\,562q_{Cl}^2 \quad (6)$$

where a_0 is the cell constant (= 9.755 Å) and

$$M \text{ (based on } V_m{}^{1/3}) = 7.330\,57 + 33.273\,422q_{Cl} + 67.838\,859q_{Cl}^2 \quad (7)$$

where $V_m{}^{1/3}$ is the cube root of the unit cell volume (= 6.145 26 Å).

* H.D.B.J. visited the Institut für Technische Elektrochemie, Technische Universität Wien, at the invitation of Professor A. Neckel and under the Royal Society European Programme. Permanent address: School of Molecular Sciences, University of Warwick, Coventry CV4 7AL, Warks, England.

We can impose two checks on these calculations. First in eq 7 if $q_{Cl} = 0$, the potassium and platinum atoms in K_2PtCl_6 have the fluorite (CaF_2) arrangement and the Madelung parameter for this structure is well documented as 7.330 58 (based on $V_m^{1/3}$).[15] Secondly Simon and Zeller[16] have recently computed M (based on a_0) = τ. From their paper, for K_2PtCl_6, using the value $q_K = +1$ and relationship 3 we find

$$\tau = [6\tau_{11} - 4\tau_{13} + \tau_{34}] + [24\tau_{11} - 12\tau_{13} - 12\tau_{15} + 12\tau_{35}]q_{Cl} + [42\tau_{11} - 36\tau_{15} + 12\tau_{57} + 3\tau_{56}]q_{Cl}^2 \quad (8)$$

Using the values of τ_{ij} quoted by Simon and Zeller we find

$$M \text{ (based on } a_0) = \tau = 11.636\,498 + 52.818\,264q_{Cl} + 107.687\,508q_{Cl}^2 \quad (9)$$

which agrees with our result, eq 6, to the five significant figure accuracy claimed for the Simon and Zeller results. Considering the electrostatic energy for the process

$$Pt^{q_{Pt}}(g) + 6Cl^{q_{Cl}}(g) \rightarrow PtCl_6^{2-}(g) \quad (10)$$

we obtain from U_M the energy U_{elec} (in kJ mol^{-1}) for the process

$$K_2PtCl_6(c) \rightarrow 2K^+(g) + PtCl_6^{2-}(g) \quad (11)$$

where $PtCl_6^{2-}(g)$ represents the gaseous ion, however, with the charge distribution and the bond distances as they occur in the crystal. We obtain for U_{elec}

$$U_{elec} = 1657.27 + 401.38q_{Cl} - 100.71q_{Cl}^2 \quad (12)$$

giving a corresponding value

$$M_{elec} \text{ (based on } a_0) = 11.636\,579 + 2.818\,304q_{Cl} - 0.707\,138q_{Cl}^2 \quad (13)$$

using the conversion factor, $K = 1389.297$ to convert e^2 Å^{-1} to kJ mol^{-1}.

The coefficients of eq 13 can be used to check the multipole expansion coefficients obtained in this paper. We now describe the calculations in detail.

Method of Calculation

The coefficients for the multipole expansions, eq 1 and 2, of the Madelung parameter were calculated using a program written by Herzig, Kuzmany, and Neckel.[17] This program is based on the discussion of the electrostatic interaction energy between cylindrical symmetrical charge distributions in a lattice.

First we consider two cylindrical symmetrical charge distributions (1) and (2). In each charge distribution we choose an origin and a coordinate system in such a way that the z axis in each charge distribution coincides with the axis of symmetry.

The vectors $\vec{r}_1$ and $\vec{r}_2$ indicate the position of the origin of the charge distribution (1) and (2), respectively. Jansen[18] has shown that for cylindrical symmetrical charge distributions the potential $V(\vec{r}_2)$, which the charge distribution (1) causes at the position of the origin of the charge distribution (2), is given by a multipole expansion of the form

$$V(\vec{r}_2) = \sum_{n=0}^{\infty} \frac{(-1)^n}{n!} Q_1^{(n)} \frac{\partial^n}{\partial z_1^n}\left(\frac{1}{|\vec{r}_2 - \vec{r}_1|}\right) \quad (14)$$

where $Q_1^{(n)}$ are the (scalar) multipole moments of order n of the charge distribution (1) and z_1 is the z axis of the charge distribution (1). If the charge distribution consists of a system of discrete point charges located along the z axis, then $Q^{(n)}$ will be given by

$$Q^{(n)} = \sum_i q_i d_i^n \quad (15)$$

q_i is the charge of the point charge i and d_i its distance from the origin of the charge distribution. The summation extends over all point charges of the charge distribution.

For the electrostatic interaction energy of the charge distribution (1) with the charge distribution (2) one obtains

$$U_{12} = \sum_{m=0}^{\infty} \frac{1}{m!} Q_2^{(m)} \frac{\partial^m}{\partial z_2^m} V(\vec{r}_2) = \sum_{m=0}^{\infty}\sum_{n=0}^{\infty} \frac{(-1)^n}{m!n!} Q_1^{(n)} Q_2^{(m)} \frac{\partial^{m+n}}{\partial z_1^n \partial z_2^m}\left(\frac{1}{|\vec{r}_2 - \vec{r}_1|}\right) \quad (16)$$

This expansion is valid only for distances $|\vec{r}_2 - \vec{r}_1|$, which are larger than the sum for the extensions of the charge distributions.

Let us now consider an ionic crystal. In a crystal the position of each lattice point is determined by a vector $\vec{r}_l + \vec{r}_k$; $\vec{r}_l$ pointing to the origin of the lth unit cell and $\vec{r}_k$ pointing from the origin of the unit cell to the atom k of the basis. The total electrostatic interaction energy in a crystal is then given by

$$U = \frac{1}{2}\sum_k \sum_{k'} \sum_{n=0}^{\infty}\sum_{m=0}^{\infty} Q_k^{(n)} Q_{k'}^{(m)} \frac{(-1)^n}{n!m!} \frac{\partial^{n+m}}{\partial z_k^n \partial z_{k'}^m} \times {\sum_l}' \frac{1}{|\vec{r}_l + \vec{r}_k - \vec{r}_{k'}|} \text{ for } \vec{r}_k = \vec{r}_{k'} \quad (17)$$

The sum over l extends over all unit cells of the (infinite) crystal; the sum over k or k' respectively extends over all ions of the basis (all ions of the unit cell). The bar on the sum over l is to indicate that for $\vec{r}_k = \vec{r}_{k'}$ the term with $\vec{r}_l = 0$ must be omitted.

In order to obtain the electrostatic interaction energy U, lattice sums of the type

$$\Psi_{z_k z_{k'}}^{(n,m)}(\vec{r}_k - \vec{r}_{k'}) = \frac{(-1)^n}{n!m!} \frac{\partial^{n+m}}{\partial z_k^n \partial z_{k'}^m} \sum_l \frac{1}{|\vec{r}_l + \vec{r}_k - \vec{r}_{k'}|} \quad (18)$$

must be evaluated.

For the calculation of these lattice sums a procedure was developed, which can be derived from Ewald's method[11] for the calculation of lattice sums of point charges (monopoles). According to this technique each lattice sum $\Psi_{z_1 z_2}^{(n,m)}$ can be split up in two sums; one sum, ${}^{real}\Psi_{z_1 z_2}^{(n,m)}(\vec{r})$, extending over the real lattice, the other sum, ${}^{rec}\Psi_{z_1 z_2}^{(n,m)}(\vec{r})$, extending over the reciprocal lattice.

$$\Psi_{z_1 z_2}^{(n,m)}(\vec{r}) = {}^{real}\Psi_{z_1 z_2}^{(n,m)}(\vec{r}) + {}^{rec}\Psi_{z_1 z_2}^{(n,m)}(\vec{r}) \quad (19)$$

${}^{real}\Psi_{z_1 z_2}^{(n,m)}(\vec{r})$ is given by

$${}^{real}\Psi_{z_1 z_2}^{(n,m)}(\vec{r}) = \sum_{\lambda=0}^{[n/2]} \binom{n}{2\lambda} \frac{(2\lambda)!}{2^\lambda \lambda!} \sum_{\mu=0}^{[m/2]} \binom{m}{2\mu} \frac{(2\mu)!}{2^\mu \mu!} \times \sum_{\nu=0}^{\min(n-2\lambda, m-2\mu)} \binom{n-2\nu}{\nu} \binom{m-2\mu}{\nu} (\vec{z}_1 \cdot \vec{z}_2)^\nu \times \sum_l ((\vec{r}_l - \vec{r}) \cdot \vec{z}_1)^{n-2\lambda-\nu} ((\vec{r}_l - \vec{r}) \cdot \vec{z}_2)^{m-2\mu-\nu} \times (-2)^{n+m-\lambda-\mu-\nu} I_{n+m-\lambda-\mu-\nu}(\vec{r}_l - \vec{r}) \quad (20)$$

$$I_t(r) = \frac{2}{\sqrt{\pi}} \int_\epsilon^\infty \alpha^{2t} e^{-\alpha^2 r^2} \, d\alpha \quad (21)$$

$$I_t(r) = \frac{1}{r^2}\left\{(t - 1/2)J_{t-1}(r) + \frac{\epsilon^{2t-1} e^{-\epsilon^2 r^2}}{\sqrt{\pi}}\right\}$$

$$I_0(r) = \frac{\text{erf}(\epsilon r)}{r} - \frac{\pi}{\Omega \epsilon^2}$$

ϵ is an arbitrarily chosen parameter, by which the convergence of the sums can be regulated.

The sum over the reciprocal lattice is given by

$$^{rec}\Psi_{z_1 z_2}^{(n,m)}(\vec{r}) = \frac{1}{\pi\Omega}(2\pi i)^{n+m} \times \sum_{l\neq 0} \frac{1}{h_l^2}(\vec{h}_l \cdot \vec{z}_1)^n (\vec{h}_l \cdot \vec{z}_2)^m e^{-\pi^2 h_l^2/\epsilon^2} e^{2\pi i(\vec{h}_l \cdot \vec{r})} \quad (22)$$

where Ω is the volume of the unit cell and $\vec{h}_l$ a vector of the reciprocal lattice.

In the case of $\vec{r}_k = \vec{r}_{k'}$ (self-potential), one has to omit the term for $\vec{r}_l = 0$ in the sum over the real lattice and to subtract, for $n + m$ = even, the term

$$\frac{2}{\sqrt{\pi}} \int_0^\epsilon \left\{ \lim_{r\to 0} \frac{\partial^{n+m}}{\partial z_k{}^n \partial z_{k'}{}^m} e^{-\alpha^2 r^2} \right\} d\alpha = (-1)^{(n+m)/2} 2^{n+1} n!m! \frac{\epsilon^{n+m+1}}{\sqrt{\pi}(n+m+1)} \times \sum_{\lambda=0}^{[n/2]} \frac{(\vec{z}_k \cdot \vec{z}_{k'})^{n-2\lambda}}{2^{2\lambda}\lambda!(n-2\lambda)!\left(\lambda + \frac{m-n}{2}\right)!} \quad \text{(for } n > m\text{)} \quad (23)$$

from the sum over the reciprocal lattice. From the electrostatic interaction energy the Madelung parameter M_{elec} is obtained by

$$M_{elec} = \frac{U_{elec} a}{e^2 N_L} \quad (24)$$

By using this technique, expansions 1 and 2 for the Madelung parameter M_{elec} were calculated.

For expansion 1 the MX_6^{2-} ion was considered as three superimposed cylindrical symmetrical "partial" ions having the configuration

$$X^{q_X} - M^{1/3 q_M} - X^{q_X}$$

and the charges specified. The expansion takes place about the center of mass of the ion. When we choose this origin the multipole moments $Q_A^{(n)}$ (referred to the parameter a) of even order for the "partial" ions are

$$Q_A^{(n)} = \frac{1}{3} q_M \left(\frac{a_M}{a}\right)^n + 2q_X \left(\frac{d_X}{a}\right)^n \quad (n = \text{even}) \quad (25)$$

With $d_M = 0$ eq 25 leads to

$$Q_A^{(0)} = 1/3 q_M + 2q_X = -2/3 \quad (26a)$$

$$Q_A^{(n)} = 2q_X \left(\frac{d}{a}\right)^n \quad \text{for } n \neq 0 \quad (26b)$$

The multipole moments for the cation M′ are

$$Q_{M'}{}^{(0)} = 1 \text{ and } Q_{M'}{}^{(n)} = 0 \quad \text{for } n \neq 0 \quad (26c)$$

The second expansion, leading to eq 2, was carried out about the positions of the chlorine atoms ($u = 0.24$) in the $PtCl_6^{2-}$ ion. The multipole moments occurring in this expansion are

$$Q_X^{(0)} = q_X, Q_X^{(n)} = q_X \left(\frac{d - 0.24a}{a}\right)^n \quad \text{for } n \neq 0 \quad (27a)$$

$$Q_M^{(0)} = q_M, Q_M^{(n)} = 0 \quad \text{for } n \neq 0 \quad (27b)$$

$$Q_{M'}{}^{(0)} = 1, Q_{M'}{}^{(n)} = 0 \quad \text{for } n \neq 0 \quad (27c)$$

This expansion was evaluated not only using a cubic unit cell but also a rhombohedral unit cell.

TABLE I: Multipole Expansion Coefficients for Expansion 1

Term	Coeff	Term	Coeff
α_0	$1.163\,657\,5 \times 10^1$		
α_2	0	β_2	0
α_4	$1.102\,911\,6 \times 10^3$	β_4	0
α_6	$-4.062\,257\,3 \times 10^3$	β_6	0
α_8	$-1.250\,907\,1 \times 10^4$	β_8	$-6.819\,662\,0 \times 10^4$
α_{10}	$1.278\,491\,8 \times 10^5$	β_{10}	$4.609\,620\,5 \times 10^3$
α_{12}	$-9.824\,513\,1 \times 10^4$	β_{12}	$8.492\,492\,3 \times 10^5$
α_{14}	$-2.780\,054\,6 \times 10^6$	β_{14}	$1.400\,990\,0 \times 10^7$
α_{16}	$1.169\,795\,5 \times 10^7$	β_{16}	$-1.802\,114\,8 \times 10^8$
α_{18}	$3.060\,689\,9 \times 10^7$	β_{18}	$1.670\,732\,6 \times 10^7$
α_{20}	$-4.018\,556\,7 \times 10^8$	β_{20}	$3.781\,912\,9 \times 10^9$
α_{22}	$5.759\,213\,9 \times 10^8$	β_{22}	$4.706\,619\,5 \times 10^{10}$
α_{24}	$8.492\,043\,7 \times 10^9$	β_{24}	$-6.012\,632\,5 \times 10^{11}$
α_{26}	$-4.415\,387\,0 \times 10^{10}$	β_{26}	$1.132\,293\,7 \times 10^{11}$
α_{28}	$-7.247\,381\,0 \times 10^{10}$	β_{28}	$1.330\,074\,5 \times 10^{13}$
α_{30}	$1.419\,983\,5 \times 10^{12}$	β_{30}	$1.654\,835\,7 \times 10^{14}$
α_{32}	$2.963\,212\,1 \times 10^{12}$	β_{32}	$-2.135\,219\,1 \times 10^{15}$

TABLE II: Contribution to M_{elec} for K_2PtCl_6 ($u = 0.24$) Calculated According to Expansion 1

Term	Contribution	Sum of Contributions
α_0	11.636 575	11.636 575
$\alpha_4 u^4$	3.659 196	
$\alpha_6 u^6$	−0.776 309	
$\alpha_8 u^8$	−0.137 694	
$\alpha_{10} u^{10}$	0.081 061	
$\alpha_{12} u^{12}$	−0.003 588	
$\alpha_{14} u^{14}$	−0.005 848	
$\alpha_{16} u^{16}$	0.001 417	
$\alpha_{18} u^{18}$	0.000 214	
$\alpha_{20} u^{20}$	−0.000 162	
$\alpha_{22} u^{22}$	0.000 013	
$\alpha_{24} u^{24}$	0.000 011	
$\alpha_{26} u^{26}$	−0.000 003	
$\alpha_{28} u^{28}$	−0.000 000	
$\alpha_{30} u^{30}$	0.000 000	
$\alpha_{32} u^{32}$	−0.000 000	
$\sum_{n=4}^{32} \alpha_n u^n$		2.818 308
$\beta_8 u^8$	−0.750 676	
$\beta_{10} u^{10}$	0.002 923	
$\beta_{12} u^{12}$	0.031 015	
$\beta_{14} u^{14}$	0.029 471	
$\beta_{16} u^{16}$	−0.021 835	
$\beta_{18} u^{18}$	0.000 117	
$\beta_{20} u^{20}$	0.001 520	
$\beta_{22} u^{22}$	0.001 090	
$\beta_{24} u^{24}$	−0.000 802	
$\beta_{26} u^{26}$	0.000 009	
$\beta_{28} u^{28}$	0.000 059	
$\beta_{30} u^{30}$	0.000 042	
$\beta_{32} u^{32}$	−0.000 031	
$\sum_{n=8}^{32} \beta_n u^n$		−0.707 100

The expansion coefficients α_n and β_n for expansion 1 up to $n = 32$ are given in Table I. In order to give some insight into the convergence, the values of the single terms of expansion 1 for K_2PtCl_6, ($d/a = 0.24$), are indicated in Table II. For M_{elec} of K_2PtCl_6 one obtains

$$M_{elec} \text{ (based on } a_0) = 11.636\,575 + 2.8183\,08 q_{Cl} - 0.707\,100 q_{Cl}^2 \quad (28)$$

TABLE III: Multipole Expansion Coefficients for Expansion 2

Term	Coeff	Term	Coeff
A_0	$1.163\,657\,5 \times 10^{1}$		
B_0	2.818 308 0	C_0	$-7.070\,970\,7 \times 10^{-1}$
B_1	$3.994\,510\,0 \times 10^{1}$	C_1	$-2.292\,206\,0 \times 10^{1}$
B_2	$1.651\,222\,9 \times 10^{2}$	C_2	$-3.196\,501\,5 \times 10^{2}$
B_3	$-7.033\,968\,1 \times 10^{1}$	C_3	$-2.475\,928\,7 \times 10^{3}$
B_4	$-1.691\,572\,0 \times 10^{3}$	C_4	$-1.148\,446\,7 \times 10^{4}$
B_5	$-4.481\,688\,6 \times 10^{2}$	C_5	$-3.357\,916\,3 \times 10^{4}$
B_6	$1.227\,325\,0 \times 10^{4}$	C_6	$-8.939\,207\,3 \times 10^{4}$
B_7	$6.888\,664\,2 \times 10^{3}$	C_7	$-4.402\,666\,5 \times 10^{5}$
B_8	$-7.478\,398\,3 \times 10^{4}$	C_8	$-2.265\,058\,6 \times 10^{6}$

TABLE IV: Contribution to M_{elec} for a Salt with $u = 0.20$ ($t = (d - 0.24a)/a = -0.04$) Calculated According to Expansion 2

Term	Contribution	Sum of contributions
A_0	11.636 575	11.636 575
B_0	2.818 308	
B_1t^1	−1.597 804	
B_2t^2	0.264 196	
B_3t^3	0.004 502	
B_4t^4	−0.004 330	
B_5t^5	0.000 046	
B_6t^6	0.000 050	
B_7t^7	−0.000 001	
B_8t^8	−0.000 000	
$\sum_{m=1}^{8} B_mt^m$		1.484 966
C_0	−0.707 097	
C_1t^1	0.916 882	
C_2t^2	−0.511 440	
C_3t^3	0.158 459	
C_4t^4	−0.029 400	
C_5t^5	0.003 439	
C_6t^6	−0.000 366	
C_7t^7	0.000 072	
C_8t^8	−0.000 015	
$\sum_{m=1}^{8} C_mt^m$		−0.169 466

This equation should be compared to eq 13 whence agreement between the two equations is satisfactory and verifies the accuracy of the coefficients α_n and β_n.

The coefficients A_0, B_m, and C_m of expansion 2 up to $m = 8$, calculated using a cubic and a rhombohedral unit cell, are found in Table III. Both calculations agree within eight significant figures. Substituting $d = 0.24a_0$ for K_2PtCl_6, i.e., omitting all terms in the sums over m except the terms with $m = 0$, we generate

$$M_{elec} \text{ (based on } a_0) = 11.636\,575 + 2.818\,308q_{Cl} - 0.707\,097q_{Cl}^2 \quad (29)$$

In order to check the convergence of expansion 2 we calculated M_{elec} for some salts with K_2PtCl_6 structure,[1] e.g., Cs_2GeF_6 ($a_0 = 9.021$ Å), Rb_2MnF_6 ($a_0 = 8.340$ Å), Rb_2SiF_6 ($a_0 = 8.452$ Å), Tl_2SiF_6(8.568 Å), having $u = 0.20$. Table IV shows the individual contributions to the Madelung parameter. As a check on these results, from Simon and Zeller's paper directly we calculate (for the case $u = 0.20$), that the Madelung constant, M, is given by

$$M = 11.636\,566 + 61.484\,940q_{Cl} + 129.904\,119q_{Cl}^2 \quad (30)$$

where M is based on a_0.

The Madelung constant, related to the self-energy of the $PtCl_6^{2-}$, can be worked out very simply, in terms of the Pt–Cl distance in the ion, d, and is given (based on a_0) by the equation

$$M_{SE} = -(12a_0/d)q_{Cl} - ((36 - 3/2 - 6\sqrt{2})/d)q_{Cl}^2a_0 \quad (31)$$

substituting $d = 0.20a_0$, we find

$$M_{SE} = -60.000\,000q_{Cl} - 130.073\,593q_{Cl}^2 \quad (32)$$

Whereupon, M_{elec} ($= M + M_{SE}$), becomes

$$M_{elec} \text{ (based on } a_0) = 11.636\,566 + 1.484\,94q_{Cl} - 0.169\,474q_{Cl}^2 \quad (33)$$

Comparison of this result with that given in Table IV shows the required agreement.

From Tables II and IV it can be seen that both expansions converge sufficiently quickly and lead to almost the same results. On the basis of these comparisons the expansions seem satisfactory and are important in their direct applicability in studying direct minimization methods for lattice energy calculations.

Acknowledgment. H. D. B. Jenkins gratefully acknowledges the receipt of a Study Visit Award in the European Programme of the Royal Society. The Austrian Academy of Sciences is also thanked for payment of a subsistence allowance as part of this program.

The calculations have been carried out at the Rechenzentrum der Technischen Universität Wien.

References and Notes

(1) R. W. G. Wyckoff, "Crystal Structures", 2d ed, Interscience, New York, N.Y., 1965.
(2) R. H. Busch, E. E. Galloni, and C. R. Hartz, *An. Assoc. Quim. Argent.*, **39**, No. 192, 55 (1951).
(3) H. D. B. Jenkins and T. C. Waddington, *Chem. Phys. Lett.*, **31**, 369 (1975).
(4) H. D. B. Jenkins, *J. Chem. Soc., Faraday Trans. 1*, in press.
(5) A. Neckel and G. Vinek, *Z. Phys. Chem.*, **42**, 129 (1964).
(6) A. Neckel and G. Vinek, *Z. Phys. Chem.*, **48**, 61 (1966).
(7) G. Vinek, *Monatsh. Chem.*, **98**, 24-0 (1967).
(8) G. Vinek, A. Neckel, and H. Nowotny, *Acta. Chim. Acad. Sci. Hung.*, **51**, 193 (1967).
(9) A. Neckel, P. Kuzmany, and G. Vinek, *Z. Naturforsch. A*, **26**, 561 (1971)
(10) A. Neckel, P. Kuzmany, and G. Vinek, *Z. Naturforsch. A*, **26**, 569 (1971)
(11) P. P. Ewald, *Ann. Phys.*, **64**, 253 (1921).
(12) H. P. Dixon, H. D. B. Jenkins, and T. C. Waddington, *J. Chem. Phys.*, **57**, 4388 (1972).
(13) E. F. Bertaut, *J. Phys. Radium*, **13**, 499 (1952).
(14) H. D. B. Jenkins and B. T. Smith, *J. Chem. Soc., Faraday Trans. 1*, **72**, 353 (1976).
(15) T. C. Waddington, *Adv. Inorg. Chem. Radiochem.*, **1**, 158 (1959).
(16) G. Simon and G. R. Zeller, *J. Phys. Chem. Solids*, **35**, 187 (1974).
(17) P. Herzig, P. Kuzmany, and A. Neckel, unpublished work.
(18) L. Jansen, *Physica*, **23**, 599 (1957)

Thermal Expansion and Structure of Leucite-Type Compounds

Kazuyuki Hirao,* Naohiro Soga, and Masanaga Kunugi

Department of Industrial Chemistry, Faculty of Engineering, Kyoto University, Sakyo-ku, Kyoto, Japan *(Received October 10, 1975)*

The thermal expansion and structure of leucite-type ferrisilicates and aluminosilicates, namely, $M'FeSi_2O_6$ (M' = K, Rb, Cs) and $MAlSi_2O_6$ (M = K, Rb), have been investigated by means of a high temperature x-ray diffractometer. New x-ray diffraction data for $RbAlSi_2O_6$ and $RbFeSi_2O_6$ are presented, and it is suggested that $RbAlSi_2O_6$ should be called rubidium leucite rather than rubidium analcite from the structural point of view. In these compounds, K, Rb, or Cs ions are considered to occupy W sites (large cavities) in the (Si, Al or Fe)–O framework, unlike Na ions in analcite where Na ions are known to occupy S sites (small cavities). The thermal expansion curves for leucite-type compounds are found to be divided into three different stages, similar to those for cristobalite. The results are interpreted by considering the distortion of the (Si, Al, or Fe)–O framework, the rotation of tetrahedra in the framework, and the transition of the framework from the collapsed state to the uncollapsed state.

I. Introduction

The thermal expansion behaviors of framework silicates, particularly those of aluminosilicates, have been studied widely in the past, mainly because some aluminosilicates show very low or even negative thermal expansion.[1] From these studies, a number of interesting thermal behaviors of aluminosilicates have been revealed. One of them is the similarity in polymorphic transitions between aluminosilicates and silica. For example, eucryptite, nepheline, and carnegieite show polymorphic transitions similar to those of quartz, tridymite, and cristobalite, respectively.[2-6] The thermal expansion of synthetic β-spodumene is characterized by a pronounced anisotropy much the same as that of keatite,[7-9] while the thermal expansion of leucite shows a phase transition from the tetragonal α form to the cubic β form, which resembles the behavior of cristobalite.[10,11]

A close look at the thermal expansion curves for these framework silicates, however, reveals some differences between aluminosilicates and silica. Particularly noteworthy is a lack of distinct or sudden change in thermal expansion at the inversion temperature in many alkali aluminosilicates. Instead, they show a gradual deviation from the expansion curve of the low-temperature form at temperatures well below the inversion temperature. The interpretation of this phenomenon has been based on the concept that their frameworks show varying degrees of collapse near the inversion temperature, depending upon the nature of the interframework cation.

Although a number of reports which deal with the positions of interframework cations in sodalite and zeolite mineral groups can be incorporated to comprehend the role of interframework cations on thermal expansion and transition behaviors, little is known about the positions of interframework cations in other groups of framework silicates. An investigation is under way in the author's laboratory to clarify the positions of interframework cations through the determination of thermal and electrical properties of various types of silicate compounds.

The present paper describes the results of the experiment on thermal expansion of silicates having compositions of $MAlSi_2O_6$ (M = K, Rb) and $M'FeSi_2O_6$ (M' = K, Rb, Cs), which are found to belong to the same family as leucite in the present study. Ferrisilicates were chosen, in addition to aluminosilicates, because the hydrothermal synthesis is not required to obtain various solid solutions of ferrisilicates, unlike the case of the corresponding isostructural aluminosilicates. Thus the effect of interframework cations on thermal expansion behaviors can be pursued easily. A detailed study of the thermal expansion of the sodalite group of minerals and the leucite group of minerals was very helpful in interpreting the thermal expansion behaviors of ferrisilicates.[12-14]

II. Structure of $MAlSi_2O_6$ and $M'FeSi_2O_6$

Leucite, $KAlSi_2O_6$, is tetragonal with lattice parameters, a = 13.0 Å and c = 13.8 Å at room temperature. On heating at about 625 °C, it changes to a cubic structure with a = 13.4 Å.[15] $RbAlSi_2O_6$ takes the same two types of polymorphs, which have been interpreted as Rb analcite I with a = 13.2 Å and c = 13.6 Å and Rb analcite II with a = 13.56 Å, respectively.[16] Although the framework structures of these compounds are considered to be similar to that of analcite, $NaAlSi_2O_6 \cdot H_2O$, or pollucite, $CsAlSi_2O_6$, the exact positions of K or Rb ions have not been well established.

According to the studies by Wyart[17] and by Náray-Szabó,[18] one unit cell of analcite or pollucite contains $16(MAlSi_2O_6)$, or $48(Si,Al)O_4$ tetrahedra which are interconnected as shown in Figure 1. This figure shows only the lower half of the cell in order to provide a clear picture of the arrangement. In such a framework structure, there are two different types of cavities in which interframework cations can be located. The first one, which is represented by a large circle in Figure 1 and designated as a W site, is coordinated by 12 oxygens and is in line with the center of large channels formed by the six-membered rings, which run along four nonintersecting triad directions. There are 16 equivalent positions of this type in a unit cell. The second one, which is represented by a small circle in Figure 1 and designated as a S site, is situated at the center of four coplanar oxygens of the framework. There are 24 equivalent positions of this type in a unit cell. In the case of analcite, water molecules occupy W sites and sodium ions S sites, while in pollucite, cesium ions are located at W sites and S sites remain vacant. The structures of $M'FeSi_2O_6$ have not been studied in detail, but they are generally considered to be isostructural with $MAlSi_2O_6$ from the viewpoint of crystal chemistry.

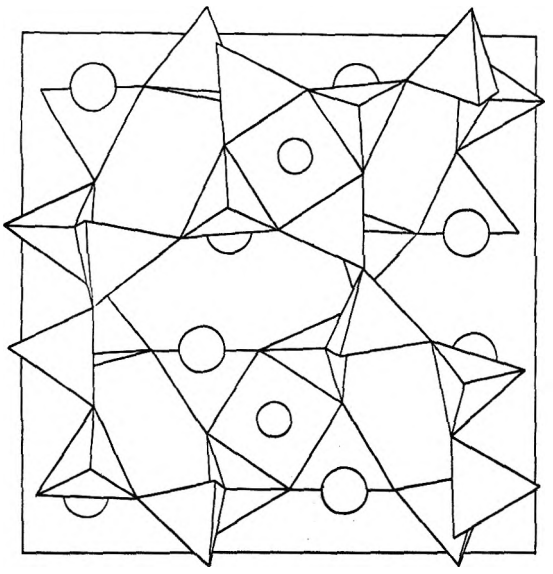

Figure 1. The lower half of the cell structure of analcite or pollucite. Large circles represent W sites and a part of small circles represent S sites.

III. Experimental Section

The batches for $MAlSi_2O_6$ (M = K, Rb) and $M'FeSi_2O_6$ (M' = K, Rb, Cs) were prepared by weighing out the appropriate proportions of chemical reagent grade K_2CO_3, Rb_2CO_3, or Cs_2CO_3 and high-purity Al_2O_3, Fe_2O_3, and SiO_2. After thorough mixing, they were melted at 1300–1650 °C in platinium crucibles and stirred during melting. The melting furnace was heated electrically with SiC elements. The melts crystallized when they were subjected to certain heat treatments. Rb analcite was crystallized by hydrothermal synthesis in a manner similar to that employed by Barrer et al.[19]

Room-temperature x-ray diffraction traces of all specimens were taken with standard Norelco equipment. High-temperature x-ray diffraction data were obtained from 25 to 900 °C by using a diffractometer with a high temperature attachment. The thermocouples were attached to the back of a sample holder and their readings were accurate within ±3 °C of the actual temperature of the specimen. The angular positions of the nickel diffraction peaks, as a function of temperature, were determined from the peak positions of MgO, for which the thermal expansions were known. All high-temperature x-ray diffraction traces were reproduced at least three times, with pure nickel and silicon as the internal standard. The indexing of the reflections was made based on the structural determination after Náray-Szabó (1942), and the cell parameters of a specimen were determined by the least-squares method using the peak positions in the range 15–50° 2θ (Cu Kα) at various temperatures between 25 and 900 °C. Because of the interference of coalescing peaks, it was not possible to obtain satisfactory cell parameters at temperatures just below the inversion temperature.

IV. Experimental Results

The x-ray diffraction data for $RbAlSi_2O_6$ and $RbFeSi_2O_6$ at 25 °C are listed in Table I, along with the appropriate indices. The data for other compounds were almost identical with the values given in ASTM cards.

The linear thermal expansion curves along the a and c axes for $KAlSi_2O_6$ and $RbAlSi_2O_6$ are illustrated in Figure 2. It is clear that both $KAlSi_2O_6$ and $RbAlSi_2O_6$ behave similarly,

TABLE I: X-Ray Diffraction Data for $RbAlSi_2O_6$ and $RbFeSi_2O_6$

$RbAlSi_2O_6$ (Rb leucite)			$RbFeSi_2O_6$ (Rb ferrileucite)		
d	*I*	*hkl*	*d*	*I*	*hkl*
3.610	80	213	3.675	60	213
3.402	80	004	3.616	80	312
3.311	100	400	3.477	80	004
3.160	80	303	3.355	100	400
2.976	60	420	3.055	60	420
2.852	100	323	2.901	80	323
2.648	80	314	3.688	60	314
2.376	80	404	2.415	80	404
2.291	10	334	2.366	20	440
2.263	20	315	2.189	50	532
2.112	10	602	1.988	40	613
2.168	80	610	1.868	40	640

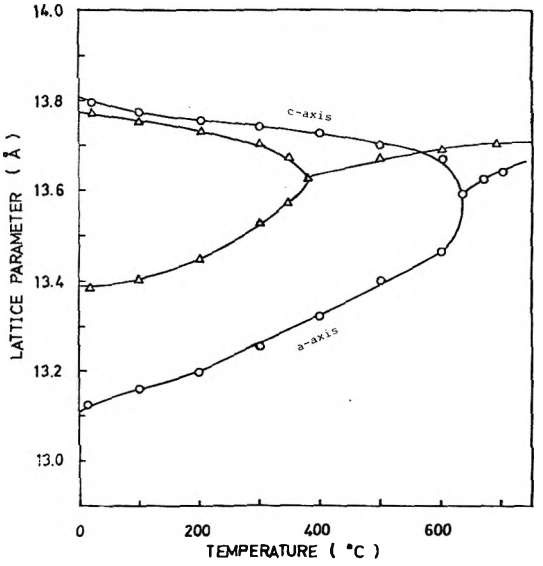

Figure 2. Thermal expansion curves along a and c axes for (O) $KAlSi_2O_6$ and (▲) $RbFeSi_2O_6$.

having inversion temperatures from the tetragonal to the cubic form of 620 and 360 °C, respectively. The cell parameter, a, increases with increasing temperature up to the inversion temperature, while the cell parameter, c, decreases with increasing temperature. The thermal expansion curve for leucite determined by Taylor has a very similar form (inversion temperature, 605 °C), but it is displaced to lower cell sizes than those reported here.[20]

Taylor and Henderson suggest that the reason for the difference is not clear, but that it is most likely due to the presence of Na and other elements in solid solution in leucite.

The thermal expansion curves for $KFeSi_2O_6$ and $RbFeSi_2O_6$ are shown in Figure 3. As mentioned before, ferrisilicates were chosen, because various solid solutions of ferrisilicates, unlike the case of corresponding isostructural aluminosilicates, were synthesized easily. This figure indicates inversion temperatures of 570 °C for $KFeSi_2O_6$ and 320 °C for $RbFeSi_2O_6$. These temperatures are slightly lower than those of the corresponding aluminosilicates, but the shape of the curves are similar.

The thermal expansion curve for a solid solution having the composition of $(K_{0.5}Rb_{0.5})FeSi_2O_6$ is shown in Figure 4. This figure clearly indicates that both the inversion temperature

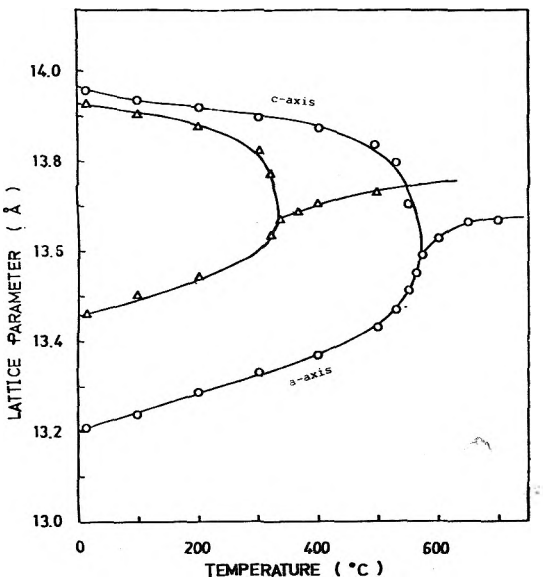

Figure 3. Thermal expansion curves along *a* and *c* axes for (O) $KFeSi_2O_6$ and (Δ) $RbFeSi_2O_6$.

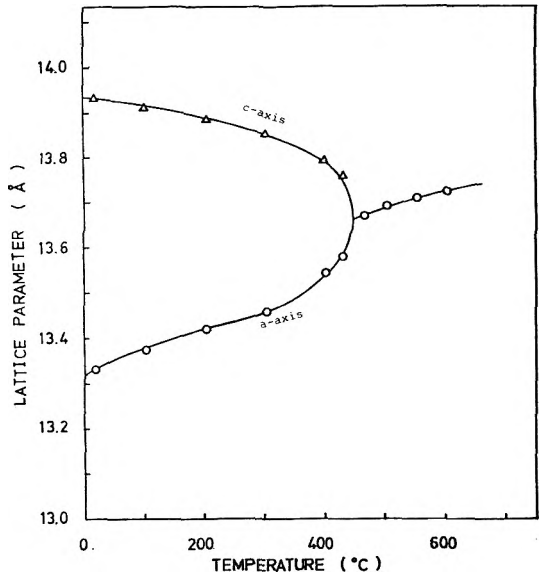

Figure 4. Thermal expansion curves along *a* and *c* axes for a solid solution having the composition $(K_{0.5}Rb_{0.5})FeSi_2O_6$.

and axial ratio *c/a* of this solid solution at 25 °C are close to the average of the respective values for $KFeSi_2O_6$ and $RbFeSi_2O_6$. When Rb ions in $RbFeSi_2O_6$ are partially replaced with Cs ions, the inversion temperature becomes lower with increasing Cs content and the *c/a* axial ratio at 25 °C approaches one, as shown in Figure 5. Both $CsAlSi_2O_6$ and $CsFeSi_2O_6$ were found to be cubic at room temperature, as has been reported previously, but their thermal expansion curves were not so simple.

V. Discussion

1. *X-Ray Diffraction Data of $RbAlSi_2O_6$ and $RbFeSi_2O_6$.* As described in section II, the mineral $RbAlSi_2O_6$ was named as rubidium analcite.[21,22] According to the ASTM card, the *d* spacings, 3.40 and 3.31 Å, of $RbAlSi_2O_6$ have been regarded as (004) and (104) reflections, respectively. However, the present data show that these two spacings join together at the

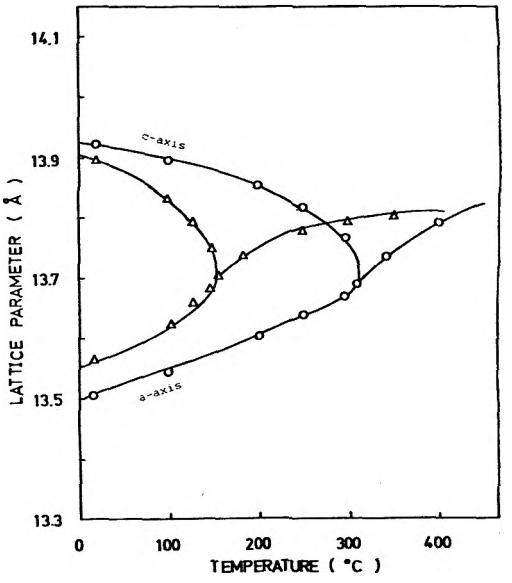

Figure 5. Thermal expansion curves along *a* and *c* axes for $(Rb_{1-x}Cs_x)FeSi_2O_6$: (O) $Rb_{0.9}Cs_{0.1}$; (Δ) $Rb_{0.8}Cs_{0.2}$.

inversion temperature and form one diffraction line. This behavior is similar to that of $KAlSi_2O_6$, in which the corresponding lines have been indexed as (004) and (400) reflections. Consequently, it is concluded that the *d* spacing of 3.31 Å for $RbAlSi_2O_6$ is not (104) reflection but (400) reflection, and that the cell parameters for the low-temperature α form of $RbAlSi_2O_6$ are a = 13.40 Å and c = 13.79 Å, and that for the high-temperature β form a = 13.67 Å. No x-ray diffraction data for $RbFeSi_2O_6$ seem to exist in the literature.

It should be pointed out here that the name of Rb analcite for $RbAlSi_2O_6$ is misleading, because this name implies that Rb ions occupy the same interframework sites as Na ions in analcite. However, as will be described later, Rb ions are too large to occupy S sites in the (Si, Al)–O framework shown in Figure 1, so that they should exist in W sites like K ions in leucite. From these results, it is suggested here that $RbAlSi_2O_6$ should be called rubidium leucite instead of rubidium analcite.

2. *Dependence of the Axial Ratio c/a on Ionic Radii of Interframework Cations.* As the temperature is raised, the cell parameter *a* expands but c contracts in $MAlSi_2O_6$ or $M'FeSi_2O_6$ (M, M′ = K, Rb) until both of the parmeters attain the same value at the inversion temperature. This change is completely reversible. These results seem to indicate that the (Si, Al, or Fe)–O framework is distorted in the tetragonal α form in comparison with that in the cubic β form and that such distortion is released completely at the inversion temperature. If so, the degree of distortion at 25 °C, which can be represented by the axial ratio *c/a* at 25 °C, should depend upon the size of interframework cations.

In Figure 6, the values of axial ratio *c/a* at 25 °C for $MAlSi_2O_6$ and $M'FeSi_2O_6$ are plotted against the ionic radius of interframework cations. It is clear that a fairly good linear correlation exists between the axial ratio *c/a* and the ionic radius for $M'FeSi_2O_6$. The extrapolation of the linear line to the point *c/a* = 1 yields an ionic radius close to that of cesium ion. Although there are only two data points for $MAlSi_2O_6$, a line drawn through these points gives a value slightly smaller than that of the cesium ion. This implies that no distortion appears in the framework of both $CsAlSi_2O_6$ and $CsFeSi_2O_6$ at 25 °C and that the framework takes a cubic structure. This consideration agrees with the fact that $CsAlSi_2O_6$ and $CsFeSi_2O_6$[23] are cubic at 25 °C.

TABLE II: Inversion and Discontinuity Temperatures and Mean Thermal Expansion Coefficients for Various Leucite-Type Compounds

Name	Tetragonal–cubic inversion temp, T_i	Discont temp, T_d	Lattice parameter a_i at T_i	Lattice parameter a_d at T_d	Expansion coef, × 10^5 Stage I $\frac{1}{a}\frac{\Delta a}{\Delta t}$	Stage I $\frac{1}{c}\frac{\Delta c}{\Delta t}$	Stage I $\frac{1}{v}\frac{\Delta v}{\Delta t}$	Stage II $\frac{1}{a_i}\frac{\Delta a}{\Delta t}$	Stage II $\frac{1}{v_i}\frac{\Delta v}{\Delta t}$
$KFeSi_2O_6$	570 ± 10	810 ± 10	13.57	13.71	5.14	−5.13	5.05	4.24	13.01
(0.5K · 0.5Rb) $FeSi_2O_6$	400 ± 10	700 ± 10	13.62	13.72	5.00	−5.11	4.83	3.04	9.23
$RbFeSi_2O_6$	320 ± 10	610 ± 10	13.66	13.75	4.44	−5.02	3.63	2.75	8.66
(0.1Cs · 0.9Rb) $FeSi_2O_6$	310 ± 10	500 ± 10	13.68	13.77	4.15	−6.04	3.46	2.74	8.30
(0.2Cs · 0.8Rb) $FeSi_2O_6$	160 ± 10	400 ± 10	13.70	13.78	9.31	−10.65	5.81	2.43	7.61

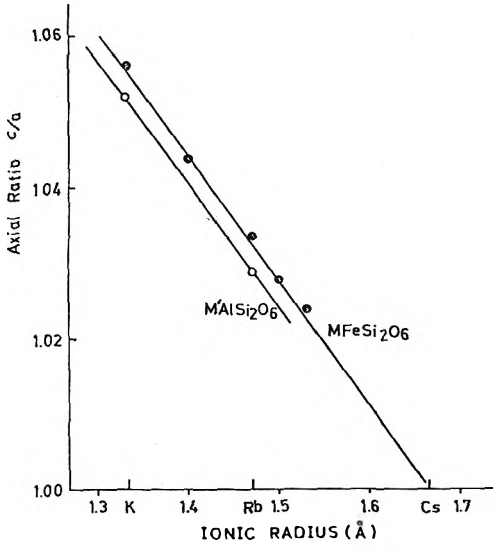

Figure 6. Relationship between axial ratio c/a and ionic radius of interframework cations.

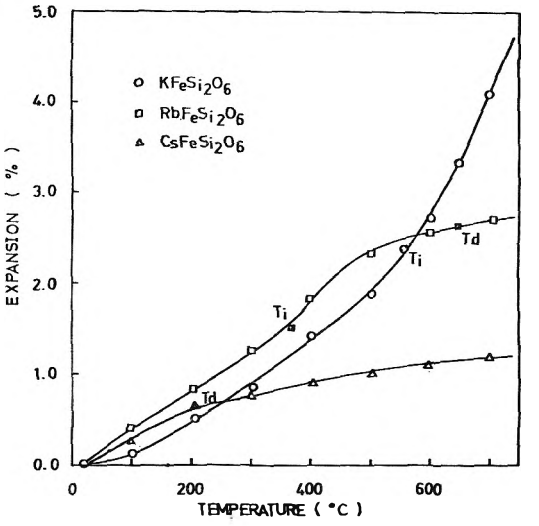

Figure 7. Volume thermal expansion curves of $KFeSi_2O_6$ and $RbFeSi_2O_6$.

As described in section II, it has been established that cesium ions in pollucite are located at W sites as Cs ions in pollucite. However, these K or Rb ions are smaller than the size of the large cavities of W sites, so that the surrounding (Si, Al, or Fe)–O framework is contracted and distorted. It is reasonable that the distortion becomes larger as the size of interframework cations becomes smaller. However, if the interframework cations becomes too small, they no longer occupy W sites but enter into S sites, as in the case of Na ions in analcite.

3. *Volume Expansion and Rotation of Framework in Ferrisilicates.* The thermal expansion curves shown in Figures 3–5 indicate that the (Si, Fe)–O framework does not expand linearly with temperature above the inversion temperature, even though the framework takes a cubic structure. In order to discuss this behavior in detail, the volume thermal expansion curves for $M'FeSi_2O_6$ were calculated from their linear thermal expansion curves. The results are shown in Figure 7, where the inversion temperature is marked as T_i. It appears that the volume expansion curve for a compound can be divided into three stages on the basis of the rate of thermal expansion, as in the case of cristobalite given by Wyckoff and Johnson et al.[24,25] Below the inversion temperature, or in stage I, the thermal expansivity shows an increase from room temperature to the inversion temperature. Above the inversion temperature, the thermal expansivity is still higher at the beginning but becomes smaller as temperature rises (stage II). A further change in thermal expansivity to a low value takes place at higher temperatures (stage III). The transition temperature from stage II to stage III may be referred to as the discontinuity temperature T_d as in the case of cristobalite.

The inversion temperature, T_i, and the discontinuity temperature, T_d, for $M'FeSi_2O_6$ are listed in Table II. Also listed are the lattice parameter coefficients in stages I and II.

VI. Conclusion

The volume thermal expansion curves of leucite-type ferrisilicates are found to be divided into three stages having different thermal expansivity, similar to those for cristobalite. From the similarity in thermal expansion behaviors between cristobalite and $M'FeSi_2O_6$ (M′ = K, Rb, Cs, and their solid solutions), the high thermal expansivity in stage II for ferrisilicates is considered to be due to the rotation or untwisting of the tetrahedra, causing the structure to change from the collapsed state to the uncollapsed state. However, unlike cristobalite, the transition from the collapsed state to the uncollapsed state is slow in ferrisilicates because of the presence of interframework cations. This means that in ferrisilicates the transition from stage II to stage III is not sharp such as T_i and furthermore, the thermal expansivity above T_d is rather high in comparison with that of β-cristobalite. The

present data in Figure 7 seem to support such consideration.

However, it is not clear whether the ideal, fully expanded state such as cristobalite is achieved at T_d. Taylor and Henderson assumed that leucites and sodalites were prevented from attaining the fully expanded state at T_d because of the interframework cation–framework anion bonds. Subsequently, Taylor (1972) suggested that the temperature affected not only the degree of rotation of the tetrahedra but also the amount of anisotropic thermal motion of the framework oxygens, and that consequently the ideal fully expanded state was probably achieved at T_d.

Studies of this kind indicate the need for high-temperautre structure determinations.

References and Notes

(1) T. Y. Tien and F. A. Hummel, *J. Am. Ceram. Soc.*, **47**, 584 (1964).
(2) O. F. Tuttle and J. V. Smith, *Am. J. Sci.*, **255**, 282 (1957).
(3) D. M. Roy and R. Roy, *Bull. Geol. Soc. Am.*, **69**, 1637 (1958).
(4) F. H. Gillery and E. A. Bush, *J. Am. Ceram. Soc.*, **42**, 175 (1959).
(5) J. Schulz, *J. Am. Ceram. Soc.*, **57**, 313 (1974).
(6) J. S. Moya, A. G. Verduck, and M. Hortal, *Trans. J. Brit. Ceram. Soc.*, **73**, 177 (1974).
(7) W. Ostertag, G. R. Fisher, and J. P. Williams, *J. Am. Ceram. Soc.*, **51**, 651 (1968).
(8) F. A. Hummel, *J. Am. Ceram. Soc.*, **34**, 235 (1951).
(9) L. Chi-Tang and D. R. Peacor, *Z. Kristallogr.*, **126**, 46 (1967).
(10) L. Chi-Tang, *Z. Kristallogr.*, **127**, 327 (1968).
(11) A. J. Majumdar and H. A. McKinstry, *Phys. Chem. Solids*, **25**, 1487 (1964).
(12) D. Taylor and C. M. B. Henderson, *Am. Min.*, **53**, 1476 (1968).
(13) D. Taylor, *Min. Mag.*, **38**, 593 (1972).
(14) D. Taylor, *Min. Mag.*, **36**, 761 (1968).
(15) Faust, *Schweiz. Mineral. Petrogr. Mitt.*, **43**, 165 (1963).
(16) R. M. Barrer and N. McCallum, *J. Chem. Soc.*, **21**, 4035 (1953).
(17) J. Wyart, *C. R. Acad. Sci. Paris*, **282**, 356 (1941).
(18) Náray-Szabó, *Z. Kristallogr.*, **99**, 277 (1938).
(19) R. M. Barrer and L. Hinds, *J. Chem. Soc.*, **21**, 1466 (1953).
(20) J. C. R. Wyart, *Acad. Sci., Paris*, **205**, 1077 (1937).
(21) R. M. Barrer and J. W. Baynham, *J. Chem. Soc.*, **24**, 2882 (1956).
(22) W. H. Taylor, *Z. Kristallogr.*, **74**, 1 (1930).
(23) Kopp, et al., *Am. Min.*, **48**, 100 (1963).
(24) R. W. G. Wyckoff, *Z. Kristallogr.*, **62**, 189 (1925).
(25) W. Johnson and K. W. Andrews, *Trans. Brit. Ceram. Soc.*, **55**, 277 (1956).

Water Dissociation Effects in Ion Transport through Composite Membrane

Gershon Grossman

Faculty of Mechanical Engineering, Technion—Israel Institute of Technology, Haifa, Israel *(Received June 25, 1975)*

A model has been developed to describe the steady-state ionic transport in composite membranes consisting of alternate layers of cation and anion exchange material. Particular attention has been given to the effects of water dissociation and water ion transport which are associated with the transport of electrolyte and play an important role in many biological and engineering applications. Membranes with various layer combinations are considered. The governing equations are presented and expressions are derived for the distributions of potential and concentrations of all ionic species. Current–voltage characteristics are obtained in terms of the membrane structure and the properties of the solution. The relative portions of current carried through the membrane by electrolyte and water ions are calculated. Homogeneous anion and cation exchange membranes are shown to have a linear current voltage characteristic. Bipolar membranes exhibit an anisotropic behavior with respect to current direction, showing electrolyte current saturation in one direction. Ion-exchange membranes with thin surface films of opposite properties exhibit a similar behavior with polarization in both directions of the current.

1. Introduction

Composite ion-exchange membranes consisting of alternate layers of cation and anion exchange material have been of interest to both biochemists and engineers. Many living systems are known to contain membranes of this type and models explaining their behavior have been proposed in terms of the ion-transport phenomena associated with the layered structure.[1–5] Laboratory experiments with synthetic composite membranes[6–9] have indicated possible industrial and other technological applications.[7] It was also found that homogeneous ion-exchange membranes in processes such as electrodialysis often exhibit a behavior peculiar to composite membranes, due to the formation of thin surface films with ion-exchange properties, which give the membrane a laminar structure. The deposition of these films, known as membrane fouling, originates from small impurities present in the water, and gives rise to undesirable effects which greatly reduce the efficiency of the system.[10–13]

In an earlier paper by Sonin and Grossman[14] a theoretical model was derived to describe ion transport through composite membranes in contact with an electrolyte solution containing a fully ionized solute in a nondissociable solvent. It was shown that current–voltage characteristics of composite membranes can be anisotropic with respect to current direction, depending on their structure. Moreover, the membrane can exhibit current saturation in one or both directions, even when there is little or no polarization in the external solution. These features, derived analytically from the transport equations,[14] had been observed and demonstrated experimentally by numerous investigators with synthetic bipolar membranes,[6–9] biological,[5] and fouled electrodialysis membranes.[10–13,15] An additional observation reported in all these

was the importance of water dissociation in the performance characteristics of the membrane. Dissociation becomes dominant and cannot be disregarded especially at high current densities. It results in a transport of large amounts of dissociated water ions which cause pH changes in the solution in contact with the membrane and reduce the current efficiencies with respect to electrolyte ions transport. Water dissociation and transport plays an important role in some biological membranes[5] and may have some interesting technological applications.[7] In the electrodialysis process, however, it reduces the efficiency of the system and has a deteriorating effect on the membranes' life.[12]

An important analysis describing water dissociation effects in a membrane–electrolyte system was made by Isaacson.[18] His model consists of a cell containing static electrolyte solution between two parallel homogeneous cation-selective membranes. The model has been proposed for studying water dissociation effects in an electrodialysis system. Ionic concentrations and potential distributions in the electrolyte have been calculated. Important results have been obtained in terms of evaluating the relative magnitude of various nonequilibrium effects and the deviation from chemical equilibrium of water ions in the solution.

The purpose of the present analysis has been to extend the model of ref 14 to take into consideration the effect of water dissociation and water ion transport. The governing equations are presented and solved for composite membranes with a laminar structure. Current voltage characteristics and concentration distributions are calculated in terms of the properties of the membrane and the solution. Some of the results are compared with experimental data obtained in other studies.

2. Model and Basic Equations

Figure 1 shows a composite membrane consisting of several homogeneous layers of ion-exchange material in contact with an aqueous electrolyte solution. The solution is dilute and contains a fully ionized salt with one positive and one negative ionic species, as well as a certain amount of dissociated water ions H^+ and OH^-. A potential difference $\Delta\phi$ is applied between the ends of the membrane, causing current at density j to flow through it. The current is due to transport of all four ionic species present in the solution, and may be divided into the part j_e carried by electrolyte ions and the part j_w carried by water ions, as shown.

We focus our attention on one of the membrane's layers. It is made of homogeneous ion-exchange material of thickness Δ_m, with uniformly distributed fixed charge at concentration c_m and valency z_m. c_m is assumed to be much larger than the concentration of any of the species in the solution. The membrane thickness Δ_m is large compared with the Debye length, which is typically a few angstroms.[16]

Under the above conditions, the steady-state, isothermal ion transport both in the membrane and in the solution is governed by the transport laws for ideal solutions.[17] The flux N_i of each species by mechanism of diffusion and migration is given by

$$N_i = -D_i\frac{dC_i}{dX} - \frac{z_iF}{\mathcal{R}T}D_iC_i\frac{d\phi}{dX} \tag{1}$$

where C_i, D_i, and z_i are the concentration, diffusion coefficient, and valency of species i, respectively, and ϕ is the electrical potential. The subscript i may be +, −, H, or OH, applying to the positive electrolyte ion, negative electrolyte ion, H^+, and OH^-, respectively. For each of the species we may

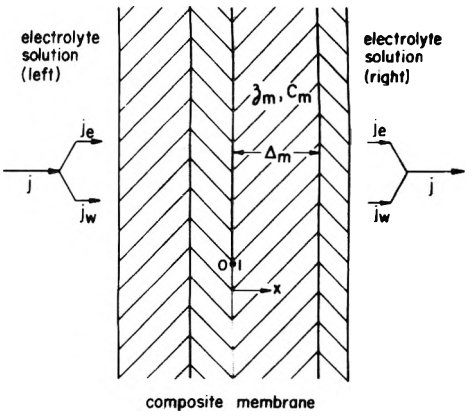

Figure 1. Model and structure of composite membrane.

write the conservation equation

$$dN_i/dX = R_i \tag{2}$$

where R_i is the net rate of formation of the species by chemical reaction. Note that for the electrolyte ions $R_+ = R_- = 0$ and for the water ions $R_H = R_{OH} = R$ where R is the rate of water dissociation per unit volume. Also in effect is the law of quasielectroneutrality:

$$\sum_i z_iC_i = \begin{cases} 0 \text{ in the solution} \\ -z_mC_m \text{ in the membrane} \end{cases} \tag{3}$$

and the condition of local chemical equilibrium of water ions

$$C_HC_{OH} = K^2 \tag{4}$$

where K^2 is the constant of dissociation for the given temperature. We thus have ten equations ((1) and (2) each for the four different species, (3) and (4)) to be solved for the four unknown ionic fluxes and concentrations, R and ϕ.

The above equations are applicable in their present form everywhere in the membrane and in the solution except on surfaces of discontinuity, notably the interfaces between the membrane and the solution and between two layers of the membrane. The laws expressed by (3) and (4) break down in the region of the double layer near the interface.[16] We have assumed that the membrane is thick compared with the Debye length and therefore this region occupies only a small part of the domain under consideration. The double layer is dealt with as part of the interface across which all ionic species are in Donnan equilibrium[17] described by the relation:

$$\frac{F}{\mathcal{R}T}(\phi_1 - \phi_0) = -\frac{1}{z_+}\ln\left(\frac{C_{+1}}{C_{+0}}\right) = -\frac{1}{z_-}\ln\left(\frac{C_{-1}}{C_{-0}}\right) = -\ln\left(\frac{C_{H_1}}{C_{H_0}}\right) = \ln\left(\frac{C_{OH_1}}{C_{OH_0}}\right) \tag{5}$$

where subscripts 0 and 1 apply to the left and right sides of the interface, respectively, as shown in Figure 1.

Finally, the current density may be expressed in terms of the ionic fluxes by

$$j = F\sum_i z_iN_i \tag{6}$$

j consists of j_w and j_e which are given by

$$j_w = F(N_H - N_{OH}) \tag{6a}$$

$$j_e = F(z_+N_+ + z_-N_-) \tag{6b}$$

j_e may be further divided into the part j_+ carried by positive

electrolyte ions and the part j_- carried by negative electrolyte ions:

$$j_\pm = Fz_\pm N_\pm \tag{6c}$$

The conditions of local chemical equilibrium of water ions (3) and of quasielectroneutrality (4) deserve further clarification. The equilibrium condition means that, locally, the rate of production of water ions by dissociation equals the rate of recombination. Let us refer to eq 2 which may be rewritten explicitly for the water ion fluxes as follows:[18]

$$\frac{dN_H}{dX} = \frac{dN_{OH}}{dX} = k_d - k_r C_H C_{OH} = R \tag{2a}$$

where k_d and k_r are the constants of dissociation and recombination. Equation 2a expresses the net rate of water ion formation R as the difference between the production by dissociation (which is independent of local concentration) and the rate of recombination (which is proportional to C_H and C_{OH}). Now, if $k_d \gg R$, then eq 2a reduces to the equilibrium condition (4), which holds throughout most of the membrane and the solution.[18] However, near the surfaces of discontinuity, where the changes in ionic fluxes become large, the quasiequilibrium condition (4) is no longer valid. The thickness of this nonequilibrium zone can be shown to be very small compared to that of the membrane.[18] The condition of electroneutrality, likewise, is maintained throughout most of the membrane and solution and implies that an equal amount of positive and negative charges must be present at each point. This is valid only as long as the dimensions of the domain under consideration are much larger than the Debye length, which under the presently assumed conditions of dilute solutions is of the order of a few angstroms. Electroneutrality does not hold in a thin region near the surfaces of discontinuity, known as the double layer.[16] Since the thickness of this layer is of the order of the Debye length, it may be dealt with as part of the interface, as may also the thin layer of nonequilibrium. To do this, the flux equation (1) for each ionic species is integrated across the interface and the two thin layers on both sides, which yields

$$\frac{F}{\mathcal{R}T}(\phi_1 - \phi_0) = -\frac{1}{z_i}\ln\left(\frac{C_{i1}}{C_{i0}}\right) - \int_0^1 \frac{N_i}{z_i D_i C_i}\,dX$$

The rightmost term in this equation is usually very small as long as there is no resistance to diffusion through the interface. The end result is therefore the Donnan equilibrium condition (5) across the interface.

We now proceed to determine the scaling laws of the problem and write the equations in a dimensionless form. For simplicity we choose to limit the discussion to an electrolyte for which $z_+ = -z_- = 1$ and $D_+ = D_- = D$. This limitation is not essential and a more general solution may be obtained which would yield basically the same physical results. Let us define the following dimensionless variables:

$$\left.\begin{aligned} &x = \frac{X}{d} \\ &c_i = \frac{C_i}{C_0} \quad c_m = \frac{z_m C_m}{C_0} \quad \psi = \frac{F}{\mathcal{R}T}\phi \\ &\gamma_i = \frac{D_i}{D} \quad k = \frac{K}{C_0} \quad r = \frac{d^2}{DC_0}R \\ &i = \frac{d}{FDC_0}j \quad i_e = \frac{d}{FDC_0}j_e \quad i_w = \frac{d}{FDC_0}j_w \quad i_\pm = \frac{d}{FDC_0}j_\pm \end{aligned}\right\} \tag{7}$$

where d is some characteristic length and C_0 some characteristic concentration in the solution. By combining eq 1 and 6 and introducing the new variables from (7), the following set of dimensionless equations is obtained:

$$i_\pm = \mp\frac{dc_\pm}{dx} - c_\pm\frac{d\psi}{dx} \tag{8}$$

$$i_w = -\gamma_H\frac{dc_H}{dx} + \gamma_{OH}\frac{dc_{OH}}{dx} - (\gamma_H c_H + \gamma_{OH}c_{OH})\frac{d\psi}{dx} \tag{9}$$

and from (3) and (4):

$$c_H c_{OH} = k^2 \tag{10}$$

$$c_+ - c_- + c_H - c_{OH} = \begin{cases} 0 \text{ in the solution} \\ -c_m \text{ in the membrane} \end{cases} \tag{11}$$

Here i_+, i_-, and i_w are all constant with x, as follows from (2), and so are also i_e and i, since

$$i = i_w + i_e = i_w + i_+ + i_- \tag{12}$$

Transforming (8) and (9) with the aid of (10), (11), and (12) finally yields

$$\frac{dc_\pm}{dx} = \mp\left(i_\pm + c_\pm\frac{d\psi}{dx}\right) \tag{13}$$

$$\frac{1}{c_H}\frac{dc_H}{dx} = -\frac{1}{c_{OH}}\frac{dc_{OH}}{dx} = -\left(\frac{i_w}{\gamma_H c_H + \gamma_{OH}c_{OH}} + \frac{d\psi}{dx}\right) \tag{14}$$

$$\frac{d\psi}{dx} = -\frac{1}{(c_+ + c_- + c_H + c_{OH})}\left(i_e + \frac{c_H + c_{OH}}{\gamma_H c_H + \gamma_{OH}c_{OH}}i_w\right) \tag{15}$$

The set of equations (13–15) may be solved for the four ionic concentrations and the potential with the appropriate boundary conditions. The potential difference applied across the membrane is usually specified, which determines the current densities. The dimensionless rate of water dissociation can then be calculated from the following equation, obtained by combining (2) with (1), (14), and (10):

$$r = \frac{2i_w\gamma_H\gamma_{OH}k^2}{(\gamma_H c_H + \gamma_{OH}c_{OH})^2}\left(\frac{1}{c_H}\frac{dc_H}{dx}\right) \tag{16}$$

In the following sections, solutions of the equations are given for some important membrane configurations.

3. Homogeneous Membranes

Two homogeneous ion-exchange membranes consisting of a single layer of ion-exchange material are shown in Figure 2. One (Figure 2a) is an anion-selective membrane with high positive fixed charge concentration C_a and thickness Δ_a, in which the diffusion coefficient of electrolyte ions is D_a. The other membrane is cation selective with high concentration of negative fixed charge C_c, thickness Δ_c, and diffusion coefficient of electrolyte ions D_c. Both membranes are in contact with well-stirred solutions characterized by their electrolyte concentrations and their pH. We thus have in the solution on the left side of each membrane a positive ion concentration $C_+ = C_L$ and a hydrogen ion concentration $C_H = 10^{-pH_L}$, and similarly in the solution on the right $C_+ = C_R$, $C_H = 10^{-pH_R}$. The interfaces between the membranes and the solutions are marked by numerals on both sides, as shown. From the equations of electroneutrality and chemical equilibrium 10 and 11 in the solution, we find for both types of membranes:

$$\begin{aligned} &c_{+1} = c_L \quad c_{H1} = h_L \quad c_{OH1} = k^2/h_L \\ &c_{-1} = c_L + h_L - k^2/h_L \end{aligned} \tag{17a}$$

$$\begin{aligned} &c_{+4} = c_R \quad c_{H4} = h_R \quad c_{OH4} = k^2/h_R \\ &c_{-4} = c_R + h_R - k^2/h_R \end{aligned} \tag{17b}$$

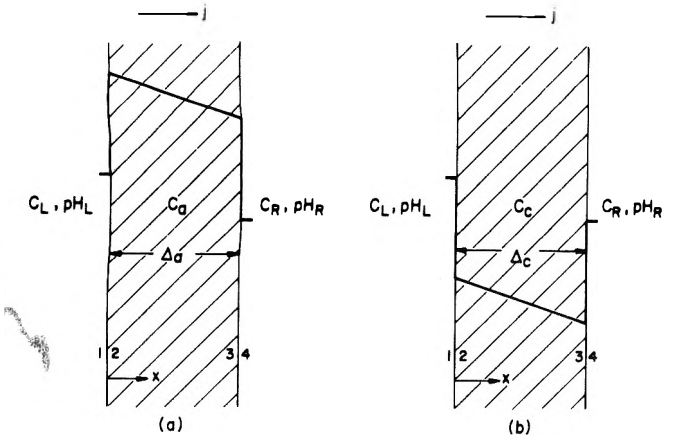

Figure 2. Homogeneous ion-exchange membranes: (a) anion membrane; (b) cation membrane. Heavy line describes typical potential distribution.

where

$$c_L = C_L/C_0 \quad h_L = 10^{-pH_L}/C_0$$
$$c_R = C_R/C_0 \quad h_R = 10^{-pH_R}/C_0 \tag{18}$$

Consider first the anion-exchange membrane. Normalizing its characteristic parameters with respect to those of the solution, we define a dimensionless fixed charge concentration c_a, thickness δ_a, and electrical resistance ρ_a as follows:

$$c_a = C_a/C_0 \quad \delta_a = \Delta_a/d \quad \rho_a = \Delta_a D/dD_a \tag{19}$$

Using the equations developed in the previous section we have here $c_m = c_a$ where c_a is very large compared with the concentrations of the coions c_+ and c_H in the membrane. The equation of electroneutrality (11) reduces to

$$c_- + c_{OH} = c_a \tag{20}$$

applying the Donnan equilibrium condition (5) across the interface 1–2, we find, using (20) and (10):

$$\left.\begin{aligned} c_{+2} &= \frac{c_L}{c_a}(c_L + h_L) \quad c_{H_2} = \frac{h_L}{c_a}(c_L + h_L) \\ c_{OH_2} &= c_a \frac{k^2}{h_L(c_L + h_L)} \\ c_{-2} &= c_a\left[1 - \frac{k^2}{h_L(c_L + h_L)}\right] \end{aligned}\right\} \tag{21a}$$

$$\psi_2 - \psi_1 = \ln\left(\frac{c_a}{c_L + h_L}\right) \tag{22a}$$

and similarly, for the interface 3–4:

$$\left.\begin{aligned} c_{+3} &= \frac{c_R}{c_a}(c_R + h_R) \quad c_{H_3} = \frac{h_R}{c_a}(c_R + h_R) \\ c_{OH_3} &= c_a \frac{k^2}{h_R(c_R + h_R)} \quad c_{-3} = c_a\left[1 - \frac{k^2}{h_R(c_R + h_R)}\right] \end{aligned}\right\} \tag{21b}$$

$$\psi_4 - \psi_3 = \ln\left(\frac{c_R + h_R}{c_a}\right) \tag{22b}$$

In the membrane we obtain, from (15):

$$\frac{d\psi}{dx} = -\frac{1}{c_a}\left(i_e + \frac{c_H + c_{OH}}{\gamma_{OH}c_H + \gamma_{OH}c_{OH}} i_w\right)\frac{\rho_a}{\delta_a} \tag{23}$$

where the term ρ_a/δ_a accounts for the effect on dimensionless current density of the change in electrolyte diffusion coefficient from D in the solution to D_a in the membrane. $d\psi/dx$ from (23) may be substituted in (14) with $c_{OH} = k^2/c_H$ from (10) to give an equation in c_H alone, integrable with respect to x. Once c_H is found, c_{OH} can be determined from (10) and c_- from (20). c_H and c_{OH} are substituted back in (23) which can then be integrated to find ψ. Finally, c_+ is determined from (13) where $d\psi/dx$ is now known. Thus, the potential and concentration distributions of all ions in the membrane are obtained.

The solution following the above procedure may be simplified by making use of the fact that in an anion exchange membrane with high fixed charge concentration $c_H \ll c_{OH}$ except for very low pH of the outside solution, as can also be seen from (21a) and (21b). (23) then reduces to

$$\frac{d\psi}{dx} = -\frac{\rho_a}{c_a\delta_a}\left(i_e + \frac{i_w}{\gamma_{OH}}\right) = -\frac{i_a}{\delta_a} \tag{24}$$

and hence

$$\psi = \psi_2 - \frac{i_a}{\delta_a}x \tag{25}$$

$$c_H = c_{H_2}\frac{e^{(i_a/\delta_a)x}}{1 + \dfrac{\rho_a}{\gamma_{OH}c_{OH_2}}\dfrac{i_w}{i_a}(e^{(i_a/\delta_a)x} - 1)} \tag{26}$$

$$c_+ = c_{+2}e^{(i_a/\delta_a)x} - \rho_a\frac{i_+}{i_a}(e^{(i_a/\delta_a)x} - 1) \tag{27}$$

where $0 < x < \delta_a$, and

$$c_{OH} = k^2/c_H \tag{10a}$$

$$c_- = c_a - c_{OH} \tag{20a}$$

The relation between the water and electrolyte current densities may now be obtained by setting $c_H = c_{H_3}$ and $x = \delta_a$ in (26). With the aid of (24) and (10) we find

$$\frac{i_w}{i_e} = \gamma_{OH}\frac{c_{OH_3}}{c_{-3}}\left(\frac{e^{i_a} - \dfrac{c_{H_3}}{c_{H_2}}}{e^{i_a} - \dfrac{c_{-2}}{c_{-3}}}\right) \tag{28}$$

Of particular interest is the case where the solutions on both sides of the membrane are at the same concentrations and pH. We then have $c_{H_3} = c_{H_2}$ and (28) becomes

$$\frac{i_w}{i_e} = \gamma_{OH}\frac{c_{OH_1}}{c_{-1}} = \gamma_{OH}\frac{c_{OH_4}}{c_{-4}} \tag{28a}$$

The ratio i_w/i_e is, therefore, independent of the applied voltage and directly proportional to the concentration ratio of hydroxide to negative electrolyte ions in the external solutions. Since usually $c_{OH_1} \ll c_{-1}$ and γ_{OH} is of order unity, i_w is usually small compared to i_e.

It can be shown that (28a) is a good approximation of (28) in many cases when the solutions on both sides of the membrane are not at the same concentrations. The exception here is at small values of i, when a difference in pH between the two solutions can cause a current carried by water ions even when there is none due to electrolyte ions. In this case, eq 28 rather than eq 28a should be used.

The part of the current density carried by positive ions i_+ may now be determined from (27) by setting $c_+ = c_{+3}$ and $x = \delta_a$. With the aid of (28) we find

$$\frac{i_+}{i_e} = \frac{c_{+2}}{c_{-3}}\left(\frac{e^{i_a} - \dfrac{c_{+3}}{c_{+2}}}{e^{i_a} - \dfrac{c_{-2}}{c_{-3}}}\right) \tag{29}$$

again, when the solutions on both sides of the membrane are at the same concentrations, and in many other cases (29) may be reduced to

$$i_+/i_e = c_{+2}/c_{-2} \tag{29a}$$

which indicates that the fraction of the current carried by positive electrolyte ions is independent of the applied voltage and is very small, as expected in an anion exchange membrane. The ratio c_{+2}/c_{-2} thus provides a criterion for the membrane's selectivity.

A typical potential distribution as described by (22) and (25) is plotted in Figure 2a. The total potential drop across the membrane is found by adding (22a), (22b), and (25):

$$\Delta\psi = \psi_1 - \psi_4 = \ln\left(\frac{c_L + h_L}{c_R + h_R}\right) + i_a \tag{30}$$

The current–voltage characteristic of the membrane expressed by $i(\Delta\psi)$ would thus be linear for equal concentrations on both sides, and close to linear for many other cases, except at small i, as explained above.

Typical concentration distributions as described by (21), (26), (27), (10a), and (20a) are plotted in Figure 3a.

Consider now the cation exchange membrane. The analysis and the results are in complete analogy with those of the anion-exchange one, with the positive and negative ions interchanging their roles. We define the dimensionless properties of the membrane

$$c_c = \frac{C_c}{C_0} \quad \delta_c = \frac{\Delta_c}{d} \quad \rho_c = \frac{\Delta_c D}{dD_c} \tag{31}$$

where c_c is much larger than c_- and c_{OH} in the membrane and hence from (11):

$$c_+ + c_H = c_c \tag{32}$$

The concentrations and potential at surfaces 2 and 3 are obtained again by applying the Donnan equilibrium conditions across the interfaces 1–2 and 3–4, respectively:

$$\left.\begin{aligned} c_{+2} &= c_c\frac{c_L}{(c_L + h_L)} \quad c_{H_2} = c_c\frac{h_L}{(c_L + h_L)} \\ c_{OH_2} &= \frac{k^2}{c_c}\frac{(c_L + h_L)}{h_L} \quad c_{-2} = \frac{(c_L + h_L)^2}{c_c}\left(1 - \frac{k^2}{(c_L + h_L)h_L}\right) \end{aligned}\right\} \tag{33a}$$

$$\psi_2 - \psi_1 = \ln\left(\frac{c_L + h_L}{c_c}\right) \tag{34a}$$

$$\left.\begin{aligned} c_{+3} &= c_c\frac{c_R}{(c_R + h_R)} \quad c_{H_3} = c_c\frac{h_R}{(c_R + h_R)} \\ c_{OH_3} &= \frac{k^2}{c_c}\frac{(c_R + h_R)}{h_R} \quad c_{-3} = \frac{(c_R + h_R)^2}{c_c}\left(1 - \frac{k^2}{(c_R + h_R)h_R}\right) \end{aligned}\right\} \tag{33b}$$

$$\psi_4 - \psi_3 = \ln\left(\frac{c_c}{c_R + h_R}\right) \tag{34b}$$

The distribution of potential and ionic concentrations in the membrane (except for very high pH in the external solution) are obtained by integrating (15), (14), and (13) assuming $c_H \gg c_{OH}$

$$\psi = \psi_2 - \frac{i_c}{\delta_c}x \tag{35}$$

$$c_{OH} = c_{OH_2}\frac{e^{-(i_c/\delta_c)x}}{1 + \frac{\rho_c}{\gamma_H c_{H_2}}\frac{i_w}{i_c}(e^{-(i_c/\delta_c)x} - 1)} \tag{36}$$

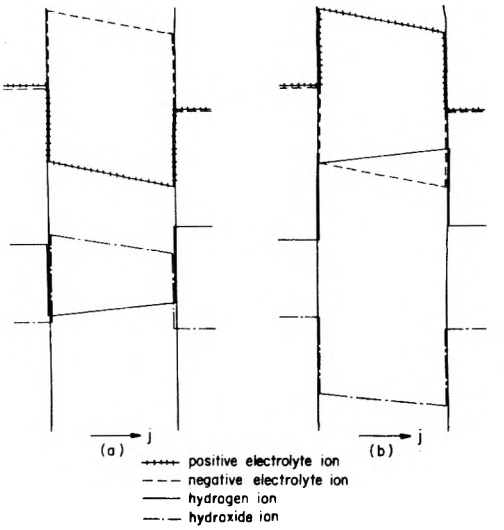

Figure 3. Typical concentration distributions of the four ionic species in homogeneous membranes: (a) anion membrane; (b) cation membrane.

$$c_- = c_{-2}e^{-(i_c/\delta_c)x} - \rho_c\frac{i_-}{i_c}(e^{-(i_c/\delta_c)x} - 1) \tag{37}$$

where

$$i_c = \frac{\rho_c}{c_c}\left(i_e + \frac{i_w}{\gamma_H}\right) \tag{38}$$

and

$$c_H = k^2/c_{OH} \tag{10b}$$

$$c_+ = c_c - c_H \tag{32a}$$

The ratio of water to electrolyte ion current density is found to be

$$\frac{i_w}{i_e} = \gamma_H\frac{c_{H_3}}{c_{+3}}\left(\frac{e^{-i_c} - c_{OH_3}/c_{OH_2}}{e^{-i_c} - c_{+2}/c_{+3}}\right) \tag{39}$$

in particular, when the solutions on both sides of the membrane are at the same concentration and pH

$$\frac{i_w}{i_e} = \gamma_H\frac{c_{H_1}}{c_{+1}} = \gamma_H\frac{c_{H_4}}{c_{+4}} \tag{39a}$$

The part of the current density carried by negative ions i_- is given by

$$\frac{i_-}{i_e} = \frac{c_{-2}}{c_{+3}}\left(\frac{e^{-i_c} - c_{-3}/c_{-2}}{e^{-i_c} - c_{+2}/c_{+3}}\right) \tag{40}$$

and for the same concentrations on both sides of the membrane

$$i_-/i_e = c_{-2}/c_{+2} \tag{40a}$$

Finally, the total potential drop across the membrane is

$$\Delta\psi = \psi_1 - \psi_4 = \ln\left(\frac{c_R + h_R}{c_L + h_L}\right) + i_c \tag{41}$$

Typical potential and concentration distributions in the cation-exchange membrane are plotted in Figure 2b and 3b. The performance of the membrane is similar to that of the anion exchange one with a linear current–voltage characteristic, high selectivity, and ratio of water to electrolyte ion current density independent of the applied voltage.

4. Bipolar Membranes

Bipolar membranes consisting of one cation and one anion exchange layer are the simplest form of composite membranes

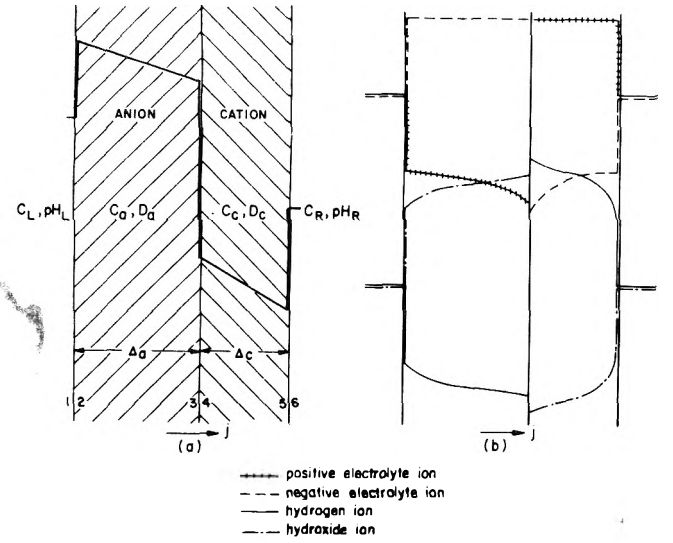

Figure 4. Bipolar membrane: (a) membrane structure and potential distribution; (b) concentration distributions of the four ionic species.

and have been the subject of several studies over the past two decades.[3-9] Figure 4a describes a bipolar membrane with a homogeneous anion exchange layer on the left and a homogeneous cation exchange layer on the right at fixed charge concentrations c_a and c_c and thicknesses Δ_a and Δ_c, respectively. The membrane is in contact on both sides with well-stirred solutions characterized by their electrolyte concentration and their pH, as shown.

Some of the equations developed in the previous section for the homogeneous membranes may be readily applied here. First, the dimensionless properties of the anion and cation exchange layers may be defined by eq 19 and 31, respectively. The ionic concentrations in the external solutions on the left and right of the membrane are given by (17) with the subscript 4 replaced by 6 to match the notation used in Figure 3. For the surfaces 2 and 5 inside the membrane eq 21a and 33b are used, with the subscript 3 replaced by 5 in (33b). Also the potential drops across the interfaces 1–2 and 5–6 are given by (22a) and (34b), with subscripts 3 and 4 replaced by 5 and 6, respectively.

The potential and concentration distributions in the anion exchange layer may be described by eq 25–20a. Here x is measured from the surface 2 to the right, and varies between 0 and δ_a. In particular, at the surface 3

$$c_{+3} = c_{+2}e^{i_a} - \rho_a \frac{i_+}{i_a}(e^{i_a} - 1) \tag{42a}$$

$$c_{H_3} = c_{H_2} \frac{e^{i_a}}{1 + \dfrac{\rho_a}{\gamma_{OH} c_{OH_2}} \dfrac{i_w}{i_a}(e^{i_a} - 1)} \tag{42b}$$

and the total potential drop across the layer is, from (25)

$$\psi_2 - \psi_3 = i_a \tag{43}$$

In the cation exchange layer, eq 35–32a apply with the subscript 2 replaced by 5 and the sign in front of every current density term reversed. x is measured from the surface 5 to the left, and varies between 0 and δ_c. We thus obtain, at the surface 4

$$c_{-4} = c_{-5}e^{i_c} - \rho_c \frac{i_-}{i_c}(e^{i_c} - 1) \tag{44a}$$

$$c_{OH_4} = c_{OH_5} \frac{e^{i_c}}{1 + \dfrac{\rho_c}{\gamma_H c_{H_5}} \dfrac{i_w}{i_c}(e^{i_c} - 1)} \tag{44b}$$

and

$$\psi_4 - \psi_5 = i_c \tag{45}$$

The equations listed above for each of the two layers must now be put together and matched so as to satisfy the condition of Donnan equilibrium across the interface of contact 3–4. This matching condition determines the relations between the current densities carried by the individual ions. We define

$$\Phi = \frac{c_{OH_4} c_{H_3}}{k^2} \tag{46}$$

and hence, from (5)

$$\psi_4 - \psi_3 = \ln \Phi \tag{47}$$

Also, from (5), with the aid of (20) and (32)

$$c_{+3} = c_c\Phi - c_{H_3} \tag{48a}$$

$$c_{-4} = c_a\Phi - c_{OH_4} \tag{48b}$$

Substituting these values of c_{+3} and c_{-4} in (42a) and (44a) we find

$$i_+ = \frac{i_a}{\rho_a(1 - e^{-i_a})}[c_{+2} - (c_c\Phi - c_{H_3})e^{-i_a}] \tag{49a}$$

$$i_- = \frac{i_c}{\rho_c(1 - e^{-i_c})}[c_{-5} - (c_a\Phi - c_{OH_4})e^{-i_c}] \tag{49b}$$

Since $i_+ + i_- = i_e$, (49a) and (49b) may be added to give a relation between i_w and i_e. Note that all the terms in (49) can be expressed in terms of i_a, i_c, and the various ionic concentrations at surfaces 2 and 5 which are independent of current. i_a and i_c themselves are defined in terms of i_e and i_w by (24) and (38). Now, since $i = i_e + i_w$ we can use (49) to express both i_w and i_e in terms of i for given properties of the membrane and the external solutions. Then, i_+ and i_- may be determined from (49a) and (49b). The total potential drop across the membrane is obtained by adding (22a), (34b), (43), (45), and (47):

$$\Delta\psi = \psi_1 - \psi_6 = \ln\left[\frac{(c_L + h_L)(c_R + h_R)}{c_a c_c \Phi}\right] + (i_a + i_c) \tag{50}$$

The above procedure has been implemented into a computer program which calculates i_e, i_w, i_+, i_-, and $\Delta\psi$ as functions of i for given membrane and solution properties and enables us to determine potential and concentration distributions in the membrane as well as its current–voltage characteristic. A typical potential distribution is plotted in Figure 4a showing resistive potential drops i_a and i_c across the anion and cation exchange layers, respectively, and Donnan potential differences as expressed by the first term in (50). Figure 4b shows typical concentration distributions of the four ionic species. It is important to note that for current in the positive direction as shown, the concentrations of the coions (positive ions in the anion exchange layer; negative ions in the cation exchange layer) at the interface of contact between the two layers 3–4 decrease relative to their values at the surfaces 2 and 5, which are unaffected by current. This trend reverses itself when the current direction is changed.

Figure 5 shows a typical current–voltage characteristic plotted for equal concentrations and pH of the external solutions on both sides of the membrane. The curve has been divided into two parts showing negative and low positive

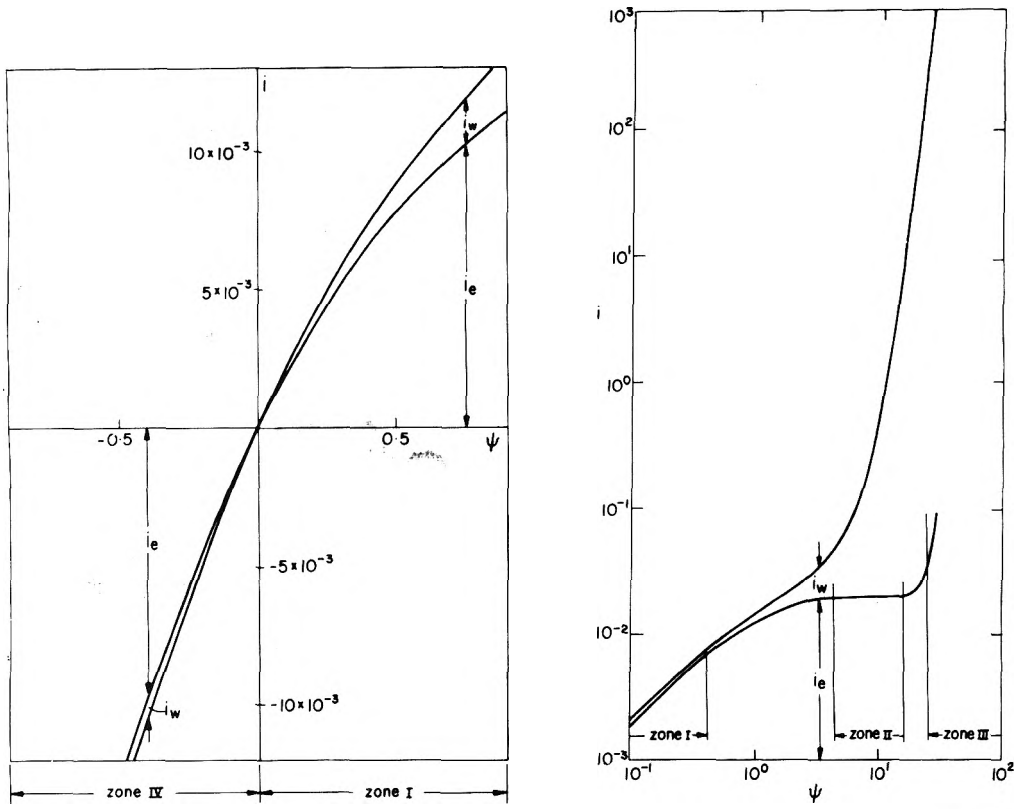

Figure 5. Current–voltage characteristic of a bipolar membrane in an aqueous solution of KCl, plotted for $c_R = c_L = 1$, $h_R = h_L = 10^{-5}$, $c_a = c_c = 10^2$, $\rho_a = \rho_c = 1$.

current densities on a linear scale, and medium to very large positive current densities on a logarithmic scale. We notice four different zones of interest in the curve, marked I to IV.

Zone I. Here the current density is very low, causing only small, practically linear variations in the concentrations within the membrane. The terms i_a, i_c, $\rho_a i_w/c_{OH_2}$, and $\rho_c i_w/c_{H_5}$ are all much smaller than unity. Equations 42, 44, and 49 may therefore be linearized by expanding the exponentials into power series where high order terms are negligible. A linear relation is obtained between i_w and i_e

$$i_e - \left[\frac{c_{H_2}}{c_{H_5}}\left(\frac{\rho_c}{\gamma_H c_{H_5}} + \frac{\rho_a}{\gamma_{OH} c_{OH_2}}\right)\left(\frac{c_{+5}}{\rho_a} + \frac{c_{-2}}{\rho_c}\right)\right] i_w = \left[\frac{1}{\rho_a}\left(c_{+2} - \frac{c_{H_2}}{c_{H_5}} c_{+5}\right) + \frac{1}{\rho_c}\left(c_{-5} - \frac{c_{H_2}}{c_{H_5}} c_{-2}\right)\right] \quad (51)$$

and the potential drop across the membrane becomes

$$\Delta\psi = \psi_1 - \psi_6 = \ln\left(\frac{h_R}{h_L}\right) + \left(\frac{\rho_a}{\gamma_{OH} c_{OH_2}} + \frac{\rho_c}{\gamma_H c_{H_5}}\right) i_w \quad (52)$$

which indicates a linear behavior of the current–voltage characteristic. Also here in zone I $i_w \ll i$.

Zone II. Here we notice saturation in the electrolyte current density i_e as the electrolyte coion concentration at the interface 3–4 has decreased to a very small value, due to increase in current in the positive direction. At the same time, however, i_w keeps rising with voltage even though the concentration of the water coion has decreased as well. This is accounted for by the fact that a decrease in water coion is accompanied by an increase in its counterion to maintain chemical equilibrium according to (10), whereas there is no similar mechanism for the electrolyte. Setting $c_{+3} \ll c_{+2}$ and $c_{-4} \ll c_{-5}$ in (42a) and (44a), (with i_a and i_c still small compared with unity) we find the saturation value of i_e:

$$i_+ = \frac{c_{+2}}{\rho_a} \quad i_- = \frac{c_{-5}}{\rho_c} \quad i_e = i_+ + i_- = \text{constant} \quad (53)$$

Zone III. When the current is very large in the positive direction, the concentrations of water coions at the interface 3–4 decrease to a limiting, very small value. Setting $i_a \gg 1$ and $i_c \gg 1$ in (42b) and (44b) we obtain

$$c_{H_3} = k^2/c_a \quad c_{OH_4} = k^2/c_c \quad (54)$$

From (10) we can then see that $c_{OH_3} = c_a$, $c_{H_4} = c_c$, and it becomes clear that practically all the current is now carried by water counterions, which have reached a concentration equal to that of the fixed charge and much larger than all other ions. From (49) with the aid of (24) and (38) we find

$$i_+ = \frac{c_{+2}}{c_a}\frac{i}{\gamma_{OH}} \quad i_- = \frac{c_{-5}}{c_c}\frac{i}{\gamma_H} \quad i_e = i_+ + i_i \ll i_w \quad (55)$$

The concentrations of the electrolyte coions may be determined by calculating the limit of (48) when $i_a \gg 1$, $i_c \gg 1$:

$$c_{+3} = \gamma_H \frac{k^2}{c_a}\frac{i_e}{i} \ll c_{H_3} \quad c_{-4} = \gamma_{OH}\frac{k^2}{c_c}\frac{i_e}{i} \ll c_{OH_4} \quad (56)$$

and finally, the current–voltage characteristic is described again by a linear relation

$$\Delta\psi = \ln\left[\frac{(c_L + h_L)(c_R + h_R)}{k^2}\right] + \left(\frac{\rho_a}{\gamma_{OH} c_a} + \frac{\rho_c}{\gamma_H c_c}\right) i \quad (57)$$

Zone IV. Here the current direction is negative and it can be shown that the water current density is usually small compared to the one carried by the electrolyte. Since $c_{H_3} > 0$ and $c_{OH_4} > 0$, the denominators in (42b) and (44b) must always remain positive, and hence

$$\frac{i_w}{i} < \frac{c_{OH_2}}{c_a}\frac{\gamma_{OH}}{(1-e^{i_a})}$$
$$\frac{i_w}{i} < \frac{c_{H_5}}{c_c}\frac{\gamma_H}{(1-e^{i_c})} \qquad (58)$$

where i_a and i_c are negative.

The anisotropic behavior with respect to current direction exhibited by the bipolar membrane and the pH effects associated with it were noticed and reported in a number of experimental studies.[3-9] Current–voltage characteristics of similar shape to Figure 5 were obtained experimentally by Ishibashi and Hirano[7] (their Figure 5). Unfortunately, a detailed comparison between the present theory and their experimental data is not possible since their membranes were heterogeneous with no distinct cation and anion exchange layers and the experiments were not run under steady-state conditions. Qualitatively the experimental curve shows very clearly the increase of current with voltage of zone I, the tendency of leveling off due to current saturation in zone II, and the linear rise of current with voltage in zone III.

5. Membranes with Thin Surface Films

It has already been mentioned that homogeneous ion-exchange membranes operating in industrial systems such as electrodialysis are often fouled with thin surface films with ion-exchange properties which cause severe deterioration in the performance of the membranes. Surface fouling has been studied experimentally by a number of investigators,[10-12,15] and a theoretical model was developed to explain its mechanism and effects.[13] It was observed, for example, that anion exchange membranes are highly susceptible to fouling by organic matter present in the water which forms a film with negative fixed charge on them.[10,11] Cation exchange membranes may be badly fouled by iron compounds.[12] Fouling is invariably manifested by changes in the pH of the electrolyte solutions in contact with the membranes, which has in fact served as an indicator for the degree of fouling in several of the above studies. In the present section we will study the effect of surface fouling in water dissociation and transport through the membranes.

Figure 6a shows an anion exchange membrane of dimensionless thickness δ_a and fixed charge concentration c_a which has acquired thin surface films with cation-exchange properties having dimensionless resistance ρ_{cf}, thickness δ_{cf}, and fixed charge concentration c_{cf}. (The dimensionless properties of the films are defined by the same equations as those of the homogeneous cation exchange membrane (31) with the subscript c replaced by cf.) For simplicity and symmetry it is assumed here that the films on both sides of the membrane are identical, although this is not necessarily always the case. Current of density j is passed through the membrane.

Again, we can use some of the equations developed before to describe the behavior of the present membrane. Equations 17 describes the concentrations in the external solutions, with subscript 4 replaced by 8 to match the notation of Figure 6. Equations 33 and 34 give the concentrations at surfaces 2 and 7, and the potential drops across the membrane–solution interfaces, with subscripts 3, 4, and c change into 7, 8, and cf, respectively. Since the films are very thin, we can assume linear variations of concentrations and potential in them. We then have, from (15) with $c_{OH} \ll c_H$:

$$\psi_3 - \psi_2 = \psi_7 - \psi_6 = -\frac{\rho_{cf}}{\delta_{cf} c_{cf}}\left(i_e + \frac{i_w}{\gamma_H}\right) \qquad (59)$$

at the surface 3 we find, using (13) and (14):

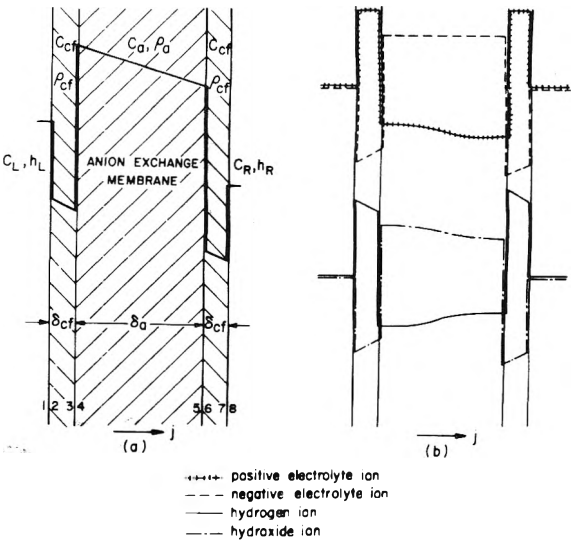

Figure 6. Anion-exchange membrane with thin cation-exchange films: (a) membrane structure and typical potential distribution; (b) concentration distributions of the four ionic species.

$$\left(\frac{c_{OH_3} - c_{OH_2}}{c_{OH_2}}\right) = -\left(\frac{c_{H_3} - c_{H_2}}{c_{H_2}}\right) = \frac{\rho_{cf}}{c_{cf}}\left(\frac{i_w}{\gamma_H}\frac{c_L}{h_L} - i_e\right) \qquad (60a)$$

$$c_{\pm 3} = c_{\pm 2} \mp \rho_{cf}\left[i_\pm - \frac{c_{\pm 2}}{c_{cf}}\left(i_e + \frac{i_w}{\gamma_H}\right)\right] \qquad (60b)$$

and similarly, at surface 6:

$$\left(\frac{c_{OH_6} - c_{OH_7}}{c_{OH_7}}\right) = -\left(\frac{c_{H_6} - c_{H_7}}{c_{H_7}}\right) = -\frac{\rho_{cf}}{c_{cf}}\left(\frac{i_w}{\gamma_H}\frac{c_R}{h_R} - i_e\right) \qquad (61a)$$

$$c_{\pm 6} = c_{\pm 7} \pm \rho_{cf}\left[i_\pm - \frac{c_{\mp 7}}{c_{cf}}\left(i_e + \frac{i_w}{\gamma_H}\right)\right] \qquad (61b)$$

Next, all concentrations and potential at surfaces 4 and 5 are determined by applying the Donnan equilibrium condition (5) across the interfaces 3–4 and 5–6. Finally, we use (26) and (27) to link the above equations from both sides of the anion exchange membrane. We may write

$$\frac{c_{H_5}}{c_{H_4}}\frac{\left(1 - \frac{\rho_a}{\gamma_{OH}}\frac{i_w}{i_a}\frac{1}{c_{OH_4}}\right)}{\left(1 - \frac{\rho_a}{\gamma_{OH}}\frac{i_w}{i_a}\frac{1}{c_{OH_5}}\right)} = e^{i_a} \qquad (62)$$

and

$$c_{+4}e^{i_a/2} - c_{+5}e^{-i_a/2} = 2\rho_a\frac{i_+}{i_a}\sinh\left(\frac{i_a}{2}\right) \qquad (63)$$

Equations 62 and 63 with the values of the concentrations substituted from where they have been calculated before, along with (12), enable us to determine the current densities carried by the individual ions in terms of i, the membrane and solution parameters. $\Delta\psi$ can then be calculated by adding the potential drops across the various layers and interfaces of the membrane, as before.

A computer program has been written to perform the steps outlined in the above procedure. Figure 6a shows a typical potential distribution in the membrane while Figure 6b shows concentrations. A current–voltage characteristic is shown in Figure 7. It is similar in properties to that of the bipolar membrane, except that it is symmetrical with respect to current, the membrane itself being symmetrical in structure. Polarization occurs at the interface 5–6 for positive current,

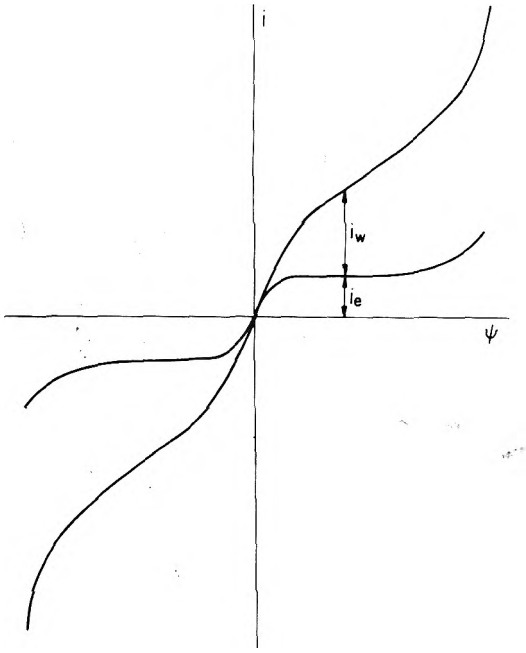

Figure 7. Typical current–voltage characteristic of membrane with thin surface films.

and at 3–4 for negative current. Zones I, II, and III of the bipolar characteristic are all present here.

The above analysis may be repeated for a cation exchange membrane with surface films of anion exchange properties. The results are in complete analogy with the ones obtained for the anion exchange membrane with cation exchange films.

6. Conclusions

A model has been developed to describe the steady-state transport of electolyte ions through composite ion-exchange membranes taking into consideration the effects of water dissociation and water ion transport. Homogeneous membranes, consisting of a single layer of ion-exchange material, were considered first. When in contact with electrolyte solutions of equal concentrations and pH on both sides, they exhibit a linear current voltage characteristic (eq 30) and the relative portions of current carried by electrolyte and water ions are independent of the applied voltage and depend only on the concentrations of those ions in the external solutions (eq 28a and 39a). The selectivity of the membrane, expressed by the fraction of current carried by the electrolyte counterion, is determined by the properties of the membrane and the solution and is also independent of the applied voltage (eq 29a and 40a). This behavior is typical also when the solutions on both sides of the membrane differ somewhat in concentration, except for very small current.

The bipolar membrane, consisting of one anion and one cation exchange layer exhibits an anisotropic behavior with respect to current direction, as shown by its current–voltage characteristic (Figure 5). The characteristic is practically linear when the current enters the membrane through the cation exchange layer, with a relatively small and constant portion of it carried by water ions. When the current is reversed, polarization occurs inside the membrane as the counterions reach very low concentrations at the interface of contact between the two layers (Figure 4). Three distinct zones are observed in the current–voltage characteristic, with increasing portions of the current carried by water ions as the applied voltage is increased.

Homogeneous membranes with thin films of opposite ion-exchange properties were also considered. With identical films on both sides, the membranes have a symmetrical current–voltage characteristic similar to that of the bipolar membrane with current in the polarizing direction.

The solutions obtained for the various membrane configurations have all been based on the aforementioned assumption of quasiequilibrium. It should be noted that when water dissociation takes place, certain nonequilibrium phenomena are present in the membrane. These include particularly the deviation from chemical equilibrium of water ions in the nonequilibrium zones near surfaces of discontinuity and the change in the equilibrium dissociation constant under increased electric fields. Both these phenomena prove to be small relative to the quasiequilibrium transport of ions which has been treated here. The first is confined to a thin layer which takes a small portion of the domain into consideration.[18] The second amounts to a change of only several percents in k^2.[19] It is only at relatively high current densities that nonequilibrium effects begin to play a significant role.

Nomenclature

C_a, C_c	fixed charge concentration in anion and cation exchange membranes, respectively
C_i	concentration of species i
C_L, C_R	concentration of positive electrolyte ion in the solution on the left and right side of the membrane, respectively
C_m	fixed charge concentration of some layer in the membrane
C_0	some characteristic concentration in the solution
c_a, c_c	dimensionless fixed charge concentration and cation exchange membranes, eq 19 and 31, respectively
c_i	dimensionless concentration of species i, eq 7
c_L, c_R	dimensionless concentrations of positive electrolyte ion in the solution on the left and right of the membrane, respectively, eq 18
c_m	dimensionless fixed charge concentration of some layer in the membrane, eq 17
D	diffusion coefficient of electrolyte ions in the solution
D_a, D_c	diffusion coefficient of electrolyte ions in anion and cation exchange membrane, respectively
D_i	diffusion coefficient of species i
d	characteristic dimension
F	Faraday's constant
h_L, h_R	dimensionless concentrations of hydrogen ion in the solution on the left and right of the membrane, respectively, eq 18
i	dimensionless current density, eq 7
$i_\pm$	dimensionless current density carried by positive or negative electrolyte ion, eq 7
i_a	combination of current densities defined by (24)
i_c	combination of current densities defined by (35)
i_e	dimensionless current density carried by both electrolyte ions, eq 7
i_w	dimensionless current density carried by water ions, eq 7

j current density
$j_{\pm}$ current density carried by positive or negative electrolyte ion
j_e current density carried by both electrolyte ions
j_w current density carried by water ions
K^2 equilibrium dissociation constant of water
k^2 dimensionless dissociation constant of water, eq 7
k_d constant of dissociation of water ions
k_r constant of recombination of water ions
N_i flux density of species i
pH_L, pH_R pH of the solution on the left and right of the membrane, respectively
$\mathcal{R}$ universal gas constant
R rate of water dissociation
R_i rate of formation of species i by chemical reaction
r dimensionless rate of water dissociation, eq 7
T absolute temperature
X coordinate transverse to the membrane
x dimensionless coordinate transverse to the membrane
z_i valency of species i
z_m valency of fixed charge in some layer of the membrane

Greek Symbols

γ_i dimensionless diffusion coefficient of species i, eq 7
Δ_a, Δ_c thickness of anion and cation exchange membrane, respectively
Δ_m thickness of some layer of the membrane
δ_a, δ_c dimensionless thickness of anion and cation exchange membranes, eq 19 and 31, respectively
ρ_a, ρ_c dimensionless resistance of anion and cation exchange membranes, eq 19 and 31, respectively
ϕ electrical potential
$\Delta\phi$ potential difference applied between the ends of the membrane
Φ parameter, defined by eq 46
ψ dimensionless potential, eq 7
$\Delta\psi$ dimensionless potential difference applied to the membrane

Subscripts

a refers to anion exchange layer
c refers to cation exchange layer
i designates any of the four ionic species. i may take on the value +, −, H, or OH: +, positive electrolyte ion; −, negative electrolyte ion; H, hydrogen ion; OH, hydroxide ion
L refers to solution on the left side of membrane
R refers to solution on the right side of membrane

References and Notes

(1) T. Teorell, *Prog. Biophys. Biophys. Chem.*, 305–369 (1953).
(2) G. Eisenman and F. Contl, *J. Gen. Physiol.*, **48**, 65 (1965).
(3) A. Mauro, *Biophys. J.*, **2**, 179 (1962).
(4) H. G. L. Coster, *Biophys. J.*, **5**, 669 (1965).
(5) H. G. L. Coster, *Aust. J. Biol. Sci.*, **22**, 365 (1969).
(6) V. Frilette, *J. Phys. Chem.*, **60**, 435 (1956).
(7) N. Ishibashi and K. Hirano, *J. Electrochem. Soc. Jpn.*, **26**, E8 (1958).
(8) N. Ishibashi, *J. Electrochem. Soc. Jpn.*, **26**, E58 (1958).
(9) N. Ishibashi and K. Hirano, *J. Electrochem. Soc. Jpn.*, **27**, E193 (1959).
(10) T. R. E. Kressman and F. L. Tye, *J. Electrochem. Soc., Electrochem. Sci.*, **116**, 25 (1969).
(11) E. Korngold, F. deKorosy, R. Rahav, and M. F. Taboch, *Desalination*, **8**, 195 (1970).
(12) G. Grossman and A. A. Sonin, *Desalination*, **10**, 157 (1972).
(13) G. Grossman and A. A. Sonin, *Desalination*, **12**, 107 (1973).
(14) A. A. Sonin and G. Grossman, *J. Phys. Chem.*, **76**, 3996 (1972).
(15) C. Forgacs, N. Ishibashi, J. Leibowitz, J. Sinkovic, and K. S. Spiegler, *Desalination*, **10**, 181 (1972).
(16) P. Delahay, "Double Layer and Electrode Kinetics", Interscience, New York, N.Y., 1966.
(17) K. J. Vetter, "Electrochemical Kinetics", Academic Press, New York, N.Y., 1967.
(18) M. S. Isaacson, M.Sc. Thesis, Massachusetts Institute of Technology, Department of Mechanical Engineering, 1970.
(19) L. Onsager, *J. Chem. Phys.*, **2**, 599 (1934).

Electrical Conductivity of Aqueous Solutions of Polystyrenesulfonate Salts Containing Simple Salts

Peter R. Holyk, Janet Szymczak, and Paul Ander*

Department of Chemistry, Seton Hall University, South Orange, New Jersey 07079 *(Received January 16, 1976)*

Publication costs assisted by Seton Hall University

Conductance measurements at 25 °C have been performed on aqueous solutions of the alkali metal salts and the ammonium salt of polystyrenesulfonate containing their respective chlorides. Specific conductances plots of these solutions are linear for the whole polyelectrolyte concentration range and are in the order LiCl < NaCl < KCl ≃ NH_4Cl < RbCl ≃ CsCl. The results are discussed in terms of the rodlike model of Manning.

Using a rodlike model for the polyion which has counterions condensed onto it above a critical charge density and uncondensed counterions and coions interacting with the polyion by Debye–Hückel interactions, Manning obtained expressions for electric conductance for the ionic species in salt-free and salt-containing solutions.[1-5] Promising accord between the theoretical predictions for electric transport properties obtained from this model and the experimental results was obtained for salts of DNA,[5] sodium carboxymethylcellulose,[6] sodium alginate,[7] sodium polygalacturonate,[7] sodium polyacrylate,[3] and salts of polystyrenesulfonate.[8,9] For salt-free solutions of monovalent salts of polystyrenesulfonate (PSS), Kwak and Hayes[8] and Szymczak, Holyk, and Ander[9] found that Manning's conductance equation correctly predicted the dependence on the nature of the counterion, but overestimated the decrease in the conductance with increasing concentration. Kwak and Johnson[6] reported excellent agreement between theory and experiment for the conductance of salt-free alkali metal ion salts of carboxymethylcellulose, a more rodlike polyelectrolyte than salts of polystyrenesulfonate. Here, we report the results of conductance measurements obtained at 25 °C for aqueous solutions of alkali metal ion salts and the ammonium salt of polystyrenesulfonate containing the respective chlorides. These results will be compared with those predicted from Manning's theory.

Experimental Section

The same LiPSS, NaPSS, KPSS, RbPSS, CsPSS, and NH_4PSS samples used in a previous study[9] were employed here. The acid form of the polystyrenesulfonate has a molecular weight of 70 000 and contains one sulfonate group per monomer unit. All solutions were prepared by weighing the dried polystyrenesulfonate salt in 50-ml class A type volumetric flasks and adding some aqueous salt solution to dissolve the polymer, followed by diluting to the mark with the salt solution. The determination of the specific conductances of these solutions were described earlier.[9]

Results and Discussion

The specific conductances κ of solutions of LiPSS, NaPSS, KPSS, RbPSS, CsPSS, and NH_4PSS were determined at 25 °C over a tenfold polymer concentration range from 0.0010 to 0.010 N in aqueous solutions of their respective simple salt chlorides of concentration 0.0010, 0.0010, and 0.010 N. Table I contains these results.[10] For each counterion studied, at a definite polymer concentration higher specific conductances were obtained for higher simple salt concentrations, as would be expected. Plots of the specific conductances of the solutions against the normality of the polyelectrolyte for the data in Table I were linear over the whole concentration range studied. Figure 1 shows the plot for 0.010 N simple salt; curves for 0.0010 and 0.000 10 N simple salt are similar except that the lines are closer together for these salt solutions. For each simple salt concentration, the trend observed for the specific conductances over the whole polyelectrolyte concentration range is LiCl < NaCl < KCl ≃ NH_4Cl < RbCl ≃ CsCl. This is the same order found for the conductances of aqueous solutions of salt-free polystyrenesulfonate solutions.[9] Also, this is the order for the specific conductances of polyelectrolyte-free simple salt solutions, indicating the importance of the nature of the counterion on the conductance of polyelectrolyte solutions. A similar order has been reported for DNA in aqueous solutions of LiCl, NaCl, and KCl at 5 °C.[5]

For each simple salt concentration the experimental results in Table I are well represented by

$$\kappa - \kappa_s = 10^{-3} A_p N_p \qquad (1)$$

where κ and κ_s are the specific conductances of the polyelectrolyte–simple salt solution and of simple salt solution in the absence of polyelectrolyte, respectively, N_p is the normality of the polyelectrolyte and A_p is an empirical coefficient obtained from the slopes of plots of κ vs. N_p. Values of A_p evaluated from linear regression plots of κ vs. N_p for the data given in Table I and their standard error are given in Table II. Correlation coefficients of better than 0.996 were obtained for all linear regression plots except for 0.010 N CsCl where the correlation coefficient was 0.990. It is noted from Table II that for a given simple salt concentration the experimental values of A_p are in the general order LiCl < NaCl < KCl ≃ NH_4Cl < RbCl ≃ CsCl, the series found for their specific conductances for one salt concentration. Also, for a definite simple salt the experimental values of A_p are approximately the same for the two lowest simple salt concentrations and slightly lower for the highest concentration. Most important is the additivity of the specific conductances of simple salt solutions and salt-free polyelectrolytes solutions suggested by the linearity obtained for all κ vs. N_p plots. To compare the values of A_p^{expt} with the values A_p^{add} obtained from additivity, the least-square slopes of the lines constructed from the sum of the specific conductances of the salt-free polyelectrolyte solutions[9] and the polyelectrolyte–free simple salt solutions[11] were de-

TABLE II: Experimental and Theoretical Values of A_p for Several Simple Salt Solutions of Polystyrenesulfonate Salts at 25 °C[a]

Salt	0.000 10 N			0.0010 N			0.010 N		
	A_p^{expt}	A_p^{add}	A_p^{theo}	A_p^{expt}	A_p^{add}	A_p^{theo}	A_p^{expt}	A_p^{add}	A_p^{theo}
LiCl	32.6 ± 0.9	32.8 ± 0.1	39.6	32.9 ± 0.3	32.8 ± 0.1	29.0	29.0 ± 0.8	32.8 ± 0.1	18.2
NaCl	38.4 ± 0.4	38.7 ± 0.0	43.0	38.2 ± 0.5	38.7 ± 0.0	32.4	33.5 ± 0.5	38.7 ± 0.0	21.4
KCl	45.6 ± 0.0	46.6 ± 0.1	49.8	45.9 ± 0.6	46.6 ± 39.2	39.2	40.3 ± 0.4	46.6 ± 0.1	28.1
RbCl	46.0 ± 1.6	48.6 ± 0.6	51.0	48.6 ± 0.4	48.6 ± 0.6	40.2	40.6 ± 2.0	48.6 ± 0.6	28.9
CsCl	47.4 ± 0.2	49.6 ± 0.2	51.0	49.6 ± 1.3	49.6 ± 0.2	40.3	43.9 ± 2.6	49.6 ± 0.2	29.0
NH_4Cl	46.0 ± 0.1	47.2 ± 0.2	49.8	45.8 ± 0.1	47.2 ± 0.2	39.2	42.1 ± 0.4	47.2 ± 0.2	28.1

[a] A_p has units of ohm^{-1} cm^2 equiv^{-1}.

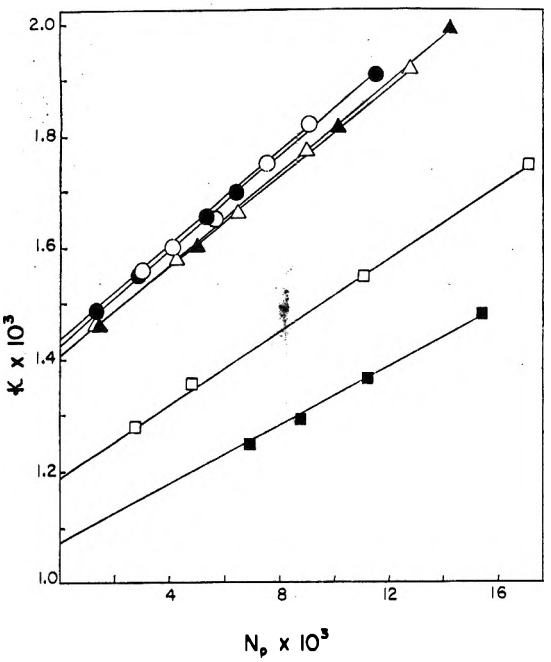

Figure 1. The specific conductivity of polystyrenesulfonate solutions as a function of polyelectrolyte normality in 0.010 N simple salt solutions of (■) LiCl, (□) NaCl, (△) KCl, (▲) NH_4Cl, (○) RbCl, (●) CsCl.

termined. These are listed in Table II, where it is noted that the values of A_p^{add} and A_p^{expt} are in very good agreement for the 0.000 10 and 0.0010 N simple salt solutions and in fair agreement for the 0.010 N solutions.

To evaluate A_p from his cylindrical model of a polyelectrolyte, Manning determined the contributions of the specific conductances of the cation, anion, and polyion to the specific conductance giving

$$A_p = \xi^{-1}\left[\left(t_{A^+}^{(s)} - \frac{1}{6}\right)\lambda_s + \lambda_p\right] \qquad (2)$$

where λ_s is the equivalent conductance of the simple salt in the absence of polyelectrolyte, $t_{A^+}^{(s)}$ is the transference number of the cation in the absence of polyelectrolyte, $\xi = e^2/\epsilon kTb$, a dimensionless polyelectrolyte charge density parameter which depends on the distance b between charges on the polyelectrolyte chain, where ϵ is the dielectric constant of bulk solvent, e is the protonic charge, T is the absolute temperature, and λ_p is the equivalent conductance of the polyion given by

$$\lambda_p = (F/300)(\epsilon kT/3\pi\eta e)|\ln Ka| \qquad (3)$$

where F is the Faraday, η is the viscosity of bulk solvent, K is the Debye screening parameter for the simple salt solution in the absence of polyelectrolyte, and a is the radius of the polyion. It was shown that the relaxation effect is not important inasmuch as it only adds a second-order term in N_p to the specific conductance and that A_p is interpreted as a measure of the interaction between the simple salt and the polyelectrolyte.

Using literature values or values obtained from Onsager's equations for λ_s and $t_{A^+}^{(s)}$,[11] $\xi = 2.85$, and $a = 8.0 \times 10^{-8}$ cm,[12] values of λ_p and A_p were calculated from eq 3 and 2, respectively. For 0.000 10, 0.0010, and 0.010 N simple salt solutions, the respective λ_p values are 93.6, 64.0, and 34.4 ohm^{-1} cm^2 equiv^{-1}. The calculated and experimental values for A_p are listed in Table II, where it is noted that, in general, good agreement is evident between the theoretical and experimental values for each simple salt for the two lowest concentrations of simple salt. At the highest simple salt concentration where coiling of the polyelectrolyte is most pronounced, the theory would be expected to be less applicable. The theory correctly predicts the order of the A_p values with respect to the nature of the counterion. Since in eq 2, λ_p and ξ do not depend on the nature of the monovalent counterion, the order of the interaction parameter A_p with respect to the nature of the counterion was found to depend on both the order of the counterions with respect to their $t_{A^+}^{(s)}$ values and the order of conductances of the simple salt without polyelectrolyte present. The fairly good agreement between theory and experiment for the most dilute simple salt solutions suggests that the omission of the relaxation effect in calculating λ_p might be justified. However, it is felt by the authors that the concentration dependence of the *equivalent* conductance of polyelectrolyte solutions containing simple salt could be experimentally represented in a manner similar to that of simple electrolytes if the salt–polyelectrolyte interactions is taken into account appropriately. Also, it is felt that the value of A_p is not merely an interaction term, but is composed of the equivalent conductance of the polyelectrolyte with a small interaction term in it.

Acknowledgment. The authors acknowledge the discussions with Dr. Marie Kowblansky.

Supplementary Material Available: A listing of specific conductances of polystyrenesulfonate salts containing simple salts where the polyanion and the simple salt contain the same cation (Table I) (1 page). Ordering information is available on any current masthead page.

References and Notes

(1) G. S. Manning, *J. Chem. Phys.*, **51**, 934 (1969).
(2) G. S. Manning, *Biopolymers*, **9**, 1543 (1970).
(3) D. I. Devore and G. S. Manning, *J. Phys. Chem.*, **78**, 1242 (1974).

(4) G. S. Manning, *J. Phys. Chem.*, **79**, 262 (1975).
(5) P. D. Ross, R. L. Scruggs, and G. S. Manning, *Biopolymers*, **14**, 1991 (1975).
(6) J. C. T. Kwak and A. J. Johnson, *Can. J. Chem.*, **53**, 792 (1975).
(7) F. M. Tuffile and P. Ander, *Macromolecules*, **8**, 789 (1975).
(8) J. C. T. Kwak and R. C. Hayes, *J. Phys. Chem.*, **79**, 265 (1975).
(9) J. Szymczak, P. Holyk, and P. Ander, *J. Phys. Chem.*, **79**, 269 (1975).
(10) See paragraph at end of text regarding supplementary material.
(11) R. A. Robinson and R. H. Stokes, "Electrolyte Solutions", 2d ed, Butterworths, England, 1970.
(12) S. Oman and D. Dolar, *Z. Phys. Chem. (Frankfort am Main)*, **56**, 1 (1967).

Self-Diffusion of Fluorine in Molten Dilithium Tetrafluoroberyllate

Toshihiko Ohmichi, Hideo Ohno,* and Kazuo Furukawa

Molten Materials Laboratory, Japan Atomic Energy Research Institute, Tokai, Ibaraki, Japan *(Received April 26, 1976)*

Publication costs assisted by the Japan Atomic Energy Research Institute

The self-diffusion coefficients of fluorine in molten Li_2BeF_4 have been measured with the capillary reservoir technique, using ^{18}F as a tracer. ^{18}F was prepared in our laboratory. The results can be described with the Arrhenius equation $D = 6.53 \times 10^3 \exp[-(30.6 \pm 3.4) \times 10^3/RT]$, where D is expressed in $cm^2\ s^{-1}$, R in cal $mol^{-1}\ deg^{-1}$, and T in K. An attempt was made to qualitatively explain the high activation energy of fluorine self-diffusion. Possible mechanisms involve the transport of fluorine resulting from the movement of fluoroberyllate anions, the exchange of fluorine between neighboring anions, and ion-pair diffusion.

Introduction

A crystalline solid BeF_2 has a three-dimensional network structure made up of BeF_4^{2-} tetrahedra which shares corners, as in crystalline SiO_2. The anions F^- are all bridged between two of the tetrahedrally coordinated central cations Be^{2+}. Its compounds readily form glass, and are highly viscous above the melting point, suggesting that it still has a network structure.

The binary molten mixture between BeF_2 and alkali metal fluoride melts shows a rapidly falling viscosity as the amount of alkali metal fluoride components is increased.[1] This indicates the breakdown of the network-type structure of BeF_2 melt with addition of alkali fluorides.

Our interest centers on how the diffusion behavior of constituent ions, in particular the fluoride ion, in the molten LiF–BeF_2 system changes with composition of melts. In general, the study of the self-diffusion of fluorine in molten fluorides still remains an unexplored field. This is because, in addition to the difficulty due to corrosion of glass or ceramic vessels in handling fluoride melts, the only applicable isotope of fluorine is limited to ^{18}F whose half-life is inconveniently short (109.7 min) as a tracer in diffusion experiments. Up to now, the only measurement of the self-diffusion coefficient of fluorine in molten fluoride was done by Harari, Lanteine, and Chemla[2] in NaF–AlF_3 melts by the capillary-reservoir technique using ^{18}F. Though the fluorine self-diffusion coefficient can be measured by the nuclear magnetic resonance method, the application of this method to molten fluoride has not been found in the literature.

The present article concerns the measurement of the self-diffusion coefficient of fluorine in molten Li_2BeF_4 (congruent melting at 459.1 °C[3]) and its temperature dependence by the capillary reservoir technique using a tracer ^{18}F. The reason for the selection of this salt composition is connected with the fact that the fluorine could preferably exist in the form of a BeF_4^{2-} ion as a result of the dissociation reaction: $Li_2BeF_4 \rightleftarrows 2Li^+ + BeF_4^{2-}$. Another motivation for study of a Li_2BeF_4 melt arises from its applicability to nuclear reactors: this is the solvent for fissile and fertile components in molten salt thermal breeder reactors and also possibly the blanket medium of D–T nuclear fusion reactors.

Experimental Section

Preparation of Radioactive Tracer. Highly purified Li_2CO_3 powder (100 mg) which was sealed in an evacuated quartz ampoule was irradiated in the JRR-2 (Japan Research Reactor-2) at a flux of greater than 10^{13} thermal $n/cm^2 \cdot s$ for 20 min. The fluorine-18 is produced by the following reactions using thermal neutrons:

$$^6_3Li + ^1_0n = ^3_1H + ^4_2He$$

$$^3_1H + ^{16}_8O = ^1_0n + ^{18}_9F$$

The presence of ^{18}F was confirmed from a half-life determination using the 0.51-MeV peak in the γ spectrum of the irradiated Li_2CO_3 powder.

After opening the irradiated ampoule, Li_2CO_3 powder was treated with aqueous hydrofluoride in a platinum crucible to produce the labeled LiF deposit. This was followed by heating to dryness.

Preparation of Li_2BeF_4. The following chemicals were used in the present work: LiF prepared by Morita Kagaku Kogyo Co., analytical reagent grade; BeF_2 prepared by Rare Metallic Co., known impurities (in ppm): K + Na, 600; Ca, 10; Si, 10; Al, 20; Cr, 30; Fe, 10; Ni, 10. A mixture of the two salts was melted in a nickel container and treated with a HF–H_2 mixture at 700 °C and then sparged with He.

Apparatus. The technique employed was the "diffusion from the capillary" method. The capillary which was 0.8 mm i.d. and 3–4 cm in length was made of Ni. Figure 1a is the cell for filling the radioactive melt into a capillary. The cell which was placed in the furnace was composed of a fused silica tube

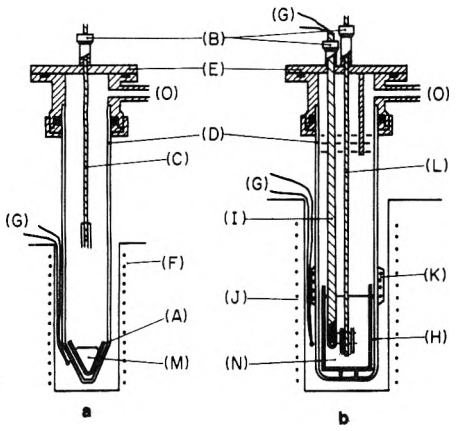

Figure 1. (a) The cell for filling a radioactive salt into capillaries. (b) The cell for diffusion run: (A,H) nickel crucible, (B) "O" ring seal, (C,L) nickel rod, (D) silica tube, (E) stainless steel flange, (F,J,K) heater, (G) chromel–alumel thermocouple, (I) nickel tube, (M) radioactive melt, (N) nonactive melt, (O) to vacuum and gas system.

(D) and a stainless steel flange (E). A Ni rod (C) was connected to the center of the flange by an "O" ring seal (B) which permitted the rod to move vertically. The Ni conical-shape vessel (A), for melting the radioactive Li_2BeF_4, was placed on the bottom of the silica tube.

Figure 1b is the diffusion cell. The Ni reservoir (H) containing nonactive melt was placed on the bottom of the silica tube (D). A movable Ni rod (L) and a Ni tube (I) were connected to the stainless steel flange. The former was used to hold capillaries and the latter was the sheath for inserting a chromel–alumel thermocouple to measure the temperature of the melt. The entire cell was held in a kanthal resistance furnace (J). An additional nichrom heater (K) was wound on the silica tube to flatten the temperature gradient. Temperature control was conducted with the thermocouple set in the space between the furnace and the silica tube and was better than ±0.5 °C as indicated by the thermocouple in the reservoir. The vertical temperature gradient in the melt was also checked by raising and lowering a thermocouple through the "O" ring seal (B) and the temperature deviation was controlled to 1 °C maximum between the top and bottom of the capillary.

Procedure. The LiF powder labeled with ^{18}F and the BeF_2 powder were weighed, mixed, and placed in the vessel (A), together with lumps of nonradioactive Li_2BeF_4 for radioactive dilution. Five–ten capillaries whose mouths faced down were wound with Ni wire to be held at the lower end of rod C, and kept above the vessel (A). The cell was evacuated for some minutes, then filled with pure dry argon. After melting the mixture, the capillaries were filled with active salt by dipping their mouths in the melt under vacuum and then feeding argon slowly back into the cell. They were then raised out of melt and were taken out of the cell after cooling for some time.

The outside of each capillary was carefully polished with abrasive paper and washed with acetone. Then the radioactivity of ^{18}F in each capillary was measured by a γ ray spectrometer with a 2-in. NaI(Tl) detector. After 1 min of radioactivity counting, the capillaries were put on the holder at the lower end of rod L and were set in the diffusion cell. The cell was evacuated and then filled with argon. The capillaries were slowly brought down and were submerged in the reservoir melt to allow diffusion to proceed for a given time. The durations of the diffusion run were in the range of 1–3 h. After the diffusion run, the capillaries were slowly lifted out of the melt and then removed from the cell. After cleaning the outside of the capillaries, their γ ray activities were measured.

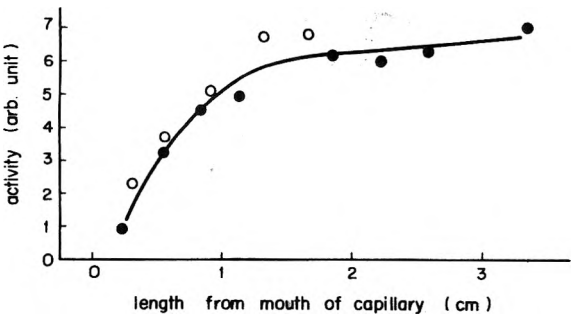

Figure 2. The distribution of ^{18}F in a capillary after a diffusion run (temperature = 568 °C, diffusion time = 70 min): (●) capillary A; (O) capillary B. The diffusion coefficient obtained from this distribution curve is shown as point S in Figure 3.

Results

Calculation of Diffusion Coefficients. There are two approaches in the determination of diffusion coefficients. One is the method of comparing the total activity in the capillary before and after the diffusion run. The other is to section the capillary at intervals of several millimeters and analyze the activity–distance curve. The determination by the latter is more direct than the former. In addition, the time necessary for sectioning is so long that the activity of ^{18}F becomes too small for accurate measurement. Thus, the former method of measuring the total activity was employed in almost all cases throughout our experiments. The self-diffusion coefficient of fluorine was calculated by the well-known solution of a diffusion equation appropriate for the present system.

$$\frac{\pi}{8}\frac{C_{av}}{C_0} = \sum_n \frac{1}{(2n+1)^2} \exp[-(2n+1)^2\pi^2 Dt/4L^2]$$

where C_0 is the initial concentration of ^{18}F, C_{av} its residual concentration, D the self-diffusion coefficient, L the length of the capillary, and t the duration. In Σ_n, the values of n up to 4 were used.

In our experiments, the liquid was not swept past the mouth of the capillary, so that it was uncertain that the boundary condition of zero activity at the mouth of capillary was always satisfied. To check this, the activity–distance curves of ^{18}F were obtained by sectioning the capillaries with a pipe cutter at two diffusion temperatures. Figure 2 illustrates the variation of concentration along the length of capillaries after diffusion run, for example, at t = 70 min, temperature = 568 °C. From this figure, the extension of the curve intersects the line of zero activity at a point in a short distance in from the mouth. It seems that thermal contraction of the salt including solidification caused the surface of salt to sink a little inward. Thus, it can be said that the boundary condition at the mouth was substantially satisfied; convection in the reservoir melt corrected this condition.

The diffusion coefficient can be determined by analyzing the curve such as Figure 2 using the relation

$$C_x = C_0 \operatorname{erf}\left(\frac{x}{2(Dt)^{1/2}}\right)$$

where C_x is the concentration of ^{18}F at distance x from the boundary after time t. The diffusion coefficients obtained in this way were in good agreement with the values obtained by the method measuring the total activity, as shown later, which indicates that the methods employed in our experiments were appropriate.

TABLE I: Self-Diffusion Coefficient Data of Fluorine in a Li_2BeF_4 Melt

Temp, °C	Expt rms values $\times 10^{-5}$ cm²/s	Std dev, %	Recommended value[a] $\times 10^{-5}$ cm²/s
513	2.55 ± 0.63	24	2.15
549	4.18 ± 1.11	27	5.00
575	7.05 ± 1.72	24	9.00
603	16.84 ± 2.46	15	16.00
623	29.09 ± 4.82	17	24.50
644	30.00 ± 4.00	13	34.50

[a] From curve of Figure 2.

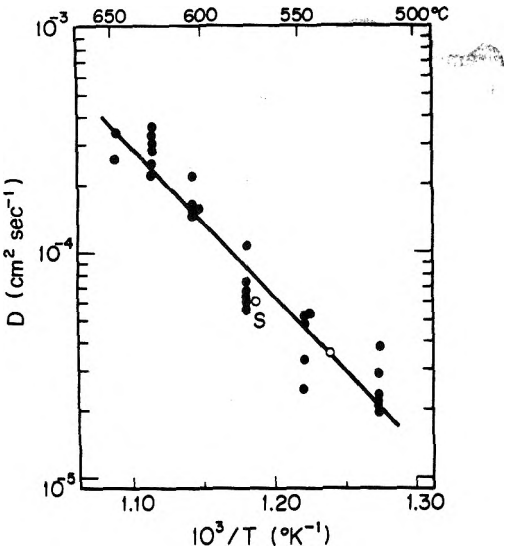

Figure 3. The self-diffusion coefficient of fluorine in a Li_2BeF_4 melt: (●) by the method of measuring total activity in a capillary; (○) by the sectioning method.

Results

The results of the experiments are given in Figure 3 as the variation of log D vs. $1/T$ (cf. Table I). The closed circles are those obtained by the method of measuring the total activity in each capillary and the opened circles are those obtained by the sectioning method. In this figure, though the points show some scattering, a linear variation of log D vs. $1/T$ is seen, at least within the temperature range under investigation; the diffusion coefficient is written in the form

$$D = D_0 \exp\left[\frac{-E_D(\mathrm{F})}{RT}\right]$$

where $E_D(\mathrm{F})$ is the activation energy of fluorine diffusion, R the gas constant, and T the absolute temperature. $E_D(\mathrm{F})$ and D_0 are calculated by the least-squares methods from all experimental data as follows: $E_D(\mathrm{F}) = 30.6 \pm 3.4$ kcal/mol; log $D_0 = 3.82 \pm 0.85$ cm²/s. These values seem too large, compared with those reported so far for other molten salt systems except for molten oxide systems.

Discussions

Our results for fluorine diffusion are considerably difficult to explain by a simple model because of the unusual combination of a relatively large diffusion coefficient and a high activation energy.

It is interesting that the results for fluorine diffusion are quite similar to those for oxygen diffusion in a molten lime–silica–alumina slag.[12,13] The magnitude of the diffusion coefficient for oxygen is a factor of 10 as large as those for metallic cations (calcium and aluminum) and the activation energy for diffusion (80 kcal/mol) is higher than those determined by viscosity[14] (50 kcal/mol) and electrical conductivity[15,16] (42 kcal/mol). In molten Li_2BeF_4, the activation energy for fluorine diffusion (30.6 kcal/mol) is also higher than those determined by viscosity[1] (9 kcal/mol) and electrical conductivity[6] (9 kcal/mol).

It must be noted that the LiF–BeF_2 melt system is quite similar to the MgO–SiO_2 melt system; this similarity is seen in the following radius ratios among the constituent ions, i.e.

$$\frac{Mg^{2+}}{O^{2-}} = 0.46 \simeq 0.50 = \frac{Li^+}{F^-}$$

and

$$\frac{Si^{4+}}{O^{2-}} = 0.28 \simeq 0.24 = \frac{Be^{2+}}{F^-}$$

and the fact that the phase diagram of MgO–SiO_2 scaled down by the relation [(t °C + 273 °C)/2.88] + 273 fit most of the diagram of LiF–BeF_2, as indicated by Thillo and Lehmann.[11] It was also recently[17] found that the physical properties, such as viscosity, electrical conductivity, and molar volume, depend on simple quantitative relationships between molten alkali fluoroberyllate system and molten alkaline earth silicate system.

Cantor et al.[1] showed in their viscosity study of molten LiF–BeF_2 that the viscosity decreases rapidly with an increase of LiF concentration, due to breaking of the fluorine bridges in a three-dimensional network of Be–F bonds, and estimated that the melt might lose its network character for a BeF_2 content smaller than 65 mol %. It appears that the Li_2BeF_4 melt does not have a network structure from the above argument. It was reported by an analysis of the Raman spectrum[4] and x-ray diffraction measurement[5] of molten Li_2BeF_4 that the fluorides may be predominant in the form of tetrahedral BeF_4^{2-} ion. However, the existence of larger ions such as $Be_2F_7^{3-}$ or free F^- ions cannot be denied and the volume fraction of various anions was also estimated by thermodynamic analysis.[18]

The fact that the magnitude of the diffusion coefficient measured in this work is extraordinarily large cannot be explained solely by mass transfer due to migration of the large fluoroberyllate anions.

Possible explanations for the large value of the fluorine diffusion coefficient could be the exchange of fluorine atoms between neighboring beryllate units including the rotation of beryllate anions, or the fluorine diffusion by means of a neutral ion pair, such as LiF, diffusion mechanism as suggested by Borucka, Bockris, and Kitchener.[9]

The above exchange mechanism involves the breaking of Be–F bonds and some steric difficulties with anion rotation, which can account for a high energy of activation for fluorine diffusion.

In ion-pair diffusion, on the other hand, the movement of fluorine with lithium involves breaking of Be–F bonds, because the content of free fluorine atoms in the present composition seems small. This mechanism can also have a high activation energy. The value of the Be–F bonding energy is not known, but it is thought that the observed value of the activation energy of fluorine diffusion (30.6 kcal/mol) is less than the Be–F bonding energy.

The processes of diffusion and electrical conductance

transport are related by the Nernst–Einstein equation. This equation suggests that if the same ions play a main part in both diffusional and electrical transport processes, the activity energy of diffusion E_{Di}, is nearly the same as that of the electrical conductance E_k. The large discrepancy in the activation energy between diffusion (30.6 kcal/mol) and electrical conductance (9 kcal/mol) will also be explained by the above mechanisms. In both cases, the movement of fluorine does not involve an electric current transfer. According to the measurement of the internal transference numbers of cations relative to fluoride ions in the Li_2BeF_4 melt, an unicationic transport by the Li^+ ions, or a practically zero mobility of Be^{2+} ions relative to fluorine, was reported.[7] Therefore, if the electrical conductance could be attributed to the movement of Li^+ ions and the mobility of Li^+ ions is much larger than that of fluoroberyllate ions, a large discrepancy between E_k and E_D(F) could be explained.

Qualitative diffusion coefficients of lithium at 762 °C have been derived in $LiBeF_3$ by electromigrational depletion measurement[19] and molecular dynamics calculation.[20] Both authors obtained a D_{Li} of about 10^{-5} cm^2 s^{-1}. As already mentioned above, there are significant similarities in the physical properties between molten alkali fluoroberyllates and alkaline earth silicates, and the magnitude of the diffusion coefficient for oxygen is about a factor of 10 as large as those for metallic cations. Therefore, the high value of the diffusion coefficient for fluorine (about 10^{-4} cm^2 s^{-1} at 650 °C) might not be so unreasonable.

The large discrepancy in the activation energy between diffusion and electrical conductance or viscosity was also found in a molten lime silica alumina slag. This fact could be closely related to some extraordinary behavior in fluorine diffusion in molten Li_2BeF_4.

Much of above discussions are in the realm of speculation. In order to obtain a reasonable picture of the diffusion mechanism in a $LiF–BeF_2$ melt, we intend to measure the diffusion coefficient of fluorine and cations over the whole range of concentration in this binary system.

Acknowledgments. The authors express their sincere thanks to Drs. H. Amano, K. Tanaka, and H. Kudoh of this institute for their helpful discussions throughout this work.

References and Notes

(1) S. Cantor, W. T. Ward, and C. T. Moynihan, *J. Chem. Phys.*, **50**, 2874 (1969).
(2) D. Harari, F. Lanteime, and M. Chemla, *J. Chem. Phys. Physicochim. Biol.*, **66**, 1286 (1969).
(3) K. A. Romberger, J. Braunstein, and R. E. Thoma, *J. Phys. Chem.*, **76**, 1154 (1972).
(4) A. S. Quist, J. B. Bates, and G. E. Boyd, *J. Phys. Chem.*, **76**, 78 (1972).
(5) F. Vaslow and A. H. Narten, *J. Chem. Phys.*, **59**, 4949 (1973).
(6) G. D. Robbins and J. Braunstein n "Molten Salts: Characterization and Analysis", G. Mamantov, Ed., Marcel Dekker, New York, N.Y., 1969, p 443.
(7) K. A. Romberger and J. Braunstein, *Inorg. Chem.*, **9**, 1273 (1970).
(8) M. H. Cohen and D. Turnbull, *J. Chem. Phys.*, **31**, 1164 (1959).
(9) A. Z. Borucka, J. O'M. Bockris, and J. A. Kitchener, *Proc. R. Soc. London, Ser. A*, **241**, 554 (1954).
(10) S. Glasstone, K. Laidler, and H. Eyring, "The Theory of Rate Processes", McGraw-Hill, New York, N.Y., 1951.
(11) E. Thillo and H. A. Lehmann, *Z. Anorg. Chem.*, **258**, 332 (1949).
(12) P. J. Kores and T. B. King, *Trans. AIME*, **224**, 299 (1962).
(13) H. Ueda and Y. Oishi, *Asahi Garasu Kogyo Gijutsu Shoreikai Kenkyu Hokoku*, **16**, 201 (1970).
(14) J. O'M. Bockris and D. C. Lowe, *Proc. R. Soc. London, Ser. A*, **226**, 425 (1954).
(15) J. O'M. Bockris, J. A. Kitchener, S. Ignatowicz, and J. W. Tomlinson, *Discuss. Faraday Soc.*, **4**, 265 (1948).
(16) J. O'M. Bockris, J. A. Kitchener, S. Ignatowicz, and J. W. Tomilinson, *Trans. Faraday Soc.*, **48**, 75 (1953).
(17) K. Furukawa, H. Ohno, and S. Iwamoto, Proceedings of the Autumn Meeting (Sapporo) of the Japan Institute of Metals, 1975, S3-7, p 90.
(18) C. F. Baes, Jr., *J. Solid State Chem.*, **1**, 159 (1970).
(19) C. E. Vallet, H. R. Bronstein, and J. Braunstein, *J. Electrochem. Soc.*, **121**, 1429 (1974).
(20) A. Rahman, R. H. Fowler, and A. H. Narten, *J. Chem. Phys.*, **57**, 3010 (1972).

On the Fourier Transformation of Dielectric Time Domain Spectroscopy Data

B. Gestblom and E. Noreland*

Institute of Physics, University of Uppsala, S-751 21 Uppsala, Sweden *(Received December 29, 1975)*

Publication costs assisted by the Institute of Physics, University of Uppsala

The polygon approximation for the evaluation of Fourier transforms, given by Cole and Tuck, has been extended to the case of step pulses as encountered in dielectric time domain spectroscopy (TDS). The accuracy of this approximation is compared with other methods, and estimates of the necessary sampling densities for TDS work are given.

Introduction

In dielectric time domain spectroscopy (TDS) the dielectric properties of a sample are determined from its response to a fast rising pulse.[1] To obtain the permittivity in the frequency domain a Fourier transformation

$$F(\omega) = \int_{-\infty}^{\infty} f(t)\, e^{-j\omega t}\, dt \qquad (1)$$

is made of the incoming step pulse and the response pulse from the dielectric. In practice the pulses are sampled at regular time intervals τ and the integral in eq 1 has to be evaluated by a discrete Fourier transform procedure, e.g.

$$F(\omega) = \tau \sum_{n=1}^{N} f(n\tau) e^{-j\omega n\tau} \qquad (2)$$

According to the Shannon sampling[2] theorem the discrete transform in eq 2 gives the true transform of the function $f(t)$ if the pulse is frequency limited $\omega < \pi/\tau$. In using the discrete

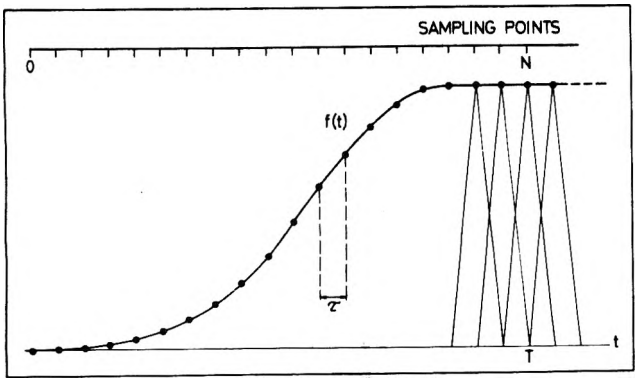

Figure 1. Typical step pulse f(*t*) in TDS work showing sampling points and polygon approximation.

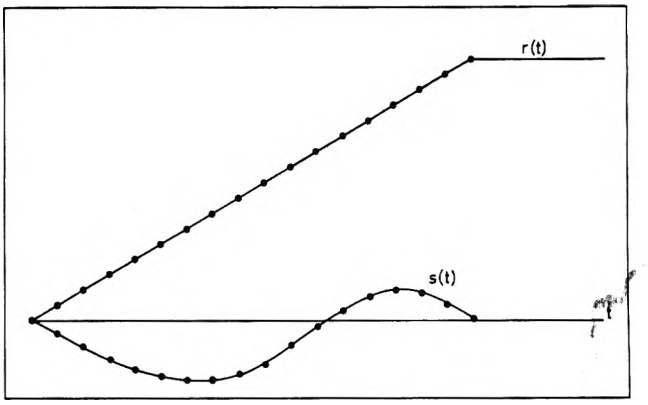

Figure 2. The non-time-limited pulse as a sum of a ramp function r(*t*) and the time-limited difference s(*t*) = f(*t*) − r(*t*).

transform to approximate (1) aliasing errors may be introduced if the sampling density is too low.

The pulses to be transformed in TDS are not generally time limited and precautions have also to be taken not to introduce serious truncation errors in evaluating the discrete Fourier transform. In TDS work the Samulon[3] modification of eq 1

$$F(\omega) = \frac{\tau}{1 - e^{-j\omega\tau}} \sum_{n=1}^{\infty} \{f(n\tau) - f((n-1)\tau)\} e^{-j\omega n\tau} \qquad (3)$$

has been widely used.

In a recent study Cole[4] has developed a TDS method in which the response pulse can be considered to be time limited. The pulse is then approximated by a polygon, connecting the sampling points. This polygon can be looked upon as a sum of triangular pulses of width 2τ. The transform of a triangular pulse is known[5] and the exact transform of the polygon is given by

$$F(\omega) = \tau\left(\frac{\sin \omega\tau/2}{\omega\tau/2}\right)^2 \sum_{n=1}^{N} f(n\tau) e^{-j\omega n\tau} \qquad (4)$$

Comparison with eq 2 shows that the simple discrete transform formula has been modulated with a $(\sin(\omega\tau/2)/(\omega\tau/2))^2$ factor. Tuck[6] tested eq 4 on the function $f(t) = e^{-|t|}$ and found it to be an improvement on the simple eq 2, in particular at higher frequencies when the Nyquist frequency $\nu_0 = 1/2\tau$ is approached.

TDS methods have been developed[7-9] which make accurate measurements possible up to frequencies of at least 10 GHz. The need to keep the sampling density as low as possible for a given accuracy, and consequently also the computational work in forming the transforms, makes a comparative study of the different transform methods valuable. It might thus be believed that eq 4 should be more suitable for evaluation of Fourier transforms in TDS work than methods used so far.[1] It is the purpose of this note to show how the polygon approximation in eq 4 can be extended to non-time-limited pulses, and to compare the accuracy of this approximation relative to eq 2 or the modifications of eq 2 used in TDS work.

Theory

The incoming step pulse monitored with the sampling system is shown in Figure 1. Straightforward application of eq 4 would lead to gross truncation errors due to the neglect of the steady part of the pulse for times $>T$. To take account of the complete pulse the approximating polygon is extended to infinity by the addition of triangular pulses as in Figure 1.

The resulting polygon is the sum of triangular pulses $p_k^n(t)$ of width 2τ and height $p_k^n(k\tau) = f(k\tau)$. The top index of the symbol $p_k^n(t)$ here indicates that the triangle is centered around $t = n\tau$ and the bottom index indicates that its height is $f(k\tau)$. The polygon can also be looked upon as the sum of the differences of successive triangles

$$f(t) = \sum_{k=1}^{\infty} \sum_{n=k}^{\infty} p_k^n(t) - p_{k-1}^n(t) \qquad (5)$$

This triangular sum can be exactly transformed:

$$F(\omega) = \tau\left(\frac{\sin \omega\tau/2}{\omega\tau/2}\right)^2 \sum_{k=1}^{\infty} \sum_{n=k}^{\infty} \{f(k\tau) - f((k-1)\tau)\} e^{-j\omega n\tau} \qquad (6)$$

After evaluation of the sum over n one obtains

$$F(\omega) = \tau\left(\frac{\sin \omega\tau/2}{\omega\tau/2}\right)^2 \frac{1}{1 - e^{-j\omega\tau}} \sum_{k=1}^{\infty} \{f(k\tau) - f((k-1)\tau)\} e^{-j\omega k\tau} \qquad (7)$$

A comparison with the Samulon[3] modification of eq 1 shows that the Samulon formula has been modulated with a $(\sin(\omega\tau/2)/(\omega\tau/2))^2$ factor. The Fourier transform in eq 7 can be evaluated at any chosen frequency.

An alternative approach to extend the polygon approximation to infinity is to use the method given by Nicolson[10] for the evaluation of eq 2. A ramp $r(t) = f(N\tau)t/T$ is subtracted from the incoming pulse giving the result $s(t) = f(t) - r(t)$. The complete, non-time-limited pulse can then be looked upon as a sum of two pulses as in Figure 2.

The true transform would thus be given by the sum of the transforms of $s(t)$ and $r(t)$. The transform of $r(t)$ is given by

$$R(\omega) = \frac{-2jf(T)\sin\dfrac{\omega T}{2}}{T\omega^2} e^{-j\omega T/2} \qquad (\omega \neq 0) \qquad (8)$$

For frequencies $\omega = k(2\pi/T)$, $R(\omega) \equiv 0$ and the transform of the pulse $f(t)$ can for these frequencies consequently be evaluated from the time-limited difference $s(t)$ by the use of eq 2 or 4. The method of subtracting a ramp voltage and use of eq 2 or 4 is thus identical with the difference methods eq 3 or 7, respectively.

The ramp subtraction method only works for certain frequencies $\omega = k(2\pi/T)$. These are precisely the frequencies used in the fast Fourier transform (FFT) algorithm.[11] This algorithm gives an extremely efficient way of handling the sum of exponentials in the discrete transform for these frequencies.

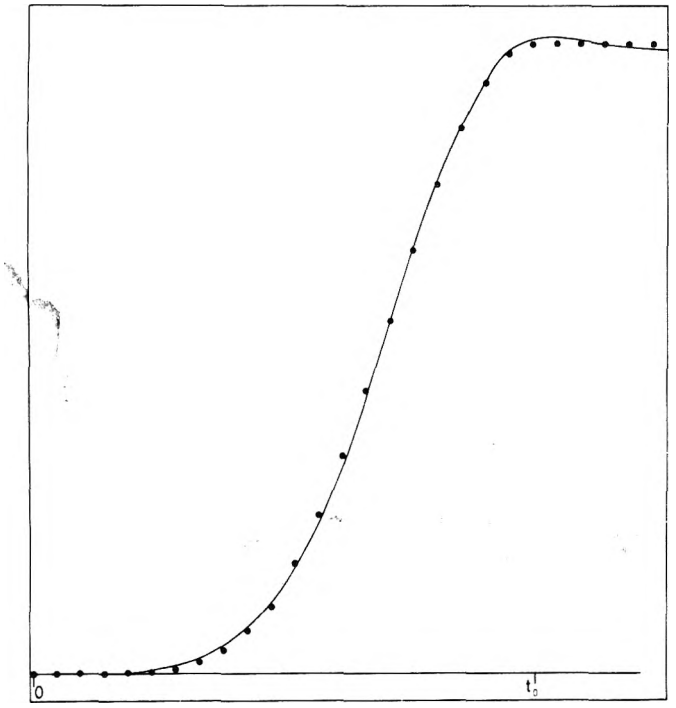

Figure 3. Experimental step pulse (full line) and $\sin^5(\pi t/2t_0)$ approximation (circles). t_0 is 80 ps.

After forming the differences in eq 7 the FFT algorithm can thus equally well be used in the evaluation of the transform according to eq 7. Computationally there is consequently nothing much to choose between the difference and the ramp voltage method, if the FFT algorithm is used. However, if one wishes to evaluate the transform at other frequencies the ramp method is not applicable and one is referred to the difference method. The same conclusion also holds for the original Samulon[3] or Nicolson[10] approaches in eq 3 and 2, respectively, where the $(\sin(\omega\tau/2)/(\omega\tau/2))^2$ term is missing.

Results

In order to study the accuracy of eq 7 an analytical step pulse was used $f(t) = \sin^5(\pi t/2t_0)p(t - t_0) + u(t - t_0)$ where $u(t - t_0) = 1$ for $t > t_0$ and $u(t - t_0) = 0$ for $t \leq t_0$ and where $p(t - t_0) = u(t) - u(t - t_0)$. This function is in fact a very close approximation to the true step in our tunnel-diode sampling system, as shown in Figure 3.

The exact Fourier transform of this pulse is given by

$$F(\omega) = -\frac{je^{-j\omega t_0}}{\omega} - \frac{j}{8}\left\{\frac{j5\pi t_0 + 2\omega t_0^2 e^{-j\omega t_0}}{25\pi^2 - 4\omega^2 t_0^2} - \frac{j15\pi t_0 - 10\omega t_0^2 e^{-j\omega t_0}}{9\pi^2 - 4\omega^2 t_0^2} + \frac{j10\pi t_0 + 20\omega t_0^2 e^{-j\omega t_0}}{\pi^2 - 4\omega^2 t_0^2}\right\} \quad (9)$$

The discrete Fourier transform was evaluated by eq 7 and the Samulon[3] eq 3, i.e., the same expression except for the $(\sin(\omega\tau/2)/(\omega\tau/2))^2$ term. The FFT algorithm was used. The results are given in Figure 4, where the deviation from the true transform has been given as a function of frequency for different sampling intervals.

As can be judged from Figure 4 the Samulon equation[3] is far more accurate than the polygon approximation in eq 7. For frequencies up to t_0^{-1} it is seen that in order to achieve the same accuracy with the polygon approximation as with the Samulon equation one has to sample the pulse almost ten times as densely. At a sampling interval of $0.1t_0$, or less, it can

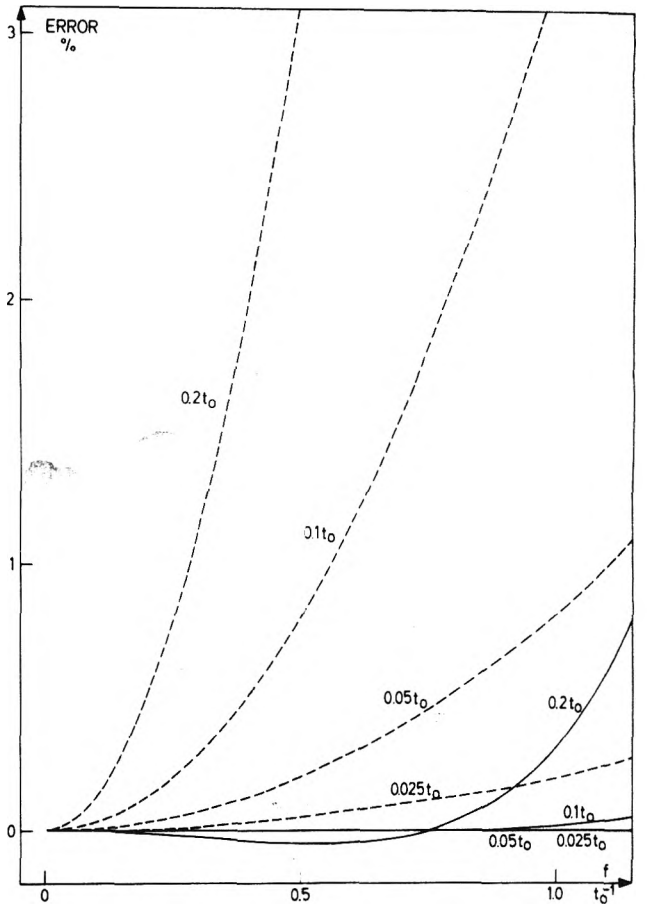

Figure 4. Relative error in the Fourier transformation of $\sin^5(\pi t/2t_0)p(t - t_0) + u(t - t_0)$ evaluated from eq 3 (full lines) and eq 7 (broken lines). The sampling interval for each curve is given.

be seen that the Samulon formula for the discrete Fourier transform is practically indistinguishable from the true transform up to frequencies t_0^{-1}.

In a TDS system t_0 is of the order of 80 ps. The frequency t_0^{-1} in Figure 4 thus corresponds to a frequency of 12.5 GHz. The sampling interval $\tau = 0.2t_0$ in Figure 4 corresponds to 16 ps, and it can be seen that even at this low sampling rate the Samulon formula gives a transform which deviates from the true transform with only 0.3%. For the same accuracy the polygon approximation requires a sampling interval as low as ~2 ps. At 25 GHz a sampling interval of 8 ps gives a relative error of 1% for the Samulon formula, and 14% for the polygon approximation.

The time for Fourier transformation using the FFT algorithm is proportional to $N \log N$ where N is the number of sampling points. Thus it can be concluded that for comparable accuracy the polygon approximation would require roughly a 100-fold effort in sampling the pulse, and a 200-fold computational effort. If the transform is evaluated directly from eq 3 and 7, not using the FFT algorithm, the polygon approximation becomes even more unfavorable since the computation time then is proportional to N^2.

In choosing between the FFT algorithm and the direct evaluation of eq 3 it should be observed, however, that for N sampling points the FFT algorithm gives the transform for N frequencies, while a considerably lower number of frequencies may be sufficient to characterize the dielectric behavior. In such a case direct evaluation of eq 3 may be preferable since the frequencies can then be chosen freely.

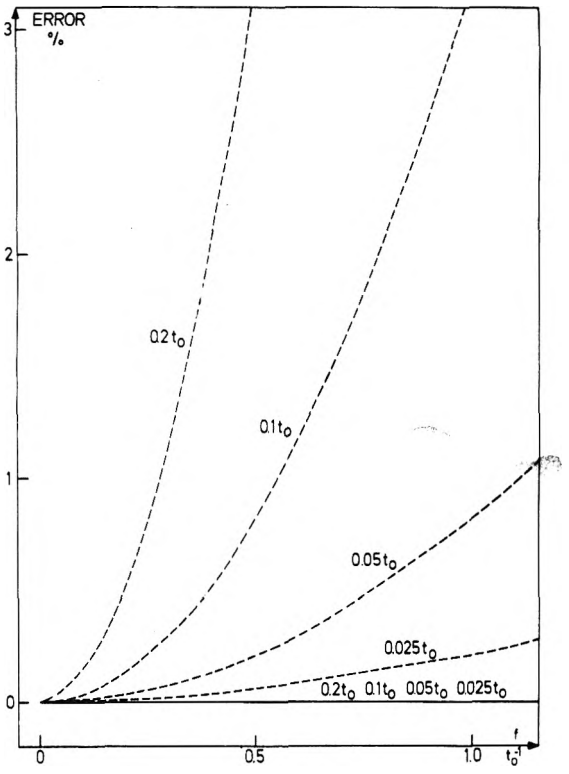

Figure 5. Relative error in the Fourier transformation of $\sin^5(\pi t/2t_0)p(t - 2t_0)$ evaluated from eq 4 (broken lines) and eq 2 (full line). The error in using eq 2 is negligible for all sampling intervals employed.

For TDS work at lower frequencies Cole[4] has used an extreme form of the polygon approximation, i.e., the step pulse is approximated with a ramp. We also tested this approximation to our analytical step pulse by approximating the $\sin^5(\pi t/2t_0)$ function with a ramp with a rise time $0.412t_0$. The transform of the ramp is given in eq 8. This approximation was found to agree with the true transform within 1% up to frequencies $0.18t_0^{-1}$, and within 2% up to frequencies $0.3t_0^{-1}$. For TDS work up to 2–3 GHz the simple ramp approximation to the incident pulse would thus be sufficient in agreement with the limit given by Cole.

The polygon approximation was also compared with the discrete Fourier transform in eq 2 for a time-limited pulse. As a test pulse here the function $f(t) = \sin^5(\pi t/2t_0)p(t - 2t_0)$ was chosen. This function should give a good representation of the fast rising edge of a response pulse in TDS work. The function $f(t)$ has the exact transform

$$F(\omega) = \frac{5\pi t_0 \cos \omega t_0 e^{-j\omega t_0}}{4}\left\{\frac{1}{25\pi^2 - 4\omega^2 t_0^2} + \frac{2}{\pi^2 - 4\omega^2 t_0^2} - \frac{3}{9\pi^2 - 4\omega^2 t_0^2}\right\} \quad (10)$$

A comparison with the discrete Fourier transform evaluated by eq 2 and 4 is given in Figure 5. The conclusion to be drawn here is the same as for the step pulse case, the discrete transform as defined in eq 2 is far more accurate than the polygon approximation for the same sampling density. Up to frequencies t_0^{-1} the discrete transform in eq 2 agrees almost exactly with the true transform. This is not unexpected in view of the Shannon[2] sampling theorem, since the frequency content in the time-limited pulse is low at higher frequencies.

It would seem that the conclusion by Tuck[6] that the polygon approximation is more accurate than the Shannon sampling theorem is a reflection of the fact that the test function $e^{-|t|}$ used by him contains a cusp at origin. Pulses met in a physical system with filtering, as in TDS work, are smoothed, and the Shannon sampling theorem in eq 2 or its modification due to Samulon's eq 3 is more accurate.

Acknowledgment. Financial support from the Swedish Natural Science Research Council is gratefully acknowledged.

References and Notes

(1) For a review, see M. J. C. van Gemert, *Philips Res. Rep.*, **28**, 530 (1973).
(2) C. E. Shannon, *Proc. IRE*, **37**, 10 (1949).
(3) H. A. Samulon, *Proc. IRE*, **39**, 175 (1951).
(4) R. H. Cole, *J. Phys. Chem.*, **79**, 1469 (1975).
(5) A. Papoulis, "The Fourier Integral and Its Applications", McGraw-Hill, New York, N.Y., 1962.
(6) E. O. Tuck, *Math. Comput.*, **21**, 239 (1967).
(7) A. M. Nicolson and G. F. Ross, *IEEE Trans. Instrum. Meas.*, **IM-19**, 377 (1970).
(8) H. W. Loeb, G. M. Young, P. A. Quickenden, and A. Suggett, *Ber. Bunsenges Phys. Chem.*, **75**, 1155 (1971).
(9) A. Suggett in "High Frequency Dielectric Measurements", J. Chamberlain and G. W. Chantry, Ed., IPC Science and Technology Press, Guildford, 1973.
(10) A. M. Nicolson, *Electron. Lett.*, **9**, 317 (1973).
(11) E. O. Brigham, "The Fast Fourier Transform", Prentice-Hall, Englewood Cliffs, N.J., 1974.

Relative Rate Constants for the Reaction of the Hydroxyl Radical with Selected Ketones, Chloroethenes, and Monoterpene Hydrocarbons

Arthur M. Winer, Alan C. Lloyd, Karen R. Darnall, and James N. Pitts, Jr.*

Statewide Air Pollution Research Center, University of California, Riverside, California 92502 *(Received January 30, 1976)*

Publication costs assisted by the University of California, Riverside

The relative rates of disappearance of three monoterpene hydrocarbons, two chloroethenes, and three aliphatic ketones were measured in an environmental chamber under simulated atmospheric conditions at 305 ± 2 K. The observed rates of disappearance were used to derive relative rates of reaction of these organic compounds with the hydroxyl radical (OH) on the previously validated basis that OH is the species dominantly responsible for the hydrocarbon disappearance under the experimental conditions employed. Absolute rate constants, obtained from the relative values using the published rate constant for OH + isobutene (3.05×10^{10} M^{-1} s^{-1}), are ($k \times 10^{-10}$ M^{-1} s^{-1}): α-pinene, 3.5 ± 0.5; β-pinene, 4.1 ± 0.6; *d*-limonene, 9.0 ± 1.4; methyl ethyl ketone, 0.20 ± 0.06 methyl isobutyl ketone, 0.9 ± 0.3; diisobutyl ketone, 1.5 ± 0.5; trichloroethene, 0.27 ± 0.08; tetrachloroethene, 0.13 ± 0.04. No previous determinations of these rate constants have been found in the literature. Rate constants for an additional nine monoterpene hydrocarbons have been derived from data recently published by Grimsrud, Westberg, and Rasmussen.

Introduction

During the last six years, the major role of the hydroxyl radical (OH) in atmospheric chemistry and photochemical air pollution has been recognized,[1-7] and kinetic data for the reaction of OH with both organic and inorganic species have increased substantially.[8] However, there are currently no published rate constant determinations for the reaction of OH with ketones, chloroethenes, or any of the naturally occurring hydrocarbons such as the monoterpenes. Such rate constant data for the reaction of OH with these three classes of compounds would be useful in part because of their increasing importance for modeling the atmospheric processes occurring both in urban and rural atmospheres. Specifically, ketones and chlorinated hydrocarbons are components of commercial solvents.[9,10] Both tri- and tetrachloroethene have been observed in the troposphere at part per trillion (ppt) concentrations of <5[11] and 20 ppt,[11,12] respectively, while methyl ethyl ketone has been observed at concentrations of 1–6 parts per billion (ppb).[13] Monoterpene hydrocarbons have been shown to be present in the atmosphere with source strengths of millions of tons annually.[14] Thus, Rasmussen[15,16] and coworkers have estimated that, on an individual basis, such naturally occurring hydrocarbons have ambient concentrations in the low ppb range and are largely responsible for the "blue haze" occurring in certain forested areas.[17]

This paper describes an extension of our recent experiments in which an environmental chamber has been employed to obtain relative rate constants for the gas phase reaction of the hydroxyl radical with a series of hydrocarbons.[18,19] In this case we report data for the reaction of OH with three ketones, two chloroethenes, and three monoterpene hydrocarbons using isobutene as a reference compound.

Experimental Section

The experimental methods and procedures employed have been described in detail elsewhere[18,19] and are only briefly summarized here. Irradiations of the hydrocarbon–NO_x–air system were carried out in a Pyrex chamber[20] of approximately 6400-l. volume equipped with externally mounted Sylvania 40-BL fluorescent lamps whose spectral distribution has been reported elsewhere[21] (photon flux at 300 nm is approximately 1% of the photon flux maximum at 360 nm). The light intensity, measured as the rate of NO_2 photolysis in nitrogen,[22] k_1, was approximately 0.4 min^{-1}. All gaseous reactants were injected into pure matrix air[23] in the chamber using 100-ml precision bore syringes. Mixtures of the liquid reactants were injected using micropipettes. During irradiation, the chamber temperature was maintained at 305 ± 2 K.

Alkene, terpene, and ketone concentrations were measured by gas chromatography (GC) with flame ionization detection (FID) using the columns and techniques developed by Stephens and Burleson.[24,25] The chloroethenes were also monitored with GC(FID) using a 10 ft × ⅛ in. stainless steel column packed with 10% Carbowax 600 on C22 Firebrick (100/110 mesh). Ozone[26] was monitored by means of ultraviolet absorption (Dasibi Model 1003 analyzer), carbon monoxide by gas chromatography (Beckman 6800 air quality analyzer), and NO–NO_2–NO_x by the chemiluminescent reaction of NO with ozone (TECO Model 14B).

The initial concentrations of reactants are shown in Table I. In addition to these compounds, ethene (20–28 ppb), ethane (48–61 ppb), acetylene (25–37 ppb), propane (13–15 ppb), and variable concentrations of formaldehyde (16–134 ppb), acetaldehyde (0–7 ppb), and acetone (3–19 ppb) were present. Initial concentrations in these experiments were 1200–2100 ppb C of total nonmethane hydrocarbons, 0.58 ppm of NO_x (with an NO_2/NO_x ratio of 0.05–0.10), 5 ppm of CO, and 2900 ppb of methane, together with water vapor at 50% relative humidity. Replicate experiments were carried out in which this mixture was irradiated for 2–3 h with continuous analysis of inorganic species, analysis of hydrocarbons every 15 min, and analysis of monoterpenes, chloroethenes, and ketones every 30 min.

All data were corrected for losses due to sampling from the chamber by subtraction of the average dilution rate (1.2% per hour) from the observed hydrocarbon disappearance rate. The HC/NO_x and NO/NO_2 ratios were chosen to delay the formation of ozone, and ozone was not detected during the irra-

TABLE I: Rates of Disappearance and Rate Constants[a] for Selected Ketones, Chloroethenes, and Monoterpene Hydrocarbons at 1 atm in Air at 305 ± 2 K

Compound	Initial concn, ppb	Relative rate of disappearance	k_{OH},[b] M^{-1} s^{-1} × 10^{-10}
Isobutene	17–20	1.0	3.05 ± 0.31
Propene	5–7	0.49	1.49 ± 0.22
cis-2-Butene	7–8	1.22	3.72 ± 0.56
Methyl ethyl ketone	50–100	0.07	0.20 ± 0.06
Methyl isobutyl ketone	20–70	0.3	0.9 ± 0.3
Diisobutyl ketone	20–32	0.5	1.5 ± 0.5
α-Pinene	10–20	1.14	3.48 ± 0.52
β-Pinene	10–20	1.33	4.06 ± 0.61
d-Limonene	10–20	2.95	9.00 ± 1.35
Trichloroethene	41–161	0.088	0.27 ± 0.08
Tetrachloroethene	14–88	0.044	0.13 ± 0.04

[a] Placed on an absolute basis using 3.05 × 10^{10} M^{-1} s^{-1} for OH + isobutene from ref 35. [b] The indicated error limits are ±15%, except in the case of the chloroethenes and ketones, for which they are ±30%. These represent the estimated overall error limits and include both experimental errors and uncertainties which may occur in assuming that hydrocarbon disappearance is due solely to reaction with OH.

diation period, except in the case of one experiment, for which a small correction for the loss of hydrocarbon due to reaction with ozone was applied to the alkene disappearance rates.

In order to obtain additional data (at lower OH concentrations) to correct for the concurrent photolysis of the ketones as discussed below, irradiations of a mixture of ketones and isobutene were carried out. In these experiments, NO_x, CO, and other hydrocarbons were not added, and, under these conditions, relatively low concentrations of OH (<5 × 10^5 radicals cm^{-3}) were obtained.

Hydroxyl Radical Source in this System. As discussed previously,[19] the major sources of OH and its precursors in our experimental system are probably the reactions[4,5,27,28]

$$NO + NO_2 + H_2O \rightleftarrows 2HONO \quad (1)$$

$$HO_2 + NO_2 \rightarrow HONO + O_2 \quad (2)$$

$$HONO + h\nu\ (290\text{–}410\ nm) \rightarrow OH + NO \quad (3)$$

$$HO_2 + NO \rightarrow OH + NO_2 \quad (4)$$

The first reaction is now thought to occur slowly homogeneously,[29] but its rate is probably significantly faster when the reaction is catalyzed by surfaces. Thus, nitrous acid has been observed in a chamber study of simulated atmospheres carried out in our laboratory,[30] while direct evidence for formation of OH radicals in an environmental chamber has been provided recently by Niki, Weinstock, and co-workers.[31,32]

Reaction 4, of major importance, provides a further source of the OH radical. HO_2 can be formed in air[33,34] by any mechanism producing H atoms or formyl radicals (e.g., formaldehyde photolysis) via the reactions

$$H + O_2 + M \rightarrow HO_2 + M \quad (5)$$

$$HCO + O_2 \rightarrow HO_2 + CO \quad (6)$$

Thus any mechanism producing HO_2 in our system is also a means of furnishing OH radicals via reaction 4.

The concentration of OH radicals present during these irradiated HC–NO_x experiments was calculated to be (1.4–3.5) × 10^6 radicals cm^{-3} using the observed rates of isobutene disappearance (corrected for dilution) and the previously determined rate constant for OH + isobutene.[35] These concentrations are of the same order as those observed directly in ambient air.[31,32,36,37]

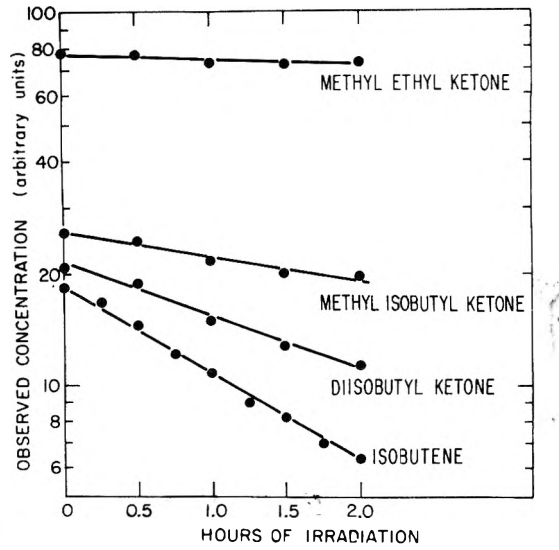

Figure 1. Concentrations of ketones (plotted on a logarithmic scale) during 2-h photolysis of HC–NO_x mixture in air at 305 ± 2 K and 1 atm.

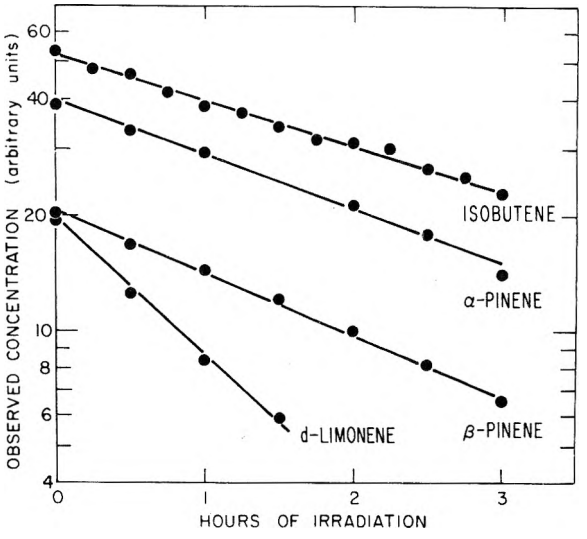

Figure 2. Concentrations of monoterpene hydrocarbons (plotted on a logarithmic scale) during 3-h photolysis of HC–NO_x mixture in air at 305 ± 2 K and 1 atm.

Results and Discussion

Typical rates of disappearance observed during a 2-h irradiation of the three ketones and 3-h irradiations of the three monoterpene hydrocarbons and the two chloroethenes are shown in Figures 1, 2, and 3, respectively. Isobutene was used as the reference compound (and is included in each figure), rather than *n*-butane which was used in our previous studies,[18,19] because its reactivity was closer to that of the terpenes, and its rate of decay could be measured more accurately in our system. In addition, the ratio of k_{OH}/k_{O_3} for isobutene is greater[32,35] than that for any of the other olefins studied, thus minimizing any contribution to the disappearance rate due to reaction with ozone. Table I gives the disappearance rates

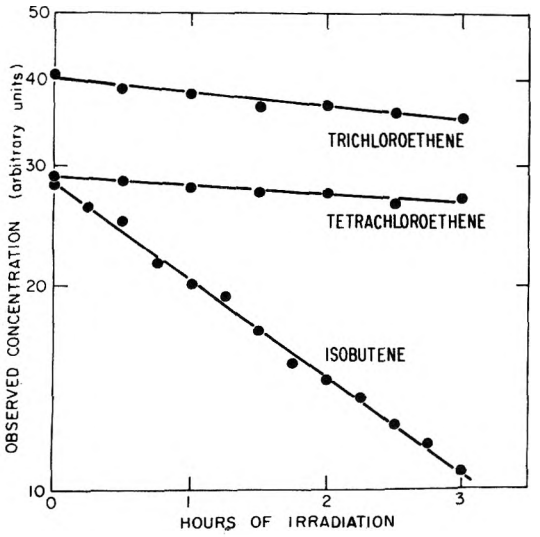

Figure 3. Concentrations of chloroethenes (plotted on a logarithmic scale) during 3-h photolysis of HC–NO_x mixture in air at 305 ± 2 K and 1 atm.

(corrected for dilution) for these reactants relative to that for isobutene based on data for the three separate experiments for monoterpenes and four separate experiments for methyl isobutyl and diisobutyl ketone and chloroethenes. Methyl ethyl ketone was present in all experiments.

Employing the fact that a range of OH concentrations (2.0×10^5–3.5×10^6 radicals cm^{-3}) was observed in these experiments, corrections to the measured rates of disappearance of the ketones were made for the possible small contribution from photolysis of these compounds. These corrections were made in the following manner. The observed rate of disappearance of a ketone is given by

$$d \ln [\text{ketone}]/dt = k_K[\text{OH}] + k_{h\nu} \quad (7)$$

where k_K and $k_{h\nu}$ are the rate constants for reaction with OH and photolysis, respectively. The isobutene disappearance rate is controlled solely by reaction with OH, hence

$$[\text{OH}] = \frac{d \ln [\text{isobutene}]}{dt\, k_{iB}} \quad (8)$$

where k_{iB} is the rate constant for reaction of OH with isobutene. Thus, substituting for [OH] in eq 7

$$\frac{d \ln [\text{ketone}]}{dt} = \frac{k_K}{k_{iB}} \frac{d \ln [\text{isobutene}]}{dt} + k_{h\nu} \quad (9)$$

Based on eq 9, the relative rates of ketone disappearance were determined from the slopes of plots of d ln [ketone]/dt vs. d ln [isobutene]/dt. The intercepts of these plots gave the rate constants for photolysis. For methyl ethyl, methyl isobutyl, and diisobutyl ketone the ratios k_K/k_{iB} were 0.07, 0.3, and 0.5, respectively, and the photolysis rate constants, $k_{h\nu}$, were 0.007, 0.014, and 0.25 h^{-1}, respectively.

On the basis that the OH radical is the species dominantly responsible for the hydrocarbon depletion during the 2- or 3-h irradiations (as discussed in detail in our earlier papers),[18,19] absolute rate constants were derived from the relative rates of disappearance using Atkinson and Pitts'[35] value of $(3.05 \pm 0.31) \times 10^{10}$ M^{-1} s^{-1} for the reaction of OH with isobutene. These results are shown in Table I. It should be noted that the ratio of rate constants (0.5 and 1.2, respectively) obtained here for propene and *cis*-2-butene relative to isobutene are in excellent agreement with the ratios obtained by Atkinson and Pitts (0.5 and 1.1, respectively).[35]

Ketones. To our knowledge, the data presented here represent the first experimental determination of rate constants for the reaction of the OH radical with any ketones in the gas phase. The only literature value for ketones is an estimated rate constant of 2.1×10^9 M^{-1} s^{-1} for the reaction of OH with methyl ethyl ketone, which was made by Demerjian, Kerr, and Calvert[5] on a thermochemical basis. This value is in remarkably good agreement with the experimental value obtained here (2.0×10^9 M^{-1} s^{-1}).

The rate constants for the reaction of OH with the two other ketones reported here are significantly larger than that for methyl ethyl ketone. Thus, the rate constant for diisobutyl ketone is about the same as that for OH + propene.[8,19,35] The dominant mode of reaction of OH with ketones is expected to be one of hydrogen abstraction. This is consistent with the increased rate constant in going from methyl ethyl ketone to diisobutyl ketone reflecting a weaker C–H bond strength in going to more highly substituted ketone.

Acetone is relatively stable under conditions employed in our photooxidation studies, and, consequently, the rate constant for OH + acetone was not measured. Based on the fact that the C–H bond strength in acetone (98 kcal) is 6 kcal stronger than that for methyl ethyl ketone (92 kcal), one would expect OH to react significantly slower with acetone than with methyl ethyl ketone.

Chloroethenes. Rate constants for the gas phase reactions of OH with tri- and tetrachloroethene (C_2HCl_3 and C_2Cl_4, respectively) have not been reported previously. The rate constants found in this study are 0.5 and 0.25, respectively, of the rate constant for OH + C_2H_4.[19] This difference in reactivity for the chloro-substituted ethenes and ethene is consistent with the results of Sanhueza and Heicklen,[38–40] who reported that the rates of reaction of $O(^3P)$ with C_2HCl_3 and C_2Cl_4 were the same and were both a factor of 10 less than that for the reaction of $O(^3P)$ with ethene.

Our results show that trichloroethene is more reactive with respect to attack by OH than tetrachloroethene. This is in agreement with the results of Lissi[41] for CH_3O reactions and Franklin et al.[42] for Cl atom reactions with these compounds. These workers found relative rates for attack on C_2HCl_3 and C_2Cl_4 of 2.2 and 2.6 for CH_3O and Cl, respectively, compared to 2.0 for OH, as found in the present study. Gay et al.[43] recently reported results from a photooxidation study of chloroethenes which, while not directly comparable to the present study due to the presence of substantial concentrations of ozone, showed that C_2HCl_3 disappeared more rapidly than C_2Cl_4 (near the beginning of their irradiations, when ozone concentrations were relatively low, the ratio of the rates of disappearance was ~2).

Since addition is likely to be the primary reaction pathway for attack by OH, the relative reactivity of C_2H_4, C_2HCl_3, and C_2Cl_4 should reflect the relative magnitudes of the ionization potentials of these molecules, which are 10.66, 9.48, and 9.34 eV, respectively. Our results are consistent with this trend.

Monoterpene Hydrocarbons. The terpenes experimentally investigated were α-pinene (I), β-pinene (II), and *d*-limonene (III). The detection limit for ozone in these experiments was

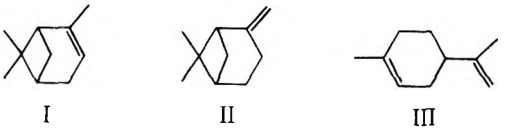

I II III

~1 ppb, and, since no ozone was detected during irradiations of the terpenes, an upper limit to the contribution due to reaction with ozone to the observed rates of terpene disap-

TABLE II: Reactivity of Selected Monoterpenes with $O(^3P)$, O_3, and OH

Compound	Rate constant, M^{-1} s^{-1}		
	$O(^3P)$[a]	O_3	OH[e]
α-Pinene	$1.60 \pm 0.06 \times 10^{10}$	2.0×10^5,[b] 1.0×10^5[c] 8.8×10^4[d]	3.5×10^{10}
β-Pinene	$1.51 \pm 0.06 \times 10^{10}$	2.2×10^4[d]	4.1×10^{10}
d-Limonene	$6.50 \pm 0.52 \times 10^{10}$	3.9×10^5[d]	9.0×10^{10}

[a] Reference 49. [b] Reference 48. [c] Reference 45. [d] Reference 16. [e] This work.

pearance can be calculated. Thus, assuming an ozone concentration of ≤1.0 ppb, and using published rate constants for the reaction of ozone with the terpenes,[16,43-45] an upper limit of 7% of the overall disappearance rate is obtained for the case of *d*-limonene (the worst case) at the lowest OH concentration present in these experiments (1.4×10^6 radicals cm^{-3}).

It is interesting to note that the rate constant, 3.7×10^{10} M^{-1} s^{-1}, obtained in this study for OH + *cis*-2-butene, a component in the hydrocarbon mix (Table I) used in this set of experiments, is in good agreement with the values of 3.2×10^{10} and 3.7×10^{10} M^{-1} s^{-1}, obtained by Atkinson and Pitts[35] and Morris and Niki,[46] respectively, although our value is somewhat higher than the value of 2.6×10^{10} M^{-1} s^{-1} obtained by Fischer et al.;[47] in these three studies, the rate constant was determined from elementary reaction measurements.

Table I shows the absolute rate constant values obtained for the terpenes. Clearly, these natural hydrocarbons react very rapidly with OH. For example, α-pinene reacts about 3×10^5 times faster with OH than with ozone.[16,48] Thus, for an ozone concentration of 3×10^{12} molecules cm^{-3} (0.12 ppm) and an OH concentration of 10^7 radicals cm^{-3}, the rates of disappearance of α-pinene due to reaction with O_3 and OH, respectively, will be essentially equal. A comparison of the rates of the three terpenes with $O(^3P)$, O_3, and OH is given in Table II.[16,45,46] Within the experimental errors for the rate constants for OH + α- and β-pinene, the trend observed for reaction with OH is the same as that observed for reaction with $O(^3P)$ and O_3.

Grimsrud, Westberg, and Rasmussen (GWR)[16] have reported the relative rates of photooxidation of a series of monoterpene hydrocarbons using mixtures of 10 ppb of the monoterpene and 7 ppb of nitric oxide, which were irradiated for periods ranging between 60 and 120 min. Making the reasonable assumption that, as in the case of our studies, OH is the major species depleting the hydrocarbon in their experiments, then a series of rate constants relative to isobutene (which was included in the GWR study) can be generated in the same manner as described above. The data from GWR are given in Table III relative to isobutene = 1.0.

Considering the uncertainties involved in this approach (including a lack of knowledge of the exact ozone concentrations formed in the experiments of GWR), the agreement between our results for the reaction of OH with α- and β-pinene and *d*-limonene and those shown in the fourth column of Table III is quite good and, except in the case of α-pinene, well within the estimated experimental uncertainty for our determinations. The fact that our value of OH + *d*-limonene is only slightly higher than GWR suggests that little or no O_3 was formed in their experiments, since there was less than 1 ppb formed during our irradiations.

TABLE III: Relative Reaction Rates of Monoterpene Hydrocarbons and Rate Constants[a] for Their Reaction with the OH Radical Based on Data from Grimsrud, Westberg, and Rasmussen (Ref 16)

Hydrocarbon	Structure	Rel reactivity	k_{OH}, M^{-1} s^{-1} $\times 10^{-10}$
p-Menthane	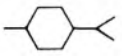	0.13	0.40
p-Cymene	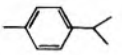	0.30	0.92 (0.78 ± 0.16)[b]
Isobutene		1.0	3.05
β-Pinene	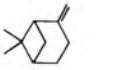	1.3	4.0 (4.1 ± 0.6)[c]
Isoprene		1.5$_5$	4.7 (4.6 ± 0.9)[d]
α-Pinene	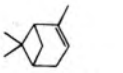	1.5$_5$	4.7 (3.5 ± 0.5)[c]
3-Carene	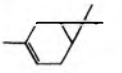	1.7	5.2
β-Phellandrene	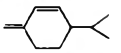	2.3	7.0
Carvomenthene	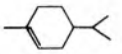	2.5	7.6
d-Limonene	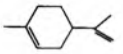	2.9	8.8 (9.0 ± 1.4)[c]
Dihydromyrcene	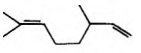	3.6	10.1
Myrcene	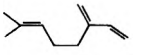	4.5	13.7
cis-Ocimene	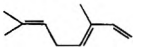	6.3	19.2

[a] Placed on an absolute basis using 3.05×10^{10} M^{-1} s^{-1} for OH + isobutene from ref 35. [b] For *p*-ethyltoluene which is structurally similar (ref 19). [c] Present work (see Table II). [d] For 1,3-butadiene which is structurally similar (ref 19).

A further check on the validity of using the results of Grimsrud, Westberg, and Rasmussen[16] to obtain OH rate constant data is provided by the values derived for the reaction of OH with *p*-cymene and isoprene. *p*-Cymene is structurally very similar to *p*-ethyltoluene, and hence the OH rate constants for these two compounds should be comparable. In fact, this is the case with the value for OH + *p*-cymene of 9.1×10^9 M^{-1} s^{-1} derived from the data of GWR being very close to that obtained for OH + *p*-ethyltoluene, 7.8×10^9 M^{-1} s^{-1}, in our previous study.[19] Likewise, isoprene is structurally similar to 1,3-butadiene, and the rate constant derived for isoprene of 4.7×10^{10} M^{-1} s^{-1} is consistent with that previously measured[19] for OH + 1,3-butadiene of 4.6×10^{10} M^{-1} s^{-1}. On the basis of these comparisons, it appears valid to use the photooxidation data of Grimsrud, Westberg, and Rasmussen[16] to obtain OH rate constant data for the series of monoterpenes which they investigated.

Conclusion

Relative rate constants have been experimentally determined for the reaction of OH with eight compounds, and these rate constants have been placed on an absolute basis using the literature value for the rate constant for OH + isobutene.[35] In the same manner, rate constants for the reaction of OH with nine additional compounds (monoterpene hydrocarbons) for

which no previous rate constants are available have been derived from data recently published by Grimsrud, Westberg, and Rasmussen.[16]

The comparatively large rate constants obtained for the ketones and monoterpene hydrocarbons indicate that they will be quite reactive in the troposphere. The implications for photochemical oxidant control strategies of the chemical reactivity of the ketones, chloroethenes, and terpenes are discussed in detail elsewhere.[50,51]

Acknowledgments. The authors gratefully acknowledge the helpful comments of Drs. R. Atkinson and E. R. Stephens during the preparation of this manuscript, G. Vogelaar and F. Burleson for the gas chromatographic analyses, and W. D. Long for valuable assistance in conducting the chamber experiments.

This work was supported in part by the California Air Resources Board (Contract No. 5-385) and the National Science Foundation–RANN (Grant No. AEN73-02904-A02). The contents do not necessarily reflect the views and policies of the California Air Resources Board or the National Science Foundation–RANN, nor does mention of trade names or commercial products constitute endorsement or recommendation for use.

References and Notes

(1) J. Heicklen, K. Westberg, and N. Cohen, Publication No. 114-69, Center for Air Environmental Studies, Pennsylvania State University, University Park, Pa., 1969.
(2) D. H. Stedman, E. D. Morris, Jr., E. E. Daby, H. Niki, and B. Weinstock, presented at the 160th National Meeting of the American Chemical Society, Chicago, Ill., Sept 14–18, 1970.
(3) B. Weinstock, E. E. Daby, and H. Niki, "Discussion on Paper Presented by E. R. Stephens", in "Chemical Reactions in Urban Atmospheres", C. S. Tuesday, Ed., Elsevier, New York, N.Y., 1971, pp 54–55.
(4) H. Niki, E. E. Daby, and B. Weinstock, *Adv. Chem. Ser.*, **No. 113,** 16 (1972).
(5) K. L. Demerjian, J. A. Kerr, and J. G. Calvert, "Advances in Environmental Science and Technology", Vol. 4, Wiley-Interscience, New York, N.Y., 1974, p 1.
(6) H. Levy, II, "Advances in Photochemistry", Vol. 9, Wiley-Interscience, New York, N.Y., 1974, p 1.
(7) S. C. Wofsy and M. B. McElroy, *Can. J. Chem.*, **52,** 1582 (1974).
(8) R. F. Hampson, Jr., and D. Garvin, Ed., "Chemical Kinetic and Photochemical Data for Modeling Atmospheric Chemistry", NBS Technical Note No. 866, June 1975.
(9) A. Levy and S. E. Miller, "Final Technical Report on the Role of Solvents in Photochemical Smog Formation", National Paint, Varnish, and Lacquer Association, Washington, D.C., 1970.
(10) M. F. Brunelle, J. E. Dickinson, and W. J. Hamming, "Effectiveness of Organic Solvents in Photochemical Smog Formation", Solvent Project Final Report, County of Los Angeles Air Pollution Control District, July 1966.
(11) E. P. Grimsrud and R. A. Rasmussen, *Atmos. Environ.*, **9,** 1014 (1975).
(12) J. E. Lovelock, *Nature (London)*, **252,** 292 (1974).
(13) E. R. Stephens and F. R. Burleson, private communication of unpublished data.
(14) R. A. Rasmussen and F. W. Went, *Proc. Natl. Acad. Sci. U.S.A.*, **53,** 215 (1965); R. A. Rasmussen, *J. Air Pollut. Control Assoc.*, **22,** 537 (1972).
(15) R. A. Rasmussen and M. W. Holdren, "Analysis of C_5 to C_{10} Hydrocarbons in Rural Atmospheres", *J. Air Pollut. Control Assoc.*, Paper no. 72-19; presented at 65th Annual Meeting (June 1972).
(16) E. P. Grimsrud, H. H. Westberg, and R. A. Rasmussen, "Atmospheric Reactivity of Monoterpene Hydrocarbons, NO_x Photooxidation and Ozonolysis", Proceedings of the Symposium on Chemical Kinetics Data for the Upper and Lower Atmosphere, Warrenton, Va., Sept 15–18, 1974; *Int. J. Chem. Kinet., Symp. No. 1,* 183 (1975).
(17) F. W. Went, *Nature (London)*, **187,** 641 (1960).
(18) G. J. Doyle, A. C. Lloyd, K. R. Darnall, A. M. Winer, and J. N. Pitts, Jr., *Environ. Sci. Technol.*, **9,** 237 (1975).
(19) A. C. Lloyd, K. R. Darnall, A. M. Winer, and J. N. Pitts, Jr., *J. Phys. Chem.*, **80,** 789 (1976).
(20) J. N. Pitts, Jr., P. J. Bekowies, A. M. Winer, G. J. Doyle, J. M. McAfee, and K. W. Wilson, "The Design and Construction of an Environmental Chamber Facility for the Study of Photochemical Air Pollution", Final Report, California ARB Grant No. 5-067-1, in preparation.
(21) Sylvania Technical Bulletin No. 0-306, Lighting Center, Danvers, Mass. 01923, 1967.
(22) J. R. Holmes, R. J. O'Brien, J. H. Crabtree, T. A. Hecht, and J. H. Seinfeld, *Environ. Sci. Technol.*, **7,** 519 (1973).
(23) G. J. Doyle, P. J. Bekowies, A. M. Winer, and J. N. Pitts, Jr., *Environ. Sci. Technol.*, accepted for publication.
(24) E. R. Stephens, "Hydrocarbons in Polluted Air", Summary Report, CRC Project CAPA-5-68, June 1973; NTIS No. PB 230 993/AS.
(25) E. R. Stephens and F. R. Burleson, *J. Air Pollut. Control Assoc.*, **17,** 147 (1967).
(26) Ozone measurement was based on calibration by the 2% neutral buffered KI method and was subsequently corrected from spectroscopic calibration data [see J. N. Pitts, Jr., J. M. McAfee, W. Long, and A. M. Winer, *Environ. Sci. Technol.*, in press].
(27) B. Weinstock and T. Y. Chang, *Tellus*, **26,** 108 (1974).
(28) T. A. Hecht, J. H. Seinfeld, and M. C. Dodge, *Environ. Sci. Technol.*, **8,** 327 (1974).
(29) L. Zafonte, P. L. Rieger, and J. R. Holmes, "Some Aspects of the Atmospheric Chemistry of Nitrous Acid", presented at 1975 Pacific Conference on Chemistry and Spectroscopy, Los Angeles, Calif., Oct 28–30, 1975; W. H. Chan, R. J. Nordstrum, J. G. Calvert, and J. N. Shaw, *Chem. Phys. Lett.*, **37,** 441 (1976).
(30) J. M. McAfee, A. M. Winer, and J. N. Pitts, Jr., unpublished results.
(31) C. C. Wang, L. I. Davis, Jr., C. H. Wu, S. Japar, H. Niki, and B. Weinstock, *Science*, **189,** 797 (1975).
(32) H. Niki and B. Weinstock, Environmental Protection Agency Seminar, Washington, D.C., Feb 1975.
(33) A. C. Lloyd, *Int. J. Chem. Kinet.*, **6,** 169 (1974).
(34) J. G. Calvert, J. A. Kerr, K. L. Demerjian, and R. D. McQuigg, *Science*, **175,** 751 (1972).
(35) R. Atkinson and J. N. Pitts, Jr., *J. Chem. Phys.*, **63,** 3591 (1975).
(36) D. Perner, D. H. Ehhalt, H. W. Patz, U. Platt, E. P. Roth, and A. Volz, "OH Radicals in the Lower Troposphere", 12th International Symposium on Free Radicals, Laguna Beach, Calif., Jan 4–9, 1976.
(37) D. D. Davis, T. McGee, and W. Heaps, "Direct Tropospheric OH Radical Measurements Via an Aircraft Platform: Laser Induced Fluorescence", 12th International Symposium on Free Radicals, Laguna Beach, Calif., Jan 4–9, 1976.
(38) E. Sanhueza and J. Heicklen, *Can. J. Chem.*, **52,** 3870 (1974).
(39) E. Sanhueza and J. Heicklen, *Int. J. Chem. Kinet.*, **6,** 553 (1974).
(40) E. Sanhueza, I. C. Hisatsune, and J. Heicklen, "Oxidation of Haloethylenes", Center for Air Environment Studies, The Pennsylvania State University, CAES Publication No. 387-75, Jan 1975.
(41) E. A. Lissi, private communication to authors of ref 40 and quoted therein.
(42) J. A. Franklin, G. Huybrechts, and G. Cillien, *Trans. Faraday Soc.*, **65,** 2094 (1969).
(43) B. W. Gay, Jr., P. L. Hanst, J. J. Bufalini, and R. C. Noonan, *Environ. Sci. Technol.*, **10,** 58 (1976).
(44) R. F. Lake and H. Thompson, *Proc. R. Soc., London, Ser. A*, **315,** 323 (1970).
(45) L. A. Ripperton and H. E. Jefferies, *Adv. Chem. Ser.*, **No. 113,** 219 (1972).
(46) E. D. Morris, Jr., and H. Niki, *J. Phys. Chem.*, **75,** 3640 (1971).
(47) S. Fischer, R. Schiff, E. Machado, W. Bollinger, and D. D. Davis, 169th National Meeting of the American Chemical Society, Philadelphia, Pa., April 6–11, 1975.
(48) S. M. Japar, C. H. Wu, and H. Niki, *Environ. Lett.*, **7,** 245 (1974).
(49) J. S. Gaffney, R. Atkinson, and J. N. Pitts, Jr., *J. Am. Chem. Soc.*, **97,** 5049 (1975).
(50) K. R. Darnall, A. C. Lloyd, A. M. Winer, and J. N. Pitts, Jr., *Environ. Sci Technol.*, in press.
(51) J. N. Pitts, Jr., A. C. Lloyd, A. M. Winer, K. R. Darnall, and G. J. Doyle, "Development and Application of a Hydrocarbon Reactivity Scale Basec on Reaction with the Hydroxyl Radical", to be presented at 69th Annua APCA Meeting, Portland, Oreg., June 27–July 1, 1976.

COMMUNICATIONS TO THE EDITOR

Infrared Spectra of Strong Acids and Bases[1]

Publication costs assisted by the Office of Naval Research

Sir: In an earlier paper on this subject[2] we reported the results of a study of the reflectance spectra of aqueous solutions of strong acids and bases; from measured values of spectral reflectance $R(\nu)$ we used a Kramers–Kronig analysis to obtain the real $n(\nu)$ and imaginary $k(\nu)$ parts of the complex index of refraction $\hat{N} = n(\nu) + ik(\nu)$ in the spectral region 400–5000 cm^{-1}. With regard to major absorption bands, our results were in general agreement with those obtained in the earlier absorption study of Falk and Giguere,[3] and we adopted their assignment of certain bands in the spectrum of HCl solutions to the ion H_3O^+.

It has been brought to our attention that our results and this assignment are in disagreement with those obtained by Ackermann,[4] who has made a quantitative study of the transmission spectra of strong acids and bases in the range 1100–4000 cm^{-1}. Ackermann reported that the absorption spectra of acids and bases are essentially similar and can be interpreted as mere radical modifications of the spectrum of water. In particular, he raised questions as to the assignment of bands to the H_3O^+ ion.

In order to check our earlier results we have remeasured the reflection spectrum of HBr at two concentrations and are including our results for spectral reflectance $R(\nu)$, $n(\nu)$, and $k(\nu)$ in Figures 1′–7′ (supplementary material; see paragraph at end of text regarding supplementary material). In order to determine the differences between the solution spectra and the spectrum of water, we have also prepared curves showing the *differences* between the absorption indices k(solution) and k(water) as a function of wave number; the curve for a 48% solution of HBr is shown in Figure 1. In spectral regions where k(solution) − k(water) is negative, the solution is more transparent than water; one such region occurs near 3400 cm^{-1} and is probably associated with a shift of the strong valence-vibration band of water; a second such region occurs near 700 cm^{-1} and is probably associated with a shift in the librational band of water.[5]

Three strong maxima occur near 2800, 1750, and 1100 cm^{-1} in the curve shown in Figure 1. Each of these maxima is in close proximity to a band reported for the H_3O^+ ion in crystal hydrates.[6–8] This agreement between the frequencies of bands observed in solution and in hydrated crystals is our major reason for attributing the solution bands to the H_3O^+ ion. Since the H_3O^+ ion is isoelectronic with NH_3 and is probably pyramidal, the observed bands appear in the anticipated spectral regions.[2]

The value k(solution) − k(water) in Figure 1 is positive throughout the entire spectral region between 3200 and 900 cm^{-1}; this indicates that the HBr solution is more strongly absorbing than water. Similar strong general absorption was noted for solutions of HCl, NaOH, and KOH in our earlier study.[2] With respect to this generally increased absorption for both acids and bases as compared with water, our results agree with those of Ackermann. However, the shapes of the absorption curves for acids and bases are quite different. No strong absorption maxima near 1750 and 1100 cm^{-1} appear in the hydroxide spectra. Although a region of strong absorption occurs near 2800 cm^{-1} in the hydroxide spectra, the shape of the hydroxide absorption curve in this region is quite different from the shape of the acid absorption curve.

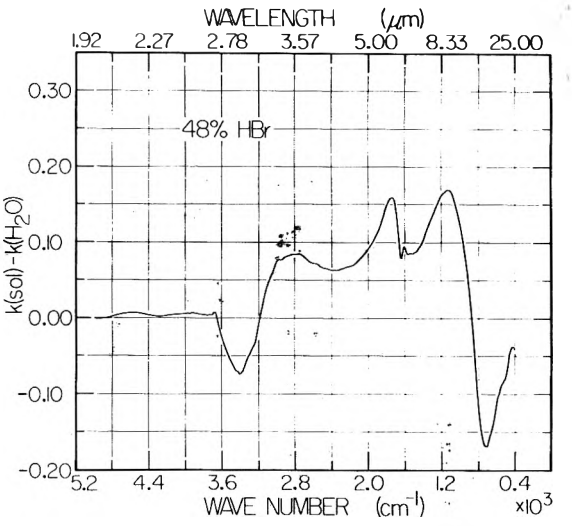

Figure 1. Difference between the spectral absorption index of a 48% aqueous solution of HBr and the corresponding index of water (T = 25 °C).

We conclude by noting that our results agree with the experimental results of Ackermann with regard to generally increased absorption of acid and hydroxide solutions throughout most of the near infrared but disagree with his results with regard to the shapes of the absorption curves. Our interpretation of the peaks shown in Figure 1 in terms of the H_3O^+ ion is in sharp disagreement with Ackermann's conclusions.

Supplementary Material Available: Spectral reflectance at near-normal incidence, refractive index, and absorption index for 24 and 48% HBr solutions (Figures 1′–7′, 7 pages). Ordering information is available on any current masthead page.

References and Notes

(1) Supported in part by the Office of Naval Research.
(2) P. Rhine, D. Williams, G. M. Hale, and M. R. Querry, *J. Phys. Chem.*, **78**, 1405 (1974).
(3) M. Falk and P. A. Giguere, *Can. J. Chem.*, **35**, 1195 (1957).
(4) T. Ackermann, *Z. Phys. Chem. (Frankfurt am Main)*, **27**, 253 (1961).
(5) D. A. Draegert and D. Williams, *J. Chem. Phys.*, **48**, 401 (1968).
(6) D. E. Bethell and N. J. Sheppard, *J. Chim. Phys.*, **50**, C72 (1953).
(7) C. C. Ferriso and D. F. Hornig, *J. Am. Chem. Soc.*, **75**, 4113 (1953).
(8) C. C. Ferriso and D. F. Hornig, *J. Chem. Phys.*, **23**, 1464 (1959).

Editor's note: Professor Ackermann[4] has communicated to us his agreement with the assignment of the solution bands to H_3O^+, based on these new data obtained with an improved experimental technique. He further indicates his conclusion that "there are two different types of characteristic changes in the infrared spectra of strong acids:

(i) The appearance of characteristic absorption bands, which can be attributed to the H_3O^+ ion;

(ii) A generally increased absorption, which can be observed in the infrared spectra of bases as well as acids."

Department of Physics
Kansas State University
Manhattan, Kansas 66506

Harry D. Downing
Dudley Williams*

Received February 13, 1976

On the Cross Section of O^- Formation in e–O_2 Collisions between 9 and 17 eV

Sir: Negative ion production in oxygen has been detected[1-3] at electron beam energies between 9 and 17 eV, in addition to the well-known direct dissociative attachment peak at 6.7 eV[3-10] produced by the reaction

$$e^- + O_2 \leftrightarrows O^- + O \qquad (1)$$

However, in some work, for example, Hagstrum,[8] no O^- ions were found in this energy range. There have been some reports on the study of the dependence of the O^- formation cross section on pressure,[4,10,11] and some suggested interpretations.[11,12]

The purpose of this work was to determine what an elementary theory predicts for the cross section for O^- formation in the energy range 9–17 eV, and to compare this theory with the available data.

The Franck–Condon principle[13] applies to the optical transition probabilities between states belonging to different electronic levels. According to this principle, the intensity in absorption from the level $v'' = 0$ is proportional to

$$vR_{k0}^2$$

where

$$v = (E_k - E_0)/h$$

and

$$R_{k0} = \int \psi_k \psi_0 \, dr$$

is the overlap integral, ψ_k and ψ_0 are the wave functions for the upper unbound level designated by k ($k = \sqrt{2mE}/h$), and the lower bound vibrational level with quantum number $v'' = 0$, respectively.

For a transition from the ground state with $v'' = 0$ to some upper state k on the energy scale, the value of R_{k0} is a maximum when the broad maximum of the oscillating outgoing wave function of the unbound state lies approximately above the bell-shaped wave function of the ground state, as shown in Figure 1.

One may hypothesize that the Franck–Condon principle might be applicable to electron–molecule collisions. With this assumption, the square of the overlap integral R_{k0}^2 is proportional to the cross section, and will be a maximum for some value of k, e.g., 6 Å^{-1}. For large k, the value of R_{k0}^2 becomes very small but not zero.

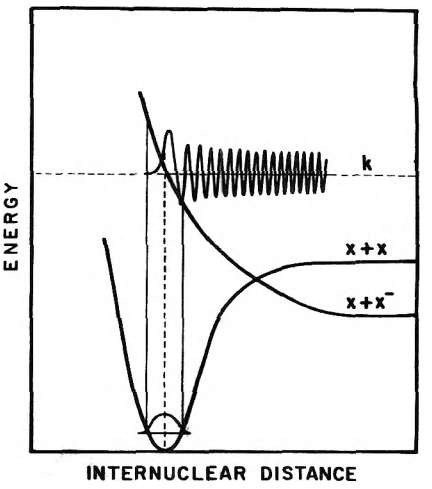

Figure 1. Hypothetical potential curves for the ground state of a diatomic molecule X_2 and a repulsive state of negative ion X_2^- with a outgoing oscillatory wave function. Vertical lines (solid and broken) are drawn at the center of the distribution and at the classical turning points of X_2. These delimit the Franck–Condon region.

Let us relate this to the energy of the incoming electrons. Consider the energy of the incoming electrons to be increased from zero onward. At about 4 eV the value of the cross section σ begins to increase. In addition when the energy of the electrons is about 7 eV, σ is maximum. For energies greater than 7 eV the value of σ decreases and becomes very small for $E \geq 9$ eV. Since the value of R_{k0} is small but nonzero (because of some net overlap after cancellation) σ is predicted to be small but nonzero at energies above 9 eV. As the energy is further increased σ stays nonzero but small, with very sharp variations. For energies of the incoming electrons $\geq$20 eV the phenomena of ion-pair formation becomes the dominant process.

Small peaks in this intermediate region (9 to 17 eV) can be explained simply in terms of the values of R_{k0}. Since the cancellation of the overlap is not the same for all values of k (i.e., $k \geq 12$ Å^{-1}) the values of R_{k0} are different, and so are the values of transition probabilities. Therefore, in this region of energy, small peaks occur because of different overlap of the wave functions for different k values.

To see if this qualitative description holds quantitatively, calculation of the overlap integrals was carried out using an IBM 370 computer. The Schrödinger equation with a repulsive potential curve of the form

$$V(x) = A \exp(-x/L) \qquad (2)$$

was transformed[14] to

$$y^2F'' + yF' + (p^2 - y^2) = 0 \qquad (3)$$

where

$$p = 2Lk$$

and

$$y = p \exp(x/2L)$$

The standard solutions[15] were used to solve eq 3 in terms of the Bessel's function with real arguments and pure imaginary large orders designated here by y and p, respectively.

The repulsive potential curve of O_2^- used was taken from Rapp and Briglia[16] and was corrected to take into account the survival probability[6] with $A = 477.76$ eV and $L = 0.2625$ Å defined in eq 2.

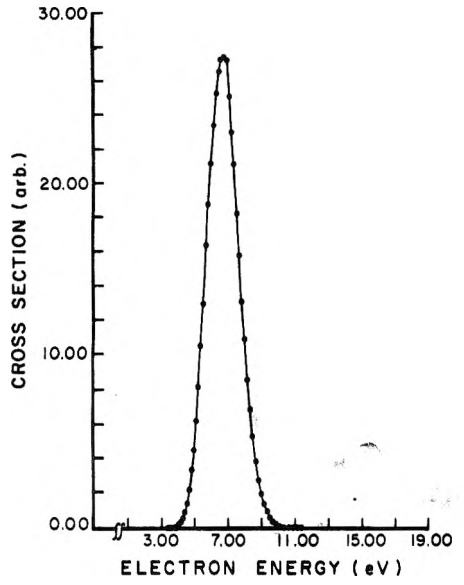

Figure 2. Cross section for negative ion formation in O_2 by electron impact vs. the incoming electron energy.

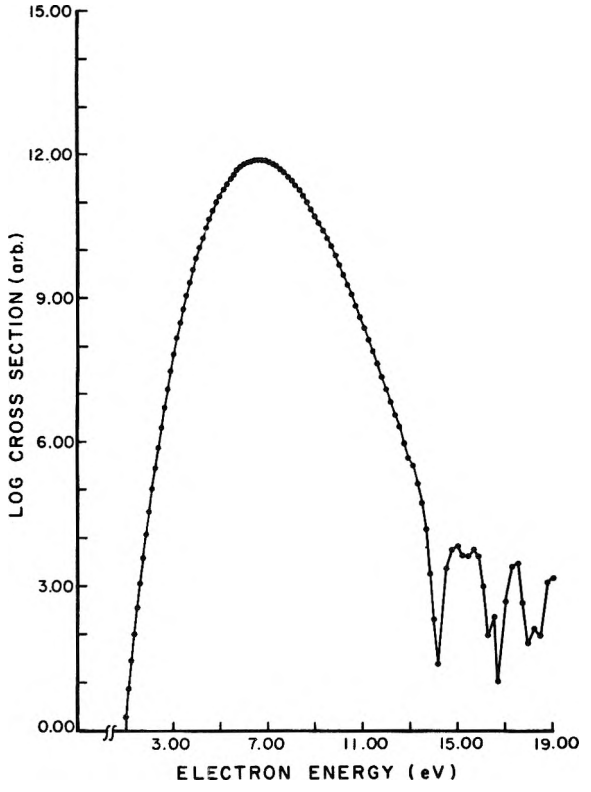

Figure 3. Log of the cross section for negative ion formation in O_2 by electron impact vs. the incoming electron energy.

For the ground state a simple harmonic oscillator solution of the Schrödinger equation for the O_2 molecule was used.

The spline fit method was used to calculate the overlap integrals with a 0.001-Å resolution. The square of the overlap integrals which is proportional to the cross section are calculated for an energy from 4.32 to 12.60 eV. The values of cross section vs. the energy are plotted as shown in Figure 2.

It can be seen that the value of cross section rises sharply at 4.7 eV, peaks at 6.69 eV, and falls off rather slowly at about 9 eV. The cross section curve is not symmetrical about its peak. Small spikes and nonzero cross section between 9 and 17 eV are not seen.

However, if we go to a higher accuracy; e.g., 1 in 10^8, we do see the spikes and nonzero cross section. This kind of accuracy is beyond the experimental measurements in these sort of experiments. However, when we plot the log of the cross section vs. energy we obtain Figure 3.

The following conclusions are drawn:

(1) Elementary theory does not support a measurable cross section in the energy range 9–17 eV. It is possible that more sophisticated theories might give a satisfactory explanation.

(2) In at least one case, the observed cross section was the effect of three-body or other processes not accounted for by the reaction

$$e^- + O_2 \rightleftarrows O^- + O$$

It is not clear whether this is true in all cases.

(3) Hagstrum's observation that the cross section is zero in the energy range 9–17 eV is in conformity with elementary theory.

Acknowledgment. I wish to acknowledge the support and help of Professor D. Rapp and Mr. Y. Jani of The University of Texas at Dallas.

References and Notes

(1) W. W. Lozier, *Phys. Rev.*, **46**, 268 (1934).
(2) W. L. Fite and R. T. Brackmann, General Atomics Report No. GA-4313, June 1963; also Proceeding of the 7th Conference on Ionized Gases, Paris, France, July, 1963.
(3) D. Rapp and D. D. Briglia, *J. Chem. Phys.*, **43**, 1480 (1965).
(4) G. J. Schulz, *Phys. Rev.*, **128**, 178 (1962).
(5) W. R. Henderson, W. L. Fite, and R. J. Brackman, *Phys. Rev.*, **183**, 157 (1969).
(6) T. F. O'Malley, *Phys. Rev.*, **155**, 59 (1967).
(7) D. Spence and G. J. Schulz, *Phys. Rev.*, **188**, 280 (1969).
(8) H. D. Hagstrum, *Rev. Mod. Phys.*, **23**, 185 (1951).
(9) P. J. Chantry, *Phys. Rev.*, **172**, 125 (1968).
(10) P. J. Chantry and G. J. Schulz, *Phys. Rev.*, **156**, 134 (1967).
(11) P. J. Chantry, *Phys. Rev.*, **55**, 185 (1971).
(12) R. K. Curran, Proceeding of the Mass Spectrometry Conference, New Orleans, 1962 (unpublished).
(13) G. Herzberg, "Spectra of Diatomic Molecules", Wiley, New York, N.Y.
(14) J. M. Jackson and N. F. Mott, *Proc. R. Soc. London, Ser. A*, **137**, 703 (1932).
(15) H. Bateman, "Higher Transcendental Function", Vol. 2, California Institute of Technology, 1953, p 87.
(16) D. Rapp and D. D. Briglia, Lockheed Missiles and Space Co., Report No. LMSC 6-74-64-65 (1964).
(17) Address correspondence to the Department of Physics, York University, Downsview, Ontario, M3J 1P3 Canada.

Department of Physics
The University of Texas at Dallas
Richardson, Texas 75080

M. Yaqub Mirza[17]

Received July 3, 1975

Anisole Radical Cation Reactions in Aqueous Solution

Publication costs assisted by the Danish Atomic Energy Commission

Sir: Recently O'Neill, Steenken, and Schulte-Frohlinde[1] published a paper in which they discuss the formation and properties of radical cations of methoxylated benzenes in aqueous solution.

Pulse radiolysis work in our laboratory on radical cations of methylated benzenes[2] led us to make studies of radical cations of methoxylated benzenes, especially anisole, in order to compare their properties with those of the methylated compounds.

For anisole, the absorption band of the OH adduct is λ_{max} 320 nm, the extinction ϵ_{320} 3400 M^{-1} cm^{-1}, and the decay constant for the bimolecular reaction $2k = 1.4 \times 10^9$ M^{-1} s^{-1}. The H adduct absorbs at the same wavelength with ϵ_{320} 4000 M^{-1} cm^{-1} and $2k = 3.8 \times 10^9$ M^{-1} s^{-1}. We measured the spectrum of the anisole radical cation produced from the OH adduct in acid solution (pH 0–3) and in neutral (pH 6–10) produced by SO_4^- formed in the reaction of 2–10 mM $K_2S_2O_8$ with the solvated electron. The spectrum consists of two bands λ 280 nm, ϵ_{280} 7400 M^{-1} cm^{-1}, and λ 430 nm, ϵ_{430} 3200 M^{-1} cm^{-1}. These data are in good agreement with ref 1.

The assignment of this transient to the anisole radical cation is additionally confirmed by its unreactivity toward oxygen and the reactions with Fe^{2+} and OH^-.

Oxygen saturation of the acid solution of the anisole removes the H adduct absorption band from the transient spectrum by scavenging the H atom forming HO_2, but has no influence on the decay kinetics of the 280- and 430-nm bands, which is a characteristic cationic behavior.[2,3] The radical cation reacts with ferrous ions (eq 1) with a rate constant k_1

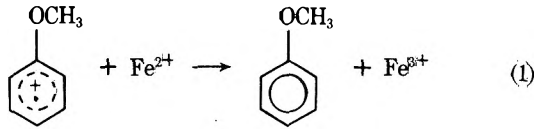

(1)

$= 6 \times 10^8$ M^{-1} s^{-1} at pH 1.0. In the Fenton reagent system Jefcoate and Norman[4] found a drastic decrease in the yield of hydroxylated anisoles (the yield decreases from 14.6 to 0.018) when going from pH 3.6 to 0.8. This is to be expected as the OH adduct in strong acid solution is converted into the radical cation and the reaction of the radical cation with ferrous regenerate the parent molecule, so that the net reaction in the system is an oxidation of the ferrous ions.

In alkaline solution (pH 8–11) containing 5 mM $K_2S_2O_8$, the anisole radical cation reacts with OH^- (eq 2) with a rate

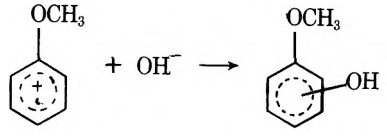

(2)

constant $k_2 = (1.0 \pm 0.2) \times 10^9$ M^{-1} s^{-1}. The SO_4^- radical reacts with the anisole forming the radical cation with a rate constant of 4.9×10^9 M^{-1} s^{-1}.[1] Even at pH 11 with 10^{-4} M anisole about 90% of the SO_4^- radicals will react with the substrate and not with OH^- to form OH radicals ($k_{SO_4^- + OH^-} = 6.5 \times 10^7$ M^{-1} s^{-1}).[5] The rate constant for reaction 2 was determined by the decay rate of the radical cation at 430 nm as function of the OH^- concentration. The product of reaction 2 was identified by the buildup of a spectrum similar to and with the same extinction as that measured in N_2O saturated solution for the OH adduct. The kinetics of reactions 1 and 2 are ionic strength dependent and the plot log k/k_0 vs. $\mu^{1/2}/(\mu^{1/2} + 1)$ (Figure 1) is consistent with the species having a unit positive charge.

In a saturated anisole solution (14 mM) the anisole radical cation reacts with the solute, eq 3 (eq 1 in ref 1). The rate constant for this reaction measured in acid solution (pH 0–2) is $k_3 = 1 \times 10^7$ M^{-1} s^{-1}. The product of this reaction has absorption bands at 380–420 nm (Figure 2) with λ_{max} 405 nm and ϵ_{405} 2500 M^{-1} cm^{-1}. The product decays in a second-order reaction with a rate constant $2k = 2 \times 10^9$ M^{-1} s^{-1}.

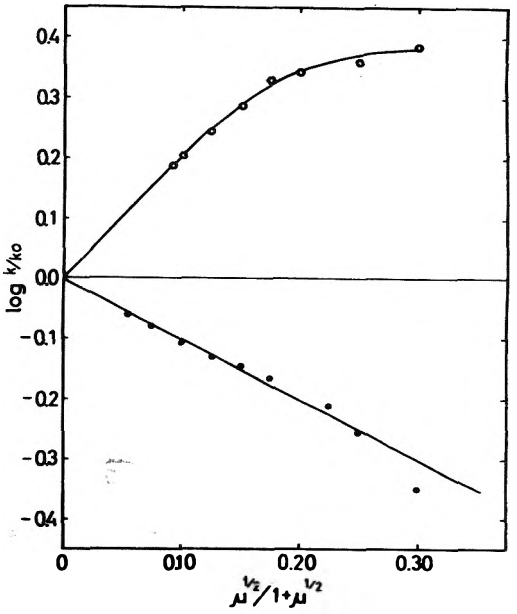

Figure 1. The effect of ionic strength, μ, on the rate of anisole radical cation reactions: O, reaction with Fe^{2+}, eq 1; ●, reaction with OH^-, eq 2.

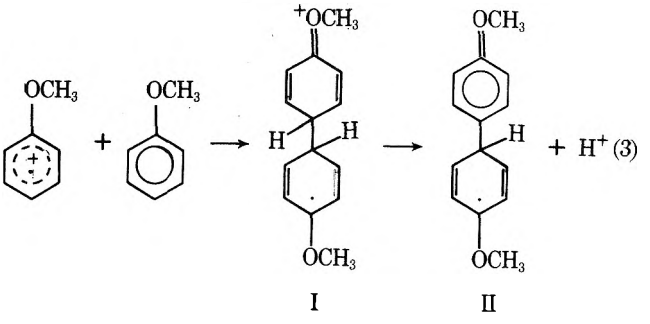

(3)

We assume the absorption at 380–420 nm to be the absorption of II on the basis of its second-order decay and the similarity to the absorption spectrum of the biphenyl H adduct.[3] An indication of the formation of such dimeric products is found in the nitromethane–boron trifluoride system, where Allara et al.[6] concluded that the dimeric radical cation is derived from a reaction between the monomeric radical cation and the substrate. They observed the same ESR spectrum for the radical cation for anisole and 4,4′-dimethoxybiphenyl and found that the latter compound was a product of the reaction of anisole.

An electrophilic attack by the radical cation on the electron-rich parent compound molecule seems to be an important ability of radical cations of aromatic compounds. It was observed in anodic oxidation of mesitylene[7] and suggested as an important process in oxidative substitution of arenes by cobalt(III).[8] However, it was not observed for radical cations of methylated benzenes,[2] but conditions with low solubility of the substrates and low stability of the corresponding radical cations are unfavorable in the water system. A fast reaction with the solute confirms the assignment of the radical cation to a monomer species.

As pointed out by O'Neill et al.,[1] the anisole radical cation in dilute anisole solution (10^{-4} M) decays in a second-order

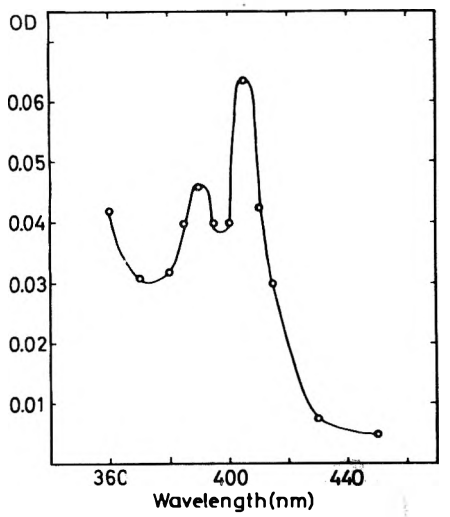

Figure 2. Transient absorption spectra of the product from the reaction of the anisole radical cation with the solute molecule, eq 3.

reaction with a rate constant in neutral solution of $2k = 1 \times 10^9$ M^{-1} s^{-1}. We find the kinetics of this reaction strongly dependent on pH, which qualitatively may be explained essentially as an ionic strength effect. The rate constant measured at pH 0 and 1 is $2k = 1.2 \times 10^{10}$ and 4×10^9 M^{-1} s^{-1}, respectively. The determination was made with and without oxygen which had only a minor influence on the rate, but from the higher yield of the product in oxygen-saturated solutions we estimate that the H adduct reacts with the radical cation at a rate corresponding to the rate given for the OH adduct.[1] The product of the bimolecular reaction has a broad weak absorption in the region of 660–850 nm with λ_{max} 810 nm and $\epsilon_{810} \simeq 300$ M^{-1} cm^{-1} taking the yield of the product equal to half of the anisole radical cation yield. The absorption at 810 nm decays by first order with a half-life of 90 μs. This first-order decay may correspond to the deprotonation reaction that is considered to be a step leading to a biphenyl product. It was found that 2,2′,5,5′-tetramethoxydiphenyl was a product of 1,4-dimethoxybenzene radical cation.[9]

In the case of methylated benzenes the main decay path for their radical cations is the proton loss from the methyl group leading to the benzyl radical.[2] As O'Neill et al.[1] we find no indications of a proton split off from the methyl group in the anisole and higher methoxylated benzenes. A pH-independent first-order decay of the radical cation was not observed. This is in good agreement with the molecular orbital calculations[10] which show the increase of negative charge on a methyl group under ionization of anisole, whereas the methyl group of toluene becomes more positive.

Concerning the formation of radical cations from the cyclohexadienyl radical, O'Neill et al.[1] assume that the rate of H-atom abstraction from substituents by the OH radical is two orders of magnitude lower than the rate of addition. This assumption does not apply in the case of methylated benzenes,[11] where for toluene the rate for the direct H abstraction is only about one order of magnitude lower than the rate of addition. Furthermore this rate is proportional to the number of methyl substituents which yields an appreciable amount of directly formed methylbenzyl radicals from the higher methylated benzenes.

We find strong indications of a direct H abstraction reaction in the methoxylated benzenes too. In a 0.6 M NaOH, N_2O-saturated solution of anisole, we observe a transient with a peak at 280 nm that can be ascribed to the phenoxymethyl radical, as O^- is known to abstract an H atom from the methyl group rather than add to the ring.[11,12] The spectrum of the OH adduct in neutral solution has a shoulder in this region, which could be characteristic of the OH adduct spectrum, but may as well be explained by an absorption due to a second radical, the phenoxymethyl radical.

Further support for a direct H-abstraction reaction by OH radicals is the slightly lower yield of the radical cation in acid solution (5–10% lower) as compared to the yield in neutral solution. The yields of the primary radicals, OH in acid and e_{aq}^- (SO_4^-) in neutral solution, are about equal, which indicates that a small fraction of OH radicals reacts in another reaction if we assume a complete conversion of the OH adduct into the radical cation, which is the case for the methylated benzenes.[2] The transient spectrum obtained with 1,3,5-trimethoxybenzene both in neutral N_2O-saturated and at pH 1 in argon-saturated solutions shows a peak at 260 nm that can be ascribed to the product of a direct H-atom abstraction from the methyl group. Additionally, phenol is recognized as a product in γ-radiolysis[13] and in Fenton reagent hydroxylation[4] of anisole. In the last case, the phenol yield is independent of pH, in contrast to the yield of methoxyphenols, and constitutes about 7% of the yield of methoxyphenols at pH 3.6. We consider the H-atom abstraction from the methyl group to be a possible source of phenol. This point may be important to the explanation of the lower yields of radical cations obtained in acid solution in relation to the OH-radical yield. However, it does not seem to explain some very low yields, 45–60%, obtained by O'Neill et al.[1]

References and Notes

(1) P. O'Neill, S. Steenken, and D. Schulte-Frohlinde, *J. Phys. Chem.*, **79**, 2773 (1975).
(2) K. Sehested, J. Holcman, and E. J. Hart, to be submitted for publication.
(3) K. Sehested and E. J. Hart, *J. Phys. Chem.*, **79**, 1639 (1975).
(4) C. R. E. Jefcoate and R. O. C. Norman, *J. Chem. Soc. B*, 48 (1968).
(5) E. Hayon, A. Treinin, and J. Wilf, *J. Am. Chem. Soc.*, **94**, 47 (1972).
(6) D. L. Allara, B. C. Gilbert, and R. O. C. Norman, *Chem. Commun.*, 319 (1965).
(7) L. Eberson in "Organic Electrochemistry", M. M. Baizer, Ed., Marcel Dekker, New York, N.Y., 1973, p 462.
(8) J. K. Kochi, R. T. Tang, and T. Bernath, *J. Am. Chem. Soc.*, **95**, 7114 (1973).
(9) A. Nishinaga, H. Hayashi, and T. Matsuura, *Bull. Chem. Soc. Jpn.*, **47**, 1813 (1974).
(10) B. Cantone, F. Grasso, and S. Pignataro, *Mol. Phys.*, **11**, 221 (1966).
(11) K. Sehested, H. Corfitzen, H. C. Christensen, and E. J. Hart, *J. Phys. Chem.*, **79**, 310 (1975).
(12) P. Neta and R. H. Schuler, *Radiat. Res.*, **64**, 233 (1975).
(13) J. H. Fendler and G. L. Gasowski, *J. Org. Chem.* **33**, 2755 (1968).

Danish Atomic Energy Commission
Research Establishment Risø
Accelerator Department
DK-4000 Roskilde, Denmark

Jerzy Holcman*
Knud Sehested

Received March 10, 1976

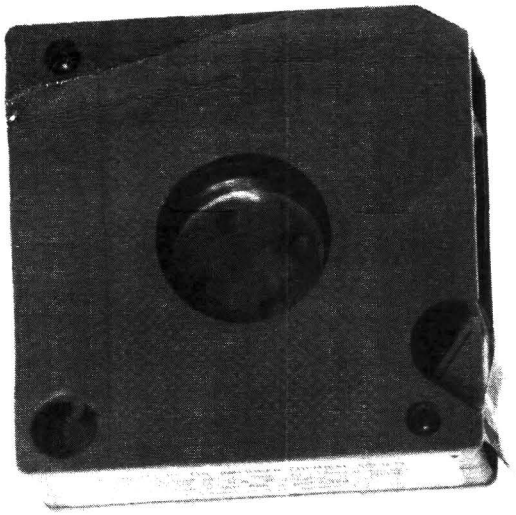

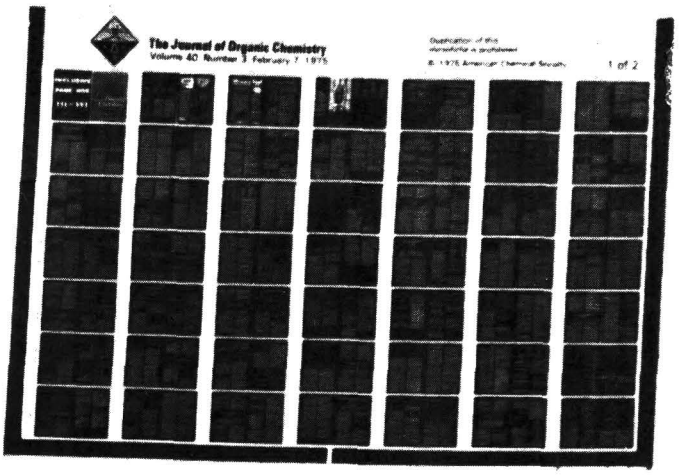

MICROFORMS

American Chemical Society publications in microform

MICROFILM OR MICROFICHE?

With the ACS microform program you can receive either, or both

Microfilm

All periodical publications back to volume one

Copying privileges included with current subscriptions

All non-print supplementary materials provided free on microfiche

Archival quality silver halide film supplied as you request; positive or negative; 16 or 35mm; cartridge, reel, or cassette.

For microfilm information:

Special Issues Sales
American Chemical Society
1155 16th Street, N.W.
Washington, D.C. 20036
(202) 872-4363

Microfiche

Current issues of primary journals, beginning with January 1975

Individual issues or full volumes available

Supplementary materials also available on microfiche

Fiche supplied are archival quality silver halide, negative, 105 x 148mm (4" x 6"); 24x, with eye legible headers, start and end targets, and page numbers

For microfiche information:

Business Operations
Books and Journals Division
American Chemical Society
1155 16th Street, N.W.
Washington, D.C. 20036
(202) 872-4444